

# Development of Cost-Effective Nitrogen-Doped Carbonaceous Materials for Oxygen Reduction Reaction in Polymer Electrolyte Membrane Fuel Cells

Thesis Submitted to AcSIR for the Award of  
the Degree of  
DOCTOR OF PHILOSOPHY  
In Chemical Sciences



By  
T. Palaniselvam  
Registration Number: 10CC11J26013

Under the guidance of  
Dr. Sreekumar Kurungot

CSIR-National Chemical Laboratory  
Pune - 411008, India.

## DECLARATION

I, hereby declare that all the experiments embodied in this thesis entitled, **“DEVELOPMENT OF COST-EFFECTIVE NITROGEN-DOPED CARBONACEOUS MATERIALS FOR OXYGEN REDUCTION REACTION IN POLYMER ELECTROLYTE MEMBRANE FUEL CELLS”** submitted for the degree of Doctor of Philosophy in Chemistry, to the AcSIR-NCL have been carried out by me at the Physical and Materials Chemistry Division, National Chemical Laboratory, Pune - 411 008, India, under the supervision of Dr. K. Sreekumar. The work is original and has not been submitted in part or full by me, for any degree or diploma to this or to any other University.

Date: 07-07-2014



T. Palaniselvam

Physical and Materials Chemistry Division,  
National Chemical Laboratory,  
Pune - 411 008. India.



# सीएसआयआर-राष्ट्रीय रासायनिक प्रयोगशाला

(वैज्ञानिक तथा औद्योगिक अनुसंधान परिषद)

डॉ. होमी भाभा मार्ग, पुणे - 411 008. भारत

## CSIR-NATIONAL CHEMICAL LABORATORY

(Council of Scientific & Industrial Research)

Dr. Homi Bhabha Road, Pune - 411008. India



### CERTIFICATE

This is to certify that the work incorporated in the thesis entitled, **“DEVELOPMENT OF COST-EFFECTIVE NITROGEN-DOPED CARBONACEOUS MATERIALS FOR OXYGEN REDUCTION REACTION IN POLYMER ELECTROLYTE MEMBRANE FUEL CELLS”** submitted by **Mr. T. Palaniselvam**, has been carried out by him under my supervision at the Physical and Materials Chemistry Division, National Chemical Laboratory, Pune, 411 008, India. All the materials from other sources have been duly acknowledged in the thesis.

Date: 7-7-2014

Place: Pune

**Dr. Sreekumar Kurungot**

(Research Guide)

Communication  
Channels

NCL Level DID : 2590  
NCL Board No. : +91-20-25902000  
EPABX : +91-20-25893300  
: +91-20-25893400

FAX

Director's Office : +91-20-25902601  
COA's Office : +91-20-25902660  
COS&P's Office : +91-20-25902664

WEBSITE

[www.ncl-india.org](http://www.ncl-india.org)

*Dedicated to*

*My Family . . . .*

## *Acknowledgments*

At this point of the journey of my life, I wish to thank many people who have contributed significantly to help me reach this level. Thus, I believe that acknowledging their effort could be a humble way to remember them as I complete this dissertation.

At this juncture, I take it as my privilege to express my gratitude to my Research Guide Dr. Sreekumar Kurungot who introduced me to the electrochemistry world. I have been fortunate enough to have an advisor who gave me freedom to explore on my own ideas with essential guidance to help me recover back when at times of uncertainty. He taught me how to express ideas and focus from miniature to a wide spectrum. I admire his sincerity to do high quality of research which I would like to follow for the rest of my life. I believe that his constructive criticism had helped me improve my patience in all quarters of my life apart from science. The morning meetings, monthly plans, work presentations and weekly presentations gave me the confidence to start an independent research career. Having spent five years under his guidance, all I can say is that, he has been a fatherly figure during my stay at NCL. His patience and support helped me overcome many precarious situations and reach this awaiting point of my life. I also extend my deep thanks to his family, Nihara madam, Neerav and Niranjana for giving me cherished moments.

I wish to thank Dr. Sourav Pal, the Director, CSIR-NCL for providing me all infrastructural facilities. I am also grateful to Dr. Anil Kumar, Head and Chairman of Physical and Materials Chemistry Division, for allowing me to use all the available facilities in the division.

My special and sincere thanks go to Dr. K. Vijayamohanan for all his support, suggestions and advices during the course of this study. I am very grateful to Dr. Rahul Banerjee for an effective collaboration, help, optimistic criticism, and encouragement during the course of this study. My sincere

gratitude to his student Bishu P. Biswal for his productive collaboration and significant role in ZIF related experiments.

I would like to thank the rest of my DAC members Dr. K. Krishnamoorthy and Dr. Sudip Roy for their encouragement, perceptive comments, and hard questions.

My earnest gratitude to Drs. P. A. Joy, A. Lele, U. K. Kharul, S. Ogale, Neelima, B. L. V. Prasad, C. Gopinath, T. Raja, Nithyananthan and C. P. Vinod for their advice and help. I am highly indebted to Dr. K. R. Patil, Mr. A. B. Gaikwad, Mr. Naren Mr. Anuj and Mr. Ketan for helping me in characterizing my samples. The timely help by Mr. Deepak and Mr. Punekar in the Physical Chemistry office deserves the best of my compliments. The entire library staffs are gratefully acknowledged for providing excellent facilities. Student Academic Committee is gratefully acknowledged for their speedy response. Most importantly, I gratefully acknowledge CSIR for the financial support throughout.

I can never forget the help from my labmates, Beena, Kuttan, "Dholya" Vishal, Hussain, Dhanu, Joy, Vinisha, "Bighu" Bihag, Harshitha, Vrushali, Bipin, Ranjith, Nilesh, "BHU" Santosh, Pandiaraj, Kashyap, Robi, Rajith, Sidhu, Neeta, Sachya, Prithe, Ajinkya, Manzoor who have helped me in all possible ways during the tenure of my work at NCL. I would like to convey my thanks and regards to the projects students Irshad and Manila who have worked with me.

I would also like to express my sincere thanks to all my divisional and other divisional colleagues for their encouragement and support. A special thanks goes to my Tamil seniors Vijay anna, Nellai Nagaraj, Suresh, Sridar, Mohan, Dharma, and friends Venki, Senthil, Ramsundar, Perumal, Arul, Deva, Senthil-Rajambal, Vasu, Suresh, Ashok, Venkat, Mohan, Periyasamy, Kutti Mani and Balaji anna & Family.

I express my deep gratitude to my dearest friends 'Maman' Edwin, 'Karuva' Lenin and Dhanalakshmi akka who were always with me during my

tough times and gave me the strength to overcome it. I extend my gratitude to my senior, Kanna anna for his love, advice, help, constant support and encouragement.

I find no words to express my feelings for my parents (Thangavelu-Vasanth) whose moral support, love and constant encouragement have helped me reach this level. I wish to thank my brothers Rajangam, Kabilar and sister Rathi for their support. I definitely need to acknowledge my dear brother Kanna and who inspired me to do M.Sc and Ph.D.

I wish to express my gratitude to my in-laws, Mohan Mama, Selvi Amma, Ela-Priya, and 'Alumoonchi' Pavai for their encouragement, love and moral support.

Finally, I deem that I could not find any word to express my special thanks to my wife Silambarasi for standing behind me throughout my Ph.D. and for several wakeful nights she had to bear with, in helping me to complete my paper work and dissertation. I am greatly indebted to my beloved daughter 'Kuttima' Nethra whose smile always reminds me to 'never give up' and to whom I dedicate myself to. I owe all of my accomplishment to both of them.

Above all, I thank God, my good father, his almighty, for his blessings.

T. Palaniselvam

## List of Abbreviations

<b><u>Abbreviation</u></b>	<b><u>Expansion</u></b>
<b>AFC</b>	Alkaline Fuel Cells
<b>AEMFCs</b>	Anion Exchange Membrane Fuel Cells
<b>BGr</b>	Boron Doped Gr
<b>CO</b>	Carbon Monoxide
<b>CNF</b>	Carbon Nanofibers
<b>CNS</b>	Carbon Nano Structures
<b>CNTs</b>	Carbon Nanotubes
<b>CA</b>	Chronoampermetric
<b>CE</b>	Counter Electrode
<b>CV</b>	Cyclic Voltammetry
<b>DOE</b>	Department of Energy
<b>DMFCs</b>	Direct Methanol Fuel Cells
<b>EDAX</b>	Energy Dispersive X-ray Analysis
<b>EXAFS</b>	Extended X-ray Absorption Fine Structure
<b>Gr</b>	Graphene
<b>GO</b>	Graphene Oxide
<b>GQDs</b>	Graphene Quantum Dots
<b>HOMO</b>	Highest Occupied Molecular Orbital
<b>HRTEM</b>	High Resolution Transmission Electron Microscopy
<b>ICEs</b>	Internal Combustion Engines

<b>K-L equation</b>	Koutecky-Levich equation
<b>LUMO</b>	Lowest Unoccupied Molecular Orbital
<b>MEA</b>	Membrane Electrode Assembly
<b>MCFCs</b>	Molten Carbonate Fuel Cells
<b>MWCNT</b>	Multiwalled Carbon Nanotube
<b>NGr</b>	Nitrogen Doped Graphene
<b>N-CNS</b>	Nitrogen-Doped Carbon Nanostructures
<b>NPMC</b>	Non-Pt Metal Catalysts
<b>ORR</b>	Oxygen Reduction Reaction
<b>PFSA</b>	Perfluoro Sulphonic Acid
<b>PAFC</b>	Phosphoric Acid Fuel Cells
<b>PBI</b>	Polybenzimidazole
<b>PEFCs</b>	Polymer Electrolyte Fuel Cells
<b>P-Gr</b>	Phosphorus Doped Gr
<b>PLQY</b>	Photoluminescent Quantum Yield
<b>RE</b>	Reference Electrode
<b>RDE</b>	Rotating Disc Electrode
<b>RRDE</b>	Rotating Ring Disc Electrode
<b>SEM</b>	Scanning Electron Microscopy
<b>SWCNT</b>	Single Walled Carbon Nanotube
<b>SOFC</b>	Solid Oxide Fuel Cells

<b>ToF-SIMS</b>	Time of Flight Secondary Ion Mass Spectroscopy
<b>TEM</b>	Transmission Electron Microscope
<b>TPB</b>	Triple Phase Boundary
<b>VA-CNT</b>	Vertically Aligned Carbon Nanotubes
<b>WE</b>	Working Electrode
<b>XRD</b>	X-ray Diffraction
<b>XPS</b>	X-ray Photo Electron Spectroscopy
<b>YSZ</b>	Ytria Stabilized Ziconia
<b>ZIF</b>	Zeolitic Imidazolate Framework

# Table of Contents

	<b>Abstract</b>	1-6
	<b>Chapter 1</b>	
	<b>Introduction</b>	7-62
1.1	General Background	8
1.2	Fuel Cells	8
1.3	Advantage of Fuel Cells	10
1.4	Classification of Fuel Cells	10
1.4.1	Solid Oxide Fuel Cells	12
1.4.2	Molten Carbonate Fuel Cells	12
1.4.3	Phosphoric Acid Fuel Cells	13
1.4.4	Direct Methanol Fuel Cells	13
1.4.5	Alkaline Fuel Cells	14
1.4.6	Anion Exchange Membrane Fuel Cells	15
1.4.7	Proton Exchange Membrane Fuel Cells	15
1.5	Working Principles of Polymer Electrolyte Fuel Cells	17
1.6	Barricades of PEFC's Commercialization	19
1.7	Catalysts in Fuel Cells	20
1.8	Electrochemical Oxygen Reduction Reaction	21
1.9	Mechanism of ORR	22
1.10	Pt based Catalyst for ORR	23
1.11	Pt Based Alloy	24
1.12	Pt Based Core Shells	26

1.13	Role of Carbon Nanostructures	27
1.13.1	Fullerenes	28
1.13.2	Carbon Nanotubes	29
1.13.3	Carbon Nanofiber	30
1.13.4	Graphene	32
1.13.5	Graphene Quantum Dots	33
1.14	Non-Noble Electrocatalysts	35
1.14.1	Metal-Macrocyclic Compound for ORR	35
1.14.2	M-N/C Catalyst for ORR	37
1.14.3	Influences of Surface Properties of Carbon	38
1.14.4	Type and Content of Metal Ions	39
1.14.5	Nature and Structure of M-N/C Active Sites	40
1.14.6	Metal-free Nitrogen-Doped Carbon Nanostructures for ORR	41
1.14.6.1	Nature of Nitrogen-Doped Carbon Active Site	41
1.14.6.2	Chemical Structure of N-Doped Carbon Active Sites	42
1.14.7	Overview of N-CNS towards ORR	43
1.14.8	Mechanism of ORR on N-Doped Graphene	45
1.14.9	Other NPMC Electrocatalysts	48
1.14.10	Present Status of NPMC	50
1.14.11	Effect of Edge Planes of Carbon Nanostructures	51
1.15	Scope and Objectives of the Present Study	51
1.16	References	54

## Chapter 2

	<b>Experimental Methods and Characterization Techniques</b>	63-83
2.1.1	Chemicals Required	64
2.1.2	Preparation of Iron-Nitride Doped Carbon Catalyst	64
2.1.3	Preparation of Pt based Electrocatalyst by Modified Polyol Process	65
2.1.4	Preparation of Graphene Oxide	66
2.1.5	Preparation of Graphene from Graphene Oxide	67
2.1.4	Electrode Preparation	67
2.2	Material Characterization Techniques	68
2.2.1	Transmission Electron Microscopy	68
2.2.2	Scanning Electron Microscopy and Energy Dispersive X-ray Analysis	69
2.2.3	Powder X-ray diffraction pattern	70
2.2.4	X-ray Photoelectron Spectroscopy	72
2.2.5	Raman Spectroscopy	74
2.2.6	Surface Area Measurements	76
2.3	Electrochemical Study	78
2.3.1	Cyclic Voltammetry	78
2.3.2	Rotating Disc Electrode	79
2.4	References	81

## Chapter 3

	<b>Facile Preparation of Iron Nitride-Doped Carbon Nanofiber as a Pt-Free Electrocatalyst and for the Development of Low-Pt Electrocatalyst</b>	84-134
3.1	Introduction	85
3.2	Experimental Section	88
3.2.1	Synthesis of FeN <sub>x</sub> CNF Catalyst:	88
3.2.2	Preparation of PtFeN <sub>x</sub> CNF	89
3.3	Results and Discussion	90
3.3.1	XRD Analysis	90
3.3.2	Raman Spectra Analysis	91
3.3.3	XPS analysis	92
3.3.4	EDAX analysis	95
3.3.5	HRTEM Analysis	96
3.3.6	Surface Area Measurements	101
3.3.7	Electrochemical studies	102
3.3.7.1	Cyclic Voltammetric Analysis	102
3.3.7.2.	Rotating Disc Electrode (RDE) Method	103
3.3.8	Conductivity Measurements	106
3.3.9	Stability test	107
3.3.10	Mechanism	109
3.3.11	Development of low-Pt Electrocatalyst	110

3.3.11.1	HRTEM Analysis	111
3.3.11.2	XPS Analysis	114
3.3.11.3	XRD Analysis	118
3.3.11.4	Raman Spectra Analysis	120
3.3.11.5	Electrochemical Studies	121
3.3.11.6	Single Cell Analysis	125
3.4	Conclusions	128
3.5	References	131

## **Chapter 4**

### **An Efficient Oxygen Reduction Electrocatalyst From Graphene by Simultaneously Generating Pores and Nitrogen Doped Activesites** 135-161

4.1	Introduction	136
4.2	Materials and Methods	139
4.2.1	Synthesis of Graphene Oxide	139
4.2.2	Synthesis of Partially Reduced GO	140
4.2.3	Pore Generation and Nitrogen Doping	140
4.3	Results and Discussion	142
4.3.1	HRTEM Analysis	142
4.3.2	XRD Analysis	146
4.3.3	Raman Spectra Analysis	147
4.3.4	X-ray Photoelectron Spectroscopy Analysis	148

4.3.5	EDAX Analysis	152
4.3.6	Electrochemical Studies	153
4.4	Conclusions	157
4.5	References	159

## Chapter 5

### **Novel Route for the Preparation of Nanoporous Graphene by Quantum Dots Removal and its Conversion as Potential Oxygen Reduction Electrocatalyst *via* Nitrogen Doping**

162-200

5.1	Introduction	163
5.2	Experimental Method	166
5.2.1	Preparation of Graphene Oxide	166
5.2.2	Preparation of Graphene From GO	166
5.2.3	Preparation of Porous Graphene and Graphene Quantum Dots by Hydrogen Peroxide Oxidation of Gr.	167
5.2.4	Preparation of Nitrogen-Doped Porous Graphene	167
5.3	Results and Discussion	168
5.3.1	HRTEM Analysis.	168
5.3.2	Optical Property Study	171
5.3.3	Mechanism	174
5.3.4	FT-IR Spectra	175
5.3.4	Surface Area Measurements	176
5.3.5	XRD and Raman Spectra Analysis	179
5.3.4	XPS Analysis	181

5.3.5	Electrochemical Studies	183
5.3.5.1	Cyclic Voltammetry	183
5.3.5.2	Rotating Ring Disc Electrode Method	184
5.3.6	Single Cell Polarization Test	188
5.3.7	Structural Analysis	190
5.4	Conclusions	194
5.5	References	196

## Chapter 6

	<b>Zeolitic Imidazolate Frameworks Derived Hollow Core Nitrogen-Doped Carbon Nano Structures for Oxygen Reduction Reaction in Fuel Cells</b>	201-230
6.1	Introduction	202
6.2	Experimental Section	205
6.2.1	General Remarks	205
6.2.2	Synthesis of ZIF-70	205
6.2.3	Synthesis of ZIF-68 and 69	205
6.2.4	Synthesis of Fe-N-Doped Porous Carbon (FeNC-70)	206
6.3	Results and Discussion	207
6.3.1	HRTEM Analysis	207
6.3.2	Surface Area Measurements	209
6.3.3	Thermogravimetry Analysis	211
6.3.4	XRD Analysis	213
6.3.5	XPS Analysis	215
6.3.6	EDAX Analysis	217

6.3.7	Raman Spectral Analysis	218
6.3.8	Electrochemical Studies	219
6.3.8.1	Cyclic Voltammetry	219
6.3.8.1	Rotating Disc Electrode Method	221
6.3.8.3	Koutecky-Levich Plots	221
6.3.8.4	Accelerated Durability Test	223
6.3.8.5	Methanol Tolerance Study	224
6.3.9	Structure of Active Sites	225
6.4	Conclusions	226
6.5	References	228

## **Chapter 7**

<b>Conclusions</b>	231-239
--------------------	---------

<b>List of Publications</b>	240-241
-----------------------------	---------

<b>Erratum</b>	242
----------------	-----

## Abstract

One of the main challenges for human beings in the near future is global warming caused by various energy sources. This alarming issue has prompted the mankind to urgently develop efficient cleaner energy sources to replace the existing fossil fuel-based energy sources. To attain a more sustainable society with adequate renewable energy and less environmental pollution, more versatile, robust and efficient approaches in electric energy storage and conversion are needed. In this regard, Polymer Electrolyte Fuel Cells (PEFCs) are contemplated as the alternative energy source to afford cleaner energy for catering diverse applications. In the last few decades, much attention has been given for the development of commercially viable PEFCs. To date, the state-of-the-art Pt or Pt-based alloys supported on carbon nano structures (CNSs) are the best options for the electrocatalysis in PEFCs. However, fluctuating cost associated with scarcity and sluggish kinetics of ORR on Pt significantly hampers the prospects of commercialization of PEFCs. To tackle this challenge, development of potential Pt-free or low-Pt electrocatalysts which possess matching performance characteristics of the state-of-the-art catalysts has become an urgent requirement.

The inspiration for the present thesis work is from the potential application of nitrogen doped carbonaceous materials in electrochemical devices such as biosensors, lithium-ion batteries etc. These hetero atom doped catalysts are specifically regarded as realistic candidates for the replacement of Pt in PEFCs. For example, nitrogen-doped carbon nanotubes have shown excellent activity towards the oxygen reduction reaction (ORR) which in some cases are even comparable to Pt. This gives a bright prospect for the realization of a non-precious cathode electrocatalyst for PEFCs. However, the

performance of the heteroatom doped catalyst is depending upon various factors including nitrogen content, nature of active sites and morphology of the carbon material *etc.* There are several ongoing research works on the basis of M/N/C (M stands for Fe or Co) electrocatalysts for ORR in PEFCs. However, the role of metal (M) for accomplishing the effective nitrogen doping is still a topic of debate. Although the ORR activity of such non-precious systems is mainly limited by the availability of nitrogen, improvement of the level of nitrogen doping is essential to meet the activity of the state-of-the-art Pt catalysts. Hence, the primary goal of this thesis work is the development of various nitrogen doped carbon materials which can be potential replacements for the Pt/C catalysts for ORR in PEFCs. Further, as another key objective of the present study, investigation of the influence of carbon morphology on nitrogen doping to generate the desired ORR active sites is also targeted by varying the carbon morphology from one dimension (1-D) to three dimension (3-D).

Chapter 1 presents a brief introduction about the importance and challenges of low temperature fuel cells. Also, the chapter describes the role of different carbonaceous materials as the catalyst and/or support in the energy based devices. The influence of edge sites and defects of the carbonaceous materials on the electrocatalytic activity has been discussed. A survey on the various methodologies available for the heteroatom doping such as nitrogen, phosphorous, boron and sulfur is included in the chapter. Moreover, various factors determining the oxygen reduction reaction (ORR) activity such as content of nitrogen, surface area, morphology of the carbon material, pH of the electrolyte, surface defects and edge sites of the carbon have been discussed. The present status of the development of non-Pt catalysts and their fuel cell activity are also explained

briefly in this chapter. Finally, we concluded this chapter by highlighting the various challenging problems which need to be solved in the understanding of nitrogen doping on carbonaceous materials in order to make better design of efficient non-noble metal based electrocatalysts for low temperature fuel cells to replace the expensive component Pt from the systems.

Chapter 2 deals with the synthesis strategies adopted for developing various nitrogen-doped carbonaceous materials such as iron nitride-doped carbon nanofiber ( $\text{FeN}_x\text{CNF}$ ), nitrogen-doped carbon nanofiber (NCNF), nitrogen-doped porous graphene (NpGr) and iron nitride-doped porous carbon (FeNGr). The chapter also describes the preparation of an active low-Pt electrocatalyst by imparting small order dislocations on the graphene layers of a carbon nanofiber through nitrogen doping followed by dispersion of Pt along the dislocated centers. Along with the various aspects of catalyst preparation, this chapter also briefly describes the working principle of various physico-chemical and electrochemical methods to elucidate the structure and activities of the prepared catalysts.

In Chapter 3, a detailed discussion on the preparation, characterization and electrochemical property/activity evaluations of the iron nitride-doped carbon nanofiber ( $\text{FeN}_x\text{CNF}$ ) as a Pt-free electrocatalyst is given. The nitrogen-doped carbon nanofiber (NCNF) is also prepared by the same method without adding the Fe precursor. The  $\text{FeN}_x\text{CNF}$  and its counter catalyst *i.e.* NCNF are structurally thoroughly characterised by various physico-chemical methods. The idea behind to construct the active  $\text{FeN}_x$  doping on CNF is to utilise the availability of highly exposed edged planes and slit pores originated by virtue of its cup-stack structure and slanting graphene planes which terminate on the wall surfaces. Here, the resulting nitrogen-doped composite catalysts

exhibit significant ORR activity in acid medium. Remarkably, the nitrogen-doping results into pentagonal defects on the graphene layers, thereby, causing surface unsaturation of the carbon and enhanced interlayer distance of the graphene layers. This surface unsaturations on graphene layers are termed as ‘nanopockets’ in the thesis. In an extension, these ‘nanopockets’ are effectively utilised for the development of a low-Pt electrocatalyst by depositing Pt on FeN<sub>x</sub>CNF (10 wt. % PtFeN<sub>x</sub>CNF). The results of a single cell evaluation using this catalyst are also included in Chapter 3.

The ORR activity of the prepared FeN<sub>x</sub>CNF catalyst as detailed in Chapter 3 is limited by poor mass transfer diffusion and higher overpotential difference for ORR due to less accessibility of nitrogen doped active sites along the inner wall of CNF. To tackle this, an effective nitrogen-doped catalyst is prepared by making holes *i.e.* pores on high surface area graphene sheets and subsequently the edge sites of pores are utilized for nitrogen doping. This work is discussed in Chapter 4. The main highlight of this work is an efficient method for preparing porous graphene with the aid of the *in-situ* generated Fe<sub>2</sub>O<sub>3</sub> nanoparticles and creation of potential nitrogen-doped active sites along the pore openings. The drilling of nanoholes on graphene is assisted by pre-formed Fe<sub>2</sub>O<sub>3</sub> nanoparticles and conversion of the later to Fe<sub>3</sub>C through carbon spillover from Gr. This porous graphene enriched with the nitrogen-doped active sites effectively reduces oxygen molecule through a 3e<sup>-</sup> pathway, suggesting a preferential shift towards the more favourable 4e<sup>-</sup> route compared to the greater contribution from the 2e<sup>-</sup> reaction kinetics as reported for many nitrogen-doped carbon nano morphologies.

Chapter 5 deals with the preparation and electrochemistry of porous graphene (pGr) and nitrogen doped porous graphene (NpGr) formed by initially generating pores

on Gr by the removal of small graphene quantum dots (GQDs) from Gr surface by simple hydrogen peroxide ( $\text{H}_2\text{O}_2$ ) oxidative treatment. This chemical oxidation process helped to knock out small pieces of Gr through epoxide formation, which subsequently resulted into the generation of GQD and pGr simultaneously. Since pore openings are expected to give more unsaturation and defect sites in the system and are thus being treated as fertile regions for heteroatom doping, pGr is further subjected to nitrogen doping by annealing with 1, 10 phenanthroline in Ar atmosphere (NpGr). The material thus formed display excellent activity towards electrochemical oxygen reduction reaction (ORR) compared to nitrogen-doped non-porous graphene (NGr) and many other reported nitrogen-doped carbon materials. The overall enhancement in the performance characteristics of NpGr is attributed to the higher content of nitrogen (7.8 wt. %) and its large proportion of desired chemical environment, which could be established by utilizing the high level of carbon unsaturation around the pore openings.

In Chapter 6, the preparation and activity characteristics of well defined iron nitride-doped porous carbon (FeNC-70) derived from Zeolitic-Imidazolate Framework (ZIF) as the template is demonstrated. The active catalyst is prepared by embedding iron phenanthroline complex ( $\text{Fe}[(\text{phen})_3]^{2+}$ ) into the inner cavity of ZIF-70 followed by pyrolysis at high temperature in Ar atmosphere. In order to study the role of pore size of ZIF, the nitrogen-doped catalyst is also prepared using other ZIFs namely ZIF-68 and ZIF-69 with variation in the pore size and the resulting catalysts are named as FeNC-68 and FeNC-69, respectively. Structural insights for active catalysts could be derived from various physico-chemical characterization methods. The active porous carbon material (FeNC-70), which is enriched with Fe-N-C moieties, reduces the oxygen molecule with

an onset potential at 0.80 V *vs* NHE through a mechanism that involves a greater contribution from the preferred 4e<sup>-</sup> pathway under acidic conditions. This benefit is mainly attributed to the unique morphology of iron nitride-doped carbon derived from ZIF-70 and availability of higher nitrogen (14.5 wt.%) in the system.

After performing all these studies, we came to a conclusion that the morphology and dimensions of the carbon material are having definite role on guiding various important properties and performance characteristics of the nitrogen-doped carbon based catalysts for the oxygen reduction reaction. An overall conclusion of the work as discussed in the previous chapters is presented in Chapter 7. The nitrogen-doping tunes the basic electronic properties and causes surface unsaturation on graphene layers of the carbon based materials. In addition, the metal coordination with nitrogen on carbon moiety *i.e.* M-N-C is identified as a potential factor which helps to narrow down the overpotential for ORR compared to the cases where only nitrogen-doped carbon catalysts are used. Along with this, the surface area and pore size distribution of the carbon morphology are the important factors for achieving greater number of active sites as required for achieving higher reduction current density from ORR. The edge sites on the carbon nanostructures play a key role to increase the content of nitrogen, which consequently leads to higher ORR activity of the catalysts. Apart from these factors, the amounts of Fe and nitrogen along with the type of nitrogen in the active catalysts are also the other factors which greatly determine the ORR activity of the derived catalysts.

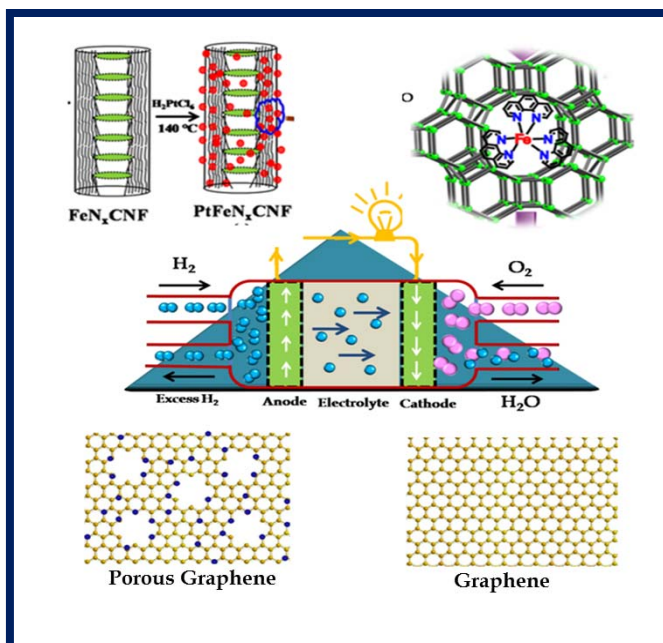
# Chapter 1

## Introduction

---

The present thesis gives a discussion on the synthetic strategy for the development of various novel non-Pt electrocatalysts for oxygen reduction reaction in polymer electrolyte fuel cells (PEFCs).

Thus, the present chapter begins with brief introduction of working principle of fuel cells, types, major components, advantages and their limitations. Also, this chapter discloses the mechanism of oxygen reduction reaction



(ORR), which is the key reaction on the cathode in PEFCs. Subsequently, the need for the alternative catalysts and their potential activity towards ORR has been discussed. Moreover, this chapter discusses the present status of the developed non-Pt catalysts and the importance of edge site effect associated with unique morphology of the carbonaceous materials. Finally, based on the understandings from the literature survey and above discussion, the objectives and scope of the present thesis are listed toward the end of the chapter.

---

## 1.1. General Background

Acute scarcity of fossil fuels has resulted in an extensive world-wide research towards the development of technologies which provide cleaner energy from the available renewable sources. To attain a more sustainable society with adequate renewable energy and less environmental pollution, more versatile, robust and efficient approaches in electric energy storage and conversion are needed. Currently, hydrogen and solar energies are the two important energy sources. In the present scenario, the development of electrochemical energy storage and conversion devices with high energy density and power density is highly desirable to provide cleaner energy with zero emission. In this regard, fuel cells and solar cells are contemplated as the alternative energy conversion devices to afford cleaner energy. Apart from their relevance in realizing the Hydrogen Economy, fuel cells are considered promising due to their high efficiency irrespective of the size of the system, modular nature, simple operation, wide range of operating temperatures and flexibility in using various fuels with reformer or direct use. For the last few decades, much attention has been given for the development of commercially available PEMFCs.

## 1.2. Fuel Cells

Electrochemical power sources are the devices which convert the chemical energy stored in reactants directly to the electrical energy. Batteries, supercapacitors and fuel cells are mainly regarded as the energy storage and conversion devices that are anticipated to meet the need of energy in future. Despite the basic energy releasing steps in all the above mentioned electrochemical power source systems occur at electrode-electrolyte interface,

variation is in the reaction for storage and energy conversion. Because of the high energy conversion efficiency and eco friendly nature, fuel cells have been highly captivated the researchers as an electrochemical power source.

The first fuel cell was developed by Sir William Grove in the mid of 1839. [1] In fuel cells, hydrogen ( $H_2$ ) or hydrogen based fuels is oxidized at the anode and oxygen gas ( $O_2$ ) is reduced at the cathode, thereby producing the electric current with byproduct of water and heat. At triple phase boundary (TPB), where the electrode, electrolyte and the gaseous molecules meet together, electrode reactions take place, leaving ions to pass through the external circuit. Fuel cells work as long as the fuels, *i.e.*  $H_2$  and  $O_2$  are supplied. It is manufactured as a stack of a number of identical cells known as membrane electrode assembly (MEA) in a modular form which can be used as the power source for various portable applications including mobile phone, laptop, automobile, stationary etc.

Among the various energy conversion devices, batteries and fuel cells exhibit high energy density while they lack high power density. On the other hand, supercapacitors are showing higher power density with poor energy density. Indeed, the Ragone plot [2] provides an effective comparison of energy density and power density of the electrochemical devices. Accordingly, it could be observed that these electrochemical energy devices independently are inferior to the internal combustion engines (ICEs) and only the hybrid devices including fuel cells and supercapacitors/batteries can provide the comparable energy density and power density equivalent to ICEs.

### 1.3. Advantage of Fuel Cells

Although fuel cells have comparable energy density and power density with batteries, batteries need to be recharged quite often due to the limited space for the reactants while fuel cells work continuously by supplying the fuels. Indeed, fuel cells have higher efficiency than ICEs. Most importantly, fuel cells eliminate the pollution caused by the burning of fossil fuels and the byproduct from the systems is only water when they use hydrogen and oxygen as the fuels. Besides, fuel cells do not necessitate conventional fuels (oils and gas) and can thus eliminate the economic dependence on politically unstable countries. Unlike ICEs, most fuel cells work silently which prevent the noise pollution. Finally, the maintenance of fuel cells is simple since there are few moving parts in the system. Due to the above mentioned advantages, intensive research efforts are taken for the development of different types fuel cells using pioneering materials.

### 1.4. Classification of Fuel Cells

The types of fuel cells are clearly distinguished according to the choice of the electrolyte used and are mainly epitomized based on their operating temperature. The following table will make the picture clearer. The comparison table signifies the different types of fuel cells, their operating temperatures, electrochemical reactions involved, electrolytes and the mobile ions. Based on the usage of the electrolyte, the fuel cells are primarily classified into five categories namely, solid oxide fuel cells (SOFCs), molten carbonate fuel cells (MOFCs), phosphoric acid fuel cells (PAFCs), alkaline fuel cells (AFCs) and polymer electrolyte fuel cells (PEFCs) *i.e.* proton exchange membrane fuel cells (PEMFCs), direct methanol fuel cells (DMFCs) and anion exchange membrane fuel cells

(AEMFCs). Among them, PEFCs are regarded as the most suitable candidates for the stationary and mobile applications due to their many associated advantages such as low temperature of operation, simpler start ups and easy handling.

**Table 1.1.** A list of various types of fuel cells with the corresponding electrochemical reactions, working temperatures and movable ions.

Type of fuel cell	Electrolyte	Cathode reaction	Anode reaction	Mobile ions
SOFC (500 -1000 °C)	YSZ - ceramics	$O + 4e^- \rightarrow 2O^{2-}$	$H_2 + O^{2-} \rightarrow H_2O + 2e^-$	$O^{2-}$
MCFC (650 °C)	Molten carbonate salts	$\frac{1}{2} O_2 + CO_2 + 2e^- \rightarrow CO_3^{2-}$	$H_2 + CO_3^{2-} \rightarrow H_2O + CO_2 + 2e^-$	$CO_3^{2-}$
PAFC (200 °C)	Phosphoric acid	$\frac{1}{2} O_2 + 2H^+ + 2e^- \rightarrow H_2O$	$H_2 \rightarrow 2H^+ + 2e^-$	$H^+$
DMFC (0-100 °C)	Polymer electrolyte membrane	$\frac{1}{2} O_2 + 2H^+ + 2e^- \rightarrow H_2O$	$CH_3OH + H_2 \rightarrow CO_2 + 6H^+ + 6e^-$	$H^+$
AFC (70 °C)	Aqueous alkaline solution in porous media	$\frac{1}{2} O_2 + H_2O + 2e^- \rightarrow 2OH^-$	$2H_2 + 2OH^- \rightarrow 2H_2O + 2e^-$	$OH^-$
AEMFC (70 °C)	Polymer electrolyte membrane	$O_2 + 2H_2O + 4e^- \rightarrow 4OH^-$	$2H_2 + 4OH^- \rightarrow 4H_2O + 4e^-$	$OH^-$
PEMFC (0-200°C)	Polymer electrolyte membrane	$O^{2-} + 2H^+ + 2e^- \rightarrow H_2O$	$H_2 \rightarrow 2H^+ + 2e^-$	$H^+$

### 1.4.1. Solid Oxide Fuel Cells (SOFCs)

As common fuel cells, SOFC consists of three compartments namely electrolyte, cathode and anode. SOFC is characterized based on the usage of solid ceramic material as the electrolyte to conduct the negative ions from the cathode to anode. The typical operating temperature is 650-1000 °C. In general, Cermet made up of nickel mixed with ceramic materials ( $Y_2O_3-ZrO_2$ ) is used as the electrolyte. The yttria stabilized zirconia (YSZ) and lanthanum strontium manganite ( $Sr_xLa_{1-x}MnO_{3-\delta}$ ) are commonly employed as the anode and cathode respectively. [3] Unlike the other low temperature fuel cells, precious metals (Pt), corrosive acids and molten materials are not employed, which added to the advantage of SOFC. Due the high temperature operation and exploitation of non-Pt catalysts, the carbon monoxide (CO) poisoning in the catalyst, which happened in low temperature fuel cells, is negligible. The another advantage of SOFC is that hydrocarbon can be used directly for the hydrogen generation without subjecting for the reformation and combined heat and power efficiency could be as high as 80 %.[4] However, the sulfur poisoning has been observed extensively which needs to be addressed by using adsorbent beds and by other means.

### 1.4.2. Molten Carbonate Fuel Cells (MCFCs)

MCFCs are characterized in the category of high temperature fuel cells. In general, MCFC operates at 600-650 °C using a variety of both direct as well as reformed hydrocarbons as fuels to generate the electricity. At high temperature, MCFCs convert the energy dense fuels into the hydrogen within the fuel cells which do not require the external reformer and the process is known as internal reforming. Owing to their high

temperature operation, the overall efficiency of the system is ~60 % as similar to SOFCs. Several MCFCs have been urbanized for natural gas and coal based power plants for electrical utility, engineering and military applications. However, the high temperature operation and the corrosive electrolyte cause corrosion in the components which limits the life of fuel cell components and consequently these R&D activities are slowly deteriorating. The electrolyte in this fuel cell is usually a combination of alkali (Na, K, Li) carbonates retained in a ceramic matrix made of  $\text{LiAlO}_2$ . [5] At the high operating temperature of this fuel cell, nickel is an adequate electrocatalyst for the anode and cathode. [6]

#### **1.4.3. Phosphoric Acid Fuel Cells (PAFCs)**

PAFC is the first commercialised fuel cells and this was developed in the mid of 1960s. [7] In PAFC, the liquid phosphoric acid is employed as the electrolyte. Porous carbon paper coated with noble Pt is employed as the electrocatalyst in anode and cathode. PAFC operates in the range of 150-200 °C, which can minimise the CO poisoning significantly. The high temperature operation results into the improved overall efficiency of the system. Moreover the existing PAFC can produce a maximum output of 200 kW and this superior performance associated with higher stability made PAFC as the potential candidate for the stationary applications. However, the fluctuating cost due to the usage of noble Pt and slow start up due to its higher temperature operation are the main drawbacks of the PAFC technology. [8]

#### **1.4.4. Direct Methanol Fuel Cells (DMFCs)**

DMFCs are mainly employed in the portable applications due to their higher efficiency and usage of inexpensive methanol fuels. Pt or Pt based alloys are being used as the

catalysts for both methanol oxidation and oxygen reduction. Since the Pt usage increases the overall cost of the system, this hinders their prospects for commercialisation. On the other hand, Pt based noble catalysts are suffered by CO poisoning, which restricts the life time of the catalyst. This issue induced the investigation of other non-noble catalysts with higher stability and efficiency. Methanol fuel crossover through the electrolyte is another limitation faced by DMFCs. Most recently, methanol powered fuel cells were demonstrated to power telecommunication installation at Mobile World Congress in Barcelona conducted by Motorola. [9]

#### **1.4.5. Alkaline Fuel Cells (AFCs)**

AFC was initially developed by Francis Bacon in the mid of 1930s followed by many other research groups. The typical AFC comprised two porous electrodes with liquid KOH electrolyte between them. In 1960s, AFCs were adopted as the primary power source in the NASA space flights namely Apollo series missions and Space Shuttle. [10] In AFC, Pt is employed as the electrocatalyst and their maximum loading is  $0.3 \text{ mg cm}^{-2}$ . However, the primary limitation of AFC is that the fuel can be easily poisoned by  $\text{CO}_2$  due to their strong interaction of KOH which leads to the formation of potassium carbonate ( $\text{K}_2\text{CO}_3$ ). Therefore, AFC operates on pure oxygen or purified air which exempts the  $\text{CO}_2$  poisoning. [11] Moreover, AFCs normally operate at 50 to 70 °C which can be easily achieved even in cold storage conditions. Owing to the low temperature operation, many metal oxides, spinels, Ni, Ag and other non-Pt metals are employed as the electrocatalysts with higher efficiency.

#### **1.4.6. Anion Exchange Membrane Fuel Cells (AEMFCs)**

AEMFC is a type of alkaline fuel cells owing to its functional similarities to AFC. AEMFC differs mainly from AFC by the usage of solid polymer electrolyte while AFC is employing aqueous KOH as the electrolyte. AEMFCs are also known as the hydroxide ion exchange fuel cells due to the transfer of hydroxide ions from cathode to anode. AEMFCs operate in the range of 50-70 °C as similar to AFC. The advantages of AEMFCs are the facile electrode kinetics, corrosion resistance under alkaline condition and usage of non-noble electrocatalyst as a cathode. The usage of methanol as anode fuel has been added additional benefit of AEMFCs. In addition, the effect of methanol crossover is negligible unlike to DMFCs due to the transport of ions in opposite direction. [12] The main limitations of AEMFCs arise from the development of electrolyte associated with poor OH<sup>-</sup> conductivity and mechanical stability. Because the diffusion rate of OH<sup>-</sup> is two times lower than the diffusion rate of H<sup>+</sup> in PEMFCs, it is important to develop polymer electrolytes with higher OH<sup>-</sup> ion exchange capacities. [13]

#### **1.4.7. Proton Exchange Membrane Fuel Cells (PEMFCs)**

PEMFCs are widely used fuel cells due to the low temperature operation, higher proton conductivity under ambient conditions and attractable design. PEMFCs are characterised in the category of polymer electrolyte membrane fuel cells (PEFCs) which transport the proton through the solid membrane while ensuring the passage of electrons through the outer circuit. PEMFCs are classified into two categories known as low temperature fuel cells (LT-PEMFCs) and high temperature fuel cells (HT-PEMFCs) based on their

working temperature. In both the cases, Pt supported on carbon is employed as the anode as well as the cathode electrocatalysts. In LT-PEMFCs, Nafion is employed as the electrolyte and their operating temperature is 50-80 °C while in HT-PEMFCs, phosphoric acid doped polybenzimidazole (PBI) membranes are used as the electrolyte and their operating temperature is 140-160 °C. In LT-PEMFCs, at low temperature, Nafion conducts the proton notably under humidified condition whereas PBI in HT-PEMFCs does not require the humidification. Due to the low temperature operation, the rate of electro kinetics towards ORR is relatively low thus decreases the overall performance of the LT-PEMFCs. Moreover, the catalyst is more sensitive towards the CO poisoning which results in the reduction of the life time of the catalyst. Besides, water management causes a serious issue in HT-PEMFCs. In order to tackle these issues faced by LT-PEMFCs, HT-PEMFCs have been deliberated with unique properties. In general, HT-PEMFCs offer enhanced kinetics towards ORR. Further, it restricts the CO poisoning on Pt electrocatalyst due to the high temperature operation. Noteworthy, PEMFCs have higher practical efficiencies over commercial combustion engines especially based on the combined heat-power generation. [14] However, the cost of the fuel cell components such as electrolyte and electrode (Pt) makes PEMFCs more expensive which hampers their practical utilization. Considering this limitation, intensive research efforts are being taken out worldwide with great enthusiasm to reduce the overall cost of the fuel cell components including catalyst and membrane.

## 1.5. Working Principles of Polymer Electrolyte Fuel Cells (PEFCs)

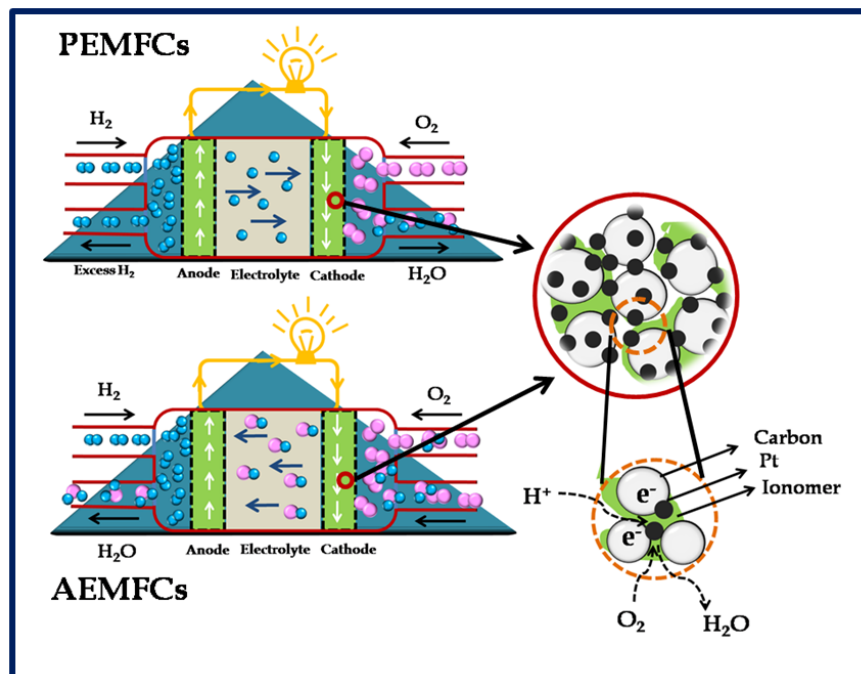


**Figure 1.1.** A schematic representation of the working of the single cells in PEMFC and AEMFC.

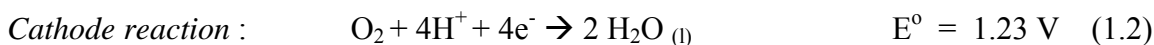
A simple example for a fuel cell is PEFC. As the name implies, the major component in a PEFC is the polymer electrolyte membrane. In fact, PEMFCs, DMFCs and AEMFCs are epitomized in this category due to the usage of polymer membrane as the electrolyte. In all the cases, the heart of the system is the membrane electrode assembly (MEA) which is a unit containing the electrolyte sandwiched by anode and cathode layers. In PEFCs, the catalyst must have a composition and configuration that maximize the fuel cell performance with long term stability. In general, Pt or Pt based alloys supported on carbon is employed as the anode as well as the cathode electrocatalysts. Similarly, the polymeric materials such as Nafion and polybenzimidazole (PBI) are used as the

membrane electrolyte. A schematic representation as given in Figure 1.1 symbolizes the working principle of PEMCs.

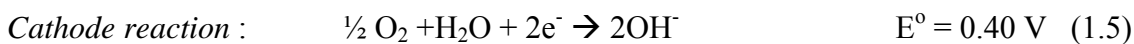
In the real cell operation, the fuels such as H<sub>2</sub> and O<sub>2</sub> have to reach the catalytic site through the gas diffusion layer where the electrochemical reactions take place and the byproduct, *i.e.* H<sub>2</sub>O, must be expelled from the cathode to prevent the water blockage and hence to maintain better access of the catalyst by the reactants. Similarly, the proton generated in the anode must reach the cathode *via* the electrolyte while the electron travels through outer circuit to reach the cathode where it reacts with the reduced product of oxygen and proton, resulting into the formation of water. Thus, the formation of triple phase boundary is an important criterion for the successful operation of a fuel cell.

The chemical reactions occurring in PEMFC and AEMFC are shown as follows:

**In PEMFC:**



**In AEMFC:**



In both the cases, hydrogen or hydrogen based fuels get oxidized at the anode giving protons and electrons while oxygen gets reduced at the cathode. In PEMFCs, the protons

produced pass through the membrane to the cathode and the electrons pass through the external circuit. These electrons are captured by oxygen molecules and get reduced forming water. On the other hand, in AEMFCs, the hydroxyl ions produced at the cathode pass through the membrane to the anode while the electrons pass through the external circuit. These electrons are captured by oxygen molecules and get reduced forming water.

### **1.6. Barricades of PEFC's Commercialization**

The spectacular performances of PEFCs toward the commercialization have been hampered by several factors mainly their cost, durability and performance, which need to be tackled.[15] For example, use of Pt as an electrocatalyst, perfluorosulphonic acid (PFSA) based membranes, bipolar plate which augments the overall cost of the PEFCs and preventing the successful commercialization of these systems. In PEFC, at present, Pt is the material of choice for hydrogen oxidation and oxygen reduction reaction. The loading of Pt lies in the range of  $0.3 \text{ mg cm}^{-2}$  which is too expensive for commercialization while the desired loading by American Department of Energy (DOE) lies in the range of  $0.03 \text{ mg cm}^{-2}$ . [16] Further, the membranes employed in low temperature fuel cells necessitate ultra pure hydrogen at low temperature operation which further increases the cost of the system. [17] Figure 1.2 exemplifies the cost analysis of the different components of PEFCs. It is clear that the catalyst, *i.e.* Pt, contributes 67 % of the total cost of the MEAs which is the main drawback of fuel cell for getting commercialized. Moreover, the Pt supported high surface area carbon faces an issue of stability under prolonged cycles. Most importantly, the kinetics of oxygen reduction reaction in the cathode is relatively low compared to the hydrogen oxidation in the anode

which further minimizes the overall performance of PEFC. The higher bond strength of oxygen molecule requires more active sites (*i.e.* Pt) to break the O=O bond which necessitate higher loading of Pt with an adverse effect on the overall cost of the system. On the other hand, the membranes used in PEFCs are limited by several factors mainly including 1) ionic conductivity under humidified conditions, 2) methanol permeability, 3) disintegration in presence of hydroxyl radicals and 4) stability. Moreover, the bipolar plates become brittle under such harm conditions. Hence, many of these limitations need to be tackled to realize successful commercialization of PEFCs.

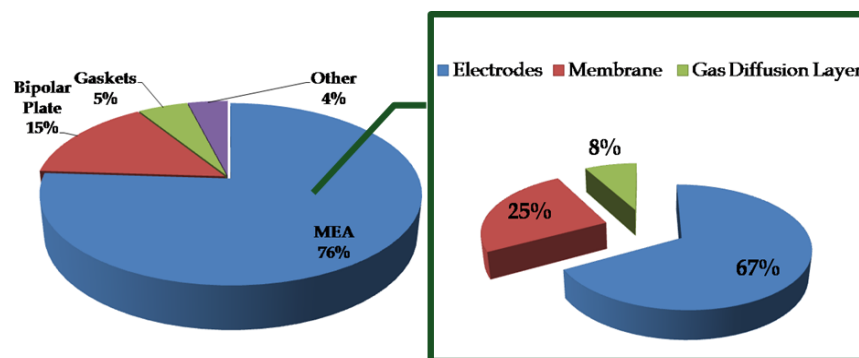


**Figure 1.2.** Cost analysis of PEFC stack and MEAs.[Ref.18]

### 1.7. Catalysts in Fuel Cells

Catalysts by definition are substances which alter the rate of a reaction without themselves undergoing any chemical change. In fuel cells, the electrode reactions occur resulting in the generation of a potential difference across the cell. To achieve enhanced rate of oxidation and reduction at anode and cathode (dissociation of hydrogen and oxygen), respectively, usually a catalyst is coated on the electrodes. To date, Pt is regarded as the most effective catalyst for the anode as well as the cathode reactions. It is

usually sprayed on a carbon coated carbon paper (diffusion layer). When hydrogen molecules come in contact to the Pt catalyst, they get broken apart and form a weak bond between Pt and hydrogen. Since  $H_2$  is now dissociated, it can undergo oxidation to form a proton and an electron and the electron will be subsequently passed through the external circuit. The remaining proton binds with water molecule on the membrane forming hydronium ion, which passes to the cathode, leaving free the Pt catalyst. At the cathode, oxygen molecules get bound to the Pt surface, get dissociated and form weak O-Pt bond. By gaining two electrons from the external circuit and two protons, oxygen moiety leaves the catalyst surface by forming a molecule of water. This reaction is termed as the oxygen reduction reaction (ORR). The Pt surface is now again available for oxygen binding. High activity, stability in acid medium and high work function (4.6 eV) make Pt a suitable electrocatalyst in fuel cells.

### **1.8. Electrochemical Oxygen Reduction Reaction (ORR)**

ORR is the most significant process in the energy conversion devices which indeed originated from the biological respiration process. In PEFCs, ORR is occurring at the cathode and the mechanism is dependent on the medium of electrolyte. The kinetics of ORR is relatively complicated than the hydrogen oxidation and the reaction involves several intermediates depending on the nature of the electrode, catalyst and medium of electrolyte.[19] Besides, the reaction kinetics is also influenced by several factors including the adsorption of  $O_2$  on the catalyst, structure, nature of bonding and energy barrier etc. Owing to that, the kinetics of ORR becomes more sluggish which limits the overall performance of PEFCs. So far, several catalysts are proposed including transition metal based alloys, carbides, nitrides and macrocyclic compounds to realize the novel

catalysts which can speed up the ORR process at the cathode. Among them, Pt still remains as the best material of choice due to its superior ORR activity compared to many other systems.

### 1.9. Mechanism of ORR

In general, ORR occurs in aqueous electrolyte mainly *via* two pathways 1) 4e<sup>-</sup> pathway, where the oxygen molecule gets reduced directly into H<sub>2</sub>O and 2) 2e<sup>-</sup> pathway, where the O<sub>2</sub> molecule gets reduced first to H<sub>2</sub>O<sub>2</sub> and further to H<sub>2</sub>O. On the other hand, in non-aqueous medium, the 1e<sup>-</sup> pathway involving the formation of superoxide (O<sub>2</sub><sup>-</sup>) from O<sub>2</sub> molecule can also occur. The nature of the activesite and the mode of interaction of O<sub>2</sub> molecule with the activesite are deemed to be the determining factors for the reaction pathway. The 2e<sup>-</sup> pathway indicates the incomplete ORR which minimizes the overall efficiency. Further, the resulting H<sub>2</sub>O<sub>2</sub> causes the stability issue in the catalyst and membrane.

The mechanism of ORR is given as follows:

#### In acid medium

*Direct pathway:*



*Indirect pathway:*



#### In alkaline medium

*Direct pathway:*



*Indirect pathway:*



### **In non-aqueous solvents**



*(The thermodynamic potentials are not mentioned as they vary with respect to the solvent)*

### **1.10. Pt based Catalyst for ORR**

As mentioned earlier, Pt or Pt based catalysts remain as the materials of choice for the hydrogen oxidation in the anode and ORR in the cathode. From the volcano plot, which measures the adsorption energy of O<sub>2</sub> molecule on the catalyst, Pt has been identified as a potential candidate over several transition metals for ORR.[20] The theoretical studies predicted that the low *d*-band center and low Pt-Pt inter atomic distance are favoring the efficient ORR on the surface of Pt. However, Pt reduces the oxygen molecule with overpotential difference of > 300 mV from the theoretical value (1.23 V). The structure sensitivity towards the adsorption of electrolyte on Pt (specific adsorption) limits the performance towards ORR immaterial of the electrolyte. Studies clearly depict that terrace, edge and corner sites are governing factors for the superior ORR activity of Pt. Besides, the sluggish kinetics of ORR in the cathode necessitates higher Pt content in the cathode side compared to that in the anode. To tackle the issues effectively, dispersion of

Pt on suitable supports is being practiced as a viable strategy. Pt or Pt based alloys supported on carbon nano structures (CNS) are widely employed as the electrocatalysts in PEFCs. However, under the highly acidic operating environment of PEMFCs (pH~1), the carbon support undergoes deterioration which leads to the agglomeration of Pt and consequently decreases the activity and stability of the metal catalyst. Further, fluctuating cost associated with scarcity and sluggish kinetics of ORR on Pt hamper the prospects of commercialization of PEFC which need to overcome to realize the practical application of the system in the energy market. To tackle this challenge, finding an alternative supporting material for the traditional carbon black is necessary. Also, in the last few decades, significant amount of efforts has been taken either in the direction of reducing Pt in the active catalyst or removing completely of Pt from the catalyst layer. One possible strategy for the reduction of Pt from the system is by developing core shell structures of Pt with less expensive transition metals whereas another strategy is by alloying Pt with non-noble metals. Preparation of non-Pt metal catalysts (NPMC) for ORR is the ultimate goal for fuel cell chemists as cost of Pt is lying as the major stumbling block in the path of commercialization of the systems.

### **1.11. Pt Based Alloys**

Although Pt is the state-of-the-art system for ORR catalysis, the kinetics of ORR is more sluggish due to the several factors including *viz.* O<sub>2</sub> adsorption energy, O-O dissociation energy and OH adsorption energy on the Pt surface. Moreover, the stability under the fuel cell operating conditions is another great challenge faced by Pt. In the last few decades, significant efforts have been given to understand the slow kinetics and mechanisms of oxygen reduction by making bi and multimetallic alloys.

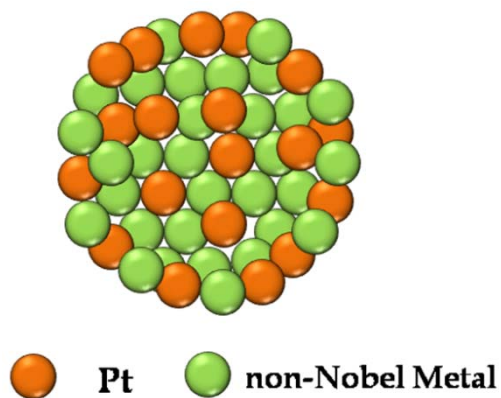


**Figure 1.3.** A pictorial representation of a Pt based alloy particle.

Accordingly, there are recent reports based on the extensive studies on the correlation between the electronic structure and the catalytic activity of the metallic alloys for ORR.[21a] The adsorption energy of oxygen molecule has direct relation with the oxygen-metal bond strength and the *d*-band centre relative to the Fermi level. The alloying of Pt with other non-noble transition metal increases the stability of Pt by preventing the metal dissolution and surface oxide formation likely at higher potential of 0.8 V in fuel cells .[21b]

For example, Mukerjee *et al* [22] prepared effective Pt-M/C (M-Co, Cr or Fe) alloy catalysts for ORR in PEMFCs. Among them, the PtCo/C system exhibits excellent ORR activity compared to Pt/C and other Pt-M/C catalysts. The enhanced activity has been attributed to the changes in the electronic structure or favourable variations in the Pt-Pt inter atomic distances due to alloy formation. In addition to that, the choice of transition metal for alloy formation and reaction condition also influences towards the higher activity for ORR. Adzic *et al* [23] demonstrated Pt for ORR which was stabilised against dissolution under potential cycling by modifying Pt nanoparticles with gold (Au)

clusters. The surface alloying of Au with Pt modifies the Pt electronic structure toward a lower Pt surface energy or lower-lying Pt *d*-band states. In 2007, Markovic *et al* [24] demonstrated that Pt<sub>3</sub>Ni (111) surface exhibits 10-fold and 90-fold enhancement in ORR compared to the corresponding Pt (111) surface and Pt/C respectively. The high activity towards ORR of Pt<sub>3</sub>Ni (111) is due to the unusual electronic structure (*d*-band centre position) and arrangement of surface atoms in the near-surface region.

### 1.12. Pt Based Core Shells

As it is recognized from the literature reports, several works are epitomized in their own way to reduce the limitations of Pt, including increased dispersion and alloying Pt with non noble transition metals. Hence, preparation of electrocatalysts with monolayer of Pt on other non-noble metal nanoparticles (*i.e.* core shell) is identified as a prominent way to tackle these issues.[25] In Pt based core shell catalysts, the inner core will usually be made with non-noble metals and, thus, reduces the cost significantly. In this perspective, Adzic *et al* exclusively worked on the development of Pt based core shell particles with monolayer Pt on various transition metals for ORR. [25a] For example, Pt monolayer on non noble metal (Au, Pd, Co, Ni) core shell particles show 4 times higher mass activity at 0.8 V compared to that of Pt/C. [25b] This is attributed mainly to the charge transfer from the monolayer to the substrate, consequently creating vacancy on the *d*-orbital of Pt. This increases the interaction between Pt and adsorbed O<sub>2</sub> molecule and thereby making the Pt skin on Co or Ni catalytically more active. [26]

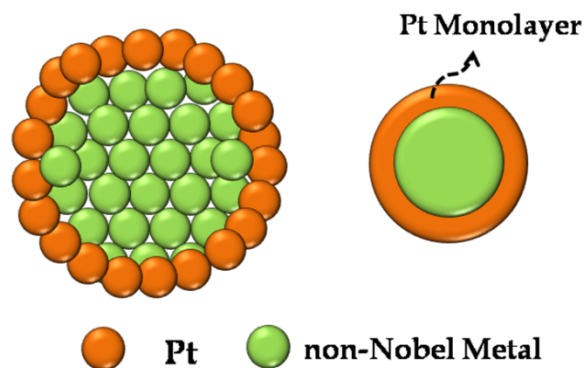


*Figure 1.4.* A pictorial representation of a Pt based core-shell particle.

Besides, several Pt based core shell catalysts are reported for ORR using variety of methods including voltammtric dealloying method, galvanic displacement reaction, electrochemical method, seed mediated method and emulsion method etc. Each method has its own advantages and limitations. However, in all these cases, the usage of Pt still remains. Since a complete switchover from Pt to a potential low-cost ORR catalyst is essential to provide momentum for commercializing fuel cells, research on developing totally Pt-free systems has gained substantial focus in recent days.

### 1.13. Role of Carbon Nano Structures (CNS)

Energy technologies have nowadays been nourished by the advancement in nanomaterials science, the most highlighted nanomaterials being the carbon nanomaterials. The remarkable properties such as high electrical conductivity, mechanical stability and unique morphological characteristics make them suitable for various energy storage as well as energy conversion device applications. Obviously, electrochemists were also mesmerized for the preparation of carbon based non-Pt electrocatalysts to replace Pt on the cathode side in fuel cells. It is well known that carbon

is the backbone of organic chemistry and its allotropes *i.e.* graphite, fullerenes and diamond have got much attention among the researchers in the field of materials chemistry. Indeed, the discovery of buckminster fullerenes [27] followed by the discovery of one dimensional carbon nanotubes (CNTs) opened a new perspective in carbon based nanomaterials chemistry. Very recently, the discovery of single layer of graphite, *i.e.* graphene (Gr), created tremendous advancement in the energy based technologies.

### 1.13.1. Fullerenes

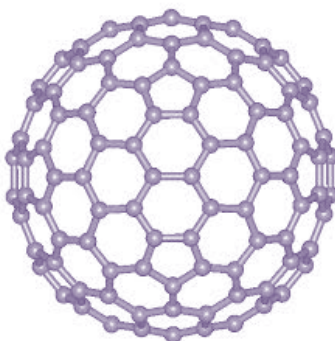


**Figure 1.5.** The pictorial representation of fullerenes with  $C_{60}$  structure.

The discovery of fullerene is being considered as the breakthrough in materials chemistry world. Fullerene possess sixty ( $C_{60}$ ) or seventy ( $C_{70}$ ) carbon atoms interlinked as pentagons and hexagons forming spherical cages imitating the patches of a soccer ball.[27] Several attempts have been reported employing fullerenes as a potential candidate to extend their significance in the energy storage and energy conversion applications. Metallo fullerenes have been suggested as excellent ORR catalysts with ultra low Pt loading for the fuel cell applications.[28] Attempts were also made for developing Fullerene-Pt nanoparticle assemblies which were prepared by attachment and

immobilisation of different Pt nanoparticles on a gold electrode using molecular layers of  $C_{60}$  as a linker system. These assemblies were active for the methanol oxidation following treatment with CO. [29] Very recently Feng *et al.* reported that nitrogen doped fullerenes are potential catalysts for hydrogen fuel cells.[30]

### 1.13.2. Carbon Nanotubes (CNTs)

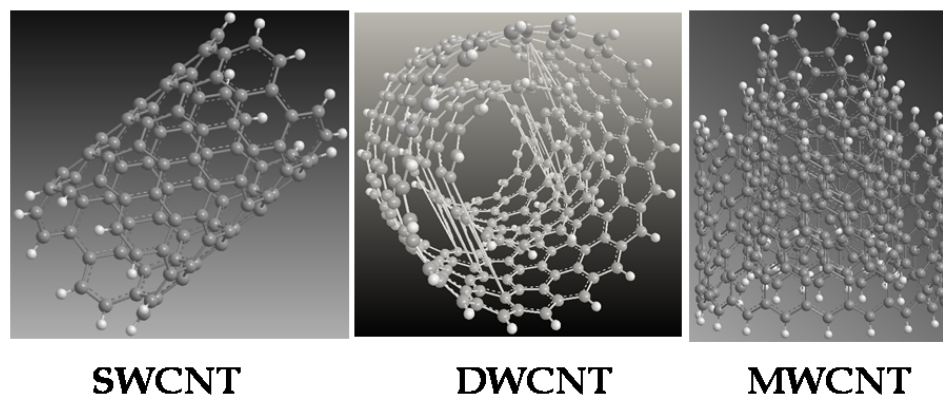


**Figure 1.6.** Structures of carbon nanotubes such as single walled (SWCNT), double walled (DWCNT) and multiwalled (MWCNT) systems.

The materials chemistry world has molded in the unique way after the pioneering work done by Iijima in 1991 who initially found the needlelike tubes known as carbon nanotubes using transmission electron microscope (TEM).[31] Due to their distinctive electrochemical properties, CNTs were attracted by many researchers and thus paved the way to a new era of material science. Carbon nanotubes are cylinders of one or more (termed as single walled carbon nanotubes (SWCNTs) and multiwalled carbon nanotubes (MWCNTs) respectively) layers of graphene sheets with open or closed ends.[32] For fuel cell applications, CNTs have become promising support materials for reducing the Pt content. Most recently heteroatom doped CNTs (*i.e.* N, B and P) are also executed to use

as non-Pt electrocatalysts to replace Pt in fuel cells. [33] It is well known that the helicity and diameter are the governing factors for both metallic and semiconducting properties of CNTs. The presence of hollow core inside the carbon nanotubes in addition to their unique metallic as well as semiconducting properties is also a topic of interest. Another fact regarding the nanotubes is their inertness towards complex formation. As a consequence, scientists are attempting to functionalize CNTs. These attempts have provided a breakthrough in nanotube chemistry. Liu *et al.* reported functionalization of carbon nanotubes using concentrated acid mixture followed by Pt decoration.[34] Attempts on Pt-Ru supported on double walled CNTs are also recently reported.[35] These composites are found to be showing remarkable activity and thus are suitable as anode catalysts for direct methanol fuel cells.

### 1.13.3. Carbon Nanofibers (CNFs)

CNFs are another promising materials coming under carbon nanotubes chemistry (Figure 1.7). CNFs are graphitic filaments similar to CNTs, with diameters ranging from 0.4 to 500 nm and their length varies from few micrometers to millimeters. Although CNFs are grown in a similar way as CNTs are synthesized, the CNFs are epitomized into 3 types namely 1) *stacked*, 2) *herringbone* (cup-stacked) and 3) *nanotubular* based on the angle of graphene layers with respect to the filament axis. The typical structures of CNFs are shown in Figure 1.7. In the stacked form, the graphene layers are perpendicular to the fiber axis whereas in the herringbone form, the graphene layers are angled to the fiber axis. In the case of the nanotubular type, the tubular graphene walls are arranged parallel to the fiber axis. Indeed, the physical properties depend upon the arrangement of graphene layers which differentiate CNFs from CNTs.

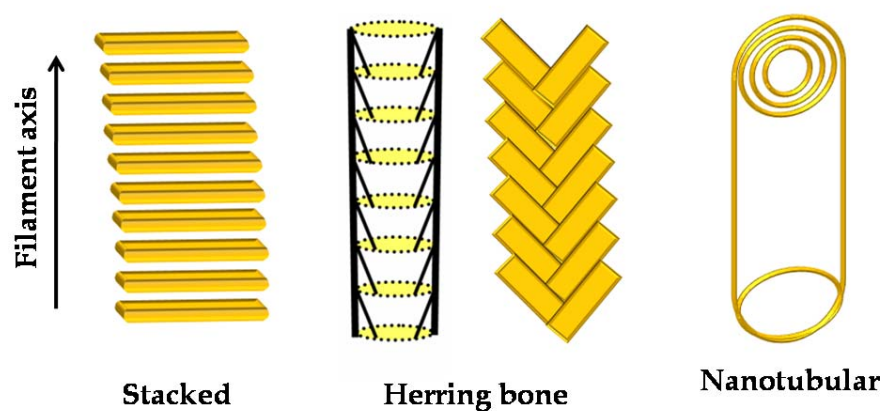


**Figure 1.7.** Pictorial representations of the structures of various CNFs as classified based on the angle of graphene layers with respect to the filament axis.

Among the three CNFs, the herringbone CNF gains much attention due to the inherent edge site exposure which is favorable for facile electrochemical reactions. Besides, the herringbone CNF is tend to be investigated exclusively for fuel cells as small entities can enter *via* open tips and subsequently can intercalate between the graphene layers. Moreover, nitrogen doping with higher degree can be achieved on the edge sites, thus broadening their utilization for the development of new electrocatalysts as well as supports. Consequently, successful attempts have been made by electrochemists to make use of CNF derivatives as effective catalysts for fuel cells with ultra low Pt loading. Recently, Beena *et al.* reported selective decoration of Pt on both inner and outer walls of CNFs which can be employed in fuel cells.[36] Hence, the aforementioned discussion indicates the effectiveness of CNF as a suitable material for fuel cell applications.

#### 1.13.4. Graphene (Gr)

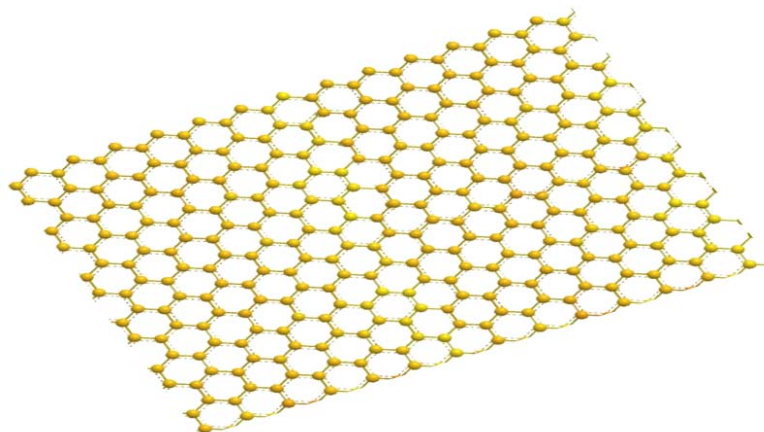


**Figure 1.8.** *The structure of graphene sheet having one atom thick two dimensional honeycomb arrangement.*

As mentioned earlier, Gr, the newborn baby of carbon allotrope which recently contemplated as the most fascinated material in the energy based research works. The discovery of Gr by Novoselov and Geim in 2004, which made them Nobel laureates of 2010 in physics, opens a new horizon in the direction of material electrochemistry world. [37] In fact, Gr is the one atom thick carbon atoms tightly packed into a two dimensional crystalline honeycomb lattice with a carbon-carbon bond distance of 0.142 nm [38] and is the mother of the graphitic materials of all other dimensionalities. The structure of one atom thick, two dimensional Gr has been shown in Figure 1.8.

The uniqueness of Gr is that it can be wrapped up into zero dimensional fullerenes, scrolled up in to one dimensional (1D) CNTs or CNFs and can be stacked into three dimensional (3D) graphite structures. Indeed, true 2D materials tend to roll or fold in order to achieve their lowest potential energy while the single layer Gr sheet is stable

enough to exist is because of the presence of imperfections which hinder the rolling up of the sheets and also suppress the thermal vibrations. Hence, the inherent electrical properties of Gr arise from its electronic configuration. It is worthy to mention that Gr is remarkably stronger even than steel and is very stretchable thereby making it applicable for flexible conductors. Gr finds as an attractive candidate where CNTs have been failed. [39] Due to its inherently high electronic conductivity, high surface area and presence of other functional groups, researchers are nowadays fascinated to design the graphene based nanomaterials as electrode materials for ORR in fuel cells. Thus, a remarkable advancement in this regard has been achieved by the fabrication of heteroatom doped Gr nanomaterials and especially Gr based nanocomposites. The implementation of Gr based materials provides high electrochemically active surface area due to the enormous specific surface area of Gr.

#### **1.13.5. Graphene Quantum Dots (GQDs)**

GQDs, another allotrope of carbon family, are defined as the zero dimensional semiconductors having particle size of 2-10 nm. GQDs are obeying the principles of quantum confinement due to the edge effect and their density of states is more discrete. The photoluminescence under UV light is the most striking properties of GQDs because they exhibit an energy gap that determines the required wavelength of radiation of absorption and emission spectra. When GQDs are subjected with light energy, electrons are jumped from the lower energy valence band to the higher energy conduction band. When this electron gets back down, it emits the captured energy in the form of light of a certain wavelength. Indeed, these wavelengths of absorption and emission are size dependent which vary with respect to the size of the particles.

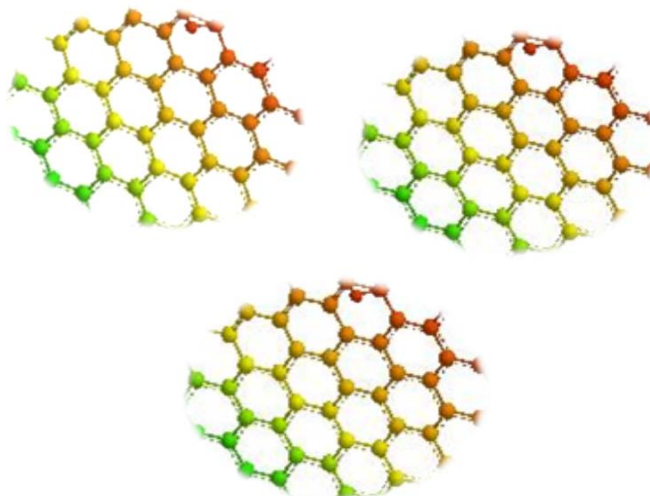


**Figure 1.9.** A pictorial representation of the structure of graphene quantum dots (GQDs) having size of a few nanometers.

Another important term regarding the quantum dots is the Photoluminescent Quantum Yield (PLQY) which measures the percentage of the absorbed photons those results in the emission of the photons. Due to intrinsic conducting properties, conversion of 2D graphene sheets into zero dimensional GQDs has been reported by several research groups. In particular, Li *et al* reported the application of electrochemically synthesized GQDs with a uniform size of  $\sim 3\text{-}5$  nm as electron acceptors in P3HT-based solar cells. [40] In view of its application as an ORR catalyst, successful attempts have been reported by several research groups. Concept of heteroatom doping has also been introduced to GQDs. Li *et al.* extend their work by reporting the nitrogen doped GQD which was showing excellent electrocatalytic activity [41] with dependence on the size of the dots. The unique features of the dots including their optical properties, excellent solubility as well as stability and surface characteristics including edge defects are promising

opportunities in overcoming the hurdles faced in the field of fabrication of energy conversion devices, biotechnology as well as optoelectronic devices.

### **1.14. Non-Noble Electrocatalysts**

While Pt group metal (PGM) based catalysts are the current active materials for ORR, their utility is limited by several factors including cost, scarcity and stability. Consequently, substantial efforts are given in the direction of development of non-precious electrocatalysts for the replacement of Pt for ORR. Preliminary investigations identified those carbon nanostructures especially after heteroatom doping with and without metal are the best options for the replacement of Pt. The current area of research can be classified mainly into metal/nitrogen doped carbon (M-N/C) and metal-free heteroatom such as nitrogen, boron, phosphorous, halogen and sulphur-doped carbons. Even though the resulting composite materials exhibit interesting ORR activity in acid as well as alkaline medium, still significant efforts are needed to develop the desired active catalyst to compete with the state-of-the-art Pt catalysts.

#### **1.14.1. Metal-Macrocyclic Compound for ORR**

Indeed, the area of development of non-precious electrocatalyst was initiated by Jasinski *et al* in mid of 1965. [42] The discovery identified the potential ORR characteristics of cobalt phthalocyanine in alkaline medium even though the catalyst suffers from low stability. In fact, the idea is originated from the ORR mechanism of heme proteins in blood cell. Since then, several research workers are interested to focus on the same direction. The initial studies proposed that the metal ion centres, Fe and Co, are main active sites responsible for the commendable ORR activity. It is commonly observed that

the Co based complexes reduce the oxygen molecule through the  $2e^-$  pathway while the Fe based complexes reduce through the  $4e^-$  pathway. Various factors are governing the ORR activity of these metal macrocyclic complexes. For example, the nature of the metal-ligand interaction of the complex also plays the role for the significant ORR activity. [43] In addition to that, the functional groups present on the outer rings of the macrocycle can also serve to tailor the electrochemical properties of these complexes. [44] For example, Baker *et al* claimed that the ORR activities of the substituted iron phthalocyanine supported on carbon (FePc/C) complexes are varied due to the change in electron densities of the metal-ion centers and ring structures resulting from the substituent groups. [45] All experimental studies over the years have recognized that these macrocyclic complexes of Fe and Co emerge to be the best. However, they suffer from low electrochemical stability and they are known to decompose either *via* hydrolysis in the electrolyte or destruction of the macrocyclic ring by hydrogen peroxide intermediates generated during the oxygen reduction reaction. [46] In order to tackle the issue of stability, the macrocyclic complexes of Fe and Co are further made up of composite with carbon support. However, there are still three main issues remaining with these adsorbed porphyrinic materials with respect to their use as the ORR catalysts. First, the overall activity of the non Pt metal (NPM) catalysts is low, with onset potentials around 0.6 V *vs* RHE which is relatively low than the desired onset potential. Second, the catalysts are not stable enough for the prolonged cycles in PEFCs. [47] Third, these systems exhibit very poor performance with supports other than graphite with edge planes (such as Au, MoS<sub>2</sub>, or even highly oriented pyrolytic graphite with basal planes). Hence, Jahnke *et al* [48] open up a new strategy of pyrolysis of metal with macrocycle in

an inert atmosphere at high temperature. The pyrolysis enforces higher catalytic activity and stability. It is widely believed that, after the pyrolysis, the structure of macrocycles will be decomposed and the resulting active site with metal coordination is more active towards ORR. Since then, numerous works have been carried out based on the pyrolysis of Fe macrocycles, Co macrocycles and mixed Fe/Co macrocycles.[49] The new catalysts exhibit remarkable ORR over the non-pyrolysed product. The annealing causes structural deformations of macrocycle and resulting into the formation of a stable catalyst with metal in coordination with nitrogen-doped carbon (M-N/C) active sites for ORR. The structural deformations of these macrocycles have been confirmed by various methods including time of flight secondary ion mass spectroscopy (ToF-SIMS), [50] X-ray photo electron spectroscopy (XPS), [50] Mossbauer spectroscopy [51] and extended X-ray absorption fine structure (EXAFS).[52] Additionally, these surface techniques provide insight of the structural characteristics of the pyrolysed catalysts. Accordingly, possible active sites on the resulting catalyst are identified as M-N<sub>4</sub>C, M-N<sub>2</sub>C and N-C, where M stands for the metal counterpart. This variation in the active site is attributed to the nature of macrocycle, temperature and duration of the annealing.

#### 1.14.2. M-N/C Catalyst for ORR

In 1989, a breakthrough was achieved by E. Yeager *et al* [54] when he demonstrated that instead of beginning with organic macrocycle, the active catalyst can be developed with equivalent activity and selectivity by individual starting material of carbon, nitrogen (NH<sub>3</sub>) and metal salts (Fe or Co). The key requirement for the preparation of active catalyst is proper metal-nitrogen coordination occurring on a carbon support resulting from heat treatment and the precursor materials of metal, nitrogen and carbon. Since then,

numerous works are reported for the preparation of M-N/C (M-Fe or Co) using different carbonaceous materials such as Vulcan carbon, CNT, [55] CNF and recently graphene. The nature of the metal-nitrogen-carbon (M/N/C) active site and mechanism of ORR at these sites is still indecisive. The classical pathway for the preparation of M-N/C catalyst is the simple heat treatment of transition metal-nitrogen precursors with suitable carbon material in inert atmosphere. The temperature range is varied from the 700 to 1000 °C, hence the optimal temperature is dependant and there is no universal temperature value at this moment. Several factors were believed to be significant which determine the overall activity and stability of the prepared M-N/C electrocatalysts, including the loading and type of transition metals, surface characteristics of carbonaceous support, nitrogen precursor and duration of the heat treatment.

### **1.14.3. Influences of Surface Properties of Carbon**

As mentioned earlier, the surface characteristics of carbon support play major role towards ORR of the prepared catalysts. Accordingly, J. P. Dodelet *et al* have exclusively worked on the area of synthesis of non-precious electrocatalyst for ORR. [56] They investigated the role of carbon support towards effective ORR by adsorbing iron acetate on 10 different carbon supports which are varied from surface defects, pore size distribution and surface oxygen content. The study concludes that the resulting catalytic activity varies greatly from one support to another. Moreover, the carbon support with more defects facilitates to get enhanced density of catalytic activesite which further consequences the improved ORR. [57] In addition, the carbon support associated with larger number of micropores in the range of 0.8-2 nm possibly increases the density of

active sites.[58] Even though, significant progress over past few decades has been accomplished in explaining these factors, the overall understanding is still inadequate.

#### **1.14.4. Type and Content of Metal Ions**

Several different non-noble transition metals have been examined as potential active centers for M-N/C catalyst, including Fe, Co, Mn, Ni, Cu and Cr. The initial investigations have identified that Fe and Co are the most active transition metal-ion centers for ORR catalysis. In addition, catalyst with more than one catalytic center exhibits remarkable ORR activity. In view of that, Jiang and co-workers prepared the MN/C catalyst with binary metal center by heat treatment of various binary metal macrocycles. The resulting binary metal centered electrocatalysts exhibit superior ORR activity than those with just one type of metal-ion centre, such as Fe, Co, Ni, or Cu. However, the stability of these binary metal centers under the fuel cell condition is the primary concern. On the other hand, several research works scrutinized the optimum content of metal for the preparation of M/N/C catalysts and found that an amount exceeding 0.5 wt. % leads to the formation of metal carbide or metal containing oxides.

#### **1.14.5. Nature and Structure of the M-N/C Active Sites**

As understood from the previous section, the majority of the studies reveal that the active NPMC catalysts are achieved by pyrolysis of metal-nitrogen chelate complex with suitable carbon support at high temperature. It is well known that the resulting catalyst is accompanied with the M-N<sub>x</sub> moieties bound with carbon activesite. It has been identified that (1) disordered carbon content with micropores, (2) metal (Fe or Co) precursor, (3)

nitrogen rich precursor and (4) surface functional groups on carbon support are the essential factors for producing an active NPMC for ORR.

To date, various activesites responsible for ORR have been proposed in literature. In general, the catalytic sites present on the catalyst prepared in the range of 500 -700 °C are labelled as “low temperature catalytic sites” [59] whereas the catalyst prepared in the range of >800 °C is labelled as “high temperature catalytic site”. [60] In 2002, Dodelet *et al* speculated the possible active sites based on the ToF-SIMS results as FeN<sub>4</sub>/C and FeN<sub>2</sub>/C while the later one exhibits relatively higher activity. [61] The study was stretched further by the same group and proposed five different possible active sites. Among them, FeN<sub>4</sub>C (*i.e.* FeN<sub>2+2</sub>/C) is concluded as the foremost active site towards ORR. [62] However, in the case of Co based M-N/C catalyst, the proposed structure is similar to the Fe based catalyst (*i.e.* CoN<sub>4</sub>/C) and there is no evidence for the presence of CoN<sub>2</sub>/C activesite in the literature.

Nevertheless, many studies do not support this view and claiming that these metal centers serve to catalyse the formation of nitrogen doping on carbon (N/C) during pyrolysis and do not participate actively for ORR.[63] However, it is widely accepted that nitrogen is the indispensable element for bringing the catalytic activity. The attached nitrogen on carbon may lead to the formation of different types of active sites. Among them, it is revealed by various studies that ORR of N/C catalysts is mainly due to pyridinic and graphitic nitrogen.[64] However, it can be concluded that the metal ions in the M-N/C catalyst have higher impact than the metal-free N/C catalyst for ORR. Therefore, the fundamental understanding on the nature and formation mechanism of the

activesite is inadequate and, hence, detailed examination is required in order to provide further insight to this area.

#### **1.14.6. Metal-free Nitrogen-Doped Carbon Nanostructures (N-CNS) for ORR**

From the previous section, we understand that the M-N/C site in the catalyst is solely responsible for the promising ORR activity. However, still their performance with respect to stability is insufficient, which is regarded as an ongoing challenge in the direct implementation of these systems for real cell applications. The origin of the instability of these materials is a subject of debate in literature while this issue is one of the reasons to trigger the activities on the development of metal-free nitrogen doped carbons as effective electrocatalysts for ORR.

##### **1.14.6.1. Nature of Nitrogen-Doped Carbon Active Site**

Recently, nitrogen doped carbonaceous materials fashioned enormous advancement in the field of energy applications. The recent literature reports proven that nitrogen doped carbon nanostructures (NCNSs) could be better alternates for Pt in fuel cell and solar cell applications. The foreign atom doping tunes the basic electronic and mechanical properties of the host and makes them perfect catalyst in energy applications. As the doped nitrogen donates the pair of electron to the carbon moiety, carbon becomes electron rich consequently increases its pH. [65]The incorporation of guest atom into the carbon nanotubes even in a small amount can strongly modify the structural and electronic properties of carbon nanotubes. [66] Thrower *et al* [67] hypothesized that the nitrogen doping causes acceleration in electron transfer kinetics and catalytic activities owing to the consequences of band gap lowering and increased electron mobility.

Sjostrom *et al* [68] noted that, basal planes on nitrogen doped carbon nanotubes are curved or buckled which are termed as pentagonal defects due to nitrogen doping. These pentagonal defects perturb the hexagonal arrangement of carbon atoms which causes the buckling of graphene layers (*i.e.* turbostratic disorder) and results the fluctuation in the interlayer distance of graphene layers of graphite. Moreover, the nitrogen doping modifies the electronic structure of carbon nanotubes by inclusion of electron donor states which brings its conduction band edge towards the Fermi level ( $\sim 0.2$  eV) as identified from the tunneling spectroscopy studies. [69]

#### 1.14.6.2. Chemical Structure of N-Doped Carbon (NCNS) Active Sites

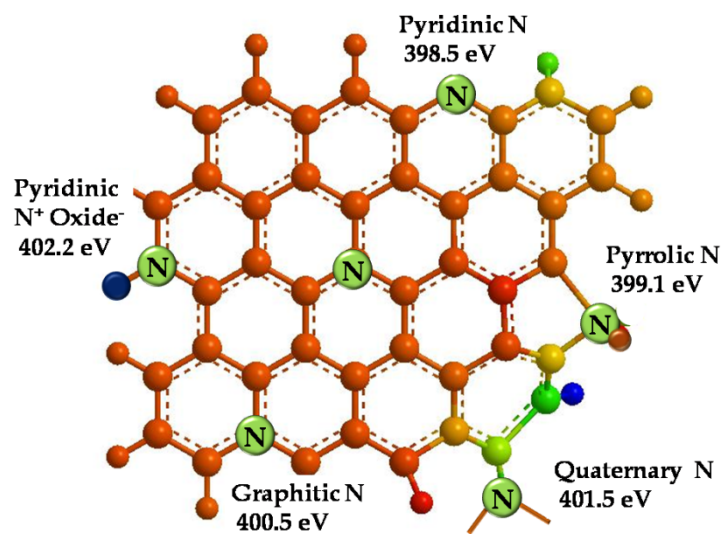


**Figure 1.10.** Pictorial representation of the types of nitrogens and their corresponding binding energy values as measured by X-ray photoelectron spectroscopy.

The spectroscopic studies classify the doped nitrogen in different forms such as pyridinic, pyrrolic, graphitic, quaternary nitrogen and N-oxides of pyridinic nitrogen. The pyridinic nitrogen is referred as nitrogen bound with two  $sp^2$  carbon in the six membered ring

while the pyrrolic nitrogen has similar coordination in five membered ring. The former nitrogen donates one p electron to the  $\pi$  system whereas the later donates two 'p' electron to the ' $\pi$ ' system. The graphitic nitrogen arises due to the substitution of carbon inside the aromatic ring. The quaternary nitrogen is the nitrogen bound with three  $sp^3$  carbon atoms. Moreover, care must be taken regarding the pyridone nitrogen. Pyridone contains one nitrogen atom in a six membered ring as similar to the pyridinic nitrogen. [70] Although the chemical structure of pyridone is similar to the pyridinic nitrogen (six membered ring), it is not found in the same binding energy as pyridinic nitrogen but it is very similar to the pyrrolic nitrogen. This is attributed to the existence of two tautomers of pyridone with stable carbonyl forms giving a matching chemical environment as that of the pyrrolic nitrogen. [71] Figure 1.10 symbolizes the type of nitrogen and its corresponding binding energy in X-ray photoelectron spectroscopy.

#### 1.14.7. Overview of N-CNS towards ORR

Recent literature reports depict the active role of the nitrogen doped carbon nanostructures as effective catalysts for various applications. The initial studies were based on nitrogen doping on Vulcan carbon and their application towards ORR. Later, the research works on the development of NPMC were extended by using different carbon nanostructures such as CNTs, CNFs, fullerene, carbon nanoplates and graphene. For example, L. Dai *et al* prepared vertically aligned carbon nanotubes (VA-CNT) for ORR and they observed remarkable ORR activity of these systems over commercial Pt/C in alkaline medium. [72] Further, VA-CNT also exhibits higher selectivity towards the methanol oxidation. This report can be considered as a breakthrough in the field of NPMC. In another work, Star *et al* [73] demonstrated nitrogen doped CNT with cup-

stacked structure with similar catalytic activity towards ORR as PtCNT. The material also could be used in the electrochemical detection of  $\text{H}_2\text{O}_2$  and glucose. In 2009, Chen *et al* [74] studied the effect of nitrogen precursors in terms of nitrogen content and activity of the resulting N-doped CNTs for ORR. Moreover, Stevenson *et al* found a strong correlation of nitrogen content with the ORR peak potential. [75]

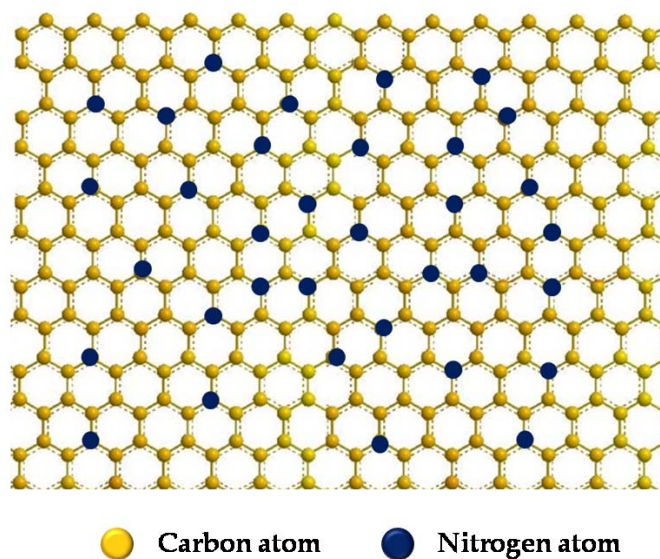


**Figure 1.11.** A pictorial representation of the nitrogen doped graphene (NGr).

In 2010, Ozkan *et al* studied the influence of edge sites of carbon nanostructures for effective nitrogen doping for ORR. [76] The study concluded that the nitrogen doping is more facile on the ‘platelets carbon nanofiber’ with more edged planes than the ‘basal plane carbon nanofiber’. The discovery of Gr opened up new era in the direction of developing new and potential nitrogen doped systems. Figure 1.11 shows the pictorial representation of the nitrogen doped graphene (NGr). Each study on the development of these materials has its own advantage and in general most of the reports highlight the importance of preparation methodology, temperature, morphology of the graphene and

nitrogen precursor and content for the effective ORR. Further, these nitrogen doped composites are retained for other energy applications including supercapacitors, [77] solar cells, [78] and Li-batteries [79] etc.

#### 1.14.8. Mechanism of ORR on N-Doped Graphene

Both theoretical and experimental studies validated that nitrogen doped CNS possesses strong catalytic activity towards ORR. Unlike on Pt, the ORR on nitrogen doped CNS (NCNS) occurs *via* either 2e- or 4e- pathways depending upon the density of the active sites, nature of the active sites and pH of the electrolyte. In fact, the ORR activity of the catalyst could be predicted as a function of the adsorption energy of oxygen molecule. The foreign atom doping facilitates the adsorption of O<sub>2</sub> molecule from end on to side on adsorption. [80]

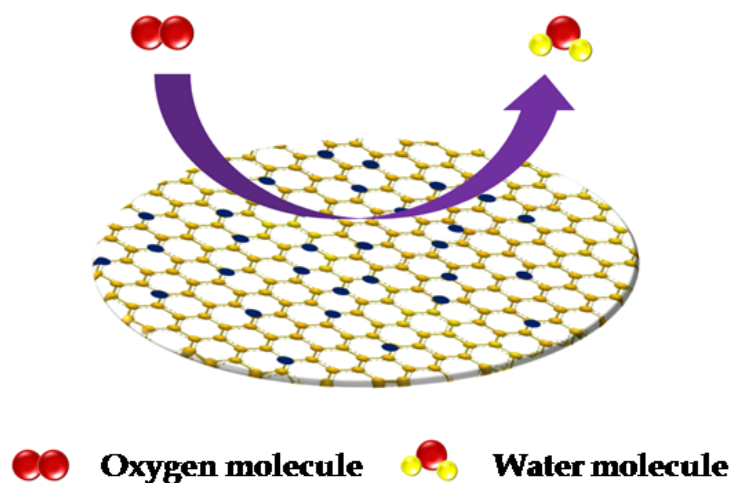
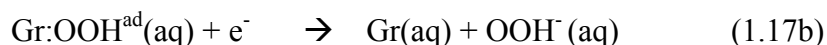
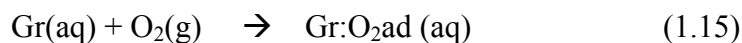


*Figure 1.12. General ORR process occurring on the nitrogen doped graphene (NGr).*

Figure 1.12 elucidates the formal ORR on the nitrogen doped graphene.

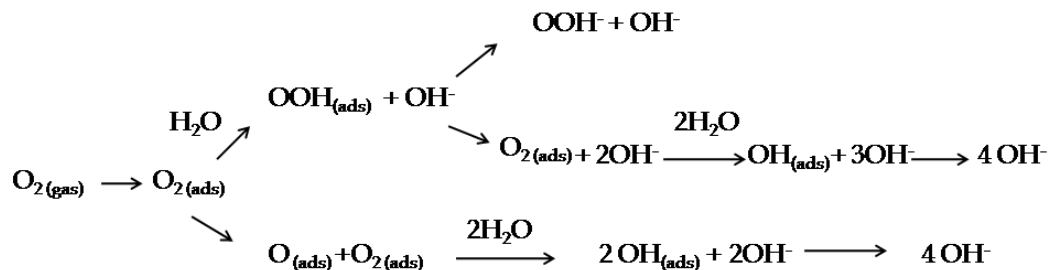
In acid medium, O<sub>2</sub> gets reduced into water either through 2e<sup>-</sup> or 4e<sup>-</sup> pathways.

The following mechanism has been proposed for ORR on NCNS in acid medium. [81]



In Equation (1.15), the Gr:O<sub>2</sub><sup>ad</sup>(aq) indicates the adsorption of oxygen molecule on the graphene surface. In 1.16, the OOH<sup>ad</sup> species is resulted by adding an electron and a proton to the adsorbed oxygen on the Gr surface. The OOH<sup>ad</sup> species proceeds *via* two different pathways by accepting an electron (step (1.17a and b)), either by breaking the O-O bond to release OH<sup>-</sup> or by breaking the Gr-O bond to liberate OOH<sup>-</sup>. The previous one corresponds to the 4e<sup>-</sup> pathway while the latter corresponds to the 2e<sup>-</sup> pathway results the production of H<sub>2</sub>O<sub>2</sub>. In 1.18, the OH<sup>ad</sup> species is resulted and in 1.19, water is released and the parent graphene site is redeveloped.

On the other hand, in alkaline medium, the O<sub>2</sub> molecule gets reduced into hydroxyl ions *via* either 2e<sup>-</sup> or 4e<sup>-</sup> pathways as similar in the acid medium. The following mechanism has been proposed in alkaline medium. [82]



The 4e- pathway results into the complete reduction of O<sub>2</sub> while the 2e- pathway results into the partial reduction leading to the formation of the unwanted OOH<sup>-</sup>. The formation of OOH<sup>-</sup> ions lowers the potential of the reaction.

As discussed previously, the doped nitrogen could be characterized into different nitrogen moieties. However, it is still controversial to predict the structure of the active nitrogen responsible for ORR. In general, the pyridinic-N is believed as the most responsible active sites for ORR due to the delocalization of the p-electron from the pyridinic-N. On the contrary, Ikeda *et al* proposed the graphitic nitrogen as the active site. [83] Most recently, Shan *et al* predicted that the Stone-Wales defect near the doped-N is a possible oxygen adsorption site for ORR due to the metallic electrons near the Fermi level. [84] The catalytic activity is mainly due to the change in the electronic configuration because of nitrogen doping. In fact, in graphene, there are two types of bonding  $\sigma$  and  $\pi$  where  $\sigma$  is supposed to be localised while  $\pi$  bonding is delocalised. When N is introduced, it creates the electron acceptor sate in the conduction band near the Fermi level. This reduces the band gap of graphene from 2.7 to 1.47 eV which makes the facile transition of electrons form the valance band to the conduction band. Moreover, the doped nitrogen donates the electron which results into the localised distribution of the molecular orbital. In addition, the doped nitrogen creates electronegativity difference

between the doped nitrogen and its adjacent carbon atoms. Thus, the chemical reactivity of graphene is significantly enhanced by the nitrogen doping.

#### 1.14.9. Other NPMC Electrocatalysts

From the inspiration of NCNS, intensive research works are carried out on the preparation of non-noble catalysts by doping with other heteroatoms such as boron (B), sulphur (S), phosphorus (P) and halogens on different carbonaceous materials. [85] Among them, B doping is relatively more facile due to its equivalent size with carbon atoms. Unlike N doping, the B atom in the matrix is positively charged and acts as the active site for ORR. [86] The doped B tunes the HOMO-LUMO band gap of Gr and subsequently increases the catalytic activity. Moreover, the B doping also alters the atomic spin and charge density of graphene which is the determining factor for ORR. [86] Several reports emphasize that the B doped Gr (BGr) can be employed as a potential non-Pt electrocatalyst for ORR. The resulting catalysts exhibit excellent ORR and higher tolerance towards methanol crossover. [87] Very recently, researchers extended their focus by preparing co-doping of Gr with N and B. [88] In the co-doped systems, both N and B can act as the active site through charge transfer with neighbouring carbon atoms. Therefore, the synergistic effect existing between B-C-N increases the overall performance of the catalyst.

It is interesting to note that, P doping on Gr moiety is also gaining much attention in the materials chemistry world. Compared to N and B, the P doping is relatively difficult owing to their bigger size which hinders the effective doping in the graphene matrix. Very few reports are available which elucidates the synthetic strategy for the preparation of P doped Gr (P-Gr) for ORR. [89] In all of them, triphenyl phosphine is

predominantly employed as the P precursor. Though the resulting catalysts exhibit appreciable ORR activity, their performance is inferior to the N doped systems and commercial Pt/C. Hence, continuous efforts are being taken to increase the ORR activity of the P-Gr based systems. Recently, it has been realized that co-doping with heteroatoms is the possible way to increase the performance of the P-Gr based samples [90].

Most recently, halogen (Cl, Br and I) doped Gr materials are also added into the list of the non-Pt electrocatalysts due to their notable ORR activity in alkaline medium. The halogen atoms create electronegativity difference (B =2.04, I = 2.66, N = 3.04, P = 2.19, S = 2.58 and C=2.55) [91] in the covalently doped graphitic carbon frameworks which further polarize adjacent carbon atoms. The quantum mechanics calculations have shown that the electron accepting/donating ability of the heteroatom dopants creates net positive/negative charges on the adjacent carbon atoms in the graphitic lattice to assist the ORR process [91]. Accordingly, Jong *et al* demonstrated a facile and scalable process for the preparation of edge halogenated graphene platelets as the ORR electrocatalysts. The resulting catalysts, particularly with Br and I, exhibit reasonably good ORR activity in alkaline medium. [91]

Among the various heteroatom doped catalysts, the N doped systems are the most attractive materials due to their higher activity. Moreover, nitrogen doping is relatively easier compared to the other cases. Further, coordination of the doped nitrogen with metal ions leads to much better activity in acid as well as alkaline medium.

### 1.14.10. Present Status of NPMC

Potential activities of the non-Pt electrocatalysts in real fuel cell tests have been recently validated extensively by various research groups. Dodelet *et al* have exclusively worked on the development of iron based non-Pt electrocatalyst for ORR. In 2009, the same group prepared Fe based catalysts by using pore filler in the slit pore of graphite and subsequent annealing in ammonia atmosphere.[92] The resulting catalyst exhibits volumetric current density from 64 to 99  $\text{Acm}^{-3}$ , which is much closer to the 2010 DOE performance target of 130  $\text{Acm}^{-3}$  for ORR on NPMCs. However, the stability of the catalyst was found to be inferior under the acidic fuel cell conditions. Prior to that, Zelenay *et al* [93] studied single cell polarisation of Co-polypyrrole composites under PEMFC conditions. The active catalyst generates a current density of 0.2  $\text{Acm}^{-2}$  at 0.50 V and a maximum power density of 0.14  $\text{Wcm}^{-2}$  with higher stability. Subsequently, several reports appeared based on the works on the development of non-Pt electrocatalysts for ORR. Specifically, very recently, Dodelet *et al* reported facile preparation of an iron based catalyst by impregnation of iron and nitrogen precursors in the pores of zeolitic imidazolate framework (ZIF) followed by thermal treatment in Ar atmosphere. The resulting catalyst showed a maximum power density of  $\sim 930 \text{ mWcm}^{-2}$  which is regarded as the benchmark for the non-Pt electrocatalysts till date. [94] In the case of AEMFCs, very few reports are available which demonstrate the ORR tendency of the non-Pt catalysts under AEMFCs conditions. Very recently, Ishikawa *et al* exploited N doped CNT (NCNT) as an ORR electrocatalyst under AEMFC conditions and found that the resulting NCNT is capable of delivering a maximum power density of  $\sim 37 \text{ mWcm}^{-2}$ , which also is regarded as the benchmark catalyst in AEMFCs. [95]

#### **1.14.11. Effect of Edge Planes of Carbon Nano Structures (CNS)**

From the wide spectrum of literature review, it is understood that a careful choice of nitrogen precursors, metal precursors, thermal conditions and suitable CNS could provide active NPMC-catalysts to outperform the Pt/C catalysts. Obviously, the nature of the active sites in NPMC is governed primarily by structural and mechanical characteristics of CNS. The ideal CNS must have high surface area, porosity, edge plane exposure, high electrical conductivity, and mechanical stability. In addition, the nano confinement of the CNS plays a key role. The nano confinement provides a distinctive condition for the facile electrochemical reaction in terms of mass transport and apparent electrokinetics. Besides, the crystalline edge planes also play a key role to determine the electro kinetic efficiency. Indeed, an electrochemical reaction on the edge planes of CNS is more facile than that on the basal planes. Further, when doped with N, it induces an additional exposure of the edge planes and, thus, a controlled interplay of these two types of active sites together contribute towards the improvement of the catalytic activity for the sluggish ORR in PEFCs.

#### **1.15. Scope and Objectives of the Present Study**

An analysis of the current research activities clearly reveals that the prospect of commercialisation of PEFCs is hampered by many challenges. In particular, electrocatalysts gain much attention as they play a crucial role in these types of energy conversion devices. Most importantly, high cost of Pt remains as one of the main stumbling blocks in the path of developing commercially viable PEFCs. Hence, development of cost competent and efficient catalysts is an important and necessary task

in the direction of bringing PEFCs from lab to market. The sluggish kinetics of ORR on the cathode catalyst is another bottleneck for PEFC commercialization. Hence, development of commercially viable, electrochemically active and stable catalysts is the only practical solution to overcome the existing challenges. Efforts are underway to develop the desired catalysts to enlarge the practical utilisation of PEFCs. Hence, the present thesis is aimed to develop novel electrocatalysts for ORR by means of nitrogen doping on different carbonaceous materials with different dimensions. In order to attain useful correlations between the support structure and ORR activity, the doping study needs to be carried out by changing the morphological characteristics of the carbon materials, preferably from one dimensional (1-D) to three dimensional (3-D). Hence, the present thesis is aimed to understand the influence of the peculiar morphological features of these carbon materials for the effective nitrogen doping and ORR. While focusing on the structure-activity correlations, development of suitable strategies for achieving efficient nitrogen doped catalytic sites having reduced overpotential for ORR is another objective of the thesis. Detailed characterization of the prepared catalysts and investigation of their ORR activity under PEFC operating conditions are other key objectives of the present work. The specific objectives of the work to be carried out are listed as follows:

1. Design a novel electrocatalyst by utilising the unique morphological characteristics of one dimensional (1-D) carbon nanofiber (CNF) having slanting planes and rough edges for the effective nitrogen doping. Further, the influence of metal coordination with the doped nitrogen for effective ORR needs to be investigated.

2. An efficient method for preparing two dimensional (2-D) porous graphene with the aid of *in-situ* generated metal oxide nanoparticles and creation of potential nitrogen-doped active sites along the pore openings. Prospects of the material as an ORR electrocatalyst have to be investigated. Further, the role of metal oxide to engrave the surface of graphene is another point of investigation in this study.
3. Development of a viable synthetic strategy for the preparation of two dimensional (2-D) porous graphene by removing small graphene quantum dots (GQDs) from the Gr surface by a simple oxidative treatment. Since the pore openings are expected to give more unsaturation and defect sites, nitrogen doping along the pore openings and detailed investigation towards ORR are two main targets of the present work.
4. Development of a 3-D structured microporous carbon framework from zeolitic imidazolate framework (ZIF) and creation of nitrogen doped active centers to make the material suitable for ORR applications.

## 1.16. References

- [1] *An Introduction to Fuel cells and Hydrogen Technology* by Brian Cook.
- [2] Conway, B. E. *Electrochemical Supercapacitors: Scientific Fundamentals and Technological Applications*; 2<sup>nd</sup> edn. Kluwer Academic Publisher, New York.
- [3] S. J. Litzelman, J. L. Hertz, W. Jung and H. L. Tuller, *Fuel Cells*, **2008**, 8, 294.
- [4] B. K. Lai, H. Xiong, N. Tsuchiya, A. C. Johnson and S. Ramanathan, *Fuel Cells*, **2009**, 9, 699.
- [5] L. G. Marianowski, E. H. Camara, H. C. Maru, *U.S. Patent* 4079171, 1977.
- [6] R. J. Berger, E. B. Doesburg, J. G. van Ommen, J. R. H. Ross, *Applied Catalysis A: General*, **1996**, 143, 343.
- [7] Retrieved from <http://en.fcc.gov.ir/Fuel-Cell-Acid-fosforic.aspx>
- [8] Viswanathan, B.; Scibioh, M. A. *Fuel Cells: Principles and Applications*. University Press, India, **2006**. Chapter 4
- [9] *Fuel cell bulletin*, **2008**, 4.
- [10] K. Kordesh, G.R. Simader, *Chem. Rev.* **1995**, 95, 191.
- [11] K. Kordesh, *Power Sources for Electric Vehicles. Modern Aspects of Electrochemistry*, Plenum Press, New York, **1975**, 10, 339.
- [12] J. R. Varcoe, R. C. T. Slade, *Fuel Cells* **2005**, 5, 187.
- [13] E Agel, J. Bouet, *J. Power Sources*, **2001**, 101, 267.
- [14] J. Kunze, U. Stimming, *Angew. Chem. Int. Ed.* **2009**, 48, 9230.
- [15] Metha, V.; Cooper, J. S. *J. Power Sources*, **2003**, 114, 32.

- [16] D. C. Montgomery, *Design and Analysis of Experiments*, John Wiley and Sons Inc, New York 1976. (b) W. E. Duckworth, *Statistical Techniques in Technological Research*, Methuen, London. 1968.
- [17] B. C.H Steele, A. Heinzl, *Nature*, **2001**, 414, 345.
- [18] <http://www.fuelcells.org/info/library/ADLCostModel.pdf> accessed on 20th September, **2013**.
- [19] O. Antoine, Y. Bultel, R. Durand, *J. Electroanal. Chem.* **2001**, 499, 85
- [20] J. T. Hwang and J. S. Chung, *Electrochimica Acta*, **1993**, 38, 2715.
- [21] (a) J. Wu, J. Zhang, Z. Peng, S. Yang, F. T. Wagner and H. Yang, *J. Am. Chem. Soc.* **2010**, 132, 4984. (b) J. Zhang, K. Sasaki, E. Sutter, R. R. Adzic, *Science*, **2007**, 315, 220.
- [22] Y. Qian, W. Wen, P. A. Adcock, Z. Jiang, N. Hakim, M. S. Saha and S. Mukerjee, *J. Phys. Chem. C* **2008**, 112, 1146.
- [23] J. Zhang, K. Sasaki, E. Sutter, R. R. Adzic, *Science*, **2007**, 315, 220.
- [24] V. R. Stamenkovic, B. Fowler, B. S. Mun, G. F. Wang, P. N. Ross, C. A. Lucas, N. M. Markovic, *Science* **2007**, 315, 493.
- [25] (a) J. Zhang, Y. Mo, M. B. Vukmirovic, R. Klie, K. Sasaki, R. R. Adzic, *J. Phys. Chem. B* **2004**, 108, 10955. (b) J. Zhang, M. B. Vukmirovic, Y. Xu, M. Mavrikakis, R. R. Adzic, *Angew. Chem., Int. Ed* **2005**, 44, 2132.
- [26] J. Zhang, F. H. B. Lima, M. H. Shao, K. Sasaki, J. X. Wang, J. Hanson, and R. R. Adzic, *J. Phys. Chem. B*, **2005**, 109, 48.
- [27] H. W. Kroto, J. R. Heath, S. C. O'Brien, R. F. Curl, R. E. Smalley, *Nature*, **1985**, 318, 162

- [28] S. A. M. Silva, J. Perez, R.M. Torresi, C.A. Luengo, E.A. Ticianelli, *Electrochim. Acta*, **1999**, *44*, 3565.
- [29] C. Roth, I. Hussain, M. Bayati, R. J. Nichols, D. J. Schiffrin, *Chem. Commun*, **2004**, 1532.
- [30] G. Feng, Z. G.Lin, Y. Shizhong, J. S. James, *J. Am. Chem. Soc.* **2013**, *135*, 3315.
- [31] S. Iijima, *Nature*, **1991**, *354*, 56.
- [32] P. J. F. Harris, *Carbon Nanotube Science - Synthesis, Properties, and Applications* (Cambridge Univ. Press, Cambridge, **2009**).
- [33] K. Gong, F. Du, Z. Xia, M. Durstock, L. Dai, *Science*, **2009**, *323*, 760.
- [34] L. Yuehe, C. Xiaoli, Y. Clive, M. W. Chien, *J. Phys. Chem. B*, **2005**, *109*, 14410.
- [35] Li. Wenzhen, W. Xin, C. Zhongwei, W. Mahesh, Y. Yushan, *J. Phys. Chem. B*, **2006**, *110*, 15353.
- [36] K. B. Beena, M. U. Sreekuttan, S. Kurungot, *J. Phys. Chem. C*, **2009**, *113*, 17572.
- [37] *Scientific Background on the Nobel Prize in Physics 2010 Class for Physics of the Royal Swedish Academy of Sciences.*
- [38] K. Novoselov, A. Geim, S. Morozov, D. Jiang, Y. Zhang, S. Dubonos, I. Grigorieva, A. Firsov, *Science*, **2004**, *306*, 666.
- [39] W. Yang, K. R. Ratinac, S. P. Ringer, P. Thordarson, J. J. Gooding, F. Brat, *Angew. Chem. Int. Ed.* **2010**, *49*, 2114.

- [40] Y. Li, Y. Hu, Y. Zhao, G. Shi, L. Deng, Y. Hou, L. Qu, *Adv. Mater.* **2011**, *6*, 776.
- [41] L. Qiqi, Z. Sheng, D. Liming, L. L. Shi, *J. Am. Chem. Soc.*, **2012**, *134*, 18932.
- [42] R. J. Jasinski, *J. Electrochem. Soc.* 1965, **112**, 526. (b) R. J. Jasinski, *Nature*, **1964**, *201*, 1212.
- [43] Z. Shi and J. J. Zhang, *J. Phys. Chem. C*, **2007**, *111*, 7084.
- [44] G. I. Cardenas-Jiron, *J. Phys. Chem. A*, **2002**, *106*, 3202. (b) J. B. Ouyang, K. Shigehara, A. Yamada and F. C. Anson, *J. Electroanal. Chem. Interfacial Electrochem.*, **1991**, *297*, 489. (c) E. H. Song, C. N. Shi and F. C. Anson, *Langmuir*, **1998**, *14*, 4315.
- [45] C. Song, L. Zhang, J. Zhang, D. P. Wilkinson and R. Baker, *Fuel Cells*, **2007**, *7*, 9.
- [46] J. A. R. van Veen, J. F. van Baar and K. J. Kroese, *Journal of Chemical Society Faraday Transactions*, **1981**, *77*, 2827.
- [47] H. Alt, H. Binder and G. Sandsted, *J. Catal.*, **1973**, *28*, 8.
- [48] H. Jahnke, M. Schonborn, G. Zimmerman, *Fortschr. Chem. Forsch.* **1976**, *61*, 133.
- [49] a) A. Biloul, F. Coowar, O. Contamin, G. Scarbeck, M. Savy, D. van den Ham, J. Riga and J. J. Verbist, *J. Electroanal. Chem.*, **1992**, *328*, 219; b) R. W. Joyner, *J. Chem. Soc., Farad. T. 1*, **1982**, *78*, 1021. c) R. Jiang and D. Chu, *J. Electrochem. Soc.*, **2000**, *147*, 4605.
- [50] G. Lalande, G. Faubert, R. Cote, D. Guay, J. P. Dodelet, L. T. Weng and P. Bertrand, *J. Power Sources*, **1996**, *61*, 227.

- [51] U. Kramm, I. Abs-Wurmbach, I. Herrmann-Geppert, J. Radnik, S. Fiechter and P. Bogdanoff, *J. Electrochem. Soc.*, **2011**, *158*, 69. (b) A. L. B. Wijnoltz, W. Visscher, J. A. R. van Veen, E. Boellaard, A. M. van der Kraan and S. C. Tang, *J. Phys. Chem. B*, **2002**, *106*, 12993. (c) Y. Nabae, S. Moriya, K. Matsubayashi, S. M. Lyth, M. Malon, L. B. Wu, N. M. Islam, Y. Koshigoe, S. Kuroki, M. A. Kakimoto, S. Miyata and J. Ozaki, *Carbon*, **2010**, *48*, 2613.
- [52] U. I. Koslowski, I. Abs-Wurmbach, S. Fiechter and P. Bogdanoff, *J. Phys. Chem. C*, **2008**, *112*, 15356. (b) U. Kramm, I. Abs-Wurmbach, I. Herrmann-Geppert, J. Radnik, S. Fiechter and P. Bogdanoff, *J. Electrochem. Soc.*, **2011**, *158*, 69.
- [53] A. L. Bouwkamp-Wijnoltz, W. Visscher, J. A. R. van Veen, E. Boellaard, A. M. van der Kraan and S. C. Tang, *J. Phys. Chem. B*, **2002**, *106*, 12993. (b) G. Liu, X. G. Li, P. Ganesan and B. N. Popov, *Electrochim. Acta*, **2010**, *55*, 2853.
- [54] S. Gupta, D. Tryk, I. Bae, W. Aldred, E. Yeager, *J. Appl. Electrochem.*, **1989**, *19*, 19.
- [55] J. Yang, D. J. Liu, N. N. Kariuki and L. X. Chen, *Chem. Commun.*, **2008**, 329.
- [56] a) G. Faubert, R. Cote, D. Guay, J. P. Dodelet, G. Denes, C. Poleunis and P. Bertrand, *Electrochim. Acta*, **1998**, *43*, 1969. b) M. Lefevre, J. P. Dodelet and P. Bertrand, *J. Phys. Chem. B*, **2002**, *106*, 8705. c) M. Lefevre, J. P. Dodelet and P. Bertrand, *J. Phys. Chem. B*, **2000**, *104*, 11238. d) M. Lefevre and J. P. Dodelet, *Electrochim. Acta*, **2003**, *48*, 2749. e) M. Lefevre, J. P. Dodelet and P. Bertrand, *J. Phys. Chem. B*, **2005**, *109*, 16718. f) J. Fournier, G. Lalande, R. Cote, D. Guay and J. P. Dodelet, *J. Electrochem. Soc.*, **1997**, *144*, 218. g)

- G. Lalande, D. Guay and J. P. Dodelet, *Chem. Mater.*, **1997**, *9*, 784. h) C. Medard, M. Lefevre, J. P. Dodelet, F. Jaouen and G. Lindbergh, *Electrochim. Acta*, **2006**, *51*, 3202.
- [57] S. Ruggerie, and J. P. Dodelet *J. Electrochem. Soc.*, **2007**, *8*, 761.
- [58] J. Herranz, M. Lefèvre and J. P. Dodelet, *J. Electrochem. Soc.*, **2009**, *156*, 593.
- [59] M. Lefevre, J. P. Dodelet, P. Bertrand, *J. Phys. Chem. B*, **2000**, *104*, 11238.
- [60] R. Cote, G. Lalande, D. Guay, J. P. Dodelet, G. Denes, *J. Electrochem. Soc.* **1998**, *145*, 2411.
- [61] F. Jaouen, S. Marcotte, J. P. Dodelet and G. Lindbergh, *J. Phys. Chem. B*, **2003**, *107*, 1376.
- [62] U. I. Kramm, J. Herranz, N. Larouche, T. M. Arruda, M. Lefevre, F. Jaouen, P. Bogdanoff, S. Fiechter, I. Wurmbach, S. Mukerjee and J. P. Dodelet, *Phys. Chem. Chem. Phys.*, **2012**, *14*, 11673. (b) U. Kramm, I. Abs-Wurmbach, I. Herrmann-Geppert, J. Radnik, S. Fiechter and P. Bogdanoff, *J. Electrochem. Soc.*, **2011**, *158*, 69.
- [63] Z. Luo, S. Lim, Z. Tian, J. Shang, L. Lai, B. MacDonald, C. Fu, Z. Shen, T. Yu and J. Lin, *J. Mater. Chem.*, **2011**, *21*, 8038.
- [64] N. P. Subramanian, X. G. Li, V. Nallathambi, S. P. Kumaraguru, H. Colon-Mercado, G. Wu, J. W. Lee and B. N. Popov, *J. Power Sources*, **2009**, *188*, 38. (b) X. G. Li, G. Liu and B. N. Popov, *J. Power Sources*, **2010**, *195*, 6373. (c) S. Maldonado and K. J. Stevenson, *J. Phys. Chem. B*, **2005**, *109*, 4707.
- [65] G. S. Szymanski, T. Grzybek, H. Papp, *Catal. Today*, **2004**, *90*, 51.

- [66] S. Latil, S. Roche, D. Mayou, J-C. Charlier, *Phys Rev Lett*, **2004**, 92, 256805.
- [67] V. V. Strelko, V. S. Kuts, P. A. Thrower, *Carbon*, **2000**, 38, 1499.
- [68] H. Sjostrom, S. Stafstrom, M. Boman, J. E. Sundgren, *Phys. Rev.Lett.* **1995**, 75, 1336.
- [69] R. Czerw , M. Terrones, J. C.Charlier , X. Blase, B. Foley, R. Kamalakaran, N. Grobert, H. Terrones, D. Tekleab, P. M. Ajayan, W. Blau, M. Ruhle and D. L. Carroll, *Nano Letts*, **2001**, 1, 457.
- [70] R. Silva, D. Voiry, M. Chhowalla, T. Asefa, *J. Am. Chem. Soc.* **2013**, 135, 7823.
- [71] G. Wu and P. Zelenay, *Acc. Chem. Res.*, **2013**, 46, 1878.
- [72] K. Gong, F. Du, Z. Xia, M. Durstock, L. Dai *Science*, **2009**, 323, 760
- [73] Y. Tang, B. L. Allen, D. R. Kauffman and A. Star, *J. Am. Chem. Soc.* **2009**, 131, 13200.
- [74] Z. Chen, D. Higgins, H. Tao, R. S. Hsu and Z. Chen *J. Phys. Chem. C* **2009**, 113, 21008.
- [75] S. Maldonado, K. J. Stevenson, *J. Phys. Chem. B*, **2009**, 109, 4707.
- [76] E. J. Biddinger, D. V. Deak, U. S. Ozkan, *Top Catal*, **2009**, 52, 1566.
- [77] H. M. Jeong, J. W. Lee, W. H. Hin, Y. J. Choi, H. J. Shin, J. K. Kang and J. W. Choi, *Nano Lett.* **2011**, 11, 2472.
- [78] M. J. Ju, J. C. Kim, H.J. Choi, I. T. Choi, S. G. Kim, K. Lim, J. Ko, J. J. Lee, I. Y. Jeon, J. B. Baek and H. K. Kim, *ACS Nano*, **2013**, 7, 5243.

- [79] Y. Li , J. Wang , X. Li , J. Liu , D. Geng , J. Yang , R. Li , X. Sun , *Electrochem. Commun.* **2011**, *13*, 668. (b) M. K. Song S. Park, F. M. Alamgir, J. Cho, M Liu, *Materials Science and Engineering*, **2011**, *72*, 203.
- [80] D. Jariwala, V. K. Sangwan, L. J. Lauhon, T. J. Marks and M. C. Hersam, *Chem. Soc. Rev.*, **2013**,*42*, 2824.
- [81] H. Kim, K. Lee, S. I. Woo and Y. Jung, *Phys. Chem. Chem. Phys.*, **2011**, *13*, 17505.
- [82] H. Kim, K. Lee, S. I. Woo and Y. Jung, *Phys. Chem. Chem. Phys.*, **2011**, *13*, 17505.
- [83] T. Ikeda, M. Boero, S. F. Huang, K. Terakura, M. Oshima and J. Ozaki, *J. Phys. Chem. C*, **2008**, *112*, 14706.
- [84] B. Shan and K. Cho, *Chem. Phys. Lett.*, **2010**, *492*, 131.
- [85] Y. Zheng, Y. Jiao, L. Ge, M. Jaroniec and S. Z. Qiao, *Angew. Chem. Int. Ed.* **2013**, *52*, 3110.
- [86] H. Wang, Y. Zhou, D. Wu, L. Liao, S. Zhao, H. Peng and Z. Liu, *Small*, **2013**, *9*,1316.
- [87] Z. H. Sheng, H. L. Gao, W. J. Bao, F. B. Wang and X. H. Xia, *J. Mater. Chem.*, **2012**, *22*, 390.
- [88] S. Wang, E. Iyyamperumal, A. Roy, Y. Xue, D. Yu and L. Dai *Angew. Chem. Int. Ed.* **2011**, *50*, 11756. (b) S. Wang, L. Zhang, Z. Xia, A. Roy, D. W. Chang, J. B. Baek and L. Dai *Angew. Chem. Int. Ed.* **2012**, *51*, 4209 (c) L. S. Panchakarla, K. S. Subrahmanyam, S. K. Saha, A. Govindaraj, H. R.

- Krishnamurthy, U. V. Waghmare and C. N. R. Rao, *Adv. Mater.* **2009**, *21*, 4726.
- [89] C. Zhang, N. Mahmood, H. Yin, F. Liu and Y. Hou, *Adv. Mater.* **2013**, *25*, 4932.
- [90] C. Choi, M. W. Chung, H. C. Kwon, S. H. Parka and S. I. Woo *J. Mater. Chem. A*, **2013**, *1*, 3694.
- [91] I. Y. Jeon, H. J. Choi, M. Choi, J. M. Seo, S. M. Jung, M. J. Kim, S. Zhang, L. Zhang, Z. Xia, L. Dai, N. Park and J. B. Baek, *Sci. Reprts*, DOI: 10.1038/srep01810.
- [92] M. Lefèvre, E. Proietti, F. Jaouen and J. P. Dodelet, *Science*, **2009**, *324*, 71.
- [93] R. Bashyam and P. Zelenay, *Nature*, **2006**, *443*, 63.
- [94] E. Proietti, F. Jaouen, M. Lefèvre, N. Larouche, J. Tian, J. Herranz and J. P. Dodelet, *Nature Comm*, DOI: 10.1038/ncomms1427.
- [95] C. V. Rao and Y. Ishikawa, *J. Phys. Chem. C*, **2012**, *116*, 4340.

## Chapter 2

### Experimental Methods and Characterization Techniques

---

The present chapter gives a brief description of various synthesis strategies adopted for the preparation of nitrogen-doped carbonaceous materials. This chapter also describes the preparation of an active low-Pt electrocatalyst based on FeN<sub>x</sub>CNF (PtFeN<sub>x</sub>CNF). Further, the chapter briefly describes the working principles of various physico-chemical methods such as high resolution transmission electron microscopy (HRTEM), scanning electron microscopy (SEM), energy dispersive X-ray analysis (EDAX), X-ray diffraction (XRD), X-ray photo electron spectroscopy (XPS) and Raman spectroscopy *etc* to elucidate the structure of the prepared catalysts. Finally, the working principles of various electrochemical techniques such as cyclic voltammetry (CV) and rotating disc electrode (RDE), which are extensively used in the present work to study the ORR activity characteristics of the above prepared catalysts, are also discussed.

---

## 2.1. Experimental Section

### 2.1.1. Chemicals Required

Carbon nanofiber (CNF) was procured from the Pyrograf Products, Inc., USA. Iron acetate ( $\text{FeOAc}$ )<sub>2</sub>, potassium hydroxide (KOH) and Hexachloroplatinic acid (IV) Hexahydrate ( $\text{H}_2\text{PtCl}_6 \cdot 6\text{H}_2\text{O}$ ) were purchased from Sigma Aldrich. Graphite powder and potassium permanganate ( $\text{KMnO}_4$ ) required for the synthesis of Graphene Oxide (GO) were purchased from Sigma Aldrich and Rankem Chemicals respectively. The acids for the abovementioned synthesis (98 % con.  $\text{H}_2\text{SO}_4$  and 88 % orthophosphoric acid) were used without further purification. Hydrogen peroxide ( $\text{H}_2\text{O}_2$ ) (30 % w/v, Thomas Baker Chemicals) was used for functionalization of graphene. Throughout the study, 1,10-phenanthroline (Aldrich 99 %) was used as the nitrogen precursor. For dialysis, dialysis bag (Membra Cel MD34 14 x 100 CLR; USA) was employed. Quinine sulphate (99 %) used as reference for the calculation of PL quantum yield was purchased from Aldrich Chemicals. Ethanol (99 %) was used devoid of further purification. Deionised water (18 m $\Omega$ ) from the milli-Q set-up was used for performing all these experiments.

### 2.1.2. Preparation of Iron-Nitride Doped Carbon Catalyst

In a typical synthesis of iron nitride-doped carbon catalyst (FeN/C), appropriate amount of suitable carbon materials was dispersed in 50 ml of ethanol (Rankem 99.9%) by ultrasonication. An excess of 1,10 phenanthroline was dissolved in 25 ml of ethanol and was allowed to fill the inner pore of carbon material by magnetic stirring for about 30 min. Further, the required amount of  $\text{Fe}(\text{OAc})_2$  in ethanol was added drop by drop to 1,10-phenanthroline in the carbon mixture. In all the cases, the weight percentage of Fe

was maintained about 0.5 %. The  $\text{Fe}(\text{OAc})_2$  reacted with 1,10 phenanthroline to form  $\text{Fe}[(\text{phen})_3]^{2+}$  chelate complex which was confirmed from the color change from pale yellow to wine red. Subsequently, the chelate complex solution was mechanically stirred for 24 h at room temperature to achieve better diffusion of iron chelate complex into the inner pore of carbon materials. The resulting mixture was placed in a beaker on an oven and the solvent was evaporated at 50 °C for about 3 h. The resulting solid material was placed in a quartz tube and pyrolysed in Ar atmosphere at 900 °C. The temperature ramp was 10 °C per minute till it reaches 900 °C and maintained at that temperature for 3 h with an Ar flow of 0.5 sccm. While heating, when the temperature reaches around 350 °C, greenish vapours came out via the outlet which indicates the decomposition of phenanthroline in the reaction mixture. This was allowed to cool to room temperature after pyrolysis with Ar flow. The pyrolysed product was then washed with ethanol, filtered to remove the chars of organic residues. The final product was dried at 100 °C for 2 h and preserved for further study. The nitrogen-doped carbon materials were also prepared by the same experimental procedure without the addition of Fe precursor.

### 2.1.3. Preparation of Pt Based Electrocatalyst by Modified Polyol Process

For the facile decoration of Pt on inner and outer wall of iron nitride-doped CNF ( $\text{FeN}_x\text{CNF}$ ) *i.e.*  $\text{PtFeN}_x\text{CNF}$ , a modified polyol process was employed. [1] In the typical synthesis of  $\text{PtFeN}_x\text{CNF}$  electrocatalyst, Hexachloroplatinic acid (IV) Hexahydrate ( $\text{H}_2\text{PtCl}_6 \cdot 6\text{H}_2\text{O}$ ) (Aldrich) was used as the Pt precursor and a mixture of ethylene glycol with water (3:2) was used as the solvent as well as the reducing agent. In order to facilitate the diffusion of Pt precursor into the inner wall of  $\text{FeN}_x\text{CNF}$ , the surface tension

of the solvent was carefully maintained by properly tuning the solvent composition. For the preparation of Pt loaded catalyst, the required amount of  $\text{FeN}_x\text{CNF}$  was well dispersed in the solvent mixture with the aid of ultrasonication. Followed by this, the Pt precursor ( $\text{H}_2\text{PtCl}_6 \cdot 6\text{H}_2\text{O}$ ), which was dissolved in the same solvent mixture, was added drop by drop and the mixture was kept for aging for about 12 h with mechanical stirring. Subsequently, the mixture was heated up to 140 °C for 8 h for the complete reduction of Pt ions. Finally, the mixture was allowed to cool and washed with DI water followed by acetone to remove the unreacted solvent molecules and dried at 80 °C in an oven for 3 h. The final product was preserved for further studies. The PtNCNF and PtCNF were also prepared by the same experimental procedure but by using NCNF and CNF as the respective support materials.

#### 2.1.4. Preparation of Graphene Oxide (GO)

GO was synthesized by improved Hummer's method. [2] Briefly, a mixture of potassium permanganate ( $\text{KMnO}_4$ ) and graphite powder (6:1 g ratio) was added slowly to the acid mixture of con.  $\text{H}_2\text{SO}_4$  and  $\text{H}_3\text{PO}_4$  (9:1 ratio) with mechanical stirring at 0 °C. Further, the temperature of the reaction mixture was allowed to increase up to 45 °C for 1 h followed by increasing the temperature up to 55 °C and maintaining the same temperature for 12 h. Subsequently, 3 ml of 30 %  $\text{H}_2\text{O}_2$  in ice water was added to the reaction mixture to stop the oxidation of the reaction. The mixture was subjected to centrifugation at 12000 rpm and the supernatant solution was decanted away. The resulting material was subjected to multiple washings with water, ethanol, acetone and polyether in sequence and conserved for further use.

### 2.1.5. Preparation of reduced Graphene oxide (r-GO) from Graphene Oxide (GO)

r-GO was prepared by the pyrolysis of GO at high temperature in inert (Ar) atmosphere. Briefly, GO was loaded in an alumina boat, which was placed in the quartz tube. Further, the tube was kept in a tubular furnace under inert atmosphere by purging Ar by maintaining a flow rate of 0.5 sccm. Subsequently, the temperature of the furnace was increased up to 900 °C and thereafter the same temperature was maintained for 3 h. This was allowed to cool down to room temperature after pyrolysis with Ar flow. The pyrolysed product was then preserved for further studies.

### 2.1.4. Electrode Preparation

The working electrode was prepared by dispersion of 5 mg of the catalyst in 1 ml of ethanol in water (3:2) solution by sonication. Subsequently, 10  $\mu\text{L}$  from the prepared slurry was placed on the GC electrode with the help of a micro syringe. Subsequently, 3  $\mu\text{L}$  of 0.1 % Fumion in N-methyl pyrrolidone or 0.1 % Nafion in ethanol solution was coated as a binder on the surface of the catalyst layer to protect the detachment of the catalyst particles. Prior to the experiment, the electrode was polished on a polishing cloth using 0.3  $\mu\text{m}$  alumina slurry followed by washing with water and acetone. Finally, this electrode was further dried under a lamp for 3 h and was used as the working electrode for the experiments. 0.1 M KOH or 0.5 M  $\text{HClO}_4$  was used as the electrolyte for all the CV and RRDE studies. All the CV experiments were carried out at a scan rate of 5  $\text{mV s}^{-1}$  whereas all the RRDE experiments were carried out at a scan rate of 10  $\text{mV s}^{-1}$ . In the electrochemical studies for non-Pt electrocatalysts, the current is normalized with area of electrode (0.19625  $\text{cm}^2$ ). However, in the case of Pt based catalysts, the current is normalized with loading of Pt. The loading the Pt for PtFeNxCNF, PtNCNF and PtCNF

is  $0.05 \text{ mgcm}^{-2}$  whereas in Pt/C the loading is  $0.1 \text{ mgcm}^{-2}$ . During the CV and RRDE experiments, oxygen and nitrogen were used to maintain the oxygen rich and inert atmosphere, respectively and the ring potential was set to 0.6 V.

## **2.2. Material Characterization Techniques**

### **2.2.1. Transmission Electron Microscopy (TEM)**

Transmission electron microscopy (TEM) is the powerful technique for the high resolution imaging in the broad range of scientific fields including biologic and physical sciences. Since TEM provides the direct evidence in the local structure and the irregularities at the atomic level of the nano materials, the technique has been used extensively to determine the size, shape, arrangement of atoms in the nanoparticles. [3] Moreover, high resolution TEM (HRTEM) enables to know atomic lattice fringes of the particles upto 1 nm or still better which helps to identify the structural arrangement of atoms in nanocrystals. In fact, TEM operates with the same principle of light microscope while employing electron instead of light. In principle, the sample to be studied is illuminated with a beam of electrons accelerated by an electric field formed by a potential difference of 200 kV and are focused by a set of condenser lenses. When the illumination of specimen with beam of electrons occurs, the electrons are either scattered by some phenomena or they remain unaffected. The later process results the non uniform appearance of electrons from the surfaces of the specimen onto a fluorescent screen or a layer of photographic film which can be detected using a charge coupled device (CCD) camera. As, an electron diffraction pattern is acquired from the angular distribution of scattering. This diffraction pattern provides information about microstructure, defects and

crystallographic nature of the specimen. However, the primary inadequacy of this technique is that it is destructive in nature and thus some specimen under investigation will get destroyed by the electron beam passage. [4]

In the present study, the high resolution transmission electron microscope (HRTEM) FEI model TECNAI G<sup>2</sup> F30 instrument operated at an accelerating voltage of 300 kV (Cs = 0.6 mm, resolution 1.7 Å) was used to characterize the structural properties of the prepared samples. For the TEM analysis, the samples were prepared by drop casting ethanol solution of the samples on 200 mesh copper grid coated with carbon film (ICON Analytical) and dried in vacuum for overnight before loading in the electron microscope chamber.

### **2.2.2. Scanning Electron Microscopy (SEM) and Energy Dispersive X-ray Analysis (EDAX)**

A scanning electron microscope (SEM) can be used for high magnification imaging to determine the morphological characteristics of the specimen. When SEM is coupled with EDX, the technique offers the topographical information and the chemical composition of the sample under study. In principle, a high energy beam of charged particles is focused onto the sample under study. The incident beam may excite an electron in an inner shell, which creates a hole *via* the ejection of an electron. In order to fill the vacancy thus formed, an electron from the higher energy outer shell jumps to the hole and the energy thus dissipated in the form of an X-ray. The ejected electrons can be emitted *via* field emission. The interaction between the electron beam and the specimen produces mainly two different signals namely secondary electrons (SE) and the backscattered electrons (BSE) which are often used to produce the SEM images. Due to the interaction between the positively charged nucleus, the electrons are getting scattered into the large angle

varied from  $0^\circ$  to  $180^\circ$ . Consequently, the primary electrons arriving at a given detector can be used to produce the SEM images. [5] An energy dispersive spectrometer is connected to find the number and the energy of the emitted X-rays. These X-rays are the characteristic of the energy between the two shells and the atomic structure of the element from which they are emitted, hence a viable technique for the measurement of elemental composition.

In the present study, EDX measurements were performed on a SEM system (FEI, Model Quanta 200 3D) equipped with EDX attachment at an operating potential of 30 kV. For the SEM imaging, the sample was well dispersed in ethanol by means of ultrasonication and drop casted on the Al grid. For the effective comparison, the experimental parameters are kept constant while analyzing the samples.

### 2.2.3. Powder X-ray Diffraction Pattern (PXRD)

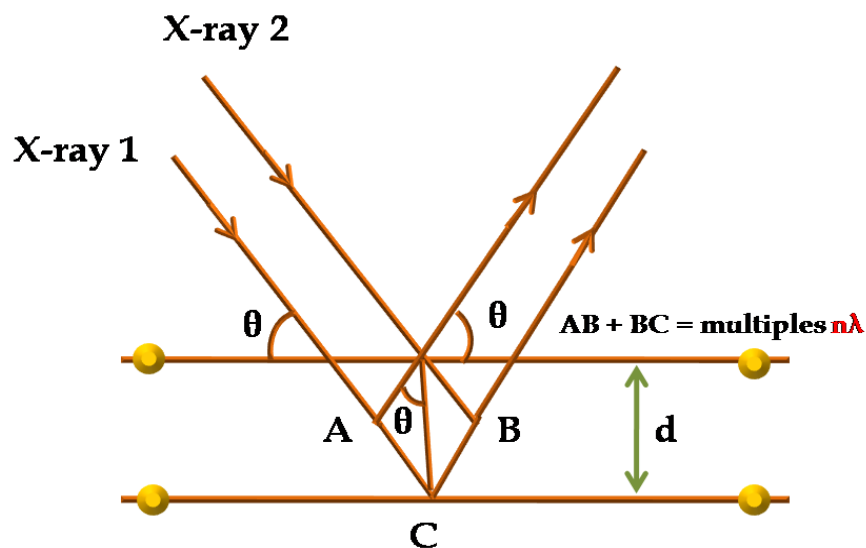


*Figure 2.1. A pictorial representation of X-ray reflections from a crystal.*

PXRD is a powerful tool to analyze the crystallinity of the materials. In fact, diffraction pattern could be observed when the X-rays interact with a crystalline substance (phase), and thus obtained pattern is the fingerprint of the substance. [6] Hence, the PXRD technique is ideally suited for characterization and identification of polycrystalline phases. Indeed, all solid matter can further described as amorphous and crystalline. In amorphous, all the atoms are arranged in a random way similar to the disorder of the particles in a liquid. Glasses are the typical examples for amorphous materials. Whereas in crystalline materials, the atoms are arranged in a regular pattern, and there is a smallest volume element that by repetition in three dimensions describes the crystal. This smallest volume element is known as the unit cell.

Figure 2.1 represents the interaction of the incident beam with atoms positioned in the two different planes. When a monochromatic X-ray beam is projected onto a crystalline material at certain angle  $\theta$ , diffraction occurs only when the distance travelled by the rays reflected from consecutive planes vary by a number ' $n$ ' of wavelengths. The incident X-radiation hits the planes at a certain angle ' $\theta$ '. The spacing between these planes is ' $d$ '. The relationship between the wavelength ' $\lambda$ ' of the X-ray beam, the angle of diffraction ' $\theta$ ' and the distance between each set of planes separated with spacing ' $d$ ' is termed as Bragg equation. [6]

$$n\lambda = 2d \sin\theta \quad (2.1)$$

where, ' $n$ ' is the order of the diffraction. Thus, measuring the diffraction pattern enables to deduce the distribution of atoms in a material and each crystalline solid has its unique characteristics X-ray diffraction pattern which is presumably used as the fingerprint for their identification. Moreover, the crystallite size of the particles can be measured by the

estimation of the full width at half maxima of the peaks in the diffraction pattern and the equation is known as Scherer equation. [6]

$$t = 0.9\lambda/\beta\cos\theta \quad (2.2)$$

where  $\lambda$  is the wavelength of X-ray,  $\beta$  is the full width half maximum of the pattern and ' $\theta$ ' is the Bragg angle.

In the present study, the X-ray diffraction (XRD) patterns of the samples were recorded using the PANalytical X'pert Pro instrument. In all the cases, the data was collected with the scan rate of 0.5°/min. using Cu K $\alpha$  (1.5418 Å) radiation.

#### 2.2.4. X-ray Photoelectron Spectroscopy (XPS)

XPS is the surface technique which is commonly employed to characterize the nanomaterials to acquire their elemental status, distribution of elements or of chemical functional groups for a particular element across the composite and chemical coordination of the substances with other species *etc.* [7] The working principle of X-ray photoelectron spectroscopy (XPS) is originated based on the photoelectric effect proposed by veteran scientist Einstein.[8] Indeed, the XPS was developed in the mid of 1960's by the Sweden scientist Kai Siegbahn. In principle, each atom in the surface has its own core electron with the characteristic binding energy which is equal to the ionization energy of that electron. When an X-ray beam impedes to the surface of the sample, the energy of the X-ray photon is tends to adsorbed by the core electron of an atom. If the photon energy, *i.e.*  $h\nu$ , is large enough, the core electron will then escape from the atom and will release out of the surface. The emitted electron with the definite kinetic energy of  $E_k$  is known as the photoelectron. The binding energy of the core electron is given by the Einstein relationship:

$$h\nu = E_b + E_k + \Phi \quad (2.3)$$

$$E_b = h\nu - E_k - \Phi \quad (2.4)$$

where,  $h\nu$  is the X-ray photon energy,  $E_b$  is the binding energy of the photoelectrons,  $E_k$  is the kinetic energy of photoelectron and  $\Phi$  is the work function induced. Since the work function,  $\Phi$ , can be compensated artificially, it is eliminated, giving the binding energy as follows:

$$E_b = h\nu - E_k \quad (2.5)$$

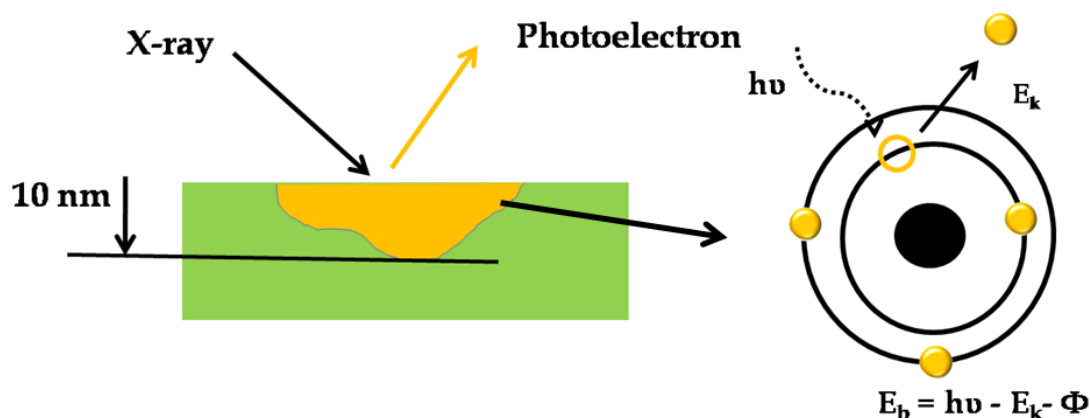


**Figure 2.2.** A pictorial representation of the working principle of XPS.

The surface sensitivity is the gorgeous feature of XPS. In fact, when the beam of X-ray impedes on the substance, the electrons on the surface are getting inelastically scattered and this leads to the ejection of electron with definite kinetic energy known as photo ejection. The electron ejection depth is depend upon the distance through a material that the photoelectron can travel and have possibility  $1/e$  of not having experienced an inelastic scattering event. The photo ejection is directly related to the kinetic energy of the ejected electron from the outer shell. Thus, electrons with high

kinetic energy (low binding energy) arise from deeper in the analyzed sample than electrons with low kinetic energy (high binding energy). Therefore, high binding energy photo peaks reflect the extreme outer surface area, compared to low binding energy photo peaks.

In the present work, A VG Microtech Multilab ESCA 3000 spectrometer equipped with an Mg K $\alpha$  X-ray source ( $h\nu = 1253.6$  eV) was used for the XPS measurements. In all the cases, the binding energy of the carbon material (C 1s peak) was fixed to 284.5 eV and the remaining peaks corresponding to other elements are calibrated with respect to this reference C 1s peak.

### **2.2.5. Raman Spectroscopy**

Raman Spectroscopy is another important technique to deduce structure, crystallinity and the purity of the carbonaceous material. The Raman spectrum was discovered by the Indian scientist C.V. Raman in 1928 based on the inelastic scattering of light known as the Raman Effect. [9] The technique is commonly employed to characterize the non-metallic materials. In principle, when the monochromatic light strikes on the molecule, two types of scattering can occur known as Rayleigh scattering and Raman scattering. In the first one, there is no energy transfer between the molecule and the incident photon known as Rayleigh scattering. On the other hand, in Raman scattering, there is energy transfer from the incident photon and molecule, leading to a variation in the energy of the scattered photon from the incident photon. This phenomenon is called the Raman Effect which offers vibration, rotation and other information about the material and, thus, helps to analyze the crystallinity, orientation of the atoms, *etc* [10]. The energy of the

scattered photon is the sum of the energy of the incident photon and the energy of the excited molecules in the sample being analyzed.

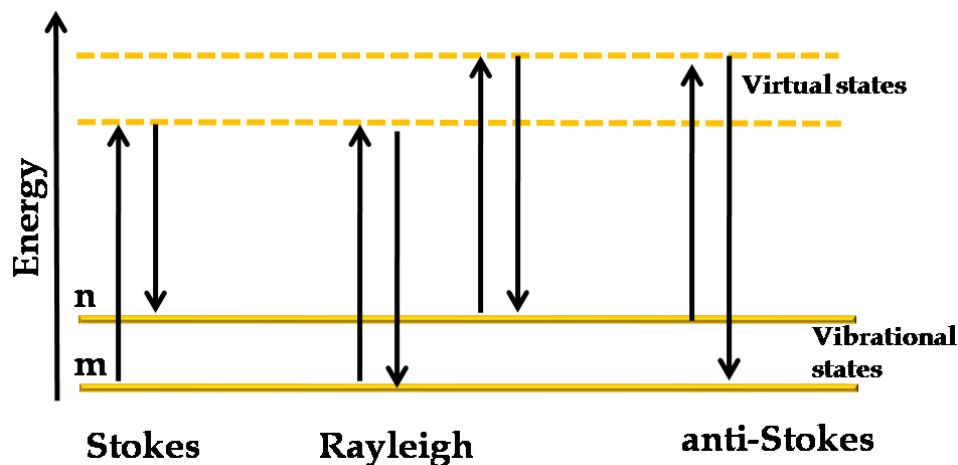


*Figure 2.3. A pictorial representation of the Rayleigh and Raman scattering processes in Raman analysis.*

Figure 2.3 is a pictorial representation of the scattering processes occurring during Raman analysis. In general, most of the molecule resides on the lowest vibrational level. When the laser light interacts with molecule, it causes polarization and induces excitement of vibrational levels. The induced energy levels of these states are depending upon the frequency of the light source used. In Rayleigh scattering, the molecule absorbs the energy from the light source and gets excited into the higher vibrational level and comes back to the original state. Unlike the Rayleigh process, in Raman scattering, the molecule in the ground state ( $m$ ) absorbs the energy and promotes to the higher vibrational level ( $n$ ) known as Stokes effect. However, some of the molecule may present in the ' $n$ ' level due to the thermal energy which depromotes to the ground state vibrational known as anti-Stokes effect. In Raman scattering the anti-Stokes effect are very weak due to the decreased population of the excited vibrational states. In fact, the

Raman effect depends upon the polarizability of the molecule which could be acquired for the molecule which does not have net dipole moment. This phenomenon provides information about the moment inertia and consequently the structure of the molecule.

In the present study, the Raman analysis was employed to determine the extent of defects on various N-doped carbonaceous materials using JASCO Confocal Raman Spectrometer with 532 nm green laser (NRS 1500 W).

### **2.2.6. Surface Area Measurements**

Surface area can be described as the external surface area of a solid object including the surface area attributed to the presence of pores. When a gas is made into contact with a solid substance, a part of it is taken up and attached to the surface; the phenomenon is known as adsorption. The solid on which adsorption occurs is called adsorbent and the substance which gets adsorbed being adsorbate. If the interaction between the adsorbent and adsorbate is weak *Van der Waals* interaction, the adsorption is known as physisorption. Whereas, if the attractive force is same as that of chemical bonds, the adsorption is known as chemisorption. In general, an adsorption isotherm is obtained by measuring the amount of gas adsorbed across a wide range of relative pressures at a constant temperature (typically liquid N<sub>2</sub>, 77 K). Conversely, desorption isotherms are achieved by measuring gas removed as pressure is reduced. The technique is known as Brunauer-Emmett and Teller (BET) gas adsorption technique which is generally used to measure the surface area and pore size distribution of solid samples. [11]

The BET equation is given as follows:

$$\frac{P}{V_a(P_o-P)} = \frac{1}{C V_m} + \frac{(C-1)P}{C V_m P_o} \quad (2.6)$$

where, 'P' is the adsorption equilibrium pressure, 'P<sub>o</sub>' is the saturation vapor pressure of the adsorbate, 'V<sub>a</sub>' is the volume of N<sub>2</sub> adsorbed at a pressure of P, V<sub>m</sub> is the volume of the adsorbate required for the monolayer coverage, 'C' is a constant that is related to the heat of adsorption and liquefaction that depends upon the adsorbate, adsorbent and temperature. The surface area of the sample can be calculated by plotting P/V<sub>a</sub>(P<sub>o</sub>-P) vs P/P<sub>o</sub>. Besides, gas adsorption measurements are habitually used for determining the pore size distribution of the porous materials. In fact, Kelvin equation is commonly employed to calculate the distribution of pore sizes which relates the pore width to the condensation pressure. The Kelvin equation is,

$$r_k = \frac{-2\gamma V_m}{RT \ln(P/P_o)} \quad (2.7)$$

where 'r<sub>k</sub>' is the Kelvin radius of the pore, 'γ' is the surface tension of N<sub>2</sub>, 'V<sub>m</sub>' is the molar volume of liquid N<sub>2</sub>, 'R' is the gas constant, 'T' is the boiling point of liquid N<sub>2</sub> and 'P/P<sub>o</sub>' is the relative pressure of N<sub>2</sub>.

In the present study, nitrogen and hydrogen adsorption-desorption experiments were conducted at 77 K using Quantachrome Quadrasorb automatic volumetric instrument. Ultra pure N<sub>2</sub> (99.9995%) was purified further by using calcium aluminosilicate adsorbents to remove trace amounts of water and other impurities before introduction into the system. A standard low-temperature liquid nitrogen Dewar vessel was used for the measurement at 77 K. Prior to the experiment, the sample was activated at room temperature (for 24 h) and at 150 °C (for 36 h) under ultrahigh vacuum (10<sup>-8</sup>

mbar) for overnight. About 40 mg of samples were loaded for gas adsorption, and the weight of each sample was recorded before and after out gassing to authenticate the complete removal of all guest molecules including the coordinated H<sub>2</sub>O in carbon based samples.

## **2.3. Electrochemical Study**

Several electrochemical techniques, particularly cyclic voltammetry and linear sweep voltammetry in rotating disc electrode method are used to investigate the ORR property of the non-Pt electrocatalysts. Further, the electrochemical properties, interfacial phenomena at the electrode surface and bulk properties of the materials on the electrode can be inferred from these techniques.

### **2.3.1 Cyclic Voltammetry (CV)**

CV is the most extensively used technique to investigate the electrochemical properties of the materials and to obtain the qualitative information about their electrochemical reactions. [12] The technique offers a rapid location of redox potentials of the electroactive species. The classical CV experiments in the olden times were done with two-electrode systems consisting of the working electrode (WE) and the reference electrode (RE). Recent analyses are mainly based on system consisting of three electrodes, namely the counter electrode (CE) along with the working and reference electrodes. In general, a potential is applied between the WE and RE, while the current is measured between the WE and CE. In CV, potential of the working electrode is changed linearly with time from non-Faradaic region to the Faradaic region where oxidation or reduction of the electrocatalyst occurs. After traversing the potential region (Faradaic

region), the direction of the linear sweep is reversed and reaches the standard potential ( $E^{\circ}$ ) in which the concentration of oxidised and reduced products of the electrochemical active species is equal on the electrode surface. In CV, the time scale of the experiment is controlled by the scan (sweep) rate. The resulting current vs potential plot is called cyclic voltammogram. [13]

In the present study, all the electrochemical studies were performed on an Autolab PGSTAT 30 (Echochemie) using a conventional three-electrode test cell received from Pine Instruments. Hg/HgO (in 1M KOH, procured from CHI instruments) and Pt wire were used as the reference and counter electrodes, respectively. A glassy carbon (GC) electrode (5 mm diameter) embedded in Teflon was used as the working electrode, which was polished on a polishing cloth using 0.3  $\mu\text{m}$  alumina slurry followed by washing with water and acetone.

### **2.3.2. Rotating Disc Electrode (RDE)**

In electrochemical reactions, the transport of ions towards or from the electrode proceeds via diffusion and convection while diffusion is the dominant process. However, there is some negligible contribution of effect of convection due to the impact of the environmental vibration and uneven temperature distribution in the electrolyte. Conversely, the rate of diffusion of ions can be increased significantly by introducing the mode of convection by increasing the relative motion of the electrode with respect to the electrolyte. The technique is called as rotating disc electrode (RDE) method. [13] When the electrode rotates, the reactant ions are dragged towards the electrode surface and the resulting products revolve away from the electrode. In fact, both diffusion and convection determine the net mass transport of the ions towards the electrode-electrolyte interface. In

RDE, the steady-state diffusion controlled process can be explained by Koutecky-Levich equation given as follows: [14]

$$1/j = 1/j_k + 1/j_d \quad (2.8)$$

where, ' $j$ ' is the measured current density, ' $j_k$ ' is the kinetic current density and ' $j_d$ ' is the diffusion limited current density. ' $1/j$ ' can be expanded as follows:

$$1/j = 1/nFkC_{O_2} + 1/0.62nFAD_{O_2}^{2/3}C_{O_2}^*v^{-1/6}\omega^{1/2} \quad (2.9)$$

$$1/j = 1/nFkC_{O_2} + 1/B\omega^{1/2} \quad (2.10)$$

$$B = 0.62nFAD_{O_2}^{2/3}C_{O_2}^*v^{-1/6} \quad (2.11)$$

where, ' $A$ ' is the area of the electrode, ' $n$ ' is the number of transferred electrons per oxygen molecule, ' $F$ ' is the Faraday constant ( $96500 \text{ C mol}^{-1}$ ), ' $D_{O_2}$ ' is the diffusion coefficient of the electrolyte, ' $C_{O_2}^*$ ' is the concentration of the dissolved oxygen in the electrolyte, ' $v$ ' is the kinematic viscosity of the electrolyte and ' $\omega$ ' is the angular velocity of the electrode. The K-L slope ( $1/B$ ) has been obtained from the plot of the inverse of the current density ( $1/j$ ) against the inverse of the square root of the angular velocity ( $1/\omega^{1/2}$ ). Subsequently, from the resulted value of  $1/B$ , the number of transferred electrons ' $n$ ' can be calculated using the equation (2.11). Further, from the kinetic current and the rate constant ' $k$ ' can be evaluated using the other parameters such as ' $n$ ' ' $v$ ' and  $C_{O_2}^*$ .

### 2.3.3. Rotating Ring Disc Electrode Method (RRDE)

As similar to the RDE, RRDE is acquired when the coaxial ring is added outside the disk electrode. In general, the ring is made up of either Pt or Au. In principle, the active species formed on the disk electrode-electrolyte interface is go from the electrode surface will be recognized on ring electrode. [15] Normally, the potential of the ring electrode is fixed at high enough for the facile reaction of the resulting product from the disc electrode. Typically, the generation the product on the disk electrode and their extent can be recognized from the potential of the ring electrode  $E_R$  and the ring current  $i_R$ . The geometry of the disk and ring electrodes control the ring current in relation with the disk current and their ratio is known as collection efficiency. [15]

$$N = i_R / i_D \quad (2.12)$$

where  $N$  is the collection efficiency,  $i_R$  is the ring current and  $i_D$  is the disk current. The  $N$  value can be determined experimentally using electro active species such as  $\text{Fe}(\text{CN})_6^{3-}$ .

In the present study, the prepared non-Pt electrocatalyst reduces the oxygen molecule through 4-electron ( $4 e^-$ ) pathway with minimal amount of hydrogen peroxide ( $\text{H}_2\text{O}_2$ ). Hence, RRDE was employed to quantify the amount of  $\text{H}_2\text{O}_2$  produced during the oxygen reduction reaction by the nitrogen doped carbonaceous materials. The amount of  $\text{H}_2\text{O}_2$  can be calculated using the following equation: [16]

$$\text{H}_2\text{O}_2 (\%) = 200 \times \frac{i_R/N}{i_R/N + i_D} \quad (2.13)$$

where  $i_R$  is the ring current,  $i_D$  is the disk current and the  $N$  is the collection efficiency.

## 2.4. References

- [1] B. K. Balan, S. M. Unni and K. Sreekumar, *J. Phys. Chem. C*, 2009, **113**, 17572.
- [2] D. C. Marcano, D. V. Kosynkin, J. M. Berlin, A. Sinitskii, Z. Sun, A. Slesarev, L. B. Alemany, W. Lu and J. M. Tour, *ACS Nano*, 2010, **8**, 4806.
- [3] D. B. Williams, C. B. Carter, *The Transmission Electron Microscopy: A Text Book for Material Science*, Springer, 2<sup>nd</sup> ed. 2009.
- [4] D. B. Williams, C. B. Carter, *The Transmission Electron Microscopy: A Text Book for Material Science, Vol I-IV*, Plenum Press, New York, 1996.
- [5] G. Lawes, *Scanning Electron Microscopy and X-ray Microanalysis*, John Wiley and Sons Ltd., Chichester, 1987.
- [6] B. D. Cullity, S.R. Stock, *Elements of X-ray Diffraction*, Addison-Wesley Reading, MA, 1978.
- [7] J. F. Watts, J. Wolstennholme, *An Introduction to Surface Analysis by XPS and AES*, John Wolstennholme, 2003.
- [8] C.D. Wagner, W. M. Riggs, L. E. Davis, J. E. Moulder, *Handbook of X-ray Photoelectron spectroscopy*; Perkin-Elmer Corp. 1979
- [9] Amer, M. S. *Raman Spectroscopy, Fullerenes and Nanotechnology*. Royal Society of Chemistry: Cambridge, United Kingdom, 2010; 43.
- [10] M. L. Bhaumik, *Am. J. Phys.* **1967**, 35, 330.
- [11] S. Braunauer, P. H. Emmet, E. Teller, *J. Am. Chem. Soc.* 1938, **60**, 309.

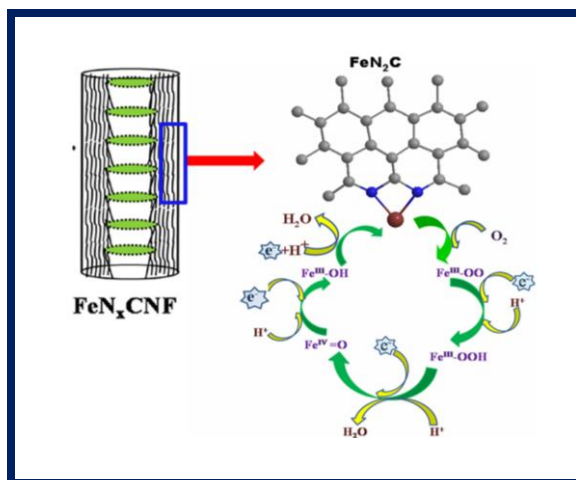
- [12] A. J. Bard, L. R. Faulkner, *Electrochemical Methods*, Wiley New York, 2001.  
(b) J. F. Rusling, S. L. Suib, *Adv. Mater.* 2004, **6**, 922.
- [13] T. Palaniselvam, H. B. Aiyappa, S. Kurungot, *J. Mater. Chem.* 2012, **22**, 23799.
- [14] V. Komanicky, A. Menzel, H. You, *J. Phy. Chem.* 2005, 109, 23550
- [15] W. J. Albery and M.L. Hitchman, *Ring-disk electrodes*, Clarendon press Oxford, 1971.
- [16] Z. S. Wu, S. Yang, Y. Sun, K. Parvez, X. Feng and K. Mullen, *J. Am. Chem. Soc.* 2012, 134, 9082.

## Chapter 3

### FACILE PREPARATION OF IRON NITRIDE-DOPED CARBON NANOFIBER AS A Pt-FREE ELECTROCATALYST AND FOR THE DEVELOPMENT OF LOW-Pt ELECTROCATALYST

---

We demonstrate a method for facile construction of iron nitride-doped carbon nanofiber (*i.e.* FeN<sub>x</sub>CNF) by effectively utilizing the existing slit pores and rough edges along the inner wall of the substrate as originated by virtue of its cup-stack structure for effectively increasing the number of active sites. The chapter also gives a discussion about the promising oxygen reduction activity of FeN<sub>x</sub>CNF. Further, we demonstrate how surface unsaturation



developed during small order buckling of graphene interlayer upon doping iron nitride (*i.e.* FeN<sub>x</sub>) moieties in CNF can be utilized as a very efficient mode of surface activation to establish fine distribution of Pt nanoparticles. The simultaneous enhancement of dispersion of Pt and oxygen reduction reaction (ORR) activity with a low weight percentage of dispersed Pt has been attained by FeN<sub>x</sub> doping, which increases the density of the active sites owing to the formation of fine and abundant delaminated regions on the CNF surface.

---

\*The contents of this chapter have been published in *Chem. Commun.* **2011**, 47, 2910 and *J. Phys. Chem. C*, **2012**, 116, 14754.

### 3.1. Introduction

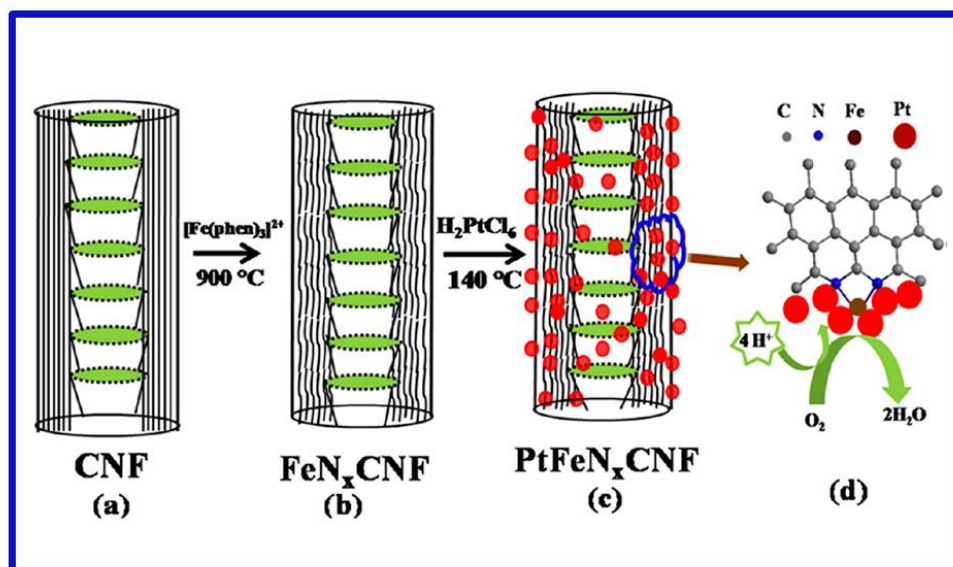
The sluggish kinetics of oxygen reduction reaction (ORR) and the scantiness with outlay of platinum (Pt) make the finding of an alternative inexpensive catalyst system indispensable to realize commercially available low temperature polymer electrolyte fuel cells (PEFCs). To tackle this challenge, significant efforts have been taken in either reducing the Pt by means of using core-shell systems [1] or complete removal of Pt from the catalyst layer. To remove Pt, many non-platinum catalyst systems have been proposed. [2-4] Among them, transition metal (Fe, Co) based chelates supported on carbons show better catalytic activity towards ORR than the other non-noble catalyst systems, particularly after treating at high temperatures in inert atmosphere.[5] Recently, nitrogen-doped carbon nanostructures are known to have encouraging catalytic activity towards ORR both as catalyst support and catalyst, although the activity was limited by the availability of nitrogen.[6-8] The increased catalytic activity is attributed to the presence of electron donating nitrogen atoms and higher exposure of edge planes. It is widely believed that the dopant nitrogen increases the basicity of CNT (pH~9) [9] by donation of its lone pair of electrons. This makes the carbon more electron rich and consequently increases the density of states towards the Fermi level [10] and, thereby, the ORR activity. Moreover, the doped-nitrogen acts as the adsorption site for the oxygen molecule (side-on adsorption) [11] which also resplay a pivotal role to increase the ORR activity. There are several on-going focused efforts on narrowing down the overpotential for oxygen reduction displayed by the N<sub>2</sub> doped materials. Noteworthy, development of M/N/C (M: Fe or Co) catalysts is an important strategy in this direction. [5] The nature of the metal-nitrogen-carbon (M/N/C) active sites and mechanism of ORR at these sites are

still unsure. Although the ORR activity of such non-precious systems has been mainly limited by the availability of nitrogen, improvement of the level of nitrogen is essential to meet the activity of state-of-the-art Pt catalysts.

On the other hand, finding a suitable carbon support which will aid in better dispersion of the active sites is a crucial task for the enhancement of the activity of the Pt electrocatalyst with minimum content. In this context, CNTs and carbon nanofibers (CNFs) are considered as wonderful support materials, especially after chemical functionalization.[12] However, the surface functionalization impairs the mechanical properties and consequently induces instability of the catalyst.[13] Significant drop in the electrical conductivity of the materials as a result of various chemical pre-treatment processes also has been reported.[14] Recently, the functionalization has been tackled by using soft foreign atom (Boron [15] and Nitrogen) doping without affecting the basic properties of CNTs. Along with this, Pt grafting on nitrogen functionalized CNT has been found to be a fascinating approach to accomplish the development of appropriate less expensive, still potentially active, electrocatalysts for ORR. The unique properties of N-doped CNTs are expected to augment the ORR activity of Pt by tailoring the morphological change of CNT. [16-22]

Therefore, the limitations faced by the nitrogen doped catalyst for the replacement of Pt triggered us to construct a composite based on iron nitride, the most active non-noble metal catalyst system, with CNF. The main advantage of CNF is the availability of highly exposed edge planes and slit pores originated by virtue of the cup-stack structure and slanting graphene planes which terminate on the wall surfaces. After realizing the presence of rich defect sites and slit pores along the inner wall of CNF, we successfully

utilized this morphological feature of  $\text{FeN}_x$  moiety, leading to significant increase in the number of active sites and consequently higher ORR activity. Further, we propose simultaneous enhancement of dispersion of Pt and activity for oxygen reduction with low weight percentage of Pt by combining the gorgeous properties of  $\text{FeN}_x\text{CNF}$  with Pt, devoid of any chemical pre-treatment in the process. As one advantage, this approach increases the density of the active sites owing to the formation of fine and abundant delaminated regions on the CNF surface. Along with this, the co-existence of the two categories of ORR sites also provides a unique opportunity to bring synergistic effect and thereby to attain significantly modified performance characteristics. Scheme 3.1 illustrates the innovative process strategy adopted to conceive these changes on the substrate matrix.



**Scheme 3.1.** Proposed pathway of synthesizing  $\text{FeN}_x\text{CNF}$  followed by  $\text{PtFeN}_x\text{CNF}$ . N-doped sites are formed along the slit pores and edge sites of the inner wall created due to the cup-stack structure of CNF.

## 3.2. Experimental Section

### 3.2.1. Synthesis of FeN<sub>x</sub>CNF Catalyst:

For all the catalysts in this work, we have used commercially obtained CNF as the support material. Iron acetate (Fe(OAc)<sub>2</sub>) (Rankem) and 1, 10 phenanthroline (phen) (Aldrich 99%) were used as the Fe and nitrogen precursors respectively. In a typical synthesis of iron nitride-doped CNF (FeN<sub>x</sub>CNF), appropriate amount of CNF was dispersed in 50 ml of ethanol (Rankem 99.9%) by ultrasonication. An excess of phen was dissolved in 25 ml of ethanol and was allowed to fill the inner pore of CNF by magnetic stirring for about 30 min. Further, the required amount of Fe(OAc)<sub>2</sub> in ethanol was added drop by drop to phen in CNF mixture. The weight percentage of Fe was maintained about 0.5 %. Fe(OAc)<sub>2</sub> reacted with phen to form Fe [(phen)<sub>3</sub>]<sup>2+</sup> chelate complex which was confirmed from the color change from pale yellow to wine red. Subsequently, the chelate complex solution was mechanically stirred for 24 h at room temperature to achieve better diffusion of iron chelate complex into the inner pore through the open ends of CNF. The resulting mixture was placed in a beaker in an oven and the solvent was evaporated at 50 °C for about 3 h. The resulting solid material was placed in a quartz tube and pyrolysed in Ar atmosphere at 900 °C. The temperature ramp was 10 °C per minute till it reaches 900 °C and maintained at that temperature for 3 h with an Ar flow of 0.5 sccm. While heating, when the temperature reaches around 350 °C, greenish vapors came out *via* the outlet which indicates the decomposition of phen in the reaction mixture. This was allowed to cool to room temperature after pyrolysis with Ar flow. The pyrolysed product was then washed with ethanol, filtered (filter paper 0.2 μm pore size, Rankem) to remove the chars of organic residues. The final product was dried at 100 °C for 2 h and preserved

for further study. We have prepared a series of catalysts with same experimental conditions in which the weight percentage of Fe was varied from 1, 2 and 5 which are represented as FeN<sub>x</sub>CNF1, FeN<sub>x</sub>CNF2 and FeN<sub>x</sub>CNF5 respectively along with the 0.5 wt. % FeN<sub>x</sub>CNF (FeN<sub>x</sub>CNF0.5). The nitrogen-doped CNF (N-CNF) was also prepared by the same experimental procedure without the addition of the Fe precursor. For comparison, we have also prepared a 10 wt. % PtCNF catalyst, where Pt was decorated selectively on the inner wall of CNF, by an in-house developed polyol process.

### 3.2.2. Preparation of PtFeN<sub>x</sub>CNF

In a typical synthesis, a modified polyol process was employed for the preparation of Pt on FeN<sub>x</sub>CNF (PtFeN<sub>x</sub>CNF) electrocatalyst. Hexachloroplatinic (IV) acid Hexahydrate (H<sub>2</sub>PtCl<sub>6</sub>. 6H<sub>2</sub>O) (Aldrich) was used as the Pt precursor and a mixture of ethylene glycol with water (3:2) was used as the solvent as well as the reducing agent. In order to facilitate the diffusion of Pt precursor into the inner wall of FeN<sub>x</sub>CNF, the surface tension of the solvent was carefully maintained by properly tuning the solvent composition. The amount of Pt was maintained as 10 wt. % with respect to FeN<sub>x</sub>CNF. For the preparation of 10 wt. % Pt loaded catalyst, the required amount of FeN<sub>x</sub>CNF was well dispersed in the solvent mixture with the aid of ultrasonication. Followed by this, the Pt precursor (H<sub>2</sub>PtCl<sub>6</sub>.6H<sub>2</sub>O), which was dissolved in the same solvent mixture, was added drop by drop and the mixture was kept for aging for about 12 h with mechanical stirring. Subsequently, the mixture was heated up to 140 °C for 8 h for the complete reduction of Pt ions. Finally, the mixture was allowed to cool and washed with deionized (DI) water followed by acetone to remove the unreacted solvent molecules and dried at 80 °C in an oven for 3 h. The final product was preserved for further studies. PtNCNF and PtCNF

were also prepared by the same experimental procedure but by using NCNF and CNF as the respective support materials.

### 3.3. Results and Discussion

#### 3.3.1. XRD Analysis

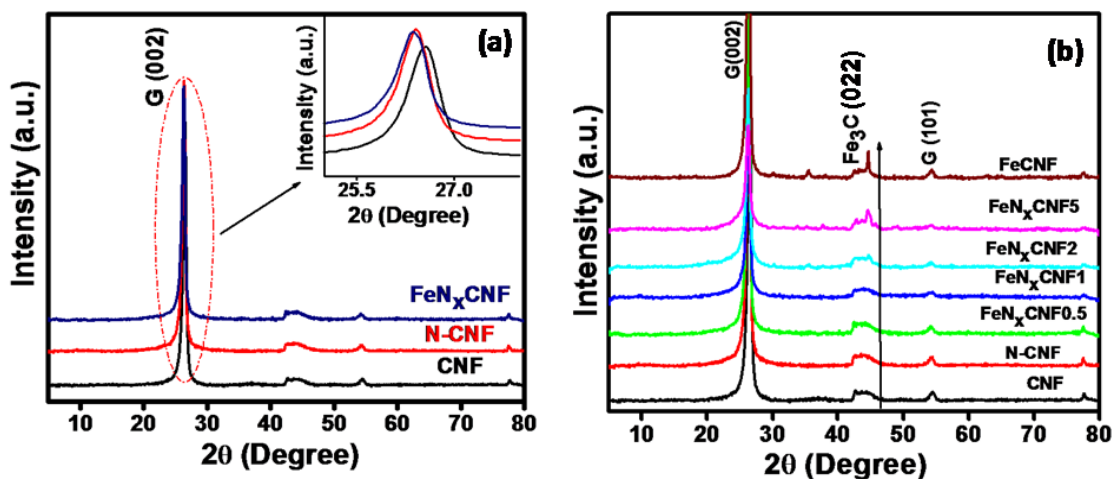


**Figure 3.1.** (a) XRD patterns of CNF, N-CNF and  $FeN_x$ CNF and (b) XRD patterns of various catalysts with different weight percentage of Fe.

The higher degree of crystallinity of the prepared materials was analyzed with aid of X-ray diffraction (XRD) pattern. In Figure 3.1a the XRD patterns of CNF, NCNF and  $FeN_x$ CNF show higher graphitic nature due to the presence of graphitic G(002) peak at  $2\theta \sim 26.5$  in the nitrogen doped composite catalysts. Interestingly, it could be observed that after nitrogen doping, the G (002) peak characteristic of graphitic carbon in CNF is shifted from  $26.5^\circ$  to  $26.3^\circ$  (inset of Figure 3.1a) with increased d-spacing (from 3.55 to 3.57 Å). This peak shift provides the glimpse of the intercalation of both nitrogen and nitrogen coordinated Fe into the ordered array of graphitic plates in CNF. [6] Moreover,

while comparing the XRD profiles of various catalyst compositions with different weight percentages of Fe, iron carbide ( $\text{Fe}_3\text{C}$ ), known to be inactive towards ORR, starts to appear with increasing the Fe content (Figure 3.1b) which could be attributed to the saturation of nitrogen atoms at 0.5 wt. % of Fe. [23] The arrow indicates the growth of iron carbide ( $\text{Fe}_3\text{C}$ ) with increased weight percentage of Fe in the catalyst. It seems only at percentages higher than that of  $\text{FeN}_x\text{CNF1}$  the iron carbide formation occurs as observed from the XRD patterns in Figure 3.1b.

### 3.3.2. Raman Spectra Analysis

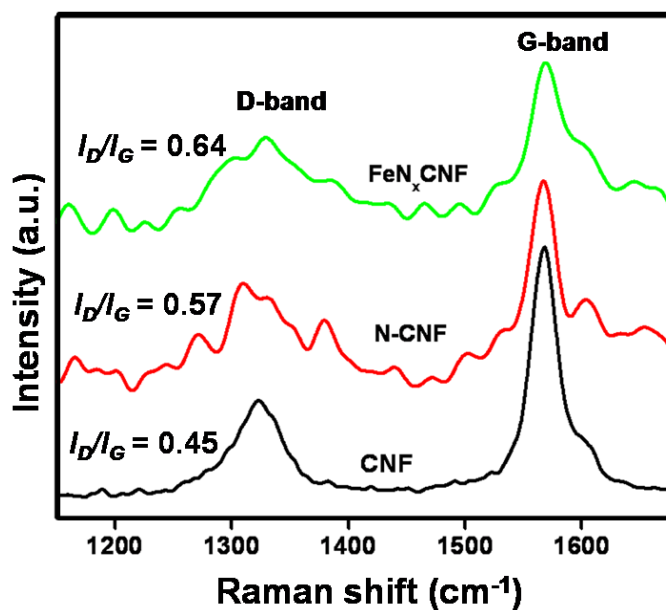


*Figure 3.2. Raman spectra of CNF, N-CNF and  $\text{FeN}_x\text{CNF}$ .*

Raman spectral analysis has been carried out in order to determine the structural changes or defects of the nitrogen-doped composite catalysts. [24] In Raman spectra, there are two distinct peaks observed for CNF as well as nitrogen-doped composite catalyst (Figure 3.2). The graphitic peak (G band) at 1565-1560  $\text{cm}^{-1}$  is due to  $E_{2g}$

vibrational mode of the C-C bond stretching and the disorder peak (D-band) at 1310-1330  $\text{cm}^{-1}$  is due to  $A_{1g}$  vibrational mode. The intensity ratio of the D-band and G-band, the  $I_D/I_G$  ratio, estimates the degree of disorder of the carbon matrix and the higher ratio values signifies the more defects present in the carbon matrix. The  $I_D/I_G$  ratios of  $\text{FeN}_x\text{CNF}$  and N-CNF have been calculated from the Raman spectra and found to have values as 0.644 and 0.574, respectively which is significantly higher than the  $I_D/I_G$  ratio of CNF (0.456). This ensures higher amount of defects present in the nitrogen-doped composite catalysts due to the effective nitrogen doping.

### 3.3.3. XPS analysis

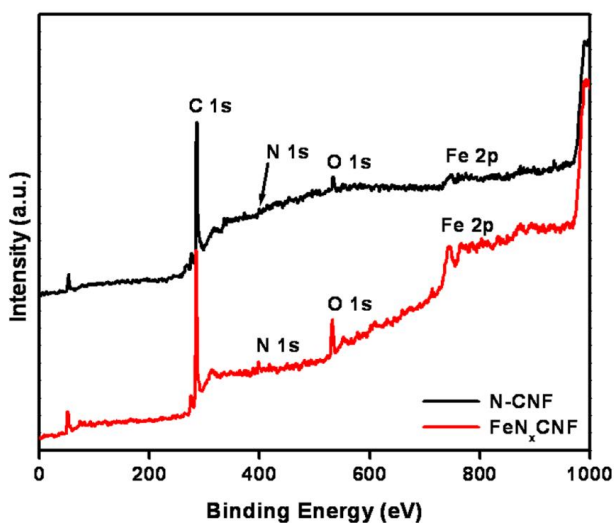


**Figure 3.3.** Full range XPS survey of N-CNF and  $\text{FeN}_x\text{CNF}$ .

The elemental surface compositions of N-CNF and  $\text{FeN}_x\text{CNF}$  were evaluated using XPS. The full range XPS survey spectra of N-CNF and  $\text{FeN}_x\text{CNF}$  are shown in Figure 3.3, where the presence of carbon, oxygen ( $\text{O}_2$ ), nitrogen ( $\text{N}_2$ ) and Fe can be clearly seen in the wide spectra. The main peak at 284.3 eV is responsible for the  $\text{sp}^2$ -

carbon which indicates that most of the carbons is in graphitic nature. The additional peaks at 398, 532 and 702 eV are corresponding to nitrogen, oxygen and Fe respectively. The peak for oxygen arises mainly due to the adsorbed oxygen at the surface of CNF. In case of N-CNF, there is a small peak for iron around 702 eV which may be due to metal impurity of CNF.

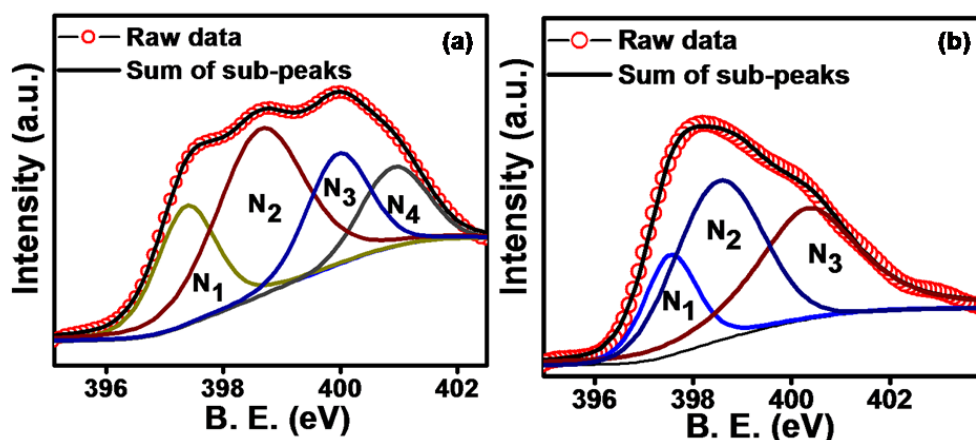


**Figure 3.4.** (a) *N 1s* spectra of N-CNF and (b) *N 1s* spectra of  $\text{FeN}_x\text{CNF}$ .

Further, in order to get more insight on the chemical environment of the doped nitrogen in the prepared catalysts, the *N1s* spectra have further deconvoluted into sub-peaks. Accordingly, Figure 3.4a shows the deconvoluted *N1s* spectra of N-CNF. Here the low binding energy peak at 397.3 eV ( $\text{N}_1$ ), which is lower than that of free nitrogen atom (398.5 eV), can be recognized as the doped nitrogen binding with Fe to form iron nitride (Fe-N). [25] The broad peak at 398.7 eV ( $\text{N}_2$ ) can be attributed to the pyridinic nitrogen in which nitrogen binds with two neighboring  $\text{sp}^2$  carbon atoms of the graphene sheet. [26] The peak at 400.0 eV ( $\text{N}_3$ ) can be ascribed to the pyrrole type nitrogen while the peak at 400.9 eV ( $\text{N}_4$ ) might arise due to graphitic nitrogen. [27] Similarly, the *N1s* spectra of  $\text{FeN}_x\text{CNF}$  (Figure 3.4b) has been deconvoluted into three peaks at 397.5,

398.6, 400.3 eV and are assigned as N<sub>1</sub>, N<sub>2</sub> and N<sub>3</sub> corresponding to Fe-N, pyridinic and pyrrole type nitrogen respectively. It could be observed that in both the cases the pyridinic nitrogen is predominant which is believed to be more active towards ORR. Further, the Fe 2p spectra of both FeN<sub>x</sub>CNF and N-CNF are deconvoluted into sub peaks. Since the impurity iron content is negligible in N-CNF, Fe 2p spectra could not be deconvoluted into sub peaks (shown in Figure 3.5a).

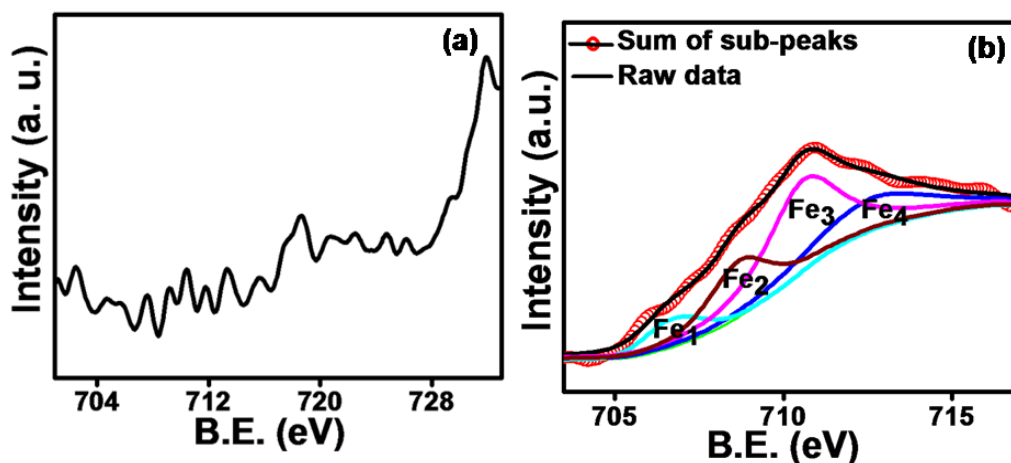


**Figure 3.5.** Comparison of a) Fe 2p spectra of N-CNF and b) FeN<sub>x</sub>CNF.

The Fe 2p spectra of FeN<sub>x</sub>CNF (Figure 3.5b) are deconvoluted into four peaks. The peak located at the low binding energy 706.8 eV is assigned as Fe<sub>1</sub> corresponding to metallic iron or iron carbide (Fe 2p<sub>3/2</sub>) indicating the presence of trace amount of iron carbide. The pair of peaks at 708.8 and 710.8 eV corresponds to the ionic state of iron (Fe 2p<sub>1/2</sub>) revealing that most of the iron is coordinated with the nitrogen atom. Interestingly, in the case of FeN<sub>x</sub>CNF (Figure 3.4b), there is no indication of quaternary nitrogen and the predominant species seems to be pyridinic nitrogen (38 %) as indicated by the higher intensity of the N<sub>2</sub> peak. This reveals the role of Fe in increasing the pyridinic nitrogen content that might help in achieving higher ORR activity.

### 3.3.4 EDAX Analysis

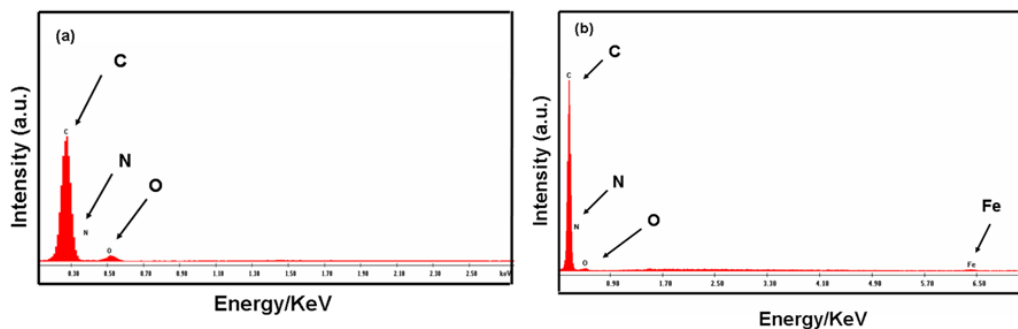


**Figure 3.6.** EDAX spectrum of (a) N-CNF and (b) FeN<sub>x</sub>CNF, showing 4.7at. wt. % of nitrogen doping in N-CNF and 3.9 at. wt. % of nitrogen doping in FeN<sub>x</sub>CNF.

The EDAX analysis of the samples was carried out to evaluate the amount of elemental doping on the resulting FeN<sub>x</sub>CNF and N-CNF based carbon materials (Figure 3.6). Accordingly, Table 3.1 summarizes the EDAX quantification of the elements present in the active catalysts FeN<sub>x</sub>CNF and N-CNF. In both the cases, the carbon is predominant which ensures the higher graphitic nature of CNF based materials. In the case of N-CNF, the content of nitrogen is 4.7 at. wt. % which is remarkably higher than that in FeN<sub>x</sub>CNF (3.93 at.wt.%). The EDAX spectrum also discloses the presence of Fe in trace amount (0.42 at. wt. %) in the active FeN<sub>x</sub>CNF catalyst as similar to the XPS analysis. Of course, oxygen molecule also present in the resulting nitrogen doped carbon material which is mainly due to the adsorbed oxygen from the atmosphere.

**Table 3.1.** EDAX quantification of N-CNF and FeN<sub>x</sub>CNF (in at. wt. %).

Catalyst	C	N	O	Fe
N-CNF	87.1	4.79	8.1	-
FeN <sub>x</sub> CNF	92.6	3.93	2.9	0.42

### 3.3.5. HRTEM Analysis

The structure and morphology of the nitrogen doped catalysts were analyzed with the help of HRTEM analysis. The Figure 3.7 shows the TEM images of CNF in different magnifications. The lower magnification image (Figure 3.7a) clearly shows the structure of pristine CNF with few micrometers in length. Unlike CNTs, the graphene layers in CNF are wrapped in a unique way and results into a cup stacked structure with open tips. Figure 3.7b demonstrates the cup stacked morphology of CNF which has an inner and outer diameter of *ca.* 50 and 100 nm respectively ended with open tips. The inner wall has the ending edges of the slanting graphene planes whereas the outer wall has a duplex structure involving deposition of parallel graphene layers covering the edges of the slanting graphene planes. Consequently, the inner wall has a rough surface whereas the outer wall has a smooth finish, which makes the inner wall inherently active and the outer wall highly inactive for any foreign species incorporation. Figure 3.7c represents the side wall of the pristine CNF where the graphene layers are arranged uniformly in a staggered manner with an average inter layer distance of 0.34 nm. These slanting planes with more edges are expected to provide distinctive circumstance for the higher nitrogen doping. It

is obvious that these CNFs have large central core and open tips which are highlighted by the blue circle (Figure 3.7d). Thus, the guest molecule can easily enter into the inner cavity of CNF through the open tips which facilitates CNF to act as the scavenger.

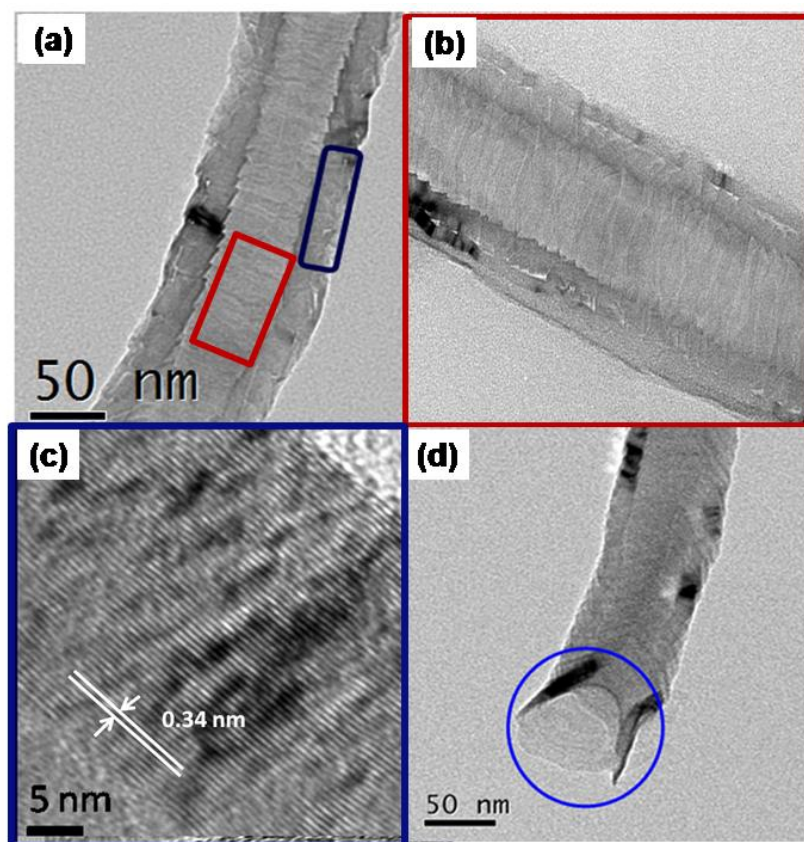


**Figure 3.7.** High-resolution TEM (HRTEM) images of (a) pristine CNF, (b) cup-stack structure of the inner side, (c) slanting arrangement of graphene layers on the side wall and (d) open tips highlighted with blue color circle.

Further, the morphology and structural characteristics of the nitrogen doped CNF composite catalysts were analyzed with the help of HRTEM. Accordingly, Figure 3.8 shows the HRTEM images of  $\text{FeN}_x\text{CNF}$  at higher Fe loading (5 wt. %) and the images confirm the presence of  $\text{Fe}_3\text{C}$  nanoparticles on the inner and outer walls of CNF which is

well in agreement with the XRD data. Figure 3.8 clearly reveals the fine distribution of 6-10 nm sized  $\text{Fe}_3\text{C}$  particles in the surface pores along the inner wall of CNF while at lower Fe loading,  $\text{Fe}_3\text{C}$  particles could not be observed. Similarly, iron nitride also could not be seen in the HRTEM images as it forms only at lower concentrations. Hence, the optimum content of Fe is once again confirmed which is 0.5 wt. % for the effective nitrogen doping and further studies are continued with catalyst with this loading of Fe.

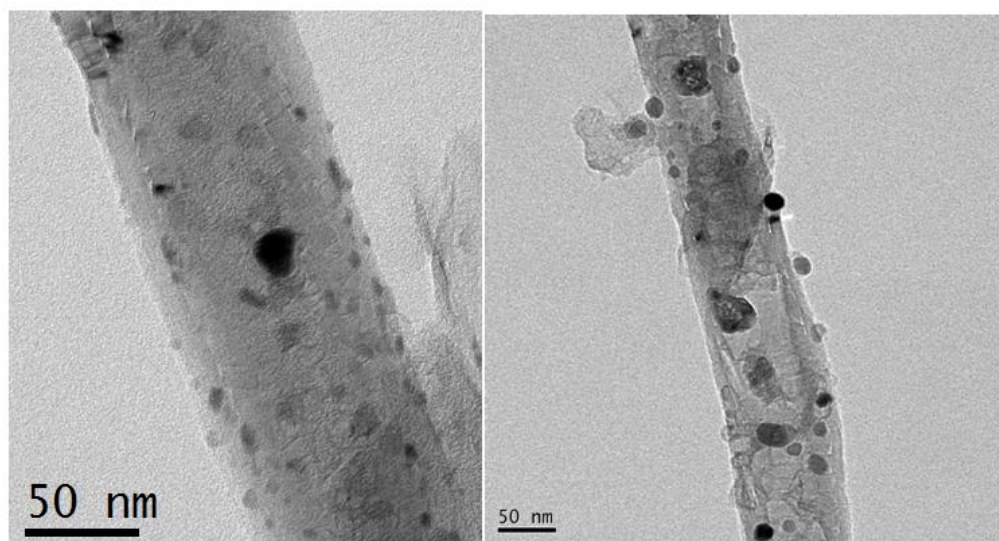


**Figure 3.8.**  $\text{FeN}_x\text{CNF}$  with 5 wt. % Fe loading showing formation of iron carbide ( $\text{Fe}_3\text{C}$ ) particles.

Figure 3.9 shows the HRTEM images of  $\text{FeN}_x\text{CNF}$  and N-CNF. Since the active pyridinic nitrogen normally resides on the edges of the CNF, HRTEM studies are mainly focused on the edges of CNF (Figure 3.9). In contrast to the pristine CNF, the features exhibited by  $\text{FeN}_x\text{CNF}$  (Figure 3.9b) and N-CNF (Figure 3.9c-d) are entirely different. Figure 3.9a represents iron nitride doped CNF which as such does not show any clear indication of structural changes due to the doping. However, a more focused image of the

sample, as shown in Figure 3.9b, clearly indicates turbo static nature of the graphene layers with more dislocations. The basal planes on the sidewalls of N-CNF (Figure 3.9c-d) also indicate a turbo static and buckled structure with distinct variation from the normal flat  $sp^2$ -hybridized plane of graphite. This is significantly different from the appearance of the surface of the un-doped CNF as displayed by the focused image in Figure 3.7c.

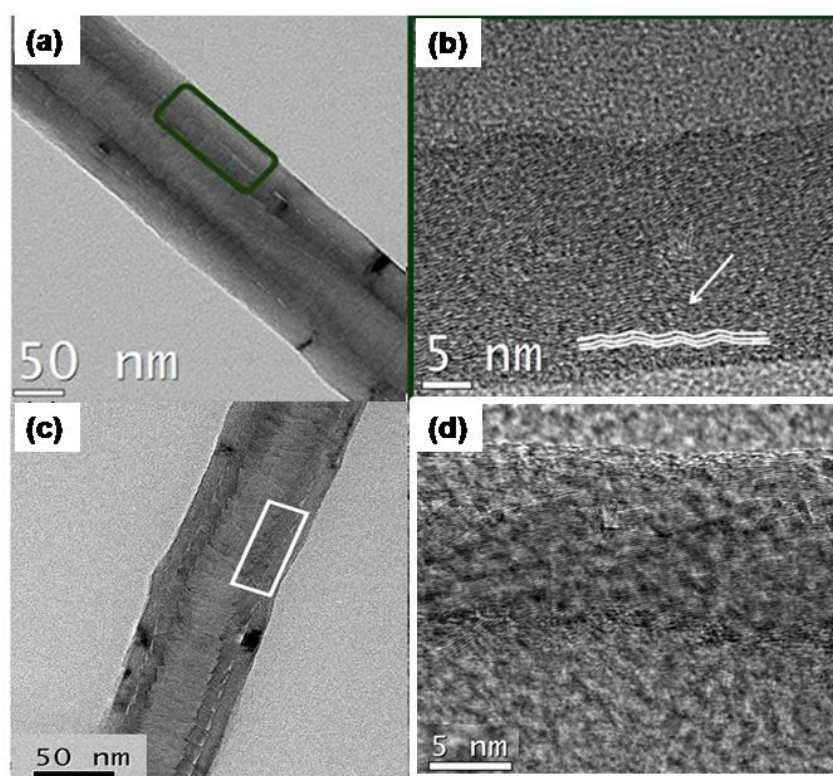


**Figure 3.9.** HRTEM images of (a)  $FeN_x$ CNF with 0.5 wt. % Fe loading, (b) buckled structure of the side wall of CNF after iron nitride doping in  $FeN_x$ CNF. (c) N-CNF and (d) buckled structure of the side wall of CNF after nitrogen doping (N-CNF).

The extent of enhancement in the  $d$ -spacing has been measured with the aid of XRD. The dislocations of the graphene layers is mainly attributed to the introduction of

pentagonal defects induced by the doped-nitrogen. [28-29] These pentagonal defects tend to cause the dislocations of uniform graphene layers which further provides the buckling of graphene layer on the side wall of CNF as evident from Figure 3.9b. It is reported that in the case of CNTs, buckling of the graphene layers can occur as a result of the penetration of the nitrogen containing precursor vapor such as ammonia into the interlayer spacing of graphene layers.[30] Compared to CNTs, the peculiar morphology of the cup-stack CNF with its open tips and slanting graphene planes with terminal edges along the inner wall can provide more facile routes to access the interlayer spacing for the vapors originated from the nitrogen precursor upon high temperature decomposition conditions. Penetration of the nitrogen moieties and subsequent heteroatom doping into the graphene framework make spacial alternations in the alignment of the graphene layers.

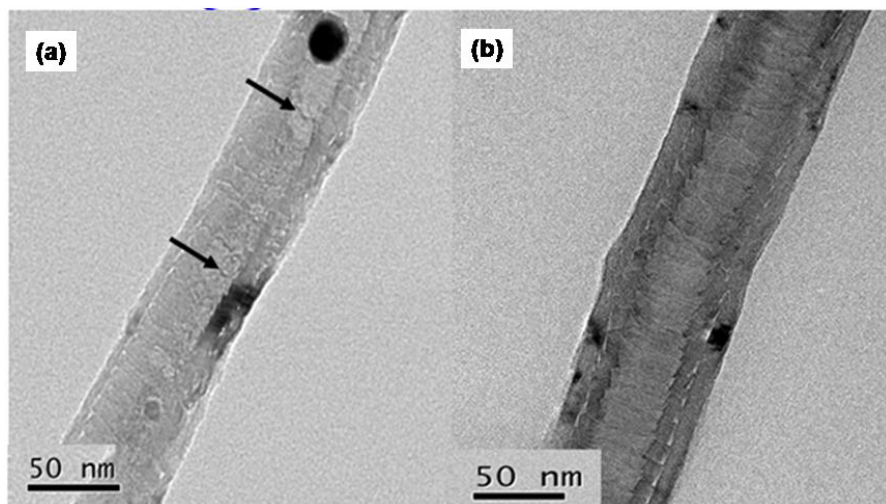


**Figure 3.10** (a) Pyrolysed  $FeN_x$ /CNF before washing and (b) after washing with ethanol.

In order to find out formation of the active site on the inner wall of CNF, HRTEM was taken after annealing prior to the ethanol washing. Interestingly, the presence of

organic residues (indicated by black arrows) can be seen clearly in the inner pore of pyrolysed product of  $\text{FeN}_x\text{CNF}$  (Figure 3.10a). After washing the catalyst with ethanol, these residues are completely removed from the catalyst (Figure 3.10b). It reveals the formation of active site predominantly in the inner pore of  $\text{FeN}_x\text{CNF}$ .

### 3.3.6. Surface Area Measurements

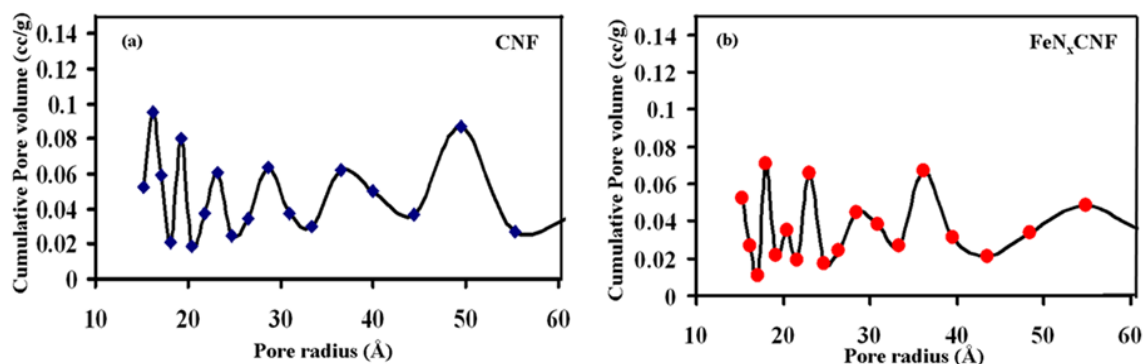


**Figure 3.11.** Pore size distribution plot of (a) CNF and (b)  $\text{FeN}_x\text{CNF}$ .

In addition, changes in the surface area and pore size distribution upon  $\text{FeN}_x$  doping provide an additional proof for selective doping along the inner wall (Figure 3.11). The surface area and pore size distribution of the nitrogen-doped composite catalysts and CNF are measured by BET nitrogen adsorption-desorption method. The surface area of  $\text{FeN}_x\text{CNF}$  ( $35.5 \text{ m}^2 \text{ g}^{-1}$ ) is smaller than the surface area of CNF ( $45.5 \text{ m}^2 \text{ g}^{-1}$ ), indicating occupancy of the active sites by the  $\text{FeN}_x$  moiety. The pore size distribution profile of bare CNF indicated distribution of pores possessing various size levels of few angstroms on the surface, possibly might have originated due to the stacking of slanting graphene layers with terminal edges. This stacking creates slit pores and edge sites mostly along the inner wall of the substrate. It is clearly visible from the figure that the peaks corresponding to each pore size distribution decrease when the  $\text{FeN}_x$  moiety

occupies the surface ( $\text{FeN}_x\text{CNF}$ ), which supplements the conclusion that the geometric feature of the surface played a major role in anchoring the active sites.

### 3.3.7. Electrochemical Studies

#### 3.3.7.1. Cyclic Voltammetric (CV) Analysis

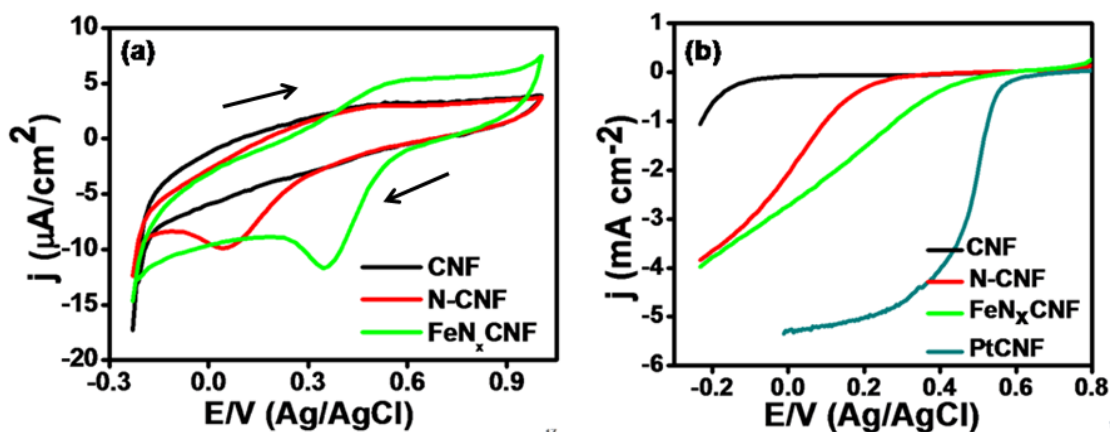


**Figure 3.12.** (a) CV for CNF, N-CNF and  $\text{FeN}_x\text{CNF}$  recorded in 0.5 M  $\text{HClO}_4$  at  $5 \text{ mV s}^{-1}$  scan rate, (b) steady state polarization plot for CNF, N-CNF,  $\text{FeN}_x\text{CNF}$  and PtCNF recorded in 0.5 M  $\text{HClO}_4$  at  $10 \text{ mV s}^{-1}$  scan rate (electrode rotating speed: 1600 rpm).

Since XRD and HRTEM gave strong indication of the formation of inactive carbides in catalysts with more than 0.5 wt. % of Fe, we have preceded further studies with  $\text{FeN}_x\text{CNF}$  having 0.5 wt. % of Fe and N-CNF only. Figure 3.12a depicts the cyclic voltammetry (CV) results of CNF, N-CNF, and  $\text{FeN}_x\text{CNF}$  electrodes in 0.5 M  $\text{HClO}_4$  solution, cycled between 1 and -0.23 V versus Ag/AgCl (saturated KCl) at a scan rate of  $5 \text{ mV s}^{-1}$ . All CV experiments were carried out without purging of oxygen at room temperature. The CV obtained for CNF alone does not show any redox property.

In contrast to CNF, the nitrogen containing composite catalysts, N-CNF and FeN<sub>x</sub>CNF are showing a well resolved cathodic peak corresponding to the reduction of O<sub>2</sub>. The ORR of N-CNF occurs at 0.04 V and the ORR of FeN<sub>x</sub>CNF occurs at 0.35 V which indicates that the active sites created on FeN<sub>x</sub>CNF exhibit higher activity for ORR in acidic environment. However, no reduction current is occurred at the same potential range for CNF. It is assumed that the ORR activity of the N-CNF and FeN<sub>x</sub>CNF observed is due to the nitrogen containing active sites which do not exist on CNF. This can be ascribed to the presence of N that is incorporated into the carbonaceous layer which leads to the lowering of band gap and increasing of the electron mobility. [31] This hypothesis was experimentally confirmed by McDermott *et al*, where the incorporation of nitrogen led to the increased disorder of the graphene layer significantly and enhances the electron transfer rate due to the modification of band gap structure. [32] This is further confirmed in our study where the HRTEM images of N-CNF and FeN<sub>x</sub>CNF reveal disordered graphene layer due to surface nitrogen functional groups which significantly enhances the electron transfer kinetics. It seems that the dopant nitrogen enhances the ability of graphene sheets of CNF to donate electron to O<sub>2</sub> for its reduction. In comparison with N-CNF, FeN<sub>x</sub>CNF exhibits enhanced peak current with higher rate of ORR at more positive potential. It appears that metal plays a significant role to enhance thermodynamic potential and kinetics of ORR.

### 3.3.7.2. Rotating Disc Electrode (RDE) Method

Further, to understand the kinetics of N-CNF and FeN<sub>x</sub>CNF towards ORR, we carried out Linear Sweep Voltammetric (LSV) measurements on rotating disc electrode (RDE) for CNF, N-CNF and FeN<sub>x</sub>CNF in 0.5 M HClO<sub>4</sub> (oxygen saturated) at 1600 rpm

(Figure. 3.12b). It is further evident that CNF has negligible or no activity towards ORR. The polarization curves of nitrogen containing composite catalyst does not exhibit plateau corresponding to limiting current which may be due to the distribution of catalytic sites in the three-dimensional interface structure.[33] The nitrogen containing composite catalysts have shown positive onset potential than CNF. This positive potential shift emphasizes that the nitrogen containing catalysts are more active for ORR which is in well agreement with the CV results. The polarization curve of N-CNF shows mixed kinetic-diffusion current between -0.2 to 0.15 V with the onset potential at around 0.24 V. However, in  $\text{FeN}_x\text{CNF}$ , this current is obtained at 0.1 to 0.35 V with an onset potential at around 0.54 V, revealing a reduction in overpotential by 300 mV. For an effective comparison, a 10 wt. % PtCNF prepared by polyol method was also investigated under the same experimental conditions. PtCNF shows an onset potential of 0.67 V for ORR at 1600 rpm which is about 0.13 V higher than that of  $\text{FeN}_x\text{CNF}$ . Thus, even though Pt still retains an advantage in terms of the onset potential,  $\text{FeN}_x\text{CNF}$  has shown significant activity towards ORR than many other non-noble catalyst systems reported in the literature.

The RDE results are analyzed by Koutecky-Levich (K-L) equation for a more quantitative estimation of electrocatalytic activity of N-CNF and  $\text{FeN}_x\text{CNF}$ . The K-L plots (Figure 3.13) further clearly demonstrate the presence of diffusion controlled process.

**K-L Equation**

$$j^{-1} = j_k^{-1} + j_d^{-1} \quad (3.1)$$

where 'j' is the measured current density,  $j_k$  is the kinetic current density for the ORR and ' $j_d$ ' is the diffusion limiting current density which can be expressed as follows:

$$j_d = B\omega^{1/2}$$

$$B = 0.62nFD_{O_2}^{2/3}C_{O_2}^* \nu^{-1/6} \quad (3.2)$$

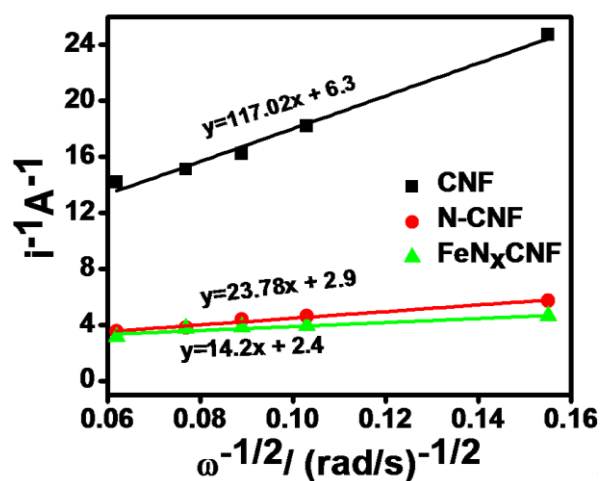


**Figure 3.13.** Kouteck –Levich (K-L) plots of CNF, N-CNF and FeN<sub>x</sub>CNF obtained from RDE measurements in O<sub>2</sub> saturated 0.5 M HClO<sub>4</sub> at a potential of -0.23 V. Sweep rate: 10 mV s<sup>-1</sup>.

where, 'B' is the Levich slope, 'n' is the number of transferred electrons per oxygen molecule, 'F' is the Faraday constant, 'D<sub>O<sub>2</sub></sub>' is the diffusion coefficient of the electrolyte, 'C<sub>O<sub>2</sub></sub><sup>\*</sup>' is the concentration of dissolved oxygen in the electrolyte, 'ν' is the kinematic viscosity of the electrolyte, 'ω' is the angular velocity of the electrode. The values for D<sub>O<sub>2</sub></sub>, C<sub>O<sub>2</sub></sub><sup>\*</sup> and 'ν' used in this study are 1.93 X 10<sup>-5</sup> cm<sup>2</sup> s<sup>-1</sup>, 1.22 X 10<sup>-6</sup> mol cm<sup>-3</sup> and 9.13 X 10<sup>-3</sup> cm<sup>2</sup> s<sup>-1</sup> respectively. K-L slop (1/B) has been obtained from the plot of 1/j<sub>k</sub> vs 1/ω<sup>1/2</sup>

as shown in Figure 3.13. Subsequently, from the resulted value of  $1/B$ , the number of transferred electrons ' $n$ ' could be calculated by using the equation (2). The calculated number of electrons (' $n$ ') transferred per  $O_2$  molecule for  $FeN_xCNF$  is 3.57, while for N-CNF is 2.37, indicating the favorable role of Fe in  $FeN_xCNF$  to facilitate the  $4e^-$  pathway. While the role of  $FeN_x$  in enhancing the activity is not clear, it presumably enhances the incorporation of nitrogen in the form of pyridinic nitrogen.

### 3.3.8 Conductivity Measurements

The nitrogen incorporation on the edges of the CNF may increase the basicity of CNF by donation of its lone pair electrons to build n-type semiconductor characteristics on CNF as the dopant increases the density of states near the Fermi level. This is further confirmed by electrical conductivity measurements where approximately one and two orders of increased conductivity are obtained for  $FeN_xCNF$  against that of N-CNF and CNF respectively. The electrical conductivity values of nitrogen doped composite catalysts and CNF have been calculated by measuring the resistivity of the catalysts using following equation.

$$K = 1/\rho \quad (3.3)$$

$$\rho = \rho_o / G_7 \text{ (W/S)} \quad (3.4)$$

$$\rho_o = (V/I) 2\pi S \quad (3.5)$$

where,  $K$  is conductivity;  $\rho$  is resistivity,  $\rho_o$  is specific resistance,  $W$  is the thickness of the pellet,  $S$  is the distance between the two probes,  $G_7$  is the correction factor,  $V$  is

voltage and  $I$  is current. The measured conductivity of CNF and nitrogen based composite catalysts is tabulated in Table 3.2.

**Table: 3.2.** Measured conductivity values of CNF and the nitrogen doped composite catalysts.

Catalyst	Conductivity (S cm <sup>-1</sup> )
CNF	0.55
N-CNF	4.34
FeN <sub>x</sub> CNF	29.42

### 3.3.9. Stability Test

More importantly, these nitrogen functionalities at the edges can act as adsorption sites for oxygen molecule and extensively increase the ORR activity. Though the nitrogen content of FeN<sub>x</sub>CNF is less than that of N-CNF, it shows higher activity than the later which indicates that the type of nitrogen (pyridinic) is more important rather than the level of nitrogen for the catalytic activity.[24] Moreover, since the stability of the cathode catalyst in fuel cell operating condition is an important issue in both Pt and non-Pt based catalysts, we have investigated the potential induced cycle life of the nitrogen containing composite catalyst by continuous cycling (25 cycles) between 1 to -0.23 V in 0.5 M HClO<sub>4</sub> at 5 mV s<sup>-1</sup> and also by Chronoampermetric (CA) experiments (Figure 3.14). CA measurements have been carried out to study the stability of the nitrogen-

doped composite catalysts by changing the initial potential from 0.7 V to a potential 0.16 V and 0.43 V for N-CNF and FeN<sub>x</sub>CNF respectively for 1000 s, where the system displayed maximum ORR activity.

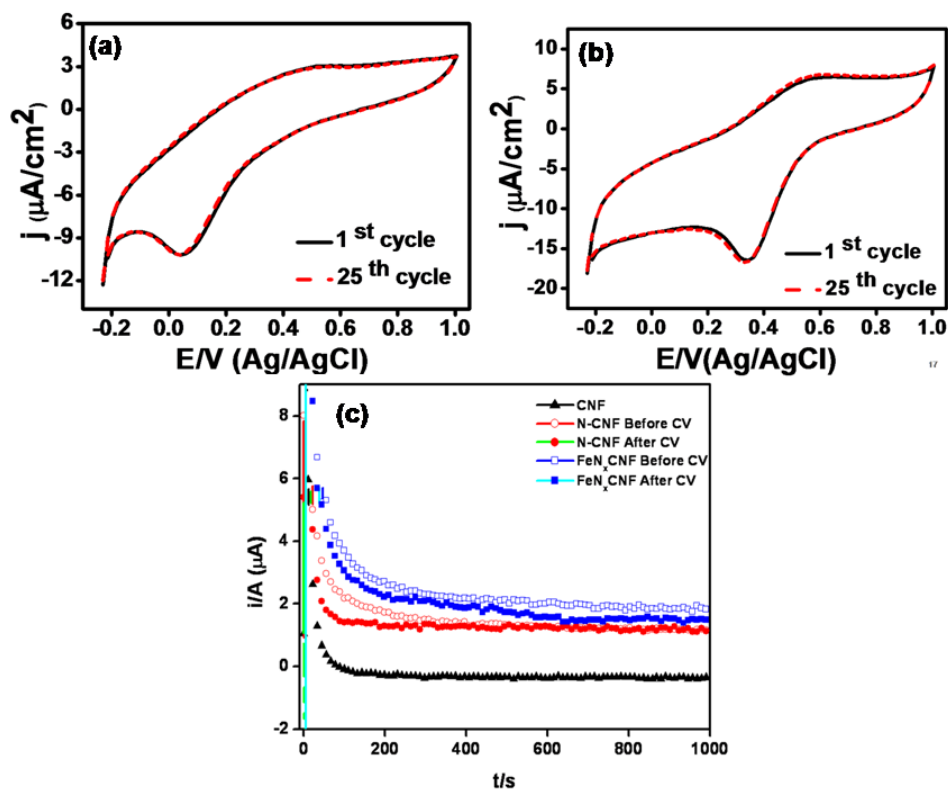


**Figure 3.14:** Electrochemical stability measurements of (a) N-CNF, (b) FeN<sub>x</sub>CNF by CV in 0.5 M HClO<sub>4</sub> at a scan rate of 5 mV/s and (c) chronoamperometry (CA) measurements of CNF, N-CNF (before and after durability measurements) and FeN<sub>x</sub>CNF (before and after durability measurements).

The experiment was performed both before and after lifetime studies by potential cycling. The peak potential and peak current in CV measurements for both N-CNF and FeN<sub>x</sub>CNF do not change even after 25 cycles (~5 h). Similarly, the CA studies also show

almost same current densities after prolonged cycling indicating no significant loss of catalytic activity in the acidic environment after continuous operation.

### 3.3.10. Mechanism

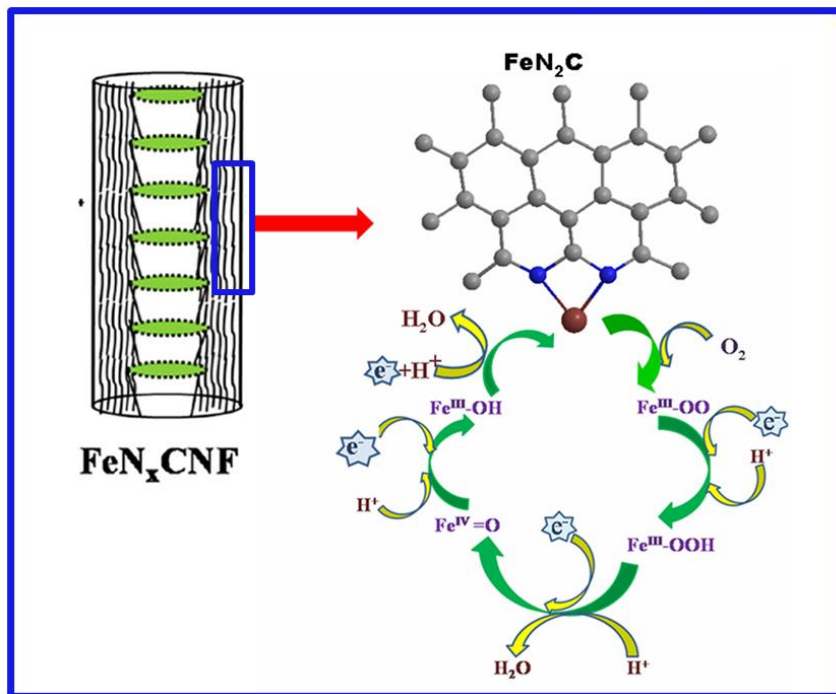


*Figure 3.15. The proposed mechanism for ORR on  $FeN_xCNF$ .*

A detailed mechanism of ORR on non-precious electrocatalysts is still unclear. Nevertheless, it can be proposed based on oxygen reduction on the heme protein [34] because the active site present in the heme protein (Fe bound with four-nitrogen atoms) is almost similar to the active site existing in the present work. The XPS measurements already indicated the formation of iron nitride and the observation of  $4e^-$  pathway by RDE further confirms that the formed catalytic site in this case is predominantly  $FeN_2C$ . Figure 3.15 shows the probable mechanism of ORR. In the first step,  $O_2$  molecule binds with  $Fe^{II}N_2C$  to form oxygenated  $Fe^{III}N_2C-OO$ . This species is protonated with one

electron to form the hydroperoxo compound ( $\text{Fe}^{\text{III}}\text{N}_2\text{C}-\text{OOH}$ ) in the second step. In the third step, second protonation associated with one electron reduction helps to form  $\text{Fe}^{\text{IV}}=\text{ON}_2\text{C}$  and  $\text{H}_2\text{O}$ . In the fourth step, again protonation associated with one electron reduction results in the formation of  $\text{Fe}^{\text{III}}\text{OHN}_2\text{C}$  which in turn in the final step combines with a proton and electron to form  $\text{H}_2\text{O}$  and the original catalytically active sites.

### 3.3.11. Development of Low-Pt Electrocatalyst

We realized that the nitrogen coordinated Fe (*i.e.*  $\text{FeN}_x$ ) doped in the graphene matrix of CNF reduces the oxygen molecule in the preferred  $4e^-$  pathway with the formation of water. The ORR activity of  $\text{FeN}_x\text{CNF}$  is mainly due to the unique properties of  $\text{FeN}_x$ , which further provides significant morphological changes of the layer-by-layer stacking of the graphene layers of CNF. The incorporation of nitrogen induces buckling of the basal planes due to pentagonal defects which results into the turbo-static nature of the graphene layers with increased interlayer distance on the side wall of CNF. High resolution transmission electron microscopy (HRTEM) analysis of  $\text{FeN}_x\text{CNF}$  provided clear evidences of such delamination, which virtually can be taken as a close distribution of ‘nanopockets’ along the surface. The ‘nanopockets’ originated in this way is expected to possess unsaturation along the surface carbons and consequently the process functions as a mode for *in situ* pre-treatment. This important benefit of attaining both ORR sites with a concomitant increase in the unsaturation along the carbon surface has given an opportunity to device a high performance ORR catalyst by adding a small amount of Pt (10 wt. %), which attains very fine particle distribution unlike that on a normal or a chemically pre-treated surface.

## 3.3.11.1 HRTEM Analysis

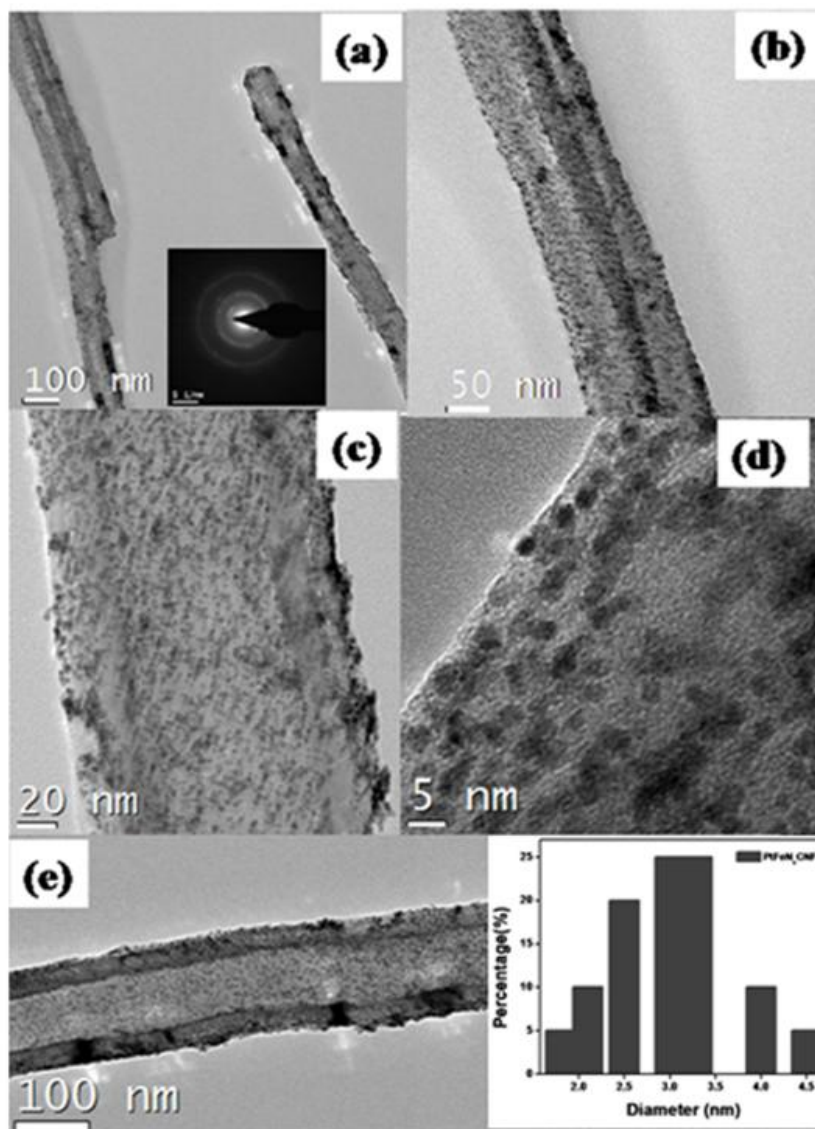


**Figure 3.16.** HRTEM images of the highly dispersed Pt on  $FeN_x$ CNF ( $PtFeN_x$ CNF). Fine distribution of Pt nanoparticles could be achieved both along the inner and outer walls of  $FeN_x$ CNF. Figures (a)-(e) are the images taken under different magnification levels whereas the insets of (a) and (e) are the diffraction pattern and distribution histogram respectively.

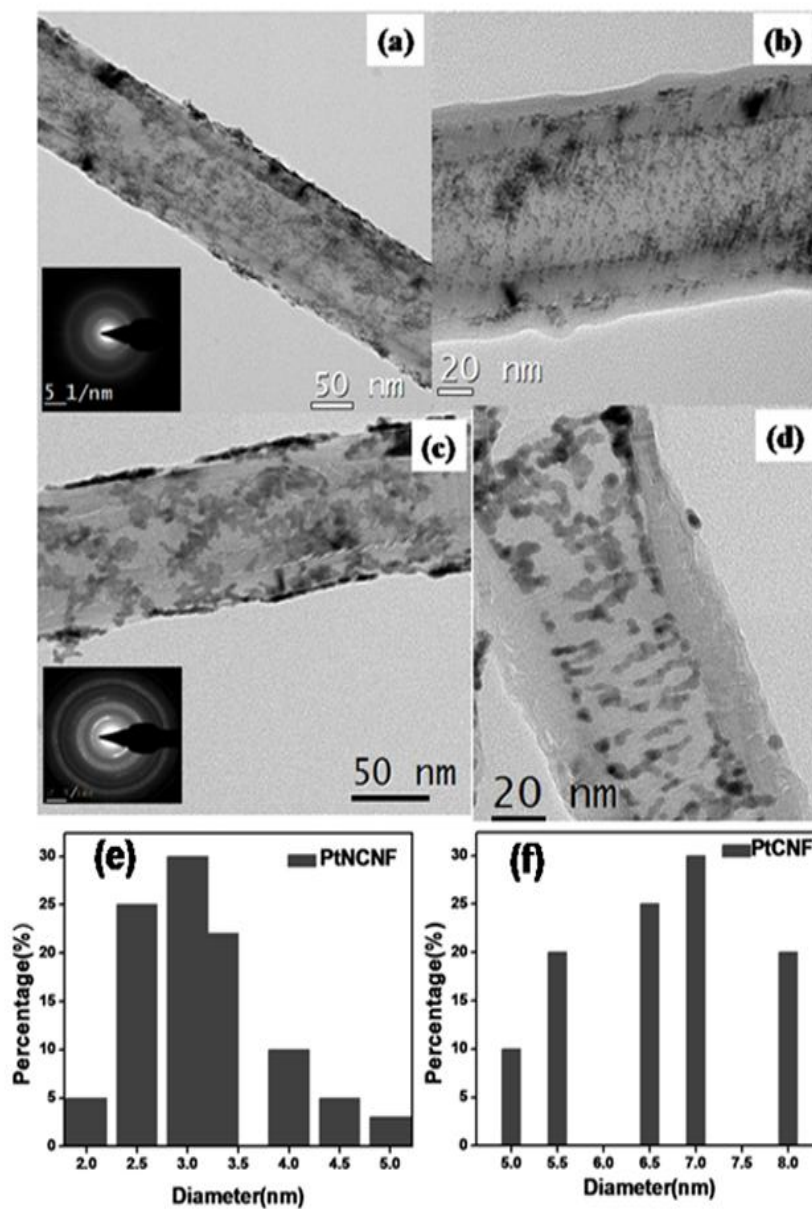


**Figure 3.17** (a) and (b) are the HRTEM images of the highly dispersed Pt on NCNF and (c) and (d) are the images of PtCNF. Plots (e) and (f) are the distribution histogram of PtNCNF and PtCNF.

The HRTEM analysis was carried out to find out the structure and morphology of the nitrogen doped CNF composite catalyst particularly after decoration of Pt

nanoparticles. Accordingly, Figure 3.16(a) to (e), reveal the distribution of Pt nanoparticles with an average particle size of 2-4 nm uniformly on both the inner and outer walls of FeN<sub>x</sub>CNF without any aggregation which otherwise would cause reduction in the activity of Pt.

For the effective comparison, the HRTEM images of the finely distributed Pt on NCNF and PtCNF are also presented in Figure 3.17. In PtNCNF (Figure 3.17a and b), all the particles are decorated predominantly on the inner wall of NCNF with an average particle size of 3-4 nm, while in PtCNF (Figure 3.17c and d) the particles are broadly distributed on CNF with aggregation (5-7 nm). We would like to mention that the broad distribution with aggregation of Pt nanoparticles is mainly due to lack of surface functional groups as the material was not subjected to any pre-treatment prior to Pt decoration to develop PtCNF. Therefore, from the observed results, it can be concluded that, Pt nanoparticles can be effectively dispersed on nitrogen based CNF than on the undoped CNF. In general, in order to obtain the uniform coverage of Pt nanoparticles on the surface of carbon nanofibers, chemical functionalization of the inert outer surface is required to afford the stable anchoring site for Pt on the surface. Due to the chemical interaction of these functional groups with Pt ions, Pt will get reduced on the surface, which further will act as the nucleation site for the growth of the nanoparticles. [12] In the present study, the incorporated FeN<sub>x</sub> active sites play several roles for the uniform distribution of Pt. Firstly, the homogeneously distributed FeN<sub>x</sub> active sites possibly enhance the wettability of CNF, thereby facilitating the formation of nucleating sites for the growth of Pt nanoparticles. Previously, we reported that Pt particles are preferably decorated on the inner pores of CNF due to the presence of

the defects on the slanting edges on CNF. [12] Since the  $\text{FeN}_x$  moiety also prefers to bind on the slanting edges of CNF, which further enhances the defects which was confirmed by Raman spectra, an increase of the nucleating sites for Pt growth is realized. Further to these, as mentioned earlier, the doping of  $\text{FeN}_x$  causes the distortion of normal flat  $\text{sp}^2$ -hybridized plane of graphite into turbo-static and buckled structure with increased inter layer distance between the two neighboring graphene sheets, which also enhances the Pt deposition. It is important to emphasize that, among the other types of nitrogen, pyridinic nitrogen plays an important role for the deposition of Pt on the edges of CNF. [35-36] Because these sites enhance the density of states towards the Fermi level, the  $\pi$  molecular orbital of carbon brings higher chemical affinity of Pt with the carbon surface. It has been reported that Fe will enhance the incorporation of stable pyridinic nitrogen in the CNF matrix and this could be the probable reason for the observed higher dispersion of Pt in the case of  $\text{PtFeN}_x\text{CNF}$  than on  $\text{PtNCNF}$ .

### 3.3.11.2. XPS Analysis

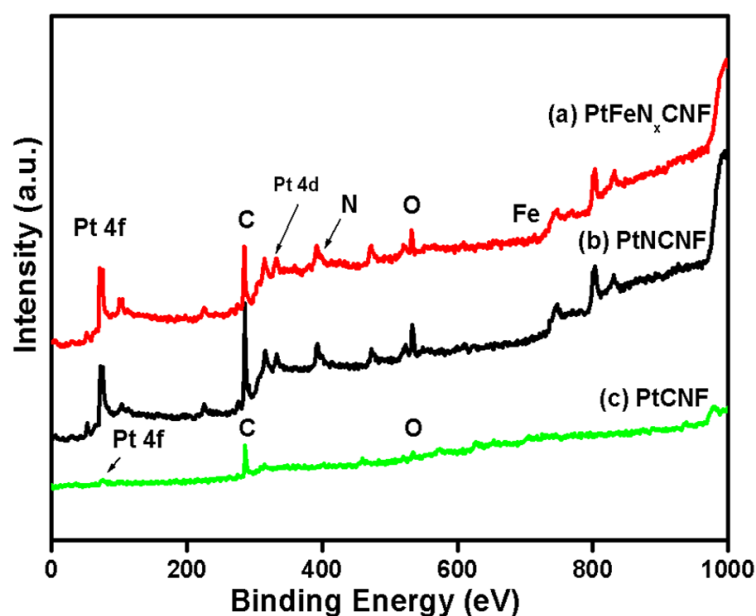


**Figure 3.18.** Full range XPS survey of (a)  $\text{PtFeN}_x\text{CNF}$  (b)  $\text{PtNCNF}$  and (c)  $\text{PtCNF}$ .

The issues delineated above have been successfully tackled with the aid of X-ray photoelectron spectroscopy (XPS). XPS reveals the possible atomic configuration of N, Fe and Pt present in the nitrogen based composite catalysts. The full range XPS survey spectra of PtFeN<sub>x</sub>CNF and PtNCNF as shown in Figure 3.18 clearly indicate the presence of carbon, oxygen (O<sub>2</sub>), nitrogen (N<sub>2</sub>), Fe and Pt. The main peak at 284.3 eV is due to sp<sup>2</sup>-carbon, which indicates the predominantly graphitic nature of the carbon framework. The additional peaks at 70, 398, 532 and 702 eV correspond to Pt, N<sub>2</sub>, O<sub>2</sub> and Fe respectively. The peak for O<sub>2</sub> arises mainly due to the adsorbed O<sub>2</sub> at the surface of CNF and due to the oxides of Pt. In the full range XPS survey spectra of PtCNF shown in Figure 3.18, the intensity of the peak appeared at 70 eV, which represents that Pt is much reduced as compared to the other nitrogen based Pt composite catalysts, emphasizing the less exposure of Pt in PtCNF.

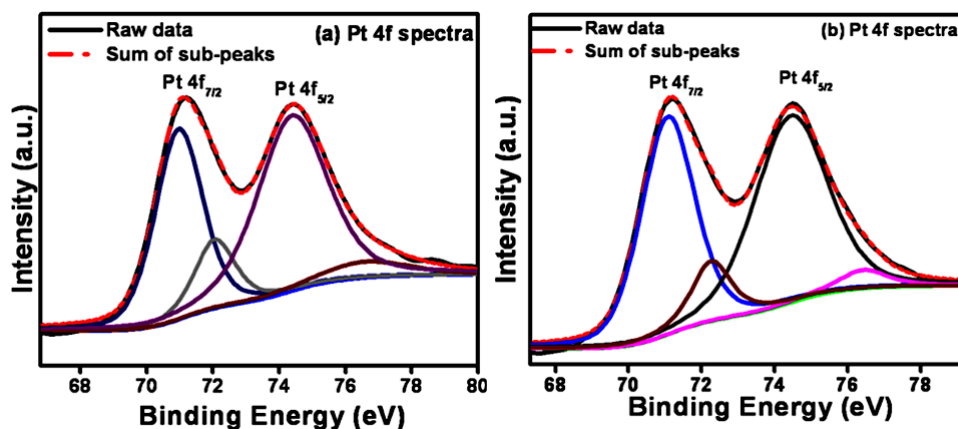


**Figure 3.19.** (a) Pt 4f spectra of PtNCNF and (b) PtFeN<sub>x</sub>CNF.

The Pt 4f spectra of PtFeN<sub>x</sub>CNF and PtNCNF as shown in Figure 3.19 are deconvoluted into two pairs of doublet. In both the cases, a pair of intensive peaks is observed at around 71.1 and 74.5 eV. These peaks correspond to the zero valent Pt which thereby ensure that the Pt nanoparticles are predominantly in the metallic state. This is

well in accordance with the SAED and XRD patterns. Also, a pair of small peaks at around 72.5 and 76.2 eV corresponding to  $\text{Pt}^{2+}$  (either Pt-O or Pt-(OH)<sub>2</sub>) could be observed.

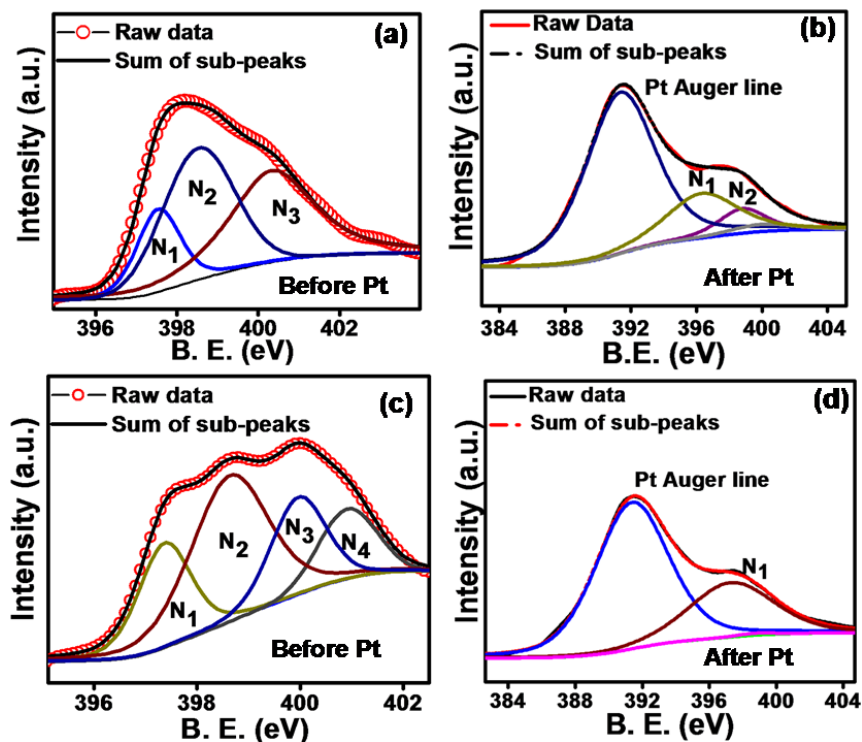


**Figure 3.20.** *N 1s spectra of (a)  $\text{FeN}_x\text{CNF}$ , (b)  $\text{PtFeN}_x\text{CNF}$ , (c)  $\text{NCNF}$  and (d)  $\text{PtNCNF}$ .*

The N 1s spectrum of  $\text{FeN}_x\text{CNF}$  (before deposition of Pt) shown in Figure 3.20a is deconvoluted into  $\text{N}_1$ ,  $\text{N}_2$  and  $\text{N}_3$  respectively corresponding to the binding energies of 397.3, 398.7 and 400.1 eV. These peaks correspond to the nitrogen bound with Fe (N-Fe), [25] pyridinic [26] and pyrrole type nitrogen [37] respectively. Interestingly, after the deposition of Pt on  $\text{FeN}_x\text{CNF}$  (Figure 3.20b),  $\text{N}_1$  peak intensity remains intact while the  $\text{N}_2$  and  $\text{N}_3$  peaks intensity decreases significantly. Similarly, N 1s spectrum of  $\text{NCNF}$  (before deposition of Pt) in Figure 3.20c, could be deconvoluted into four sub-peaks named as  $\text{N}_1$ ,  $\text{N}_2$ ,  $\text{N}_3$  and  $\text{N}_4$  corresponding to the nitrogen bound with iron (N-Fe),

pyridinic nitrogen, pyrrole type nitrogen and graphitic nitrogen respectively at 397.3, 398.7, 400.1 and 400.9 eV. After deposition of Pt on NCNF, the N1s spectrum (Figure 3.20d) could be deconvoluted only into two sub-peaks where the peak N<sub>1</sub> corresponding to N-Fe remains intact whereas the peaks N<sub>2</sub>, N<sub>3</sub> and N<sub>4</sub> are vanishing.

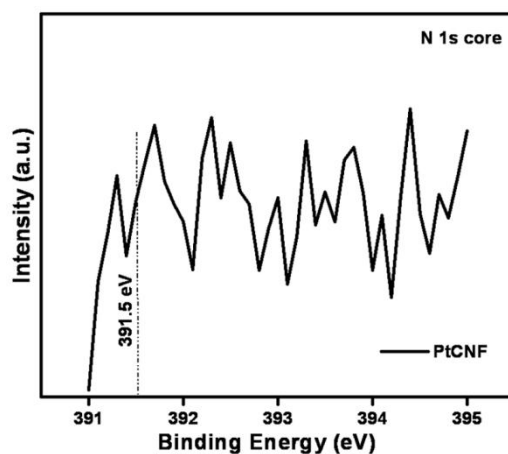


**Figure 3.21.** N 1s spectrum of PtCNF. The N 1s spectrum does not show a peak at 391.5 eV corresponding to Pt auger line on Pt nitride due to the absence of nitrogen in PtCNF.

This behavior in both PtNCNF and PtFeN<sub>x</sub>CNF is attributed to the growth of Pt nanoparticles on the doped nitrogen which results into blocking of nitrogen by Pt. [38-39] Most importantly, in both PtFeN<sub>x</sub>CNF and PtNCNF, we could observe an intense peak at around 391.5 eV. The peak probably corresponds to the Pt auger line on nitrogen, and absence of this particular peak in case of PtCNF strongly supports this conclusion [40] (Figure 3.21).

Similarly, in Fe 2p spectrum of PtFeN<sub>x</sub>CNF, the intensity of all the peaks decreases significantly (Figure 3.22). Accordingly, the Fe 2p spectra of FeN<sub>x</sub>CNF (before deposition of Pt) in Figure 3.22a are deconvoluted into four peaks. The peak at 706.8 eV which is assigned as Fe<sub>1</sub> is corresponding to the metallic iron or iron carbide (Fe 2p<sub>3/2</sub>)

indicating the presence of trace amount of iron carbide. The pair of peaks at 708.8 and 710.8 eV which are assigned as  $\text{Fe}_2$  and  $\text{Fe}_3$ , respectively are due to the ionic state of iron ( $\text{Fe } 2p_{1/2}$ ) revealing that most of the iron is coordinated with the nitrogen atom.

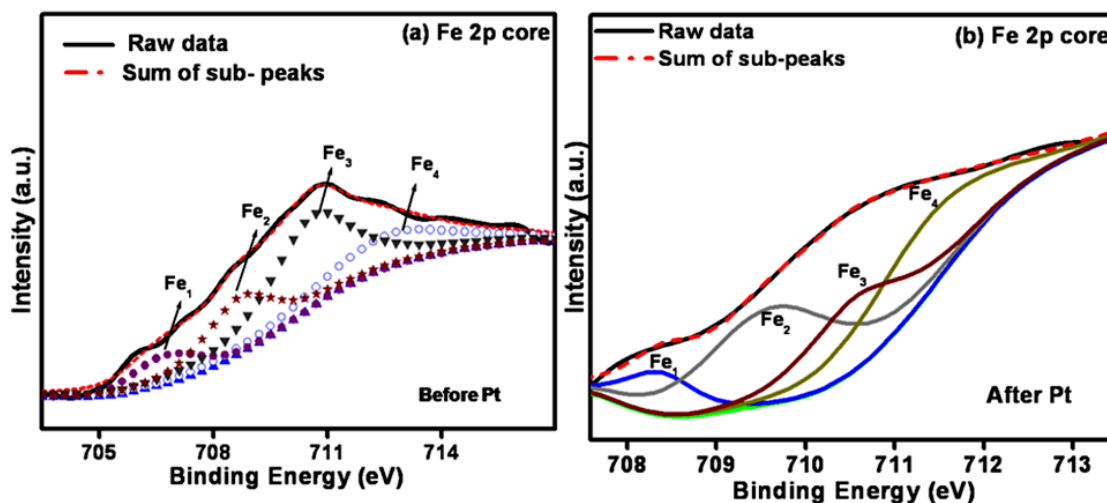


**Figure 3.22.** Fe 2p spectra (a) before Pt incorporation ( $\text{FeN}_x\text{CNF}$ ) and (b) after Pt incorporation ( $\text{PtFeN}_x\text{CNF}$ ).

After deposition of Pt, the intensity of all the peaks decreases significantly (Figure 3.22b) and thereby ensures the growth of Pt on the  $\text{FeN}_x$  moiety in  $\text{FeN}_x\text{CNF}$ . These facts reveal clearly that the Pt atoms grow preferentially on the  $\text{FeN}_x$  moiety by involving interactions between Pt and the dopant nitrogen as in the case of the bonding interaction in platinum nitride (Pt-N).[40]

### 3.3.11.3. XRD Analysis

The higher degree of crystallinity of Pt particles has been characterized with the aid of X-ray diffraction pattern (XRD). The obtained XRD patterns of  $\text{PtFeN}_x\text{CNF}$ ,  $\text{PtNCNF}$  and

PtCNF as presented in Figure 3.23 confirm the existence of Pt with the characteristic of the face-centered cubic (FCC) lattice structure. The diffraction peaks at  $2\theta$  values of 39.9, 46.3 and 67.6° are corresponding to the prominent Pt crystalline planes of (111), (200) and (220) of the FCC structure of Pt. In all the three cases, the first peak at the low  $2\theta$  value around 26.5° is associated with the graphitic planes of CNF support.

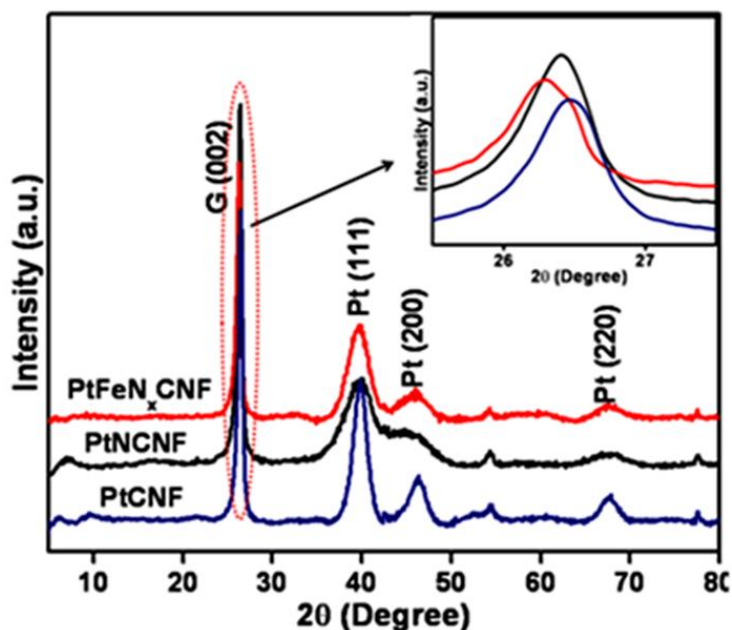


**Figure 3.23.** (a) XRD patterns of  $\text{PtFeN}_x\text{CNF}$ ,  $\text{PtNCNF}$  and  $\text{PtCNF}$ .

The average particle size of Pt of each catalyst calculated from the Pt (111) diffraction peak using Debye-Scherrer formula [41] resulted to be ~ 4.8, 2.6 and 3.5 nm for  $\text{PtCNF}$ ,  $\text{PtNCNF}$  and  $\text{PtFeN}_x\text{CNF}$  respectively. These results are in accordance with the HRTEM results. Thus, the notable reduction in the size of the Pt nanoparticles on the nitrogen doped substrates demonstrates the significance of the controlled interplay of the morphological alterations and efficient co-ordination sites in bringing high quality dispersion characteristics. In addition, a careful comparison of the G (002) peak of the

graphitic plane of CNF in PtFeN<sub>x</sub>CNF and PtNCNF (inset of Figure 3.23a) with the corresponding peak of PtCNF shows a slight shift towards the low theta value with increased d-spacing (from 3.55 to 3.57 Å). This further ensures that the doping of nitrogen and nitrogen coordinated Fe further enhances the defects in the ordered arrays of graphene matrix in CNF. [6]

#### 3.3.11.4. Raman Spectra Analysis

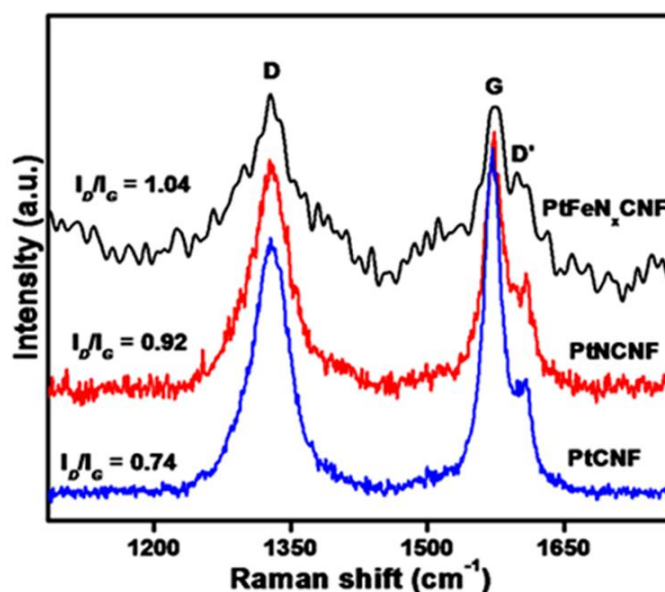


*Figure 3.24. Raman spectra of PtFeN<sub>x</sub>CNF, PtNCNF and PtCNF.*

The dislocations of CNF caused by the doping of nitrogen have exquisitely analyzed by Raman spectroscopy. The Raman spectra of the as synthesized PtFeN<sub>x</sub>CNF, PtNCNF and PtCNF are given in Figure 3.24. All the samples exhibit the D and G bands respectively at around 1330 and 1560 cm<sup>-1</sup>. The D band is attributed to the A<sub>1g</sub> vibrational mode and signifies the defects which present in the graphitic structure whereas the G band is attributed to the E<sub>2g</sub> vibrational mode of the C-C bond stretching and indicates the presence of crystalline graphitic structure. The D' band corresponds to the second-order

Raman scattering which is very sensitive to  $\pi$  electronic structure. The degree of disorder present on all the catalysts is estimated by means of the  $I_D/I_G$  ratio. N-CNF and  $\text{FeN}_x\text{CNF}$  show higher degree of defects with the  $I_D/I_G$  ratios of 0.57 and 0.64 respectively compared to the pristine CNF, which possesses an  $I_D/I_G$  ratio of 0.45. [42] After deposition of Pt, the  $I_D/I_G$  ratio has been further increased significantly as indicated by the calculated values as 1.04, 0.92 and 0.74 for  $\text{PtFeN}_x\text{CNF}$ ,  $\text{PtNCNF}$  and  $\text{PtCNF}$  respectively. This further ensures that Pt influences the enhancement of higher defects on the nitrogen-doped composite catalysts due to preferable deposition of Pt on the kinks and slanting edges of the nitrogen doped composite catalyst. This result is well in agreement with the conclusions derived from XRD, XPS and HRTEM analysis.

### 3.3.11.5. Electrochemical Studies

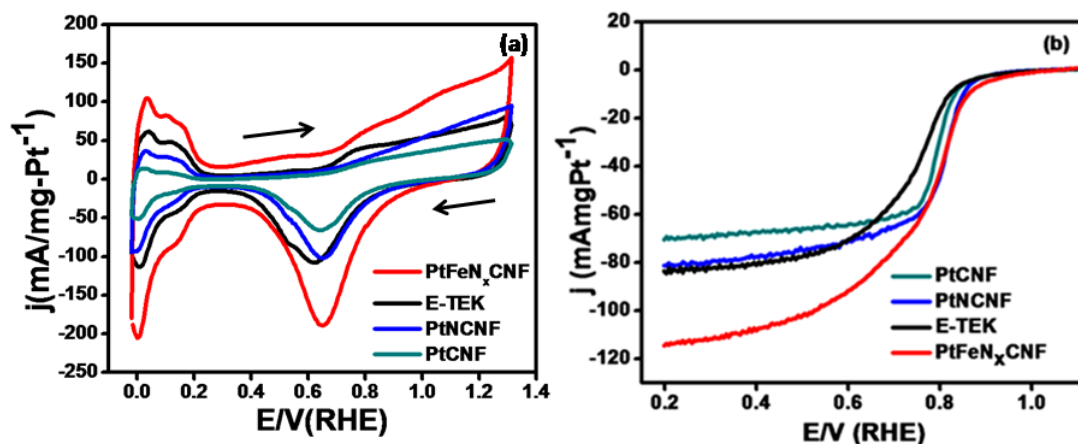


**Figure 3.25.** (a) Comparison of the electrocatalytic activity of  $\text{PtFeN}_x\text{CNF}$ ,  $\text{PtNCNF}$ , E-TEK and  $\text{PtCNF}$  by CV (b) LSVs of  $\text{PtFeN}_x\text{CNF}$ ,  $\text{PtNCNF}$ , E-TEK and  $\text{PtCNF}$  in 0.5 M  $\text{HClO}_4$ . Scan rate is  $10 \text{ mV s}^{-1}$ .

The preceding results demonstrate the uniform distribution and chemical interaction of Pt nanoparticles on nitrogen based CNF. In order to understand the influence of the co-existence and the expected synergistic effects of the N<sub>2</sub> and Pt based active sites, CV was performed in an aqueous solution of 0.5 M HClO<sub>4</sub> by cycling the potential between -0.23 to 1.1 V at room temperature. The voltammograms of PtFeN<sub>x</sub>CNF and PtNCNF are presented in Figure 3.25a, and the activity is benchmarked against both commercial 20 wt. % Pt/C (E-TEK) and 10 wt. % PtCNF. The Pt loading on the electrode surface of all electrochemical analysis was 10 μg. The CV curves show two discrete peaks associated with hydrogen adsorption/desorption between -0.23 < E < 0.02 V and ORR peak at 0.65 < E < 0.9 V. The activity is estimated by measuring the electrochemical surface area (ECSA) of all the catalysts by assuming the value of 210 μC cm<sup>-2</sup> for the desorption of hydrogen monolayer.[43] The corresponding ECSA values are 64.6, 39.1, 22.1 and 8.2 m<sup>2</sup>g-Pt<sup>-1</sup> respectively for PtFeN<sub>x</sub>CNF, E-TEK, PtNCNF and PtCNF. The ECSA value of E-TEK is comparable to the reported value. [44] The measured ESCA value for PtFeN<sub>x</sub>CNF is significantly higher than that of E-TEK. Moreover, PtFeN<sub>x</sub>CNF exhibits higher ESCA value than that of the previously reported PtCNF (23.3 m<sup>2</sup>g<sup>-1</sup>) with 40 wt. % Pt loading. [12] The highest ECSA value of PtFeN<sub>x</sub>CNF ensures a higher degree of dispersion of the much smaller particles of Pt. Although a higher dispersion is achieved in PtNCNF due to nitrogen, ECSA is significantly lower than that of PtFeN<sub>x</sub>CNF. A probable reason could be the limited accessibility of Pt on the inner wall of CNF as mentioned earlier while discussing the HR-TEM results. In contrast, the reduced ECSA exhibited by PtCNF is mainly attributed to the aggregation of Pt nanoparticles in CNF.

We next examined the kinetics of ORR of Pt based nitrogen-doped composite catalysts by LSV measurements on a RDE set-up in 0.5 M HClO<sub>4</sub> (oxygen saturated) at 1600 rpm (Figure 3.25b). The observed limiting current density of the catalysts follows the order of PtFeN<sub>x</sub>CNF (113.8 mA mg-Pt<sup>-1</sup>) > E-TEK (85.1 mA mg-Pt<sup>-1</sup>) PtNCNF (81.1. mA mg-Pt<sup>-1</sup>) > PtCNF (69.2 mA mg-Pt<sup>-1</sup>). In addition to the limiting current, the onset potential and half wave potentials are also indicative of the performance of an electrocatalyst. The half wave potentials of PtFeN<sub>x</sub>CNF, PtNCNF, E-TEK, and PtCNF are 0.81, 0.81, 0.79 and 0.76 V respectively. The ORR polarization curves of PtNCNF and PtCNF show mixed kinetic-diffusion current between 0.75 to 0.9 V with the onset potential at around 0.86 and 0.84 V, respectively whereas E-TEK shows the mixed kinetic diffusion current between 0.72 to 0.87 V with an onset potential of 0.83 V. PtFeN<sub>x</sub>CNF, on the other hand, displays the mixed kinetic-diffusion current between 0.77 to 0.93 V with an onset potential at around 0.88 V, revealing a reduction in overpotential of ~50 mV with respect E-TEK. Moreover, the mass activity of PtFeN<sub>x</sub>CNF at 0.9 V vs RHE is 4.9 mA mg Pt<sup>-1</sup> which is two times higher than that of E-TEK (2.3 mA mgPt<sup>-1</sup>). This improvement of ORR activity mainly results from the synergistic interaction between Pt and the FeN<sub>x</sub> moiety in the support. The number of transferred electrons (*n*) per oxygen molecule has been quantitatively estimated using the Koutecky-Levich (K-L) equation (detailed discussion given earlier).

Accordingly, the number of transferred electrons '*n*' could be calculated and the calculated values for '*n*' for PtFeN<sub>x</sub>CNF, PtNCNF, PtCNF and Pt/C (data not shown) are 3.6, 2.6, 2.5 and 4.1 respectively. The '*n*' values of all the catalysts are comparable to the reported values of Pt based systems in acidic medium.

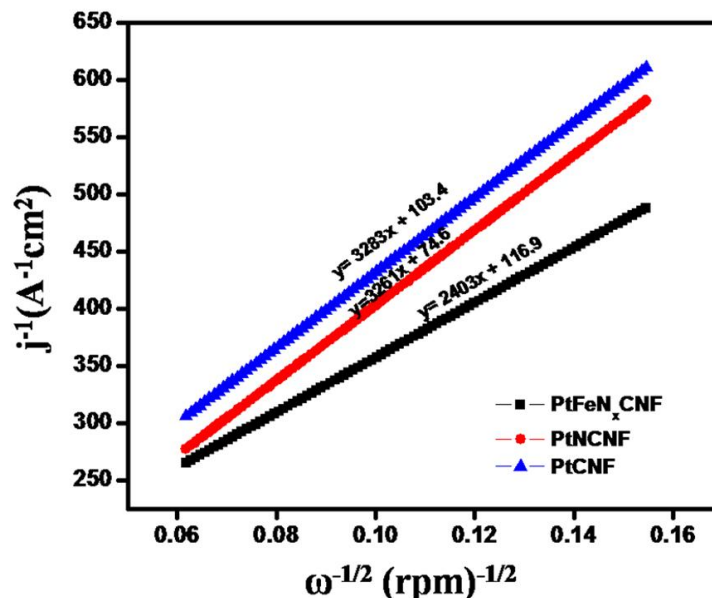


Figure 3.26. K-L plots of PtFeN<sub>x</sub>CNF, PtNCNF and PtCNF.

The improved ORR activity of PtFeN<sub>x</sub>CNF can be correlated to the specific interactions of Pt with nitrogen coordinated iron on the carbonaceous layer. FeN<sub>x</sub>CNF, which itself shows considerable ORR activity, attains significant level of surface unsaturation as a result of the incorporation of the dopant species. The ‘nanopockets’, due to their high level of surface dislocations, act as the domains for the fine distribution of the nanoparticles of Pt. HRTEM and XRD analysis unambiguously confirmed the attainment of fine distribution of Pt particles once hetero atom doping occurs in the carbon matrix. Indeed, the doped nitrogen increases electron density of the carbon surface by donation of its lone pair of electrons by imitating the n-type semiconductivity [45] and facilitates the electron transfer between the support to Pt, which subsequently results into enhancement in the ORR activity of the catalyst.[46-47] Moreover, the stronger interaction of Pt with N provides the stable incorporation of Pt on the nitrogen doped active sites as specified

by a theoretical study [48] which also has been further confirmed by the formation Pt-N auger line in XPS analysis. Finally, the synergistic effect between  $\text{FeN}_x$  with Pt also plays the significant role even though the exact nature of interaction between Pt and Fe is presently unclear as mentioned earlier. The role Fe is mainly to enhance the stable incorporation of pyridinic nitrogen in the carbon matrix of CNF. Previously, we have reported highly dispersed Pt on inner and outer wall of CNF. [12] The higher dispersion was achieved by means of chemical functionalization. Since the functional groups act as anchoring sites for Pt, the obtained ESCA of Pt-NCNF was significantly lower than that of  $\text{PtFeN}_x\text{CNF}$  which further discloses the importance of nitrogen coordinated iron active site for electrochemical activity of Pt. Also, when comparing the electrochemical activity, N derived Pt catalyst exhibits significantly lower activity than the  $\text{FeN}_x$  derived Pt catalyst, which ensures the difference in the nature of the active sites generated in the two cases. The results also show that both the nitrogen based Pt catalysts,  $\text{PtFeN}_x\text{CNF}$  and  $\text{PtNCNF}$ , exhibit higher catalytic activity than  $\text{PtCNF}$ , which gives strong evidence on the crucial role played by nitrogen to build the efficient active sites.

#### 3.3.11.6. Single Cell Analysis

To this end, demonstration of the realistic perspective of the performance aspect has been done by monitoring the current-voltage (I-V) characteristics of the membrane electrode assemblies (MEAs), where the cathode electrodes are derived from the homemade catalysts. An MEA having the cathode electrode formed from the commercial 20 wt. % Pt/C (E-TEK) was also tested for an effective comparison. In all the cases, the anode electrodes were prepared from the commercial 40 wt. % Pt/C (E-TEK). A Pt loading of

$0.2 \text{ mg cm}^{-2}$  was maintained in the cathodes as well as the anodes of the MEAs. The ohmic potential ( $iR$ ) compensated polarization plots are presented in Figure 3.27a.

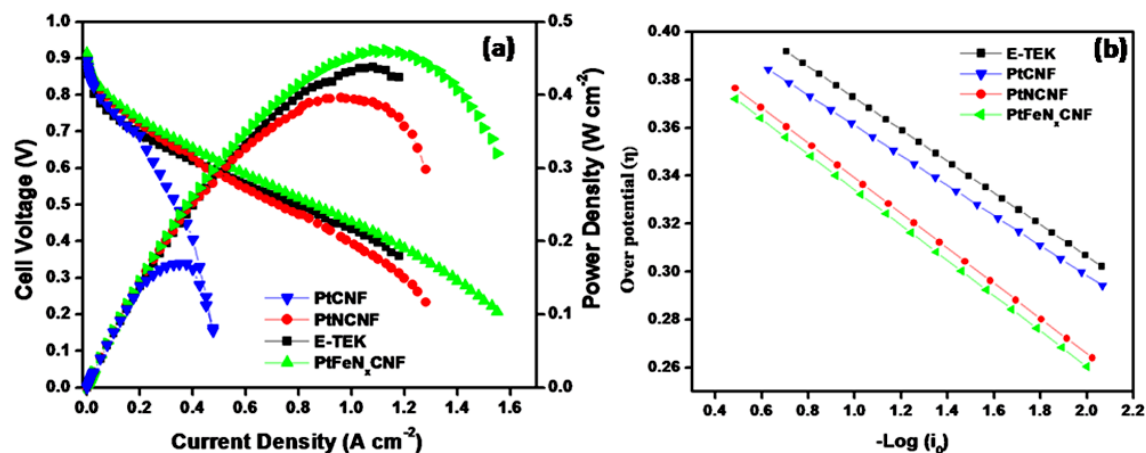


**Figure 3.27** (a) Single cell evaluation of the MEAs with the cathode electrodes formed from PtFeN<sub>x</sub>CNF, PtCNF, E-TEK and PtCNF. Commercial 40 wt. % PtC was used as the anode and a Pt loading of  $0.2 \text{ mg Pt cm}^{-2}$  was maintained in the cathode and anode. Nafion 212 was used as the membrane. Operating temperature:  $65 \text{ }^\circ\text{C}$ ,  $\text{H}_2$  and  $\text{O}_2$  flow rates:  $0.1 \text{ slpm}$ , humidity: 100% humidified  $\text{H}_2$  and  $\text{O}_2$ , pressure: 1 bar. (b)  $iR$  corrected Tafel plot of PtFeN<sub>x</sub>CNF, PtNCNF, PtCNF and Pt/C (E-TEK).

The superiority of PtFeN<sub>x</sub>CNF with respect to the ORR activity as disclosed by the RDE studies could be completely translated in terms of the single cell performance as evident from the enhanced activity characteristics of the system. The system retained this dominance throughout the polarization window, covering the activation, ohmic and concentration polarization regions. Both the nitrogen derived Pt catalysts (PtFeN<sub>x</sub>CNF and PtNCNF) exhibit an open circuit potential (OCP) of 0.92 V, which is slightly higher than the OCP values of 0.85 and 0.89 V displayed by E-TEK and PtCNF, respectively. At the cell voltage of 0.8 V, the obtained current densities of PtFeN<sub>x</sub>CNF, PtNCNF, E-TEK

and PtCNF are 0.081, 0.06, 0.04 and 0.02 A cm<sup>-2</sup> respectively. The reduced slopes of PtFeN<sub>x</sub>CNF and PtNCNF, compared to E-TEK and PtCNF, in the activation polarization region (*i.e.* in the low current density region) clearly highlight the benefits obtained from the modulated ORR activities of these catalysts. Besides, the obtained current density of PtFeN<sub>x</sub>CNF at 0.8 V vs RHE (Table 3.3) is very close to the previously reported value of Pt based catalyst with low loading of Pt.[49] At the same time, a comparison of the current outputs at 0.6 V vs. RHE, which has been considered as the most desirable operating potential for practical applications, further indicates the supremacy of PtFeN<sub>x</sub>CNF. The current density values displayed by the systems at 0.6 V vs RHE are 0.53, 0.45, 0.47 and 0.25 A cm<sup>-2</sup> respectively for PtFeN<sub>x</sub>CNF, PtNCNF, E-TEK and PtCNF. Besides, PtFeN<sub>x</sub>CNF also displays the maximum power density of 447 mW cm<sup>-2</sup>, which is higher than the corresponding values displayed by the other systems. The maximum power density displayed by E-TEK, PtNCNF and PtCNF are 410, 385 and 177 mW cm<sup>-2</sup>, respectively. Further, we measured the exchange current density ( $i_0$ ) which determines the rate of the ORR at the activation region from the Tafel plot (Figure 3.27b). The exchange current density values correspond to the all catalyst are given in the Table 3.2. PtFeN<sub>x</sub>CNF exhibits higher  $i_0$  ( $2.61 \times 10^{-6}$ ) than E-TEK ( $3.11 \times 10^{-7}$ ) which further helps to claim the higher ORR activity of PtFeN<sub>x</sub>CNF. The significantly weak performance of PtCNF can be correlated with the low electrochemically active Pt surface area of the system as originated from the poor dispersion of Pt on the substrate.

**Table 3.3.** An overview of the electrochemical activity of the catalysts.

Catalysts	ECSA ( $\text{m}^2 \text{g}^{-1}$ )	Onset Potential (V)	Half wave Potential (V)	Maximum Power Density ( $\text{mW cm}^{-2}$ )	Current Density at 0.8 V ( $\text{A cm}^{-2}$ )	Exchange current Density ( $i_0$ ) $\times 10^{-6}$
PtCNF	8.2	0.84	0.76	177	0.04	0.15
PtNCNF	22.1	0.86	0.81	385	0.06	2.27
E-TEK	39.1	0.83	0.79	410	0.02	0.31
PtFeN <sub>x</sub> CNF	64.6	0.88	0.81	447	0.081	2.61

### 3.4. Conclusions

In conclusion, preparation of iron nitride doped carbon nanofiber and its counter catalyst N-CNF as ORR catalysts was demonstrated. The nitrogen doping was initially confirmed by XRD, Raman spectra and XPS analyses. From the HRTEM analysis, the morphological alterations of the graphene layers on the side wall of CNF were observed. The nitrogen doping causes surface unsaturation in the graphene layers termed as ‘nanopockets’ without affecting the structure of CNF which leads to the higher performance of nitrogen doped composite catalysts towards ORR in acid medium. Further, the active sites for ORR are present predominantly on the inner wall of CNF which was evidenced by HRTEM analysis. Among the prepared catalysts, FeN<sub>x</sub>CNF (with less amount of nitrogen) shows better catalytic activity than N-CNF, revealing the

fact that it is not the amount of nitrogen but the nature of nitrogen in its coordination with the graphene framework, which is more important in deciding the ORR activity. In addition, the ability of FeN<sub>x</sub>CNF to reduce oxygen through a 4e<sup>-</sup> pathway highlights the importance of metal in the catalyst system to determine the reaction kinetics and thus opens great scope for considering new paths and strategies to develop effective non-precious electrocatalyst for PEMFCs. Although, FeN<sub>x</sub>CNF exhibits superior ORR activity, its performance has been hampered due to the unexposed active sites which are presents on the inner wall of CNF. The limited access of active sites eventually results into higher overpotential with respect Pt/C (130 mV). On the other hand, by taking the advantage of the surface unsaturation originated by the small order buckling of the graphene interlayers of CNF upon introducing the FeN<sub>x</sub> moiety for Pt dispersion, a new class of high performance ORR catalyst could be developed (PtFeN<sub>x</sub>CNF). The co-existence of the Pt and nitrogen based active sites built strong electronic interactions between Pt and doped nitrogen which could be concluded by the formation of Pt-N auger line from the XPS analysis. From our knowledge, this has been the first report which gives a strong evidence for the formation of Pt nitride auger line in Pt based nitrogen doped carbon catalysts for ORR. This provides a proof for the synergistic effect leading to modulated property characteristics towards ORR. The catalyst displayed unprecedented ORR activity during the dedicated experiments to explore the performance aspects. The 40 mV reduction in the overpotential for ORR over the new system compared to that over Pt/C clearly underlines the modulated property characteristics achieved by this novel preparation strategy. This benefit in terms of the ORR activity of PtFeN<sub>x</sub>CNF could be translated in terms of the current-voltage characteristics as well

during the single cell evaluation of the MEA having the cathode electrode formed from this catalyst composition. These results significantly favor the realization of a cost-effective, high-performance electrocatalyst for the ORR applications. Hence, it could be concluded that activity of non-Pt FeN<sub>x</sub>CNF was mainly due to surface unsaturation on the slanting plans of graphene layers due to nitrogen doping and the limitation on the activity was due to the unexposed active sites. Further, these nitrogen doped active sites could be used as the support for the low Pt electrocatalyst. The higher activity was mainly due to the synergistic effect of the nitrogen doped active sites and Pt.

### 3.5. References

- [1] X. B. Zhang, J. M. Yan, S. Han, H. Shioyama and Q. Xu, *J. Am. Chem. Soc.*, **2009**, *131*, 2778.
- [2] K. Gong, P. Yu, L. Su, S. Xiong and L. Mao, *J. Phys. Chem. C*, **2007**, *111*, 1882.
- [3] R. Bashyam and P. Zelenay, *Nature*, **2006**, *443*, 63.
- [4] J. P. Collman, N. K. Deveraj, R. A. Decreau, Y. Yang, Y. L. Yan, E. Ebina, T. A. Eberspacher and C. E. D. Chidsey, *Science*, **2007**, *315*, 1565.
- [5] (a) M. Lefevre, E. Proietti, F. Jaouen and J. P. Dodelet, *Science*, **2009**, *307*, 71. (b) J. Yang, D. J. Liu, N. N. Kariuki and L. X. Chen, *ChemComm.*, **2008**, *3*, 329.
- [6] L. Qu, Y. Liu, J. B. Baek and L. Dai, *ACS Nano*, **2010**, *4*, 1321.
- [7] (a) K. Gong, F. Du, Z. Xia, M. Durstock and L. Dai, *Science*, **2009**, *323*, 760; (b) P. H. Matter and U. S. Ozakan, *Catal. Lett.*, **2006**, *109*, 115.
- [8] S. Maldonado and K. J. Stevenson, *J. Phys. Chem. B*, **2005**, *109*, 4707.
- [9] S. Biniak, M. Walczyk and G. S. Szymanski, *Fuel Process. Technol.* **2002**, *79*, 251.
- [10] K. K. Cline, M. T. McDermot and R. L. McCreery, *J. Phys. Chem.* **1994**, *98*, 5314.
- [11] B. Lovrecek, M. Batinic and J. Caja, *Electrochim. Acta.* **1983**, *28*, 685.
- [12] B. K. Balan, S. M. Unni and K. Sreekumar, *J. Phys. Chem. C*, **2009**, *113*, 17572.
- [13] Z. Q. Tian, S. P. Jiang, Y. M. Liang and P. K. Shen, *J. Phys. Chem. B* **2006**, *110*, 5343.

- [14] Y. J. Kim, T. S. Shin, H. D. Choi, J. H. Kwon, Y. C. Chung and H. G. Yoon, *Carbon* **2005**, *43*, 23.
- [15] L. Yang, S. Jiang, Y. Zhao, L. Zhu, S. Chen, X. Wang, Q. Wu, J. Ma, Y. Ma and Z. Hu, *Angew. Chem. Int. Ed.* **2011**, *50*, 7132.
- [16] S. Jiang, Y. Ma, G. Jian, H. Tao, X. Wang, Y. Lu, Z. Hu, and Y. Chen, *Adv. Mater* **2009**, *21*, 4953.
- [17] Y. Chen, J. Wang, H. Liu, R. Li, X. Sun, S. Ye, and S. Knights, *Electrochem. Commun* **2009**, *11*, 2071.
- [18] Y. Chen, J. Wang, H. Liu, M. N. Banis, R. Li, X. Sun, S. Ye and S. Knights, *J. Phys. Chem. C.* **2011**, *115*, 3769.
- [19] D. C. Higgins, D. Meza and Z. Chen, *J. Phys. Chem. C.* **2010**, *114*, 21982.
- [20] G. Wu, C. Dai, D. Wang, D. Li and N. Li, *J. Mater. Chem.* **2010**, *20*, 3059.
- [21] B. Choi, H. Yoon, I. S. Park, J. Jang and Y. E. Sung, *Carbon*, **2007**, *45*, 2496.
- [22] F. Su, Z. Tian, C. K. Poh, Z. Wang, S. H. Lim, Z. Liu and J. Lin, *Chem. Mater.*, **2010**, *22*, 832.
- [23] M. Lefevre, P. Bertrand and J. P. Dodelet, *J. Phys. Chem. B*, **2002**, *106*, 8705.
- [24] S. Kundu, T. C. Nagaiah, W. Xia, Y. Wang, S. V. Dommele, J. H. Bitter, M. Santa, G. Grundmeier, M. Bron, W. Schuhmann and M. Muhler, *J. Phys. Chem. C*, **2009**, *113*, 14302.

- [25] E. Y. Jiang, D. C. Sun, C. Lin, M. B. Tian, H. L. Bai and S. L. Ming, *J. Appl. Phys.*, **1995**, *78*, 2596.
- [26] B. Stohr, H. P. Boehm and R. Schlogl, *Carbon*, **1991**, *29*, 707.
- [27] J. R. Pels, F. Kapteijn, J. A. Moulijn, Q. Zhu and K. M. Thomas, *Carbon*, **1995**, *33*, 1641.
- [28] H. Sjostrom, S. Stafstrom, M. Boman and J. E. Sundgren, *Phys. Rev. Lett.* **1995**, *75*, 1336.
- [29] S. Maldonado and K. J. Stevenson, *J. Phys. Chem. B* **2005**, *109*, 4707.
- [30] S. Trasobares, O. Stephan, C. Colliex, W. K. Hsu, H. W. Kroto and D. R. M. Walton, *J. Chem. Phys.* **2002**, *116*, 8966.
- [31] V. V. Strelko, V. S. Kuts, and P. A. Thrower, *Carbon*, **2000**, *38*, 1499.
- [32] K. K. Cline, M. T. McDermott and R. L. McCreery, *J. Phys. Chem.* **1994**, *98*, 5314.
- [33] R. Jiang and F. C. Anson, *J. Electroanal. Chem.*, **1991**, *305*, 171.
- [34] F. Jaouen and J. P. Dodelete, *J. Phys. Chem. C*, **2009**, *113*, 15422.
- [35] S. H. Yong, Shin, W. H.; Lee, J. W.; Kim, H. S.; Kang, J. K. *Appl. Phys. Lett.* **2007**, *90*, 013103.
- [36] A. Zamudio, A. L. Elias, J. R. Manza, F. L. Urias, G. R. Gattorno, F. Lupo, M. Ruhle, D. J. Smith, H. Terrones, D. Diaz and M. Terrones, *Small* **2006**, *2*, 346.
- [37] P. H. Matter, L. Zhang and U. S. Ozkan, *J. Catal.* **2006**, *239*, 83.

- [38] S. Shun, G. Zhang, Y. Zhong, H. Liu, R. Li, X. Zhou and X. Sun, *Chem. Commun.* **2009**, *45*, 7048.
- [39] C. L. Sun, L. C. Chen, M. C. Su, L. S. Hong, O. Chyan, C. Y. Hsu, K. H. Chen, T. F. Chang and L. Chang, *Chem. Matter.* **2005**, *17*, 3749.
- [40] J. Clavilier and J. P. Chauvineau, *J. Electroanal. Chem.* **1979**, *100*, 461.
- [41] W. Li, Liang, C.; Zhou, W.; Qiu, J.; Zhou, Z.; Sun, G.; Xin, Q. *J. Phys. Chem. B.* **2003**, *107*, 6292.
- [42] T. Palaniselvam, R. Kannan and S. Kurungot, *Chem. Commun.* **2011**, *47*, 2910.
- [43] H. J. Kim, D. Y. Kim, H. Han and Y. G. Shul, *J. Power Sources* **2006**, *159*, 484.
- [44] F. Su, Z. Tian, C. K. Poh, Z. Wang, S. H. Lim, Z. Liu and J. Lin, *Chem. Mater* **2010**, *22*, 832.
- [45] L. Panchakarla, A. Govindaraj and C. Rao, *ACS Nano* **2007**, *1*, 494.
- [46] R. Czerw, M. Terrones, J. C. Charlier, X. Blase, B. Foley, R. Kamalakaran, N. Grobert, H. Terrones, D. Tekleab and P. M. Ajayan et al. *Nano Lett* **2009**, *1*, 457.
- [47] G. Vijayaraghavan and K. Stevenson, *Langmuir* **2007**, *23*, 5279.
- [48] Y. Li, T. Hung and C. Chen, *Carbon* **2009**, *47*, 850.
- [49] M. S. Saha, A. F. Gull, R. J. Allen and S. Mukerjee, *Electrochim. Acta* **2006**, *51*, 4680.

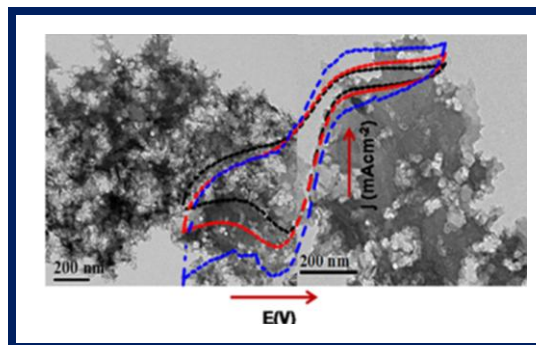
## Chapter 4

### AN EFFICIENT OXYGEN REDUCTION ELECTROCATALYST FROM GRAPHENE BY SIMULTANEOUSLY GENERATING PORES AND NITROGEN DOPED ACTIVE SITES

---

A simple way to simultaneously create pores and nitrogen doped active sites on graphene for the electrochemical oxygen reduction reaction (ORR) is developed. The key aspect of

the process is the *in-situ* generation of  $\text{Fe}_2\text{O}_3$  nanoparticles and their concomitant dispersion on graphene by pyrolyzing graphene oxide with  $\text{Fe}[(\text{phen})_3]^{2+}$  complex. Thus deposited  $\text{Fe}_2\text{O}_3$



nanoparticles act as the seeds for pore generation by etching the carbon layer along the Gr- $\text{Fe}_2\text{O}_3$  interface. Detection of the presence of  $\text{Fe}_3\text{C}$  along with  $\text{Fe}_2\text{O}_3$  confirms carbon spill-over from graphene as a plausible step involved in the pore engraving process. As the  $\text{Fe}[(\text{phen})_3]^{2+}$  decomposes and gives  $\text{Fe}_2\text{O}_3$  nanoparticles and subsequently the pores on graphene, the unsaturated carbons along the pore openings simultaneously capture nitrogen of the phenanthroline complex and provide very efficient active sites for ORR under alkaline conditions. The degree of N-doping and hence the ORR activity could be further improved by subjecting the porous Gr for a second round of N-doping using Fe-free phenanthroline.

---

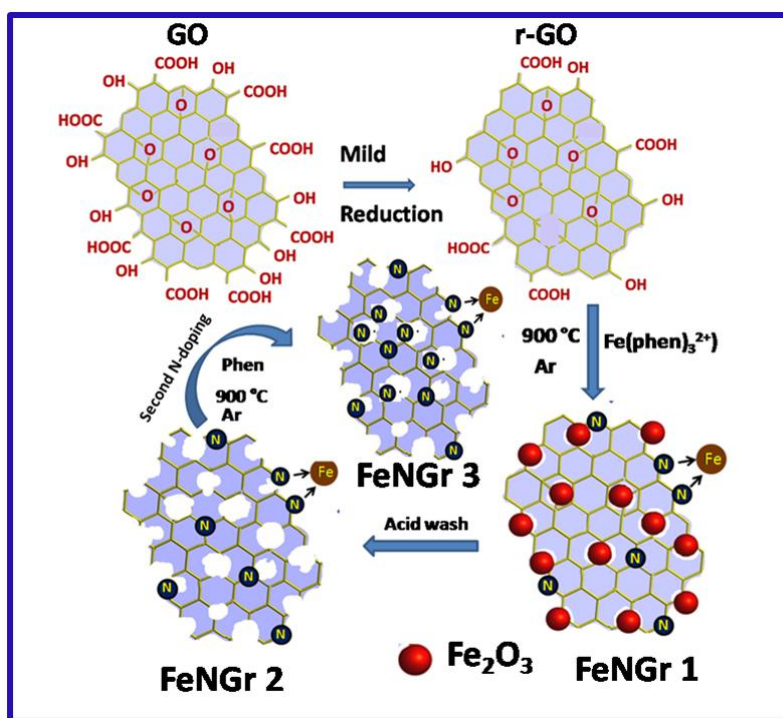
\*The contents of this chapter have been published in *J. Mater. Chem.*, **2012**, 22, 23799.

## 4.1. Introduction

Since the pioneering work of Jasinski *et al.* in the mid of 1964, several non-Pt electrocatalysts has been developed and demonstrated for polymer electrolyte membrane fuel cells (PEMFCs). In this perspective, high aspect ratio, one dimensional (1D) carbon nanotubes (CNTs) with higher nitrogen doping exhibit superior activity towards ORR in both acid and alkaline medium for PEMFCs.[1] However, several factors hampered their practical applications including low surface area, low mechanical stability, poor electrical conductivity etc. Moreover, the outer wall of CNTs is wrapped with amorphous carbon during their preparation and, hence, the outer wall needs to be activated to get enhanced nitrogen doping to increase the performance of the catalysts. [2] To tackle this issue, recently, much attention has been paid on the nitrogen doping on one atom thick two dimensional (2D) graphene (Gr) for ORR owing to its inherent high surface area, high electrical conductivity, mechanical stability *etc.* [3] Several research works have been reported for the preparation of nitrogen doped Gr with and without metal (Fe or Co) for ORR. [4]

Accordingly, inclusion of porosity into the uniform matrix of Gr is expected to modulate its mechanical, electrical, optical and thermal properties. In view of that, porous graphene (PG) has drawn significant attention recently, motivated by the uses of its ancestor two dimensional Gr in nano electronics and energy applications such as Li-ion batteries, [5] solar cells [6], supercapacitors, [7] gas sensors [8] and PEFCs. [9] However, the lack of band gap in Gr minimizes the prospects of Gr based nano materials for the solar cell applications. Preparation of Gr with preferred structures and tunable electrical conductivity is highly desired. Recent hypotheses suggest that Gr with well-defined

porous structure can be another promising material for Li-air battery [10] and gas separation. [11] Creation of porosity in Gr matrix is predicted to tune the band gap energy of Gr (3.2 eV) similar to the band gap of  $\text{TiO}_2$ . [12] However, the experimental realization of creation of porosity on Gr is conceivably challenging. Firstly, Fasel *et al.* [13] initiated the synthesis of porous graphene by the fabrication of 2D polyphenylene networks. A recent attempt was to create vacancy on Gr by pulsed vapor deposition (PLD) for single atom doping (Pt, Co and In) on the desired vacancy. [14] It is also known that the created vacancy in Gr is a perfect trapping site for heteroatom doping such as Nitrogen (N) [11], and Boron (B).



**Scheme 4.1.** Schematic representation of the process involved in the creation of pores and the nitrogen and iron nitride doped active sites in graphene.

Indeed, an electrochemical reaction on the edge planes of carbon nanostructures is more facile than that of the basal planes. Further, when doped with N, it induces additional exposure of the edge planes and, thus, a controlled interplay of these two types of active sites together contribute towards the improvement of the catalytic activity for the sluggish oxygen reduction reaction (ORR) in PEMFCs. [15-18] On the other hand, there are evidences on the metal (Fe or Co) coordinated N-doping on carbon nanostructures providing superior electrocatalytic activity than by N alone. [19-24]

In Chapter 3, we prepared the Fe coordinated nitrogen doped carbon nanofiber (*i.e.* FeN<sub>x</sub>CNF) as a non-Pt electrocatalyst for ORR. FeN<sub>x</sub>CNF reduces the oxygen (O<sub>2</sub>) molecule in the preferred 4e<sup>-</sup> pathway than the N doped-carbon nanofiber (N-CNF) in acid medium. [25] The FeN<sub>x</sub> doping could be achieved significantly on CNF due to the rich defect sites *i.e.*, the inherent slanting edges and cup-stacked structure of CNF. However, the ORR activity is limited by the unexposed nitrogen doped activesites which are existing on the inner wall of CNF which triggered us to prepare the nitrogen doped carbon catalyst with higher surface area and rich site of nitrogen.

Here, we show a proficient way to create highly densed N and iron nitride doped nano porous Gr (FeNGr) *via* the pyrolysis of the partially reduced graphene oxide (r-GO) with iron phenanthroline (Fe [(phen)<sub>3</sub>]<sup>2+</sup>) complex. The created vacancy has been effectively utilized for subsequent N doping which has further been explored for electrochemical ORR activity. Earlier, Dai *et al.* synthesized N-doped Gr by thermal annealing of GO with NH<sub>3</sub> and reported the essential role played by the different oxygen functional groups such as carboxyl, carbonyl and lactones for the effective nitrogen doping. [26] Similarly, in the present work, r-GO gets reduced into Gr during the

annealing, while the functional groups present between the basal planes of r-GO interact with Fe from iron acetate ( $\text{Fe}(\text{OAc})_2$ ) to form uniformly distributed iron oxide ( $\text{Fe}_2\text{O}_3$ ) nanoparticles. Thus formed  $\text{Fe}_2\text{O}_3$  nanoparticles trigger etching of carbon at the  $\text{Fe}_2\text{O}_3$ -Gr interface and generate multi vacancies on Gr as shown in Scheme 4.1. Moreover, the lingering iron in coordination with the 1,10 phenanthroline tends to cause iron nitride (FeN) doping during the thermal treatment process. Subsequent removal of the entrapped  $\text{Fe}_2\text{O}_3$  nanoparticles leads to exposure of the unsaturated pore openings of graphene where further N doping can be done very effectively. In this way, the number density of the active sites responsible for ORR can be increased all the while keeping the material highly porous, which is an important requirement in electrocatalysts for PEFCs, where mass transfer generally plays a key role.

## 4.2. Experimental Section

### 4.2.1. Synthesis of Graphene Oxide (GO)

GO was synthesized by improved Hummer's method. [27] Briefly, 1 g of graphite powder was ground with 6 g of potassium permanganate ( $\text{KMnO}_4$ ) and this was slowly added into the solvent mixture of con.  $\text{H}_2\text{SO}_4$ : $\text{H}_3\text{PO}_4$  (9:1 ratio) with mechanical stirring at room temperature. Further, the temperature of the reaction mixture was increased and maintained to 55 °C for 12 h. The oxidation reaction was stopped by adding the colloidal solution into 400 ml of cold water which contains 3 ml of 30%  $\text{H}_2\text{O}_2$ . The brownish yellow colored solution was centrifuged (10000 rpm) and the supernatant solution was decanted away and the resulting material was subjected to multiple washings with water, ethanol, acetone and polyether.

#### 4.2.2. Synthesis of Partially Reduced GO (r-GO)

GO obtained from the previous process was subjected to mild reduction by heating at 100 °C under Ar atmosphere to obtain the partially reduced GO (r-GO). The purpose of the mild reduction is essentially to decrease the number density of the oxygen functional groups in GO.

#### 4.2.3. Pore Generation and Nitrogen-Doping

For all the catalysts in this work, we have used commercially obtained iron acetate ( $\text{Fe}(\text{OAc})_2$ ) (Aldrich) and 1, 10-phenanthroline (phen) (Aldrich 99%) as the Fe and nitrogen precursors, respectively. In a typical synthesis of iron nitride-doped Gr (FeNGr), the weighed amount of r-GO (100 mg) was dispersed in 50 ml of ethanol (Rankem 99.9%) by ultrasonication. An excess amount of phen (200 mg) in 25 ml of ethanol was added and allowed to interleave in between the basal planes of r-GO by magnetic stirring for about 30 min. Further, the required amount of  $\text{Fe}(\text{OAc})_2$  in ethanol was added drop by drop into the phen-r-GO mixture. The final weight percentage of Fe was determined by EDAX analysis.  $\text{Fe}(\text{OAc})_2$  reacts with phen to form  $\text{Fe}[(\text{phen})_3]^{2+}$  chelate complex, which was confirmed from the color change from pale yellow to wine red. Subsequently, the chelate complex solution was mechanically stirred for 24 h at room temperature to achieve efficient diffusion of the iron chelate complex into the basal plane of r-GO. The resulting mixture was placed in a beaker inside an oven and the solvent was evaporated at 50 °C for about 3 h. The resulting solid material was placed in a quartz tube and was pyrolysed in Ar atmosphere at 900 °C. The temperature ramp was 10 °C per minute till it reaches 900 °C and the system was maintained at that temperature for 3 h with an Ar

flow of 0.5 sccm. Subsequently, the system was allowed to cool to room temperature under Ar flow. The pyrolysed product was then washed with ethanol and filtered (filter paper 0.2  $\mu\text{m}$  pore size, Rankem) to remove the chars of organic residues. The material obtained at this stage was dried at 80  $^{\circ}\text{C}$  for 2 h and was preserved for further studies (FeNGr1). During the annealing at 900  $^{\circ}\text{C}$ , r-GO gets reduced into Gr while the functional groups present between the basal plane of r-GO interact with Fe from iron acetate ( $\text{Fe}(\text{OAc})_2$ ) to form uniformly distributed iron oxide ( $\text{Fe}_2\text{O}_3$ ) nanoparticles. This in turn generates multi vacancies on Gr by knocking off the carbon atoms on the reduced Gr surface as shown in Scheme 4.1. Moreover, the lingering iron in coordination with the phenanthroline tends to cause iron nitride doping during the thermal treatment. On subsequent acid treatment,  $\text{Fe}_2\text{O}_3$  gets leached out by creating well distributed nanometer sized pores in Gr. This iron nitride-doped porous Gr is designated as FeNGr2. Successive N doping on the created pore openings of FeNGr2 was done by annealing the material with phen alone. The resulting N rich porous material is named as FeNGr3. Since the oxygen (O) functional groups reflect the relative content of the porosity and nitrogen doping on the graphene sheets, we applied the same approach to prepare another form of iron nitride doped Gr (FeNGr4) by using GO (without the mild reduction). In order to study the role of the functional groups present on the basal plane of r-GO to facilitate the  $\text{Fe}_2\text{O}_3$  formation, a sample was prepared by using prereduced GO (FeNGr5). The pre-reduction of GO was obtained by mild thermal treatment of GO at 600  $^{\circ}\text{C}$  for 1 h in Ar atmosphere. Finally, to compare the role of Fe, nitrogen doped Gr (N-Gr) was prepared by pyrolyzing r-GO directly with phen (*i.e.* by avoiding Fe addition).

## 4.3. Results and Discussion

### 4.3.1. HRTEM Analysis

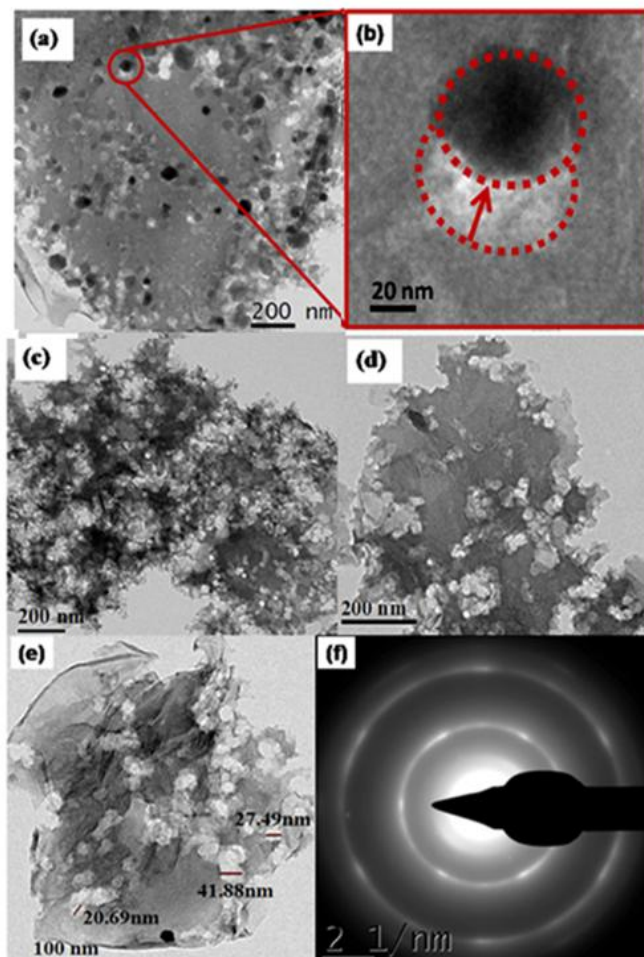


**Figure 4.1.** HRTEM images of (a) graphene with the in-situ generated  $Fe_2O_3$  nanoparticles on its surface (FeNGr1), (b) the higher magnification image of the interface between graphene and a single  $Fe_2O_3$  particle which shows the damaged graphene surface by etching of carbon, (c)-(e) porous graphene with nitrogen doped active sites formed after removal of the  $Fe_2O_3$  nanoparticles by acid treatment (FeNGr2) with different magnifications (d) selected area diffraction pattern of FeNGr2.

HRTEM was employed to examine the morphology of the obtained FeN doped Gr before and after acid treatment. Accordingly, Figure 4.1a shows the HRTEM image of FeNGr1 in which few FeNGr sheets are compressed and stacked together. Interestingly, we found that some particles are present on the Gr surface and the particles are distributed uniformly with an average size of ca. 20-50 nm. From XRD (will be discussed later), we recognized that the particles are corresponding to  $\text{Fe}_2\text{O}_3$ . [28] The oxide formation is mainly facilitated by the strong interaction of Fe with the functional groups present on the basal plane of r-GO. Interestingly, a close look at the  $\text{Fe}_2\text{O}_3$ -Gr interface reveals open portions of Gr at several places which appeared to follow the shape of the locked  $\text{Fe}_2\text{O}_3$  nanoparticles (shown in Figure 4.1b). It is expected that during the annealing process, the  $\text{Fe}_2\text{O}_3$  particles present on the Gr surface etch carbon, resulting in multi-vacancies around the particle on the Gr surface. The carbon atoms are expected to be removed as iron carbide ( $\text{Fe}_3\text{C}$ ) [29] and carbonaceous gases.[30]

Along with the holes locked with the  $\text{Fe}_2\text{O}_3$  nanoparticles, there are also lots of open holes on Gr which presumably appeared once the nanoparticles are loosed out as the pore dimension exceeds the diameter of the oxide nanoparticles. The size of  $\text{Fe}_2\text{O}_3$  particles is an important parameter which decides the size of pores and their distribution. For example, as can be seen from the HRTEM image in Figure 4.2, larger and poorly distributed holes are formed from bigger and aggregated  $\text{Fe}_2\text{O}_3$  particles. FeNGr2, prepared after the removal of the residual  $\text{Fe}_2\text{O}_3$  particles from FeNGr1 by acid treatment, is highly porous as can be seen from the HRTEM images (Figure 4.1c-e).

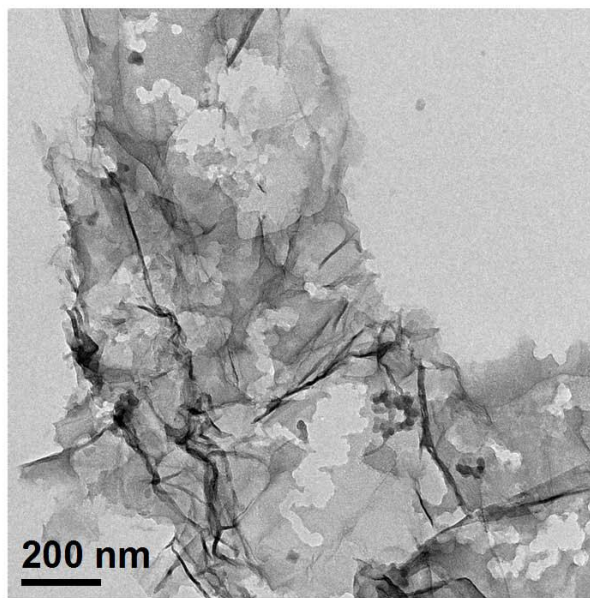


**Figure 4.2.** HRTEM image of the porous graphene derived from larger and aggregated  $Fe_2O_3$  particles.

The pores on Gr are clearly visible, and the diameter of the pores is around 20 to 60 nm which is relative to the size of the  $Fe_2O_3$  particles (shown in Figure 4.1b). Further, the HRTEM images reveal that the Gr sheets are not single layered as such and it seems like few layers are stacked together, presumably due to *van der Waals* forces during the thermal treatment. Moreover, the selected area diffraction pattern (SAED) clearly shows that the well-defined diffraction spots and rings are fully recognized as the typical hexagonal lattice for carbon atoms in FeNGr2. In FeNGr3, further nitrogen doping along the unsaturated carbons of the pore openings could be achieved during the annealing with phen. At the same time, the oxygen functional groups determine the dispersion of  $Fe_2O_3$  particles and thereby the porosity of Gr. A valid proof for this is evident from the HRTEM images of FeNGr4, which was prepared directly by pyrolyzing GO (*i.e.* without subjecting it to mild reduction) with the  $Fe[(phen)_3]^{2+}$  complex.

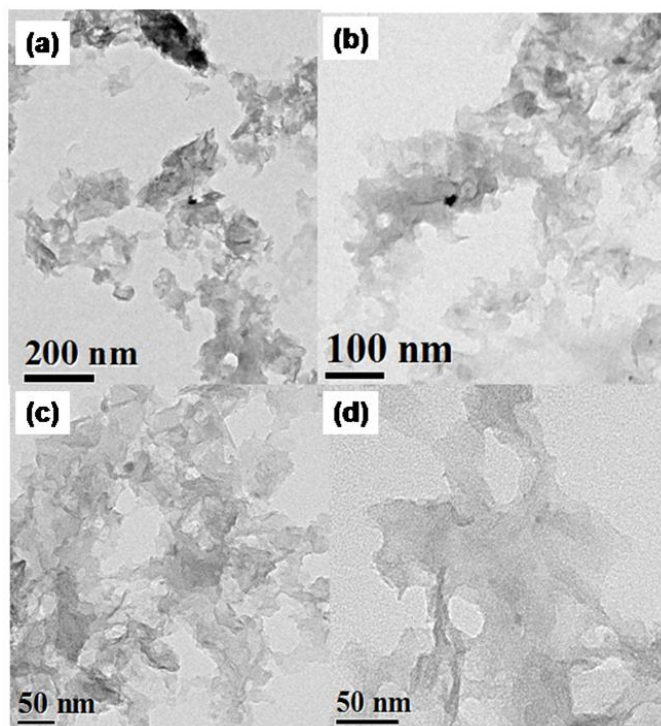


**Figure 4.3.** (a)-(d) HRTEM images of the porous graphene prepared directly from GO (FeNGr4) with different magnifications. Excess deposition of  $Fe_2O_3$  nanoparticles causes extensive degradation of the graphene sheets.

The HRTEM images of FeNGr4 as shown in Figure 4.3 reveal a crumpled nature of the material. Besides, the nature and morphology of the distribution and appearance of the pores of FeNGr4 are quite different from those of FeNGr2. Moreover, at some locations, the graphene sheets appear like nanoribbons. This can be ascribed to the enhanced consumption of the Fe particles through the relatively higher proportion of the functional groups on GO. This subsequently facilitates the formation of numerous  $Fe_2O_3$  nanoparticles and thereby enhancing the process of etching the carbon atoms from the graphene sheets during the thermal treatment. In both the cases, the primary product formed on the Gr surface is  $Fe_2O_3$  as is confirmed by the formation of pores in Gr by

HRTEM analysis. To further verify the role of Fe as a moiety responsible for engraving the pores on Gr, we prepared the nitrogen doped Gr (N-Gr). Here, the  $\text{Fe}_2\text{O}_3$  formation was prevented by avoiding the Fe precursor and r-GO was directly treated with phen. The HRTEM images (Figure 4.4) clearly show the completely reduced few-layer N-Gr without any holes, which unambiguously confirms the role of the Fe precursor for generating the nanopores on Gr.

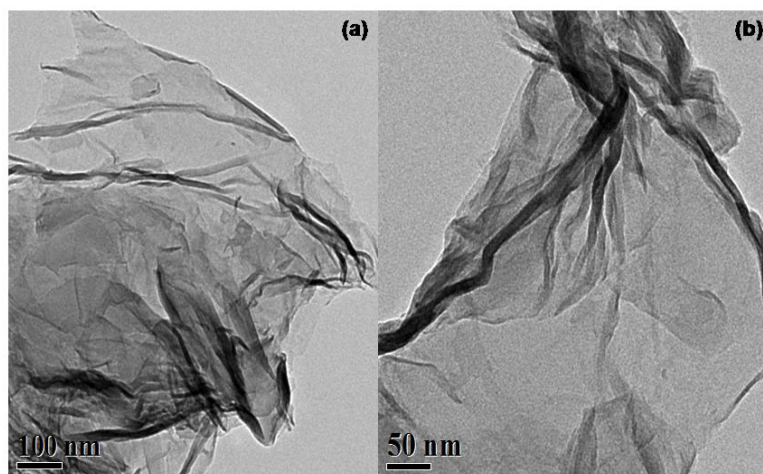


**Figure 4.4.** HRTEM images of the nitrogen doped graphene (N-Gr).

### 4.3.2 XRD Analysis

In order to find out the crystalline nature of Gr based materials and  $\text{Fe}_2\text{O}_3$ , we have carried out XRD analysis. Figure 4.5a shows the XRD pattern of the Gr based samples. In the case of GO, the (002) peak, characteristics of graphite, appears at a  $2\theta$  of  $10.3^\circ$ . This peak shifts slightly towards the higher  $2\theta$  value ( $12.1^\circ$ ) after the mild reduction (r-GO), indicating that the functional groups intercalated between the basal planes have been reduced slightly. After annealing of r-GO with Fe  $[(\text{phen})_3]^{2+}$  (*i.e.* FeNGr1), the G(002) peak shifts towards a higher  $2\theta$  value of  $26.3^\circ$ , which ensures that

the functional groups present on r-GO have been reduced significantly. Moreover, we could observe a new peak at around  $35.5^\circ$  corresponding to the (311) plane of  $\text{Fe}_2\text{O}_3$  which is absent in the case of N-Gr. The formation of  $\text{Fe}_2\text{O}_3$  is mainly due to the higher tendency of Fe from  $\text{Fe}(\text{OAc})_2$  to interact with the functional groups present on the basal plane of r-GO. The absence of the peak corresponding to  $\text{Fe}_2\text{O}_3$  in FeNGr5, which was prepared from pre-reduced Gr, (Figure 4.5b) gives strong evidence on the interaction between the functional groups and the Fe precursor as a responsible factor for the formation of  $\text{Fe}_2\text{O}_3$ . Since  $\text{Fe}_2\text{O}_3$  is inactive for ORR, we carried out acid washing to remove the  $\text{Fe}_2\text{O}_3$  particles from FeNGr1. The complete removal of the  $\text{Fe}_2\text{O}_3$  particles from FeNGr2 has been ensured by looking at the vanishing of the peak corresponding to  $\text{Fe}_2\text{O}_3$  (311), which are well supported by the HRTEM analysis (Figure 4.1a-d) as well.

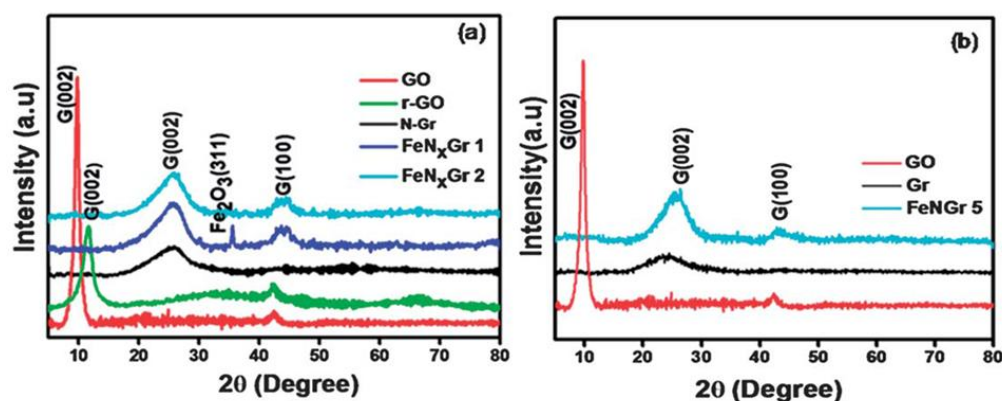


*Figure 4.5. XRD patterns of the prepared catalysts.*

### 4.3.3. Raman Spectra Analysis

Since Raman spectroscopy is an important tool to deduce the structure in particularly the defects and disorder nature of Gr based materials, we took Raman spectra of all the samples (Figure 4.6). The Raman spectra of the samples exhibit two remarkable

peaks at around 1340 and 1506  $\text{cm}^{-1}$  corresponding to the well-defined D and G bands, respectively. The graphitic peak (G band) at 1506-1510  $\text{cm}^{-1}$  is due to the  $E_{2g}$  vibrational mode of the C-C bond stretching and the disorder peak (D-band) at 1330-1345  $\text{cm}^{-1}$  is due to the  $A_{1g}$  vibrational mode. The intensity ratio of the D and G bands *i.e.* ( $I_D/I_G$  ratio) helps to estimate the defects of Gr based samples where a higher ratio ensures more defects on Gr. The calculated  $I_D/I_G$  ratios of r-GO, N-Gr and FeNGr2 are 1.08, 1.02, and 1.16, respectively. The higher  $I_D/I_G$  ratio of FeNGr2 compared to N-Gr clearly depicts the defective nature of FeNGr2 due to its porous structure. This conclusion is in good agreement with the conclusions derived from the XRD, XPS and HRTEM analyses.

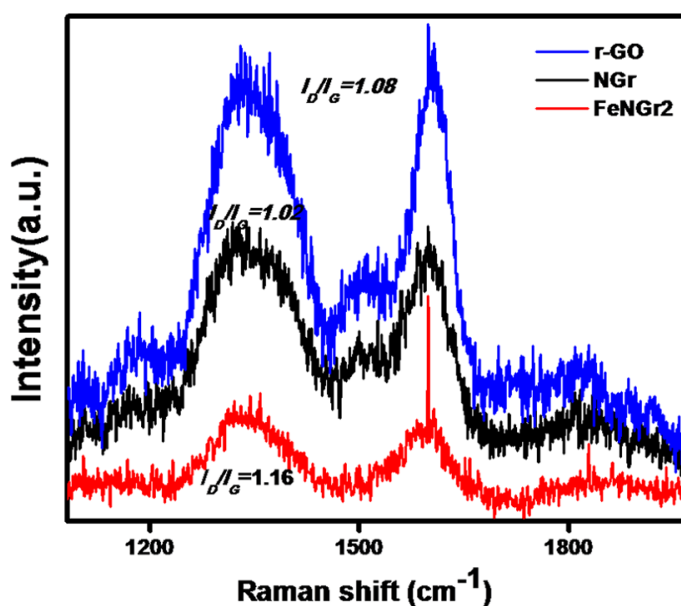


**Figure 4.6.** Raman spectra of r-GO, N-Gr and FeNGr2.

#### 4.3.4. XPS Analysis

In order to investigate the chemical nature of FeNGr2, we have carried out XPS analysis. The full range XPS reveals the presence of carbon (C), oxygen (O), nitrogen (N)

and trace amount of Fe in the prepared catalysts (Figure 4.7). The presence of large quantity of O may be due to different functional groups and unremoved oxides.

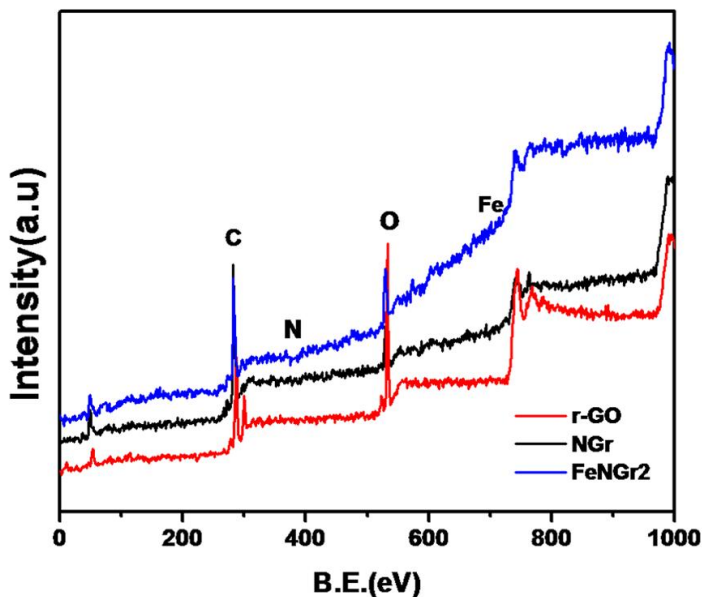


**Figure 4.7.** Full range XPS survey of (a) r-GO (b) N-Gr and (c) FeNGr2.

Figure 4.8a shows the N 1s spectra of FeNGr2. There are several N groups in the thermally reduced Gr which are characterized by different peaks. The small peak at the low binding energy of 397.4 eV ( $N_1$ ) slightly differs from the free nitrogen atom (398.5 eV) and can be recognized as the doped N bound to Fe to form the Fe-N coordination. However, the peak intensity is too less indicating that the Fe-N active sites are significantly low and the consumption of Fe for the formation of  $Fe_2O_3$  restricts the generation of Fe-N.

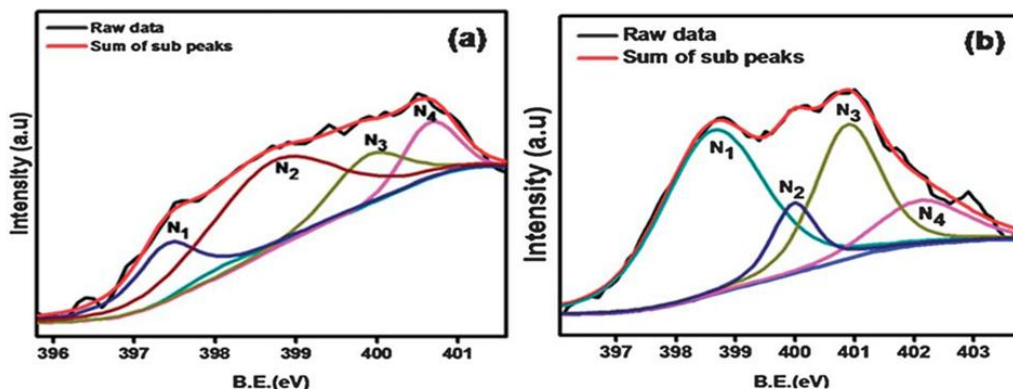


**Figure 4.8.** *N 1s* spectra of (a) FeNGr2 and (b) N-Gr.

The broad peak at 398.8 eV ( $N_2$ ) can be ascribed to pyridinic nitrogen [32] which is regarded as a main active site for ORR. The peak at 399.8 eV is ascribed to the pyrrole type nitrogen and the one at 400.2 eV is due to the graphitic nitrogen. [33] Similarly, we deconvoluted the  $N 1s$  spectra of N-Gr into four peaks (Figure 4.8b). The peaks at 398.8, 400.2, 401.5 and 402.2 eV are corresponding to the pyridinic, graphitic, quaternary and nitroso nitrogen, respectively. Obviously, we could not observe any peak corresponding to FeN due to the absence of Fe in its preparation.

The  $C 1s$  spectra of r-GO and FeNGr2 are shown in Figure 4.9. The  $C 1s$  spectra of r-GO (Figure 4.9a) are deconvoluted into four different peaks. The peak at 284.5 eV is assigned as  $C_1$  corresponding to graphitic carbon. The peaks at 286.7, 287.1 and 288.1 eV can be recognized as  $C_2$ ,  $C_3$  and  $C_4$  are corresponding to the  $sp^3$  carbon (*i.e.* carbon bound with oxygen (C-O) ), epoxy carbon (C-O-C) and carbonyl carbon (C=O), respectively. Similarly, in the case of FeNGr2 (Figure 4.9b), the  $C 1s$  spectra are deconvoluted into three peaks.

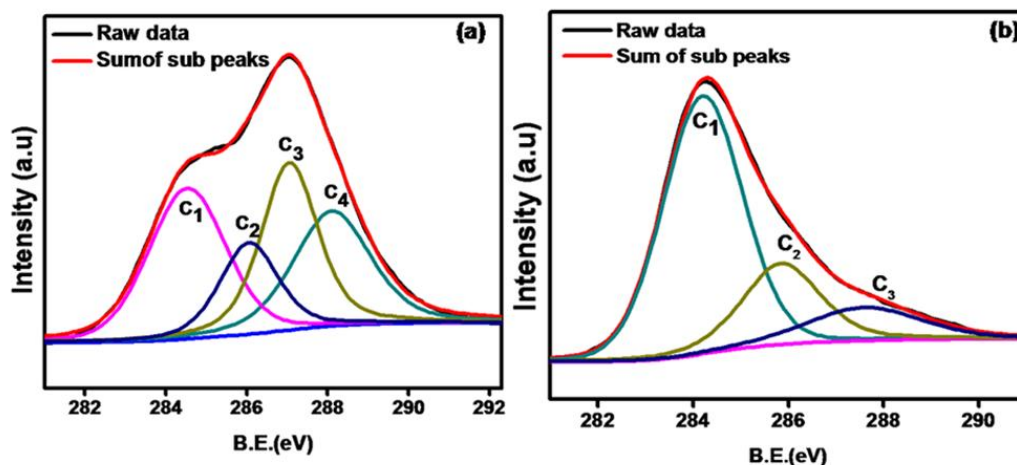


**Figure 4.9.** *C 1s spectra of (a) r-GO and (b) FeNGr2.*

The peak at 284.3, 285.7 and 287.5 eV are corresponding to the graphitic carbon, C-O and  $sp^3$  carbon (either carbon bound with oxygen or nitrogen) and epoxy carbon, respectively. Figure 4.9b also reveals strong suppression of the oxygen functional groups especially carbonyl functional groups compared to r-GO which ensures the proficient reduction of the oxygen functional groups during the thermal treatment.

The Fe2p spectra of FeNGr2 have been deconvoluted into three different peaks which are shown in Figure 4.10. The peak at the low binding energy of 706.6 eV, named as Fe1, corresponds to metallic iron carbide ( $Fe2p_{3/2}$ ) emphasizing the presence of trace amount of  $Fe_3C$  which is well line up with the XRD results. The signature corresponding to  $Fe_3C$  remains as a strong evidence on the postulation of the mechanism involving a step where  $Fe_2O_3$  etches carbon from Gr with the formation of  $Fe_3C$  or carbonaceous gases. The pair of peaks at 709.8 and 711.8 eV which are assigned as  $Fe_2$  and  $Fe_3$ , respectively, correspond to the ionic state of Fe ( $Fe2p_{1/2}$ ) and this result discloses that Fe

in the ionic state arises either from the iron coordinated with nitrogen or residual iron oxide.

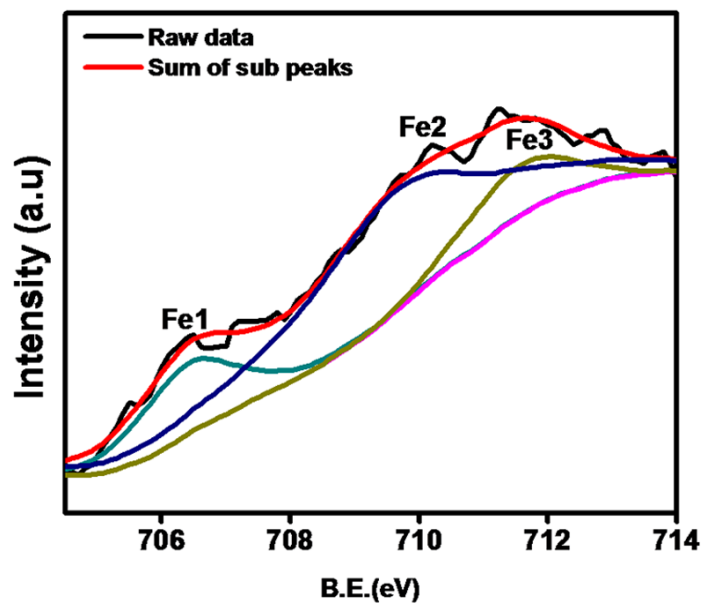


Figure 4.10. Fe<sub>2p</sub> spectra of FeNGr<sub>2</sub>.

#### 4.3.5 EDAX Analysis

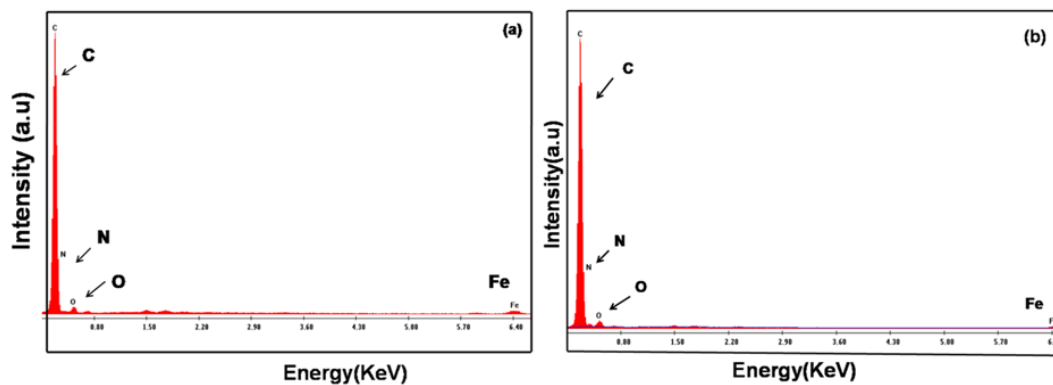
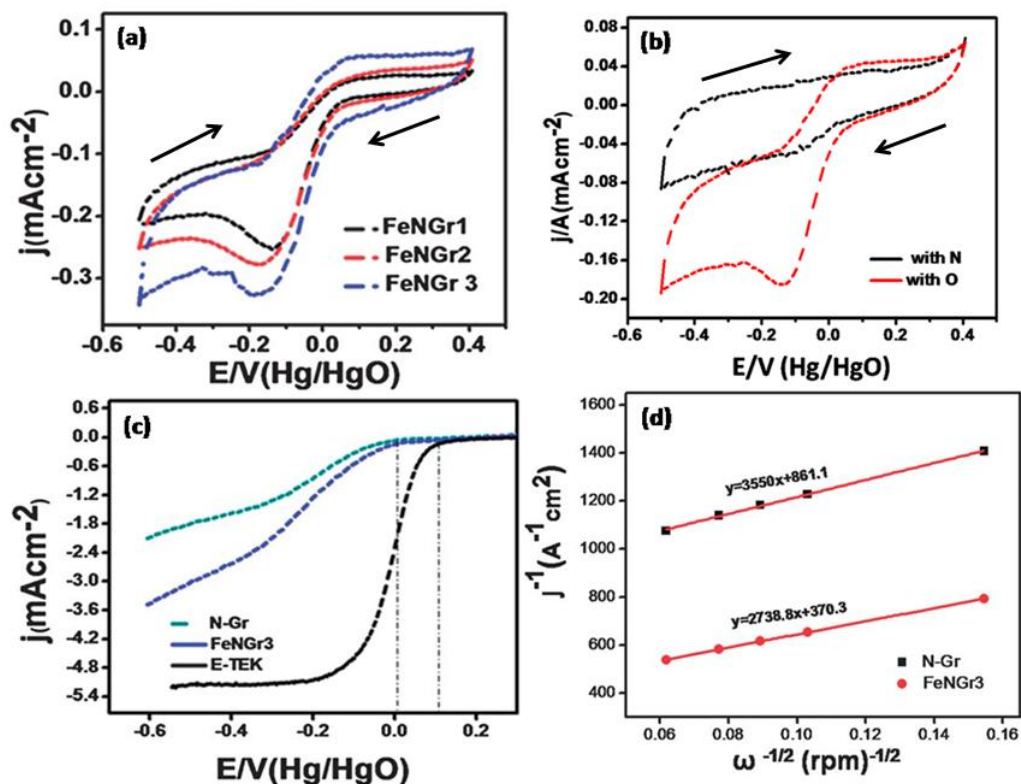


Figure 4.11. EDAX spectra of (a) FeNGr<sub>2</sub> and (b) FeNGr<sub>3</sub> showing 5.90 and 9.75 % of nitrogen doping, respectively.

The EDAX analysis shows the atomic weight percentage of C, N, O and Fe of FeNGr2 and FeNGr3 (Figure 4.11). The EDAX analysis unravels that thermal reduction of r-GO with  $\text{Fe}[(\text{phen})_3]^{2+}$  introduces the N on Gr up to 5.9 wt% which is increased up to 9.7 wt. % after subjecting the material for the second run for nitrogen doping. This experimental sequence, especially the second doping step, ensures adequate nitrogen doping on the desired vacancies created along the edges of the engraved pores once the  $\text{Fe}_2\text{O}_3$  nanoparticles are eliminated by acid washing.

#### 4.3.6. Electrochemical Studies

To investigate the electrochemical activity of the nitrogen doped catalysts, the cyclic voltammetry and RDE in 0.1 M KOH solution (saturated with  $\text{O}_2$ ) was performed to evaluate the electrochemical oxygen reduction activity of the prepared materials accordingly. Figure 4.12 summarizes the activity of the prepared catalysts. Figure 4.12a shows the cyclic voltammogram of FeN doped Gr cycled between 0.4 and -0.5 V against the Hg/HgO reference electrode at a scan rate of  $5 \text{ mV s}^{-1}$ . The FeN based composite catalysts show a well-resolved cathodic peak corresponding to ORR under oxygen saturated conditions. The ORR of FeNGr1 and FeNGr2 occurred at a similar onset potential, while the removal of  $\text{Fe}_2\text{O}_3$  by acid treatment (*i.e.* FeNGr2) slightly enhances the ORR current without altering the onset potential. This indicates that the adopted acid treatment process to get rid of the  $\text{Fe}_2\text{O}_3$  particles does not affect the active sites present on the porous graphene.



**Figure 4.12.** (a) CV for FeN-Gr1, FeN-Gr2 and FeN-Gr3 recorded in 0.1 M KOH at 5 mV s<sup>-1</sup>, (b) CV for N-Gr recorded in 0.1 M KOH at a scan rate of 5 mV s<sup>-1</sup> under nitrogen and oxygen enriched conditions, (c) steady-state polarization plots of N-Gr, FeN-Gr3 and 20 wt% Pt/C (E-TEK) recorded in 0.1 M KOH at 10 mV s<sup>-1</sup> (1600 rpm) and (d) Koutecky–Levich (K–L) plots of N-Gr and FeN-Gr3 obtained from RDE studies in O<sub>2</sub>-saturated 0.1 M KOH solution at a potential of -0.4 V.

The slight enhancement in the limiting current in FeN-Gr2 may be ascribed to the removal of the blockage of the active sites by Fe<sub>2</sub>O<sub>3</sub> in FeN-Gr1. Interestingly, in the case of FeN-Gr3, the ORR activity has been enhanced with substantial gain in both the onset potential (*ca.* 40 mV) and the limiting current values. This performance enhancement can be correlated with the improvement in the number of the active sites through the second

doping process at the edge carbons which are exposed after the removal of  $\text{Fe}_2\text{O}_3$ . Moreover, a similar experiment on NGr (Figure 4.12b) with the same experimental method shows nearly comparable performance profile as those of FeNGr1 and FeNGr2, which further emphasizes that the nature of the active sites is more or less similar in these samples. Since the contribution of Fe in FeNGr1 and FeNGr2 does not reflect due to their comparative performance with N-Gr, it seems that Fe does not participate towards the ORR activity even though it helps in establishing some coordination with N as found in XPS.

Furthermore, the performances of FeNGr3 and N-Gr are compared by using the rotating disk electrode (RDE) method in 0.1 M KOH medium (oxygen saturated) and the results obtained at 1600 rpm are presented in Figure 4.12c. The polarization curve of N-Gr shows the mixed diffusion kinetics between 0.1 and -0.4 V with an onset potential of -0.02 V. On the other hand, the mixed diffusion kinetics of FeNGr3 appears between 0.08 and -0.4 V with an onset potential of 0.01 V, which is 40 mV positive compared to N-Gr. This reveals the beneficial role played by the second nitrogen doping to effectively utilize the edge sites along the pore walls for the heteroatom doping. Moreover, the onset potential is effectively compared with the state-of-the-art 20 wt.% Pt/C (E-TEK) catalyst under identical testing conditions. The onset potential of FeNGr3, even though is more negative by 90 mV compared to E-TEK, the overpotential is significantly low compared to the few N doped graphenes reported in the literature.

For example, recently, Wong *et al.* [34] prepared a nitrogen-doped graphene by thermally annealing melamine with GO at different temperatures. The best sample reported by them displayed an onset potential of 120 mV more negative than 20 wt%

Pt/C in 0.1 M KOH by using the Ag/AgCl reference electrode. Similarly, Lin *et al.* [35] synthesised a pyridinic nitrogen-doped graphene by the thermal chemical vapor deposition of hydrogen and ethylene on Cu foils in the presence of ammonia. In this case, the prepared catalyst reduced the oxygen molecule *via* a  $2e^-$  pathway leading to an onset potential difference of *ca.* 200 mV in comparison to that of the Pt electrode using 0.1 M KOH as the electrolyte and Ag/AgCl as the reference electrode. Adding to the reduced overpotential of FeNGr3 as visualized in the previous section, the oxygen reduction reaction in the present case seems to have a greater contribution through the preferred  $4e^-$  transfer route. The number of transferred electrons per oxygen molecule in ORR has been quantitatively calculated by using the Koutecky-Levich (K-L) [33] equation, which can be represented as follows:

$$1/j = 1/nFkC_{O_2} + 1/0.62nFAD_{O_2}^{2/3}C_{O_2}^*v^{-1/6}\omega^{1/2} \quad (4.1)$$

where, ' $j$ ' is the measured current density, ' $n$ ' is the number of transferred electrons per oxygen molecule, ' $A$ ' is the area of the electrode, ' $F$ ' is the Faraday constant ( $96500 \text{ C mol}^{-1}$ ), ' $D_{O_2}$ ' is the diffusion coefficient of the electrolyte, ' $C_{O_2}^*$ ' is the concentration of the dissolved oxygen in the electrolyte, ' $v$ ' is the kinematic viscosity of the electrolyte, ' $\omega$ ' is the angular velocity of the electrode. The values for  $D_{O_2}$ ,  $C_{O_2}^*$  and ' $v$ ' used in this study are  $1.9 \times 10^{-5} \text{ cm}^2 \text{ s}^{-1}$ ,  $1.22 \times 10^{-6} \text{ mol cm}^{-3}$  and  $0.01 \text{ cm}^2 \text{ s}^{-1}$ , respectively. The K-L slope ( $1/B$ ) has been obtained from the plot of the inverse of the current density ( $1/j$ ) against the inverse of the square root of the angular velocity ( $1/\omega^{1/2}$ ) as shown in Figure 4.12d. Subsequently, from the resulted value of  $1/B$ , the number of transferred electrons ' $n$ ' at -0.4 V has been calculated using Equation (4.1). The resulting values of ' $n$ ' are 2.4 and 3.2 for N-Gr and FeNGr3, respectively. The ' $n$ ' value of 3.2 for FeNGr3 at higher

reduction potential indicates the existence of a mixed kinetics involving both  $2e^-$  and  $4e^-$  pathways to form hydrogen peroxide and water, respectively. [37] In the present work, although FeNGr3 has higher overpotential compared to that of the commercial E-TEK catalyst, it is important to note that the onset potential difference between the homemade and the standard Pt/C catalysts is far better than the previously reported values. Moreover, the favourable shift towards the preferred  $4e^-$  pathway signifies the possibilities of further narrowing down the overpotential difference between the N and Pt based systems.

#### 4.4. Conclusions

An efficient method for preparing porous graphene with the aid of the in-situ generated  $Fe_2O_3$  nanoparticles and creation of potential N-doped active sites along the pore openings has been demonstrated. The main role of Fe in this process is to create and control the pores on the Gr surface. Since abundant O functional groups are present on the basal plane of r-GO, the Fe atoms can readily react with r-GO by forming  $Fe_2O_3$  nanoparticles on the surface. Thus, the formed nanoparticles can subsequently help us to engrave nanopores on the graphene surface upon pyrolysis. The defect sites created during the pore engraving process accommodate more nitrogen during the subsequent doping process. This nano-engineered porous graphene with potential heteroatom doped sites has several important applications including as a cost-effective oxygen reduction catalyst for PEM fuel cells as demonstrated in this study. The material effectively reduces oxygen molecules through a  $3e^-$  pathway, suggesting a preferential shift towards the more favourable  $4e^-$  route compared to the  $2e^-$  reaction as reported for many N-doped carbon nanomorphologies. The 90 mV onset potential difference for oxygen reduction as

compared to the state-of-the art 20 wt.% Pt/C catalysts is significantly low compared to the overpotentials in the range of 120-200 mV reported in the literature for few N-doped graphenes. Apart from the prospects of the material as a fuel cell catalyst, the ability to create nanopores on graphene without any sophisticated instrumental assistance has provided a facile way to broaden the material prospect for diverse applications including energy, gas filtration and storage. Also, unsaturation of the carbon along the engraved pore surface can be utilized as an effective means to anchor various foreign species and to bring in diverse multifunctional and hybrid features on the surface.

## 4.5. References

- [1] K. Gong, F. Du, Z. Xia, M. Durstock, L. Dai, *Science*, **2009**, 323, 760.
- [2] B. K. Balan, S. M. Unni and K. Sreekumar, *J. Phys. Chem. C*, **2009**, 113, 17572
- [3] K. S. Novoselov, A. K. Geim, S. V. Morozov, D. Jiang, Y. Zhang, S. V. Dubonos, I. V. Grigorieva, A. A. Firsov, *Science* **2004**, 306, 666.
- [4] L. Qu, Y. Liu, J-B. Baek, L. Dai, *ACS Nano*, **2010**, 4, 1321.
- [5] E. J. Yoo, J. Kim, E. Hosono, H. Zhou, T. Kudo, I. Honma, *Nano Lett.* **2008**, 8, 2277.
- [6] X. Wang, L. Zhi, K. Mullen, *Nano Lett.* **2008**, 8, 323.
- [7] S. R. C. Vivekchand, C. S. Rout, K. S. Subramaniam, A. Govindaraj, CNR. Rao, *J. Chem. Sci.* **2008**, 120, 9.
- [8] T. H. Han, Y. K. Huang, A. T. L. Tan, V. P. Dravid, J. Huang, *J. Am. Chem. Soc.*, **2011**, 133, 15264.
- [9] L. Qu, Y. Liu, J. B. Baek, L. Dai. *ACS Nano*, **2010**, 4, 1321.
- [10] J. Xiao, D. Mei, X. Li, W. Xu, D. Wang, G. L. Graff, W. D. Bennett, Z. Nie, L. V. Saraf, I. A. Aksay, J. Liu, J. G. Zhang, *Nano Lett.* **2011**, 11, 5071.
- [11] D. Jiang, V. R. Cooper, S. Dai, *Nano Lett.* **2009**, 9, 4019.
- [12] A. Du, Z. Zhu, S. C. Smith, *J. Am. Chem. Soc.*, **2010**, 132, 2876.
- [13] M. Bieri, M. Treier, J. M. Cai, K. Ait-Mansour, P. Ruffieux, O. Groning, P. Groning, M. Kastler, R. Rieger, X. L. Feng, K. Mullen, R. Fasel, *Chem. Commun.* **2009**, 6919.

- [14] H. Wang, Q. Wang, Y. Cheng, H. Li, Y. Yao, Q. Zhang, C. Dong, P. Wang, U. Schwingenschlogl, W. Yang, X. X. Zhang, *Nano Lett.* **2012**, *12*, 141.
- [15] S. Maldonado, K. J. Stevenson, *J. Phys. Chem. B*, **2005**, *109*, 4707.
- [16] K. Gong, F. Du, Z. Xia, M. Durstock and L. Dai, *Science*, **2009**, *323*, 760.
- [17] L. Qu, Y. Liu, J. B. Baek and L. Dai, *ACS Nano*, **2010**, *4*, 1321.
- [18] R. Imranjafri, N. Rajalakshmi and S. Ramaprabhu, *J. Mater. Chem.*, **2010**, *20*, 7114.
- [19] M. Lefevre, E. Proietti, F. Jaouen, J. P. Dodelet, *Science*, **2009**, *324*, 71.
- [20] S. Li, L. Zhang, J. Kim, M. Pan, Z. Shi and J. Zhang, *Electrochim. Acta*, **2010**, *55*, 7346.
- [21] V. Nallathambi, J. W. Lee, S. P. Kumaraguru, G. Wu and B. N. Popov, *J. Power Sources*, **2008**, *183*, 34.
- [22] R. Bashyam and P. Zelenay, *Nature*, **2006**, *443*, 63.
- [23] C. Medard, M. Lefevre, J. P. Dodelet, F. Jaouen and G. Lindbergh, *Electrochim. Acta*, **2006**, *51*, 3202.
- [24] M. Lefevre and J. P. Dodelet, *Electrochim. Acta*, **2003**, *48*, 2749.
- [25] T. Palaniselvam, R. Kannan, S. Kurungot, *Chem. Commun.* **2011**, *47*, 2910.
- [26] X. Li, H. Wang, J. T. Robinson, H. Sanchez, G. Diankov, H. Dai, *J. Am. Chem. Soc.* **2009**, *131*, 15939.
- [27] D. C. Marcano, D. V. Kosynkin, J. M. Berlin, A. Sinitskii, Z. Sun, A. Slesarev, L. B Alemany, W. Lu, J. M. Tour, *ACS Nano*. **2010**, *8*, 4806.
- [28] W. Chen, X. Pan, M. G. Willinger, D. S. Su, Bao. X, *J. Am. Chem. Soc.* **2006**, *128*, 3136.

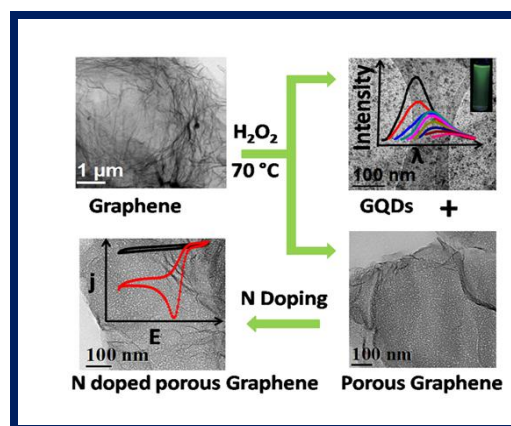
- [29] X. L. Dong, Z. D. Zhang, Q. F. Xiao, X. G. Zhao, Y. C. Chuang, S. R. Jin, W. M. Sun, Z. J. Li, Z. X. Zheng; H. Yang, *J. Mat. Sci.* **1998**, *33*, 1915.
- [30] R. T. Yang, K. L. Yang, *Carbon* **1985**, *23*, 537.
- [31] A. Reina, X. Jia, J. Ho, D. Nezich, H. Son, V. Bulovic, M. S. Dresselhaus, J. Kong, *Nano Lett.* **2009**, *9*, 30.
- [32] B. Stohr, H. P. Boehm, R. Schlogl, *Carbon* **1991**, *29*, 707.
- [33] J. R. Pels, F. Kapteijn, J. A. Moulijn, Q. Zhu, K. M. Thomas, *Carbon* **1995**, *33*, 1641.
- [34] Z. Lin, M. Song, Y. Ding, Y. Liu, M. Liua and C. Wong, *Phys. Chem. Chem. Phys.*, **2012**, *14*, 3381.
- [35] Z. Luo, S. Lim, Z. Tian, J. Shang, L. Lai, B. MacDonald, C. Fu, Z. Shen, T. Yu and J. Lin, *J. Mater. Chem.*, **2011**, *21*, 8038.
- [36] S. M. Unni, V. M. Dhavale, V. K. Pillai, and S. Kurungot, *J. Phys. Chem. C*, **2010**, *114*, 14654.
- [37] S. Wang, D. Yu, L. Dai, *J. Am. Chem. Soc.* **2011**, *133*, 5182.

## Chapter 5

### NOVEL ROUTE FOR THE PREPARATION OF NANOPOROUS GRAPHENE BY QUANTUM DOTS REMOVAL AND ITS CONVERSION AS POTENTIAL OXYGEN REDUCTION ELECTROCATALYST VIA NITROGEN DOPING

---

A simple way to produce an efficient metal-free oxygen reduction electrocatalyst from graphene by generating nanopores in the matrix and subsequently establishing nitrogen-doped active sites along the pore openings is demonstrated. Well-structured nanoporous graphene (pGr) and photoluminescent graphene quantum dots (GQDs) could be simultaneously generated by a chemically



assisted oxidative treatment of graphene. The process helped to knock out small pieces of Gr through epoxide formation, which subsequently resulted into the generation of GQD and pGr simultaneously. Further, the pore openings are being treated as fertile regions for heteroatom doping, pGr-72 was further subjected to nitrogen doping (NpGr-72). NpGr-72 displayed excellent activity towards electrochemical oxygen reduction reaction (ORR) compared to nitrogen doped non-porous graphene (NGr) and many other reported nitrogen doped carbon materials.

---

\*The contents of this chapter have been published in “*Energy Environ. Sci* **2014**, 7, 1059-1067.

## 5.1. Introduction

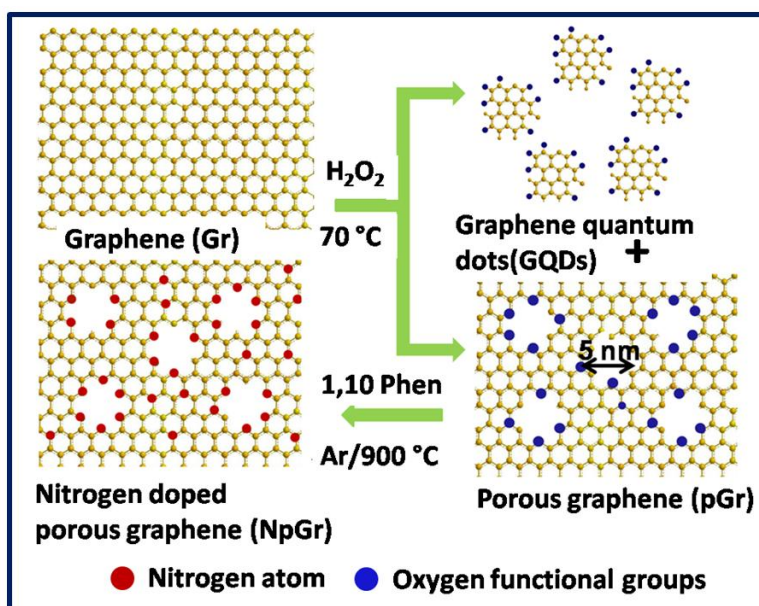
Development of nitrogen doped carbonaceous materials, especially graphene (Gr), with or without metal becomes a well known strategy to replace the platinum based catalysts in the energy storage and conversion devices. [1] Gr with high surface area ( $\sim 2650 \text{ m}^2 \text{ g}^{-1}$ ), mechanical stability and electron mobility *etc.* plays a vital role as a support and/or catalyst in the energy conversion devices. Being a zero band-gap material, [2] it is necessary to tune the band gap of Gr to facilitate its application in photovoltaics and optoelectronics. This can be achieved practically by the conversion of two dimensional Gr into graphene nano ribbons (GNRs) and zero dimensional graphene quantum dots (GQDs) due to their quantum confinement [3] and edge effects [4]. The recent efforts are intensively being focused on the preparation of GQDs by bottom-up [5] (refers, synthesis of GQDs by chemical carbon-carbon coupling reaction) and top-down (refers, cutting of Gr sheets into the GQDs) methods [6-16] for different applications. Most recent reports demonstrated the prospects of nitrogen-doped graphene quantum dot (NGQD) as a non-Pt oxygen reduction reaction (ORR) catalyst [17]. Although the aforementioned reports are effective for the preparation of GQDs, the yield of these GQDs has to be increased for practical applications. Moreover, in all these cases, hazardous concentrated acids have been employed to cut down the carbon source into GQDs and excluded the resulting parent material (*i.e.* carbon source). Hence, an efficient and environmentally benign method for the preparation of GQDs with better yield is highly desirable.

On the other hand, porous graphene (pGr) gains much attention recently in the field of nano electronics as similar to Gr. Interestingly, the band gap of Gr can be tuned as similar to the band gap of  $\text{TiO}_2$  (3.2 eV) by making holes on Gr. [18] In the previous

chapter, we have demonstrated a versatile method for drilling nanoholes on graphene assisted by pre-formed  $\text{Fe}_2\text{O}_3$  nanoparticles and conversion of the later to  $\text{Fe}_3\text{C}$  through carbon spillover from Gr. However, the carbon from the pore openings is wasted as carbonaceous gas such as CO or  $\text{CO}_2$ . Inclusion of multi carbon vacancy along the pore openings of the two dimensional Gr could be utilized for imparting ORR activity in the system through effective nitrogen doping. [19] Gr with well distributed nanopores can also be effectively utilized as a membrane for gas separation, [20] water desalination, [21] Li-ion storage in Li-air battery [22] and for the single atom doping (Pt, Co and In) [23]. Apart from the distinctive high surface area and mechanical stability of Gr, the effects of edge sites are very significant in the electrocatalytic process. Of course, the creation of porosity on the graphene surface is technically challengeable, especially in the context of controlling the sizes of the pores within few nanometers and maintaining the pore distribution homogeneously throughout the surface of Gr. Also, it would be always beneficial to develop a process which gives the nanoporous graphene without any metal contamination and extensive damage to the Gr framework.

Herein, we demonstrate a simple way to prepare pGr and graphene QGDs simultaneously by controlled hydrogen peroxide ( $\text{H}_2\text{O}_2$ ) oxidative etching of Gr under ambient condition and thereafter to convert pGr into an efficient ORR catalyst by creating nitrogen doped active sites along the pore openings.  $\text{H}_2\text{O}_2$  has been judiciously employed as the oxidant instead of other usual hard acids which results nearly 10 nm sized QGDs with the breaking of the entire structure of Gr during the vigorous acid treatment. [6] In contrary to this, we have observed that  $\text{H}_2\text{O}_2$  oxidizes Gr in a more controllable way and offers a viable and facile route for converting Gr simultaneously

into two potentially important materials *viz* pGr and GQDs. Drilling of nanopores makes the Gr surface concomitantly enriched with unsaturated carbon valancies, which are being considered as the fertile areas for heteroatom doping. This is expected to provide a convenient way to enhance the concentration of nitrogen during the doping process and also to establish greater proportions of the desired co-ordinations which are active for facilitating ORR. Considering these advantages, we have used pGr as a substrate for nitrogen doping and the material thus formed (NpGr) displays excellent performance characteristics towards electrochemical oxygen reduction compared to its nitrogen doped nonporous graphene (NGr) counterpart.



**Scheme 5.1.** A synthetic representation of the process involved in the formation of graphene quantum dots (GQDs) and porous graphene (pGr) along with the conversion of the later into nitrogen doped porous graphene (NpGr).

## 5.2. Experimental Section

### 5.2.1. Preparation of Graphene Oxide (GO)

GO was synthesized by improved Hummer's method [24]. Briefly, a mixture of potassium permanganate ( $\text{KMnO}_4$ ) and graphite powder (6:1 g ratio) was added slowly to the acid mixture of con.  $\text{H}_2\text{SO}_4$  and  $\text{H}_3\text{PO}_4$  (9:1 ratio) with mechanical stirring at 0 °C. Further, the temperature of the reaction mixture was allowed to increase up to 45 °C for 1 h followed by increasing the temperature up to 55 °C and maintaining the same temperature for 12 h. Subsequently, 3 ml of 30 %  $\text{H}_2\text{O}_2$  in ice water was added to the reaction mixture to stop the oxidation of the reaction. The mixture was subjected to centrifugation at 12000 rpm and the supernatant solution was decanted away. The resulting material was subjected to multiple washings with water, ethanol, acetone and polyether in sequence and conserved for further use.

### 5.2.2. Preparation of reduced Graphene oxide (r-GO) from GO

r-GO was prepared by the pyrolysis of GO at high temperature in inert (Ar) atmosphere. Briefly, GO was loaded in an alumina boat, which was placed in the quartz tube. Further, the tube was kept in a tubular furnace under inert atmosphere by purging Ar by maintaining a flow rate of 0.5 sccm. Subsequently, the temperature of the furnace was increased up to 900 °C and thereafter the same temperature was maintained for 3 h. This was allowed to cool down to room temperature after pyrolysis with Ar flow. The pyrolysed product was then preserved for further studies.

### **5.2.3. Preparation of Porous Graphene (pGr) and Graphene Quantum Dots (GQDs) by Hydrogen Peroxide (H<sub>2</sub>O<sub>2</sub>) Oxidation of r-GO.**

pGr and GQDs were prepared simultaneously by H<sub>2</sub>O<sub>2</sub> oxidation of r-GO. Briefly, 100 mg of r-GO was dispersed in 100 ml of H<sub>2</sub>O<sub>2</sub> (30 %) with the aid of sonication for 10 min. at room temperature and temperature of the reaction mixture was increased to 70 °C and maintained for 72 h. Subsequently, the resulting mixture was filtered by a filter paper having a pore size of 0.44 µm (Rankem Chemicals) and the filtrate (*i.e.* pGr-72) was dried at 50 °C for 3 h and preserved for further analyses. The filtrate collected in the previous step was allowed for dialysis in a dialysis bag for 3 days. The resulting aqueous solution (GQD-72) was conserved for further analysis. For effectively comparing the influence of the time of oxidative treatment on the formation of both GQD and pGr, we have collected more samples by maintaining the times of reaction as 24 and 48 h. The samples prepared at 24 h are designated as pGr-24 and GQD-24, whereas at 48 h, the samples are designated as pGr-48 and GQD-48.

### **5.2.4. Preparation of Nitrogen-Doped Porous Graphene (NpGr-72)**

NpGr-72 was prepared by the pyrolysis of pGr-72 with 1,10-phenanthroline mixture at 900 °C for 3 h in Ar atmosphere. Briefly, 50 mg of pGr-72 in ethanol solution was mixed with 100 mg of 1,10 phenanthroline (phen) in ethanol and the reaction mixture was kept for mechanical stirring for 24 h to attain effective diffusion of phen into the cavity of pGr-72. Further, the solvent was evaporated by thermal evaporation at 50 °C for 3 h. Subsequently, the resulting composite material was loaded on alumina boat which was placed in the quartz tube. Followed by this, the tube was kept in a tubular furnace and an

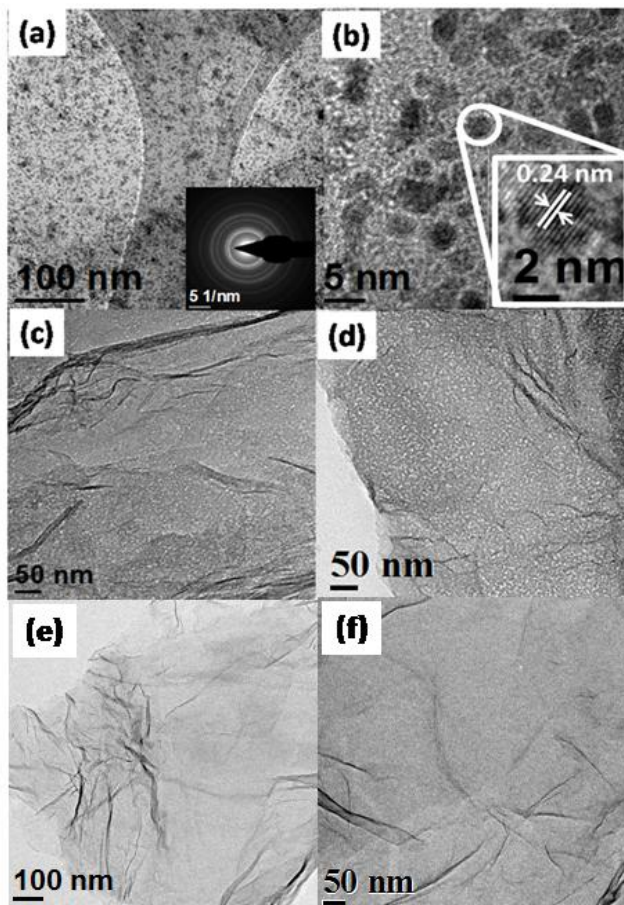
inert atmosphere was maintained with the help of Ar at a flow rate of 0.5 sccm. Further, the temperature of the furnace was increased up to 900 °C and the system was maintained at this condition for 3 h. Thereafter, the furnace was allowed for cooling to room temperature without disconnecting the Ar flow. Thus obtained pyrolysed product (NpGr-72) was then washed with ethanol and preserved for further studies. For the effective preparation, the non-porous nitrogen doped Gr (NGr) was also prepared by similar method while using r-GO as the substrate.

### 5.3. Results and Discussion

#### 5.3.1 HRTEM Analysis.

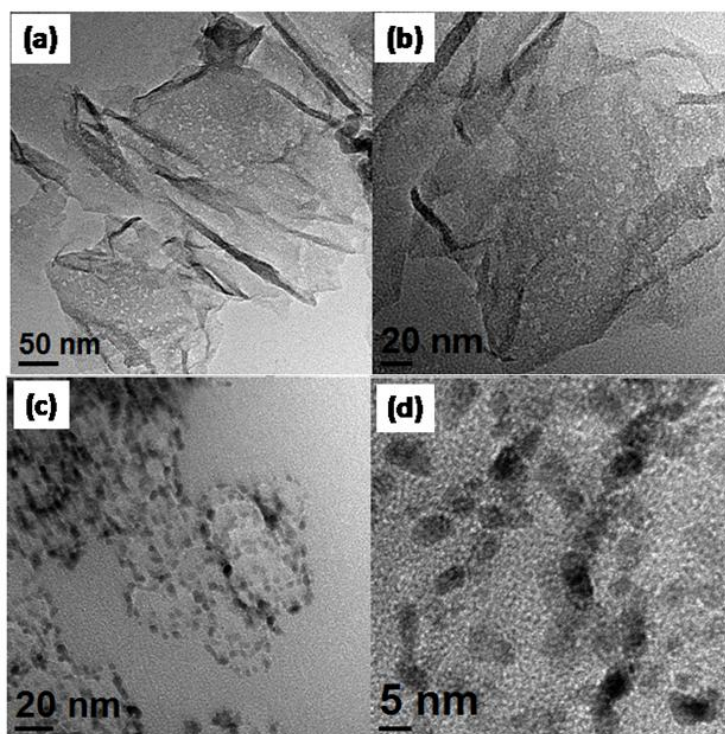
The structure and morphology of r-GO, pGr and GQDs are explored with help of HRTEM analysis. Figure 5.1a and b represent the transmission electron microscopy (TEM) images of GQD-72. As shown in Figure 5.1a, GQDs are dispersed uniformly with an average size of *ca* 3-5 nm. The diffraction pattern (inset of Figure 5.1a) and higher magnification image (inset of Figure 5.1b with a *d* value of 0.24 nm<sup>7</sup> (1120 plane of graphene) emphasize the higher crystallinity possessed by GQD-72 which is very much similar to the parent graphene. The TEM images of pGr-72, as shown in Figure. 5.1c-d clearly reveal the presence of nano sized pores on Gr surface while these are absent in the case of pure Gr sheets (Figure 5.1e-f). The 5 nm average sized pores are in well accordance with the average size of GQD-72 which highlights the derivation of these GQDs from the r-GO surface. Moreover, the pore size distribution profile of pGr-72 (will be discussed later) augments the presence of 5 nm sized pores with uniform distribution

on r-GO which further helps to authenticate the claim on the formation of GQDs from r-GO.



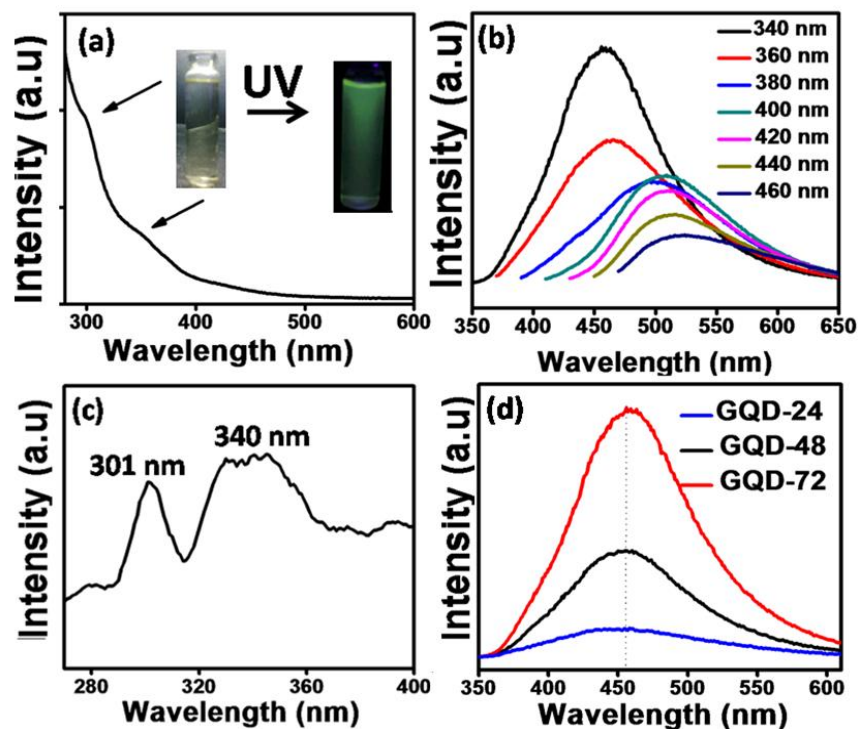
**Figure 5.1.** (a-b) TEM images of GQD-72 in different magnifications. Inset of (a) is the diffraction pattern of GQD-72, which represents the monocrystallinity of the material. Inset of (b) is the higher magnification (HRTEM) image of GQD-72, giving the corresponding lattice fringes possessing a  $d$  value of 0.24 nm. Images (c-d) represent the TEM images of pGr-72; well distributed nanopores and the characteristic features of the graphene surface are clearly visible from these images while the similar characteristics features of pores are invisible in the case of reduced graphene oxide sheet shown in (e) and (f) due to the absence of pores.

Figure 5.2a-b, depicts the TEM images of pGr-48 where the nano sized pores are observed as similar to the pGr-72. Further, the HRTEM images of GQD-48 (Figure 5. 2c-d) also show uniform dispersion of GQD with an average size of around 5 nm as similar to GQD-72. However, the overall dispersion of these particles is significantly low compared to GQD-72, indicating the formation of fewer amounts of GQDs at a reduced time of the oxidation process. The aforementioned results emphasize that the duration of the experiment does increase the yield of the GQDs and does not play the role to tune the particle size.



**Figure 5.2.** (a-b) TEM images of porous graphene (pGr-48) taken under different magnifications and (c-d) TEM images of GQD-48 taken under different magnifications.

## 5.3.2. Optical Property Study



**Figure 5.3.** (a) UV-Vis spectrum of GQD-72; (b) photoluminescent spectra of GQD-72 in water; (c) photoluminescent excitation (PLE) spectrum of GQD-72; (d) comparison of PL spectra of different GQDs (GQD-24, 48 and 72) at the excitation wavelength of 340 nm.

Figures 5.3a to c show the optical properties of GQD-72. The UV-Vis spectrum of GQD-72 in water (Figure 5.3a) show two absorption bands at 300 and 340 nm ensuring the two electronic transitions occurring under the UV light. The aqueous solution of GQD-72 shows a yellow color (inset of Figure 5.3a) and emits a strong green luminescence under the UV light which is likely to be due to the luminescent carbon particles. Figure 5.3b shows the photoluminescent (PL) spectra of GQD-72. The PL spectra of GQD-72 show the strongest emission at 457 nm with the Stokes shift of 117 nm on an excitation wavelength of 340 nm. Besides, the PL peak position has been red shifted from the lower

wavelength to higher wavelength with reduction in intensity by change in the excitation wavelength from 340 to 460 nm, elucidating the excitation dependent PL behaviour of GQD-72.

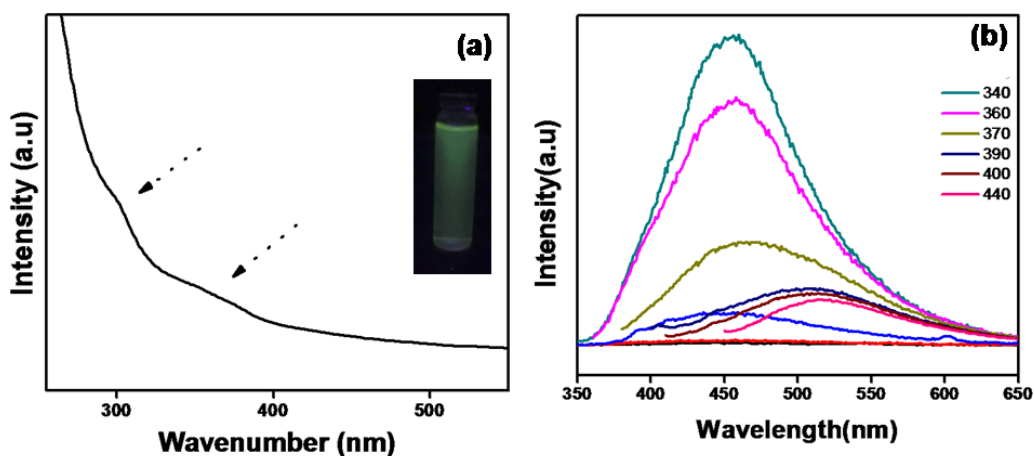


**Figure 5.4.** (a) UV-Vis spectrum of GQD-48 and (b) photoluminescent spectra of GQD-72 in water. Inset of Figure 5.4a shows the optical image of GQD-48 under the UV light.

The photoluminescent excitation (PLE) spectrum in Figure 5.3c show two sharp peaks at 301 and 340 nm as similar to the UV-Vis spectra, which further confirm the two transitions under the UV light. The UV-Vis spectra and PLE clearly reveal that the observed green luminescence is mainly due to the transitions at 300 (4.12 eV) and 340 nm (3.65 eV) i.e. the transitions from the  $\sigma$  and  $\pi$  orbital in the highest occupied molecular orbital (HOMO) to the lowest unoccupied molecular orbital (LUMO). Previously, Wu et al [6] reported a carbene like structure with triplet multiplicity for the GQDs. Indeed, the energy difference ( $\Delta E$ ) between  $\sigma$  and  $\pi$  orbital predicts the ground state multiplicity of carbene and the  $\Delta E$  must be less than 1.5 eV for the triplet ground state. [25] In the present study, the calculated  $\Delta E$  for the green luminescence is 0.47 eV, which ensures that the synthesized GQD is similar to the carbene with triplet multiplicity.

Figure 5.3d compares the PL spectra of GQD-24, 48 and 72 excited at 340 nm and Fig. 4 shows the optical properties of GQD-48 as similar to GQD-72.

Table 5.1. Quantum yield of GQDs using quinine sulphate as a reference material.

Sample	Integrated emission intensity(I)	Absorbance at 340 nm (A)	Refractive index of the solvent ( $\eta$ )	Quantum yield ( $\Phi$ ) %
Quinine	77275.0	0.06	1.33	53 (known)
GQD-24	3591.2	0.30	1.33	0.49
GQD-48	11661.3	0.20	1.33	2.39
GQD-72	26851.2	0.07	1.33	15.8

It is worth mentioning that the optical properties of GQD vary with respect to its size [7]. In the present case, the PL spectrum does not indicate shifts in the peak position even though increasing the time of the experiment increased the intensity. Recollecting our previous discussion on the HRTEM results, it has been observed that the HRTEM images of both GQD-48 and 72 exhibit a similar particle size (~5 nm) distribution with an apparent variation in the particle dispersion. In order to ensure this result, the PL quantum yield of the GQDs has been calculated using quinine sulfate as a reference [9] and the resulted values are given in Table 5.1. GQD-72 has shown the highest PL quantum yield (15.8 %) compared to the other samples. Up to our knowledge, the

reported PL quantum yield of GQD-72 is comparatively higher than that reported in the literature.

### 5.3.3. Mechanism

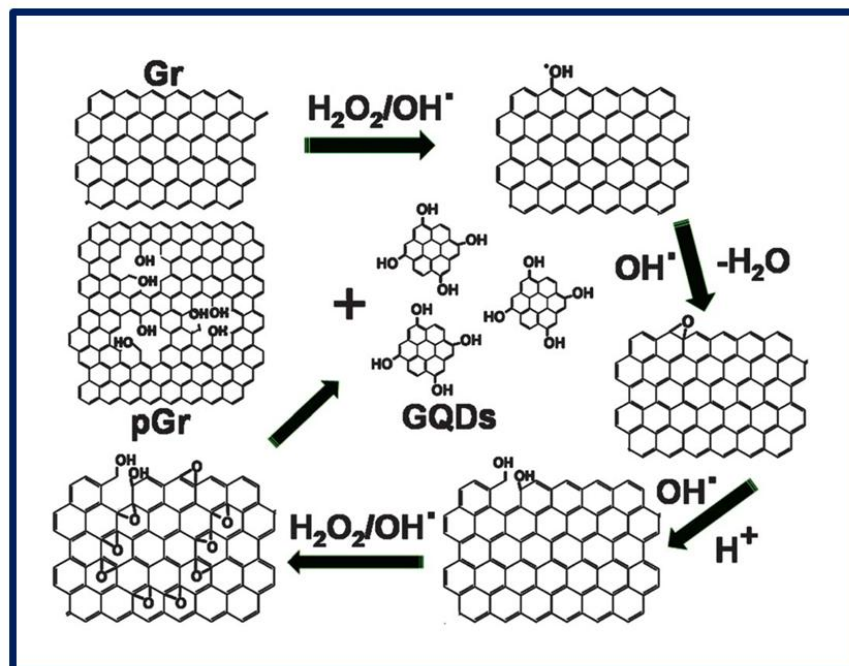


**Figure 5.5.** The proposed mechanism for the formation of porous graphene and graphene quantum dots from graphene mediated by the initial formation of epoxide moieties.

Addressing the mechanism for the simultaneous formation of pGr and GQD by chemically knocking out the flakes of graphene is an important issue. During the functionalization at 70 °C,  $\text{H}_2\text{O}_2$  is expected to produce strong oxidizing free radicals such as  $\text{OH}^\cdot$ ,  $\text{O}^\cdot$  and  $\text{HO}_2^\cdot$  which can introduce various oxygen functional groups on the  $\text{sp}^2$  carbon ( $\text{C}=\text{C}$ ) by causing the epoxide formation. According to the recent hypothesis,[26] the formation of the epoxide energetically favors further epoxide formation throughout the  $\text{sp}^2$  carbon moieties which then converts into stable hydroxyl

(OH) functionalities by ring cleavage. Eventually, continuation of this process results in the etching out of the small GQDs with - OH functionalities from the Gr surface as shown in Figure 5.5. Since,  $H_2O_2$  readily induces the formation of epoxide with the oxygen containing active free radicals, the yield of GQDs is expected to be more than that with the acid based etching strategies. In order to validate the formation of GQD through epoxide pathway, IR spectra of pGr was taken at different time intervals. In general, epoxide exhibits two bands, one at  $800-950\text{ cm}^{-1}$  corresponding to asymmetric stretching and the other one at  $1250\text{ cm}^{-1}$  corresponding to symmetric stretching of C-O bond. [27]

#### 5.3.4. FT-IR Spectra

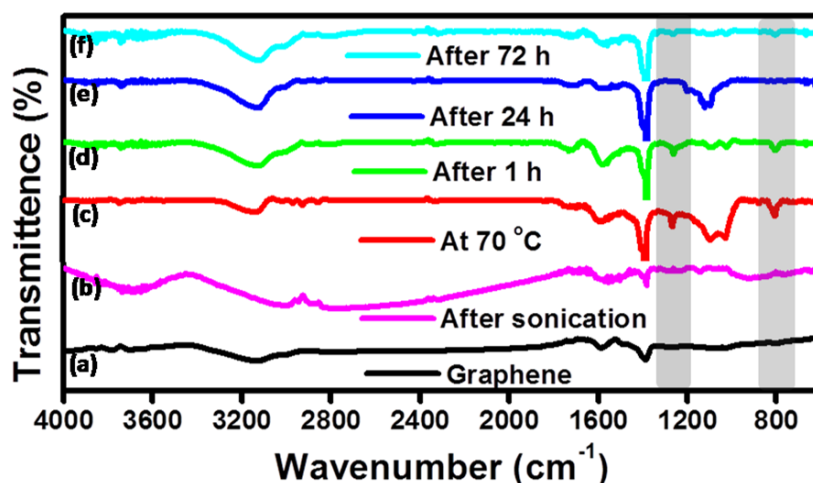


**Figure 5.6.** Infra-Red spectra of (a) r-GO, (b) material collected after sonication with  $H_2O_2$  at room temperature, (c) material collected immediately after the temperature of the reaction mixture reaches to  $70\text{ }^\circ\text{C}$ , (d) material collected after 1 h of reaction at  $70\text{ }^\circ\text{C}$  and (e) material collected after 24 h of reaction at  $70\text{ }^\circ\text{C}$  (pGr-24) (f) material collected after 72 h of reaction at  $70\text{ }^\circ\text{C}$  (pGr-72).

In the IR spectra presented in Figure 5.6a, the sample collected after 1 h shows two peaks at 800 and 1260  $\text{cm}^{-1}$  which are representative of the C-O bond in the sample in the form of epoxide. However, the two peaks gradually vanish as the reaction time increases from 1 to 72 h which provides a clear indication for the formation of GQD with the intervention of the epoxide intermediate in the reaction (Figure 5.6).

### 5.3.4. Surface Area Measurements

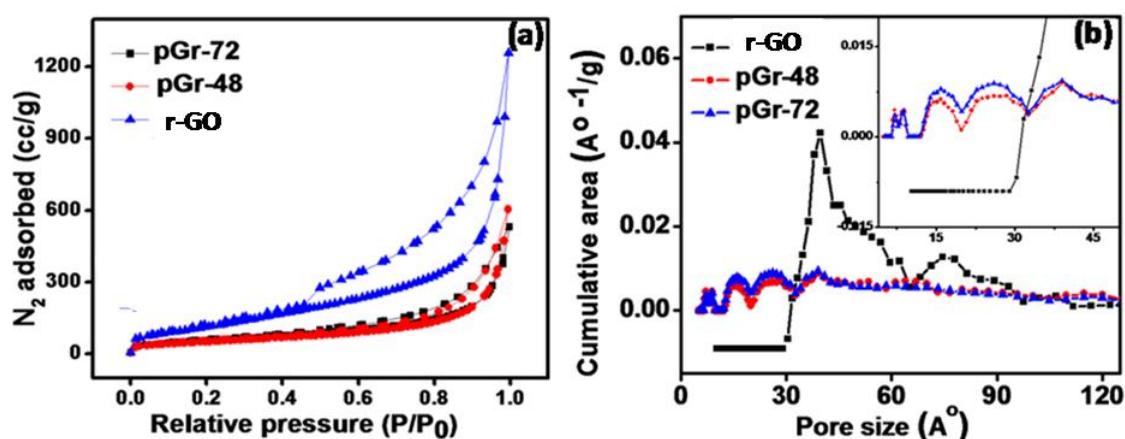


**Figure 5.7.** (a) N<sub>2</sub> adsorption-desorption profiles used for calculating the BET surface areas of r-GO, pGr-48 and pGr-72; (b) pore size distribution patterns of r-GO, pGr-48 and pGr-72.

As discussed before, the controlled removal of GQDs from the graphene surface makes the later more porous and positions itself as a highly versatile material for effective surface modifications to bring in the desired property characteristics at the surface. In this context, it is meaningful to measure the surface area and pore size distribution of the pGr samples. Figure 5.7a presents the nitrogen adsorption and desorption plots of r-GO, pGr-48 and pGr-72 which show the typical Type IV isotherms with steep increase at low

relative pressure ( $\sim 0.5$ ). Figure 5.7b, shows the comparison of the pore size distribution profiles of r-GO, pGr-48 and pGr-72 in which r-GO exhibits a relatively broad pore size distribution within the range of 5 to 9 nm probably due to the contributions from the wavy nature of the surface and space between the loosely bound sheets.[28] Interestingly, in the case of both pGr-48 and pGr-72, in addition to the 5 nm sized pores, more pores with an average size of 0.7-3 nm are also present. This augments the HRTEM observations and validates that during the  $H_2O_2$  oxidative treatment, Gr surface is getting etched out and resulting in increased proportion of nanopores of smaller dimensions in the system.

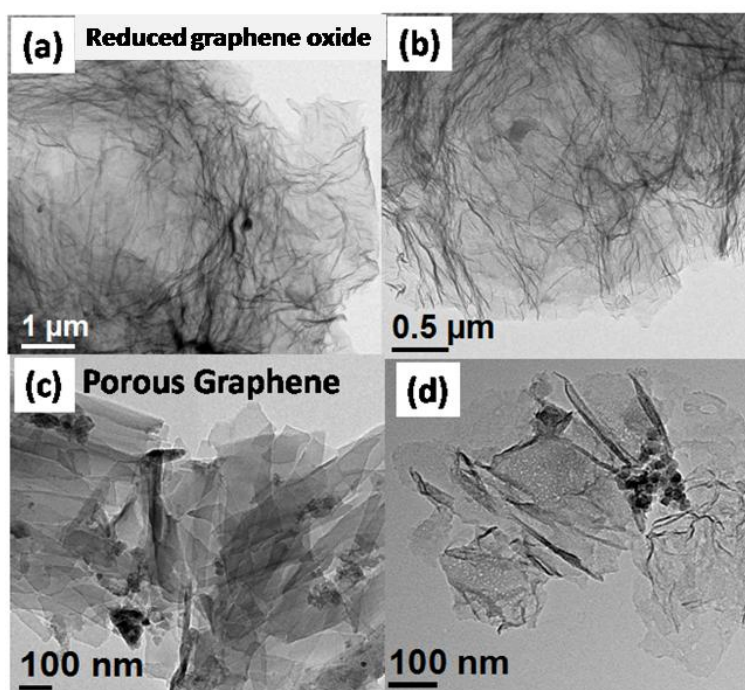


**Figure 5.8.** Comparison of the TEM images of (a-b) reduced graphene oxide and (c-d) porous graphene with reduced size, ensuring the gentle structural breakage of graphene sheets during the  $H_2O_2$  oxidation.

The significant reduction in the intensity of the larger pores in the pGr samples compared to r-GO can be attributed to the increased degree of restacking of the graphene layers after the oxidative treatment due to the better interaction between the surface layers. The measured BET surface area values of r-GO, pGr-48 and pGr-72 are 452.5, 187 and 204  $\text{m}^2 \text{g}^{-1}$ , respectively. The surface area of Gr is low compared to its predicted value of 2630  $\text{m}^2 \text{g}^{-1}$ , which is probably due to the presence of multiple graphene layers and the unremoved functional groups on the surface. Further, the surface area of the pGr samples is expected to be more than that of Gr due to the larger functionalization.[29] Moreover, GQD exhibits poor BET surface area (data is not included) compared to r-GO and pGr based samples probably due to the absence of pores on the surface of GQDs.

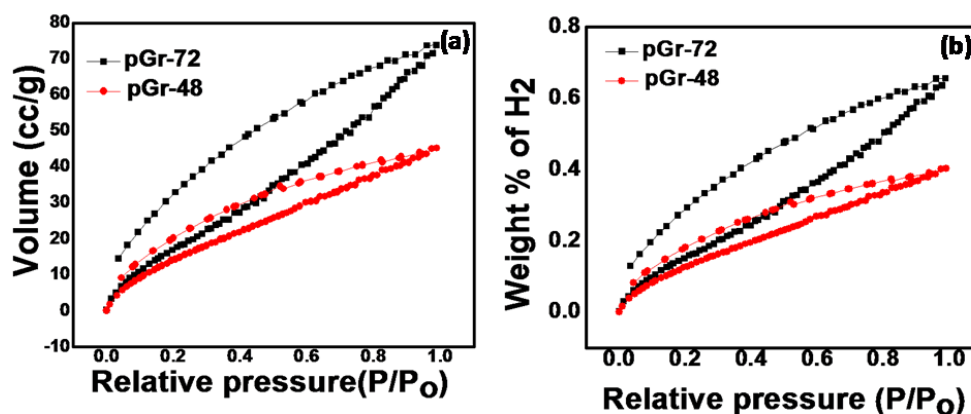


*Figure 5.9. Hydrogen adsorption-desorption isotherms of pGr-48 and pGr-72 at 1 atm pressure and 77 K and (b) weight percentage of hydrogen uptake of pGr-48 and pGr-72 at 1 atm pressure and 77 K.*

Despite, the functionalization achieved on pGr during the  $\text{H}_2\text{O}_2$  treatment of r-GO causes gentle structural breakage of Gr sheets. This leads to additional functionalization which is resulting towards the reduction in the surface area of the pGr samples during the BET

measurements as similar to graphite to graphite oxide. The structural breakage of Gr sheets has been ensured from the comparison of TEM images of r-GO and pGr (Figure 5.8).

Since the aforementioned studies shed light into the presence of greater contribution of nanopores on the r-GO surface, an adsorption study using hydrogen as the probe molecule has also been carried out as smaller pores are expected to bring in higher hydrogen storage capacity to the system. Figure 5.9a, compares the hydrogen adsorption-desorption curves for pGr-48 and 72. The pGr-based samples show a weak desorption behavior for H<sub>2</sub> due to the strong interaction between the H<sub>2</sub> and functional groups present (*i.e.* chemisorption) on Gr. Moreover, the weight percentage (wt. %) of the H<sub>2</sub> uptake for pGr-48 and 72 is calculated (Figure 5.9b) and the resulted values are 0.45 and 0.73 wt. %, respectively which are relatively lower than the previously reported value for Gr with a surface area of 1550 m<sup>2</sup> g<sup>-1</sup> (3 wt %).[30] However, the hydrogen storage capacity of pGr-72 is nearly two times higher than that of pGr-48 which ensures the better surface density of the smaller pores present on pGr-72.

### 5.3.5. XRD and Raman Spectra Analysis

The crystalline nature of r-GO, pGr-72, NpGr-72 and GQD-72 is inferred from the XRD pattern of Figure 5.10a. r-GO, pGr-72 and NpGr-72 have sharp graphitic peaks of the (002) plane centered at  $2\theta$  of 25.7° whereas GQD-72 has a broader peak with a shift in the  $2\theta$  to 23.1°, indicating the reduced size of GQDs. The  $d$ -spacing also increases from r-GO to GQD (3.53 to 3.61 Å) due to the functionalization of oxygen functional groups which results in enhanced interlayer distance.[7] A similar  $d$ -spacing shift is also

expected in the case of pGr-72 due to the oxygen functionalities. However, the relative oxygen to carbon content ratio is more in the case of GQD over pGr due to its small particle size ( $\sim 5\text{nm}$ ).

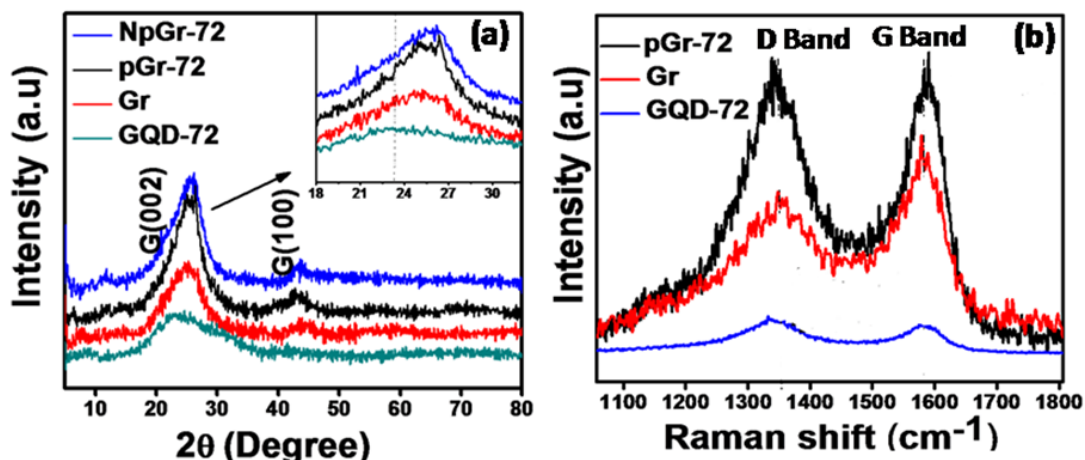


**Figure 5.10.** (a) XRD patterns of the prepared samples and (b) Raman spectra of r-GO, pGr-72 and GQD-72.

Hence, the extent of oxygen intercalation is expected to be in a significant range to make an apparent shift of the G (002) plane in XRD. In addition to XRD, Raman spectroscopy is also employed to characterize the graphitic nature of GQD and the Gr based samples (Figure 5.10b). The peak at 1584-1589 cm<sup>-1</sup>, which is corresponding to the graphitic peak (G band), is mainly due to the E<sub>2g</sub> vibrational mode of the C-C bond stretching. The peak at 1337-1346 cm<sup>-1</sup> indicates the disorder, which is due to the A<sub>1g</sub> vibrational mode of C. Here, the extent of defects present on the Gr based samples and GQD-72 has been estimated with respect to the  $I_D/I_G$  ratio and the resulted values are 0.77, 1.03 and 1.1 for Gr, pGr-72 and GQD-72, respectively. The higher  $I_D/I_G$  ratio of pGr-72 compared to Gr is due to the porosity associated with the functional groups present on pGr-72.

## 5.3.4. XPS Analysis

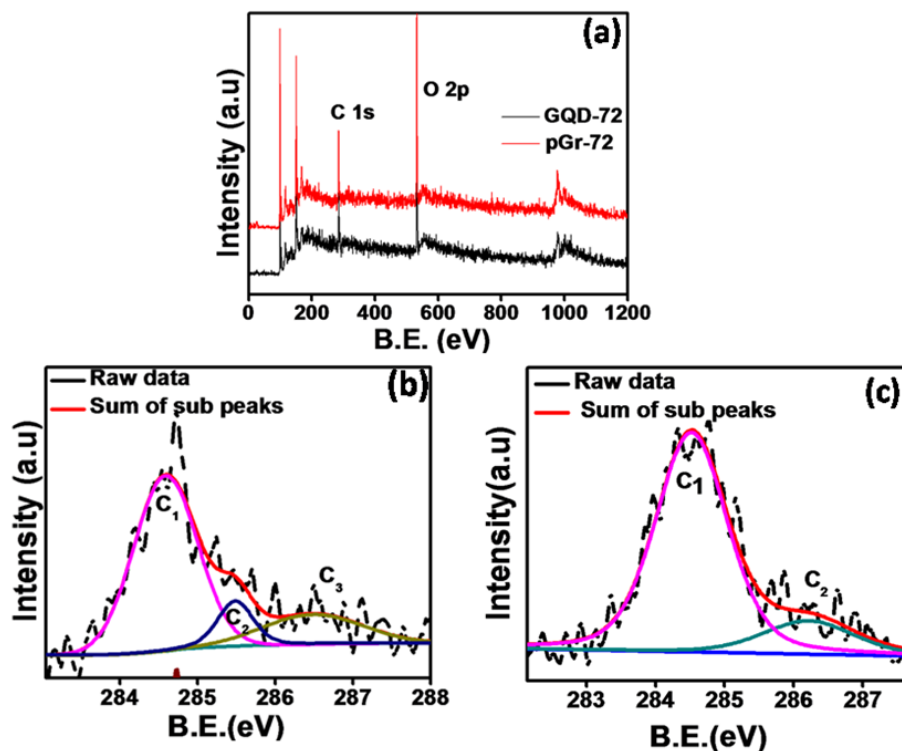


**Figure 5.11.** (a) Long range X-ray photoelectron spectra of pGr-72 and GQD-72; C1s spectra of (b) pGr-72 and (c) GQD-72.

XPS analysis was carried out to explore the chemical environment of GQDs and pGr. The full range XPS profiles of all the samples show the principal peaks at 284.5 and 532 eV corresponding to carbon and oxygen, respectively (Figure 5.11a). The peaks at around 100 to 200 eV are presumably due to silicon wafers. Figure 5.11b shows the C1s spectrum of pGr-72 which could be deconvoluted into three sub peaks. The peak C<sub>1</sub> at 284.5 eV corresponds to the graphitic carbon (C=C). The peak C<sub>2</sub> at 285.5 eV corresponds to the sp<sup>3</sup> carbon (*i.e.* C-C) and the peak C<sub>3</sub> at 286.5 eV corresponds to the

carbon bind with oxygen atom (*i.e.* C-OH). In the case of GQD-72 (Figure 5.11c), the C1s spectrum was deconvoluted into two sub peaks. The peak C<sub>1</sub> at 284.5 eV corresponds to the graphitic carbon (C=C) and the peak C<sub>2</sub> at 286.5 eV corresponds to the carbon coordinated with the oxygen moiety (*i.e.* C-OH). Interestingly, in both the cases, the peak corresponding to the carbonyl carbon is absent which is well in accordance with the FT-IR spectra of the prepared samples as presented in Figure 5.12.

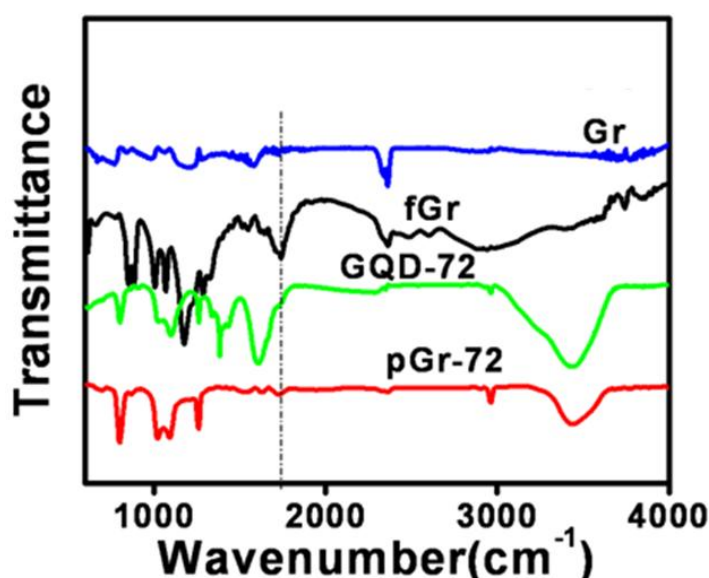


**Figure 5.12.** FT-IR spectra of Gr, fGr, GQD-72 and pGr-72.

The FT-IR spectra of pGr-72 and GQD-72 show broad peaks at 3440 cm<sup>-1</sup> which indicates the presence of -OH functional groups (Figure 5.12). Interestingly, both the samples do not show the peak corresponding to carbonyl groups at around 1730 cm<sup>-1</sup> whereas the functionalized graphene (fGr) used as the reference shows this peak. This indicates the absence carbonyl functionalities in pGr and GQD as the dominant intermediate is expected to be the epoxide moiety. Here, fGr was used as the reference which was prepared by the functionalization of Gr with con. HNO<sub>3</sub>:H<sub>2</sub>SO<sub>4</sub> mixture at

90 °C for 3 h. This result concludes that the acid mixture functionalizes Gr leading to carbonyl functionalities whereas the H<sub>2</sub>O<sub>2</sub> functionalization results in the formation of -OH functionalities on the Gr surface. The absence of carbonyl peaks in FT-IR indicates that the mechanism for the chipping out of GQDs from graphene is in accordance with the proposed mechanism in Figure 5.5, where the intermediate epoxide is playing a key role to trigger the scissoring process

### 5.3.5 Electrochemical Studies

#### 5.3.5.1. Cyclic voltammetry (CV)

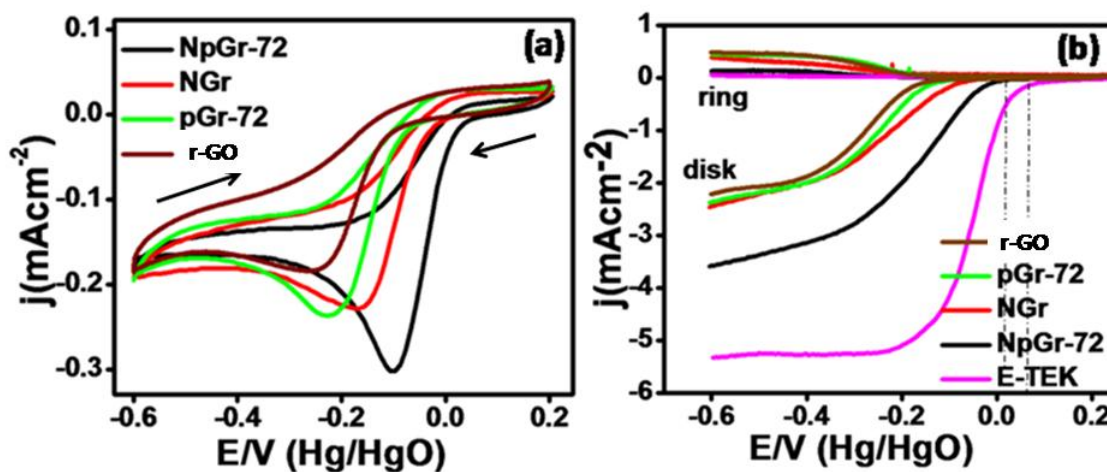


**Figure 5.13.** (a) CV for pGr-72, NGr and NpGr-72 taken at a scan rate of  $5 \text{ mV s}^{-1}$  (b) RRDE voltammograms of pGr-72, NGr, NpGr-72 and E-TEK recorded in 0.1 M KOH with the scan rate of  $10 \text{ mV s}^{-1}$  with rotation rate of 1600 rpm.

In order to understand the influence of surface porosity of Gr for nitrogen doping towards the establishment of efficient catalytic sites for ORR, we performed cyclic voltammetry (CV) for NpGr-72 in 0.1 M KOH solution (saturated with O<sub>2</sub>) and the performance has been compared with non-porous nitrogen doped graphene (NGr), pGr-

72, r-GO and commercial 20 wt % Pt/C (E-TEK). Figure 5.13a compares the cyclic voltammograms of NpGr-72, NGr, pGr and Gr taken at a potential window of 0.2 to -0.6 V against Hg/HgO reference electrode at a scan rate of  $5 \text{ mV s}^{-1}$ . The voltammograms clearly show the ORR activity of all the samples as indicated by the distinct onset potentials and peaks corresponding to oxygen reduction current during the cathodic scan. Gr shows a well resolved cathodic peak corresponding to ORR with an onset potential of -0.088 V under oxygen saturated conditions whereas pGr-72 shows the ORR with an onset potential of -0.07 V. The more positive onset potential shift occurred in the case of pGr-72 can be ascribed to the presence of functional groups on the edge sites along the pore openings of Gr. In the case of NGr, the onset potential has been shifted favorably in the positive direction with the onset at -0.03 V, which clearly validates the influential role of nitrogen towards ORR in the system. Now, when we come to the CV profile of NpGr-72, a substantial reduction in the overpotential and increased peak current for ORR compared to NGr have been visualized. NpGr-72 exhibits the cathode current onset at +0.02 V, which corresponds to an appreciable reduction in the overpotential by 50 mV compared to its nonporous nitrogen doped counterpart (*i.e.* NGr).

### 5.3.5.2. Rotating Ring Disc Electrode (RRDE) Method

Compared to CV, a rotating ring disk electrode (RRDE) analysis can give better resolution to the polarization profile and is considered as a powerful tool to analyze the ORR kinetics. The corresponding linear sweep voltammograms (LSVs) of NpGr-72, NGr, pGr and r-GO taken in 0.1 M KOH solution (oxygen saturated) at an electrode rotation rate of 1600 rpm are presented in Figure 5.13b. It can be seen that, r-GO displays mixed diffusion kinetics between -0.3 to -0.47 V with an onset potential of -0.088 V. On

the other hand, the pGr-72 shows mixed diffusion kinetics between -0.2 to -0.4 V with an onset potential of -0.07 V. Unlike r-GO and pGr, NGr shows the onset of ORR at -0.03 V, displaying mixed diffusion kinetics between -0.1 and -0.4 V. The positive onset potential reveals the beneficial role played by nitrogen doping on the Gr surface. NpGr-72, the main material of interest in the present study, outperforms both pGr-72 and NGr in terms of the overall ORR activity. NpGr-72 shows the mixed diffusion kinetics between -0.08 to -0.4 V with an onset potential of +0.02 V, which is 50 and 90 mV positive compared to NGr and pGr, respectively. With the help of Koutecky-Levich (K-L) plots, the efficiency of the catalyst can be evaluated by calculating the number of transferred electrons per oxygen molecule in ORR and kinetic current density.

Figure 5.14a shows the K-L plots obtained at -0.24 V for pGr-72, NGr and NpGr-72 (K-L plot for r-GO is not included here due to its poor ORR activity at -0.24 V). Here, the K-L slope ( $1/B$ ) has been obtained from the plot of the inverse of the current density ( $1/j$ ) against the inverse of the square root of the angular velocity ( $1/\omega^{1/2}$ ). Subsequently, the 'n' values have been calculated at different potential and the values are plotted in Figure 5.14b. The resulting values of 'n' for NpGr-72 are 3.2 - 3.8 in the potential range of -0.24 to -0.4 V which indicate that the system reduces the oxygen molecule predominantly into water *via* nearly the preferred 4-electron pathway with only negligible contribution towards  $H_2O_2$ . On the other hand, the 'n' values calculated for the other two systems are substantially lower, which emphasizes the greater contribution of the mechanism involving the 2-electron transfer process leading to  $H_2O_2$ . The y-axis intercept of the K-L plots leads to the measurement of the kinetic current ( $j_k$ ) values for the corresponding potentials. The  $j_k$  values of NpGr-72 are significantly higher compared to

both pGr-72 and NGr along the entire potential window of -0.12 to -0.4 (Figure 5.14c). For example, at -0.24 V,  $j_k$  of NpGr-72 is 3.8 mA cm<sup>-2</sup> which is 2.5 (1.5 mA cm<sup>-2</sup>) and 3.5 (1.1 mA cm<sup>-2</sup>) times higher than that of NGr and pGr-72, respectively.

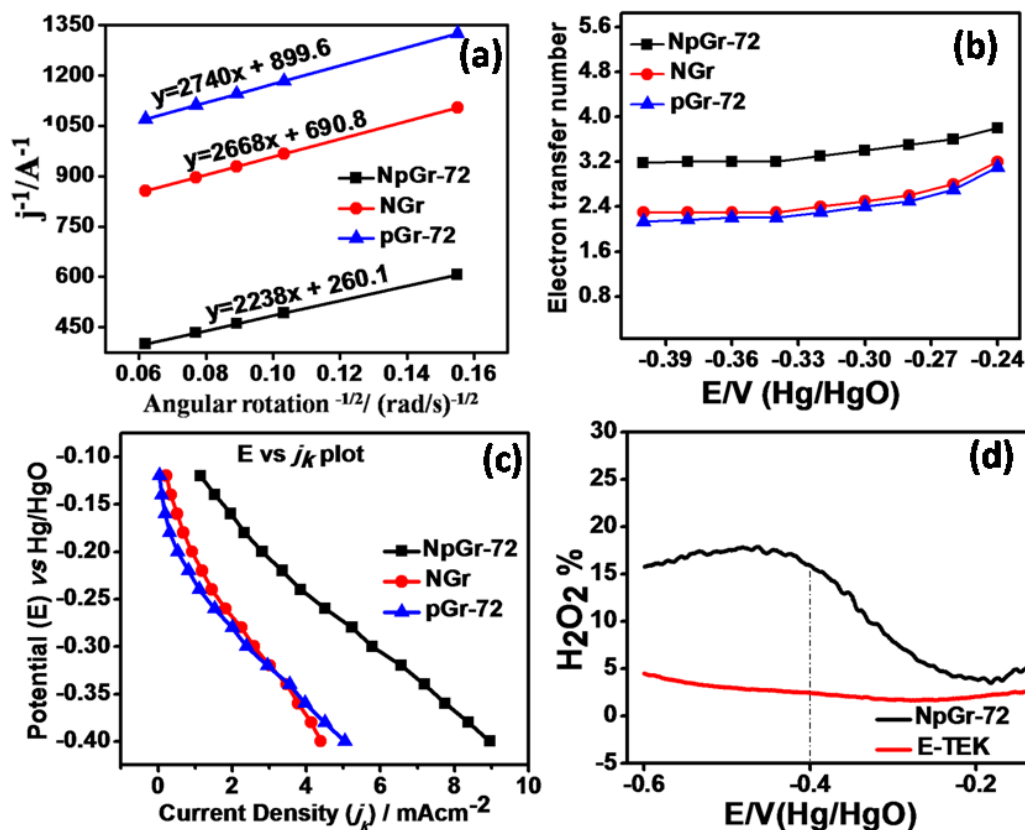


**Figure 5.14.** (a) K-L plots obtained from the RDE studies of the samples; (b) electron transfer number calculated from the slope of the K-L plots at different potentials; (c) comparison of the E vs kinetic current density ( $j_k$ ) plot of pGr-72, NGr and NpGr-72 derived from the K-L plots; (d) comparison of the peroxide percentage detected over NpGr-72 and commercial E-TEK catalysts by RRDE studies.

Further, quantification of the amount of  $H_2O_2$  formed during the oxygen reduction has been done by analyzing the ring current of the RRDE results. The lower ring current of NpGr-72 compared to NGr and pGr-72 implies that lesser amount of  $HO^{2-}$  gets

reached to the ring electrode (Pt). A comparison of the peroxide percentage detected over NpGr-72 and a commercial E-TEK catalyst is presented in Figure 5.14d. The yield of  $\text{H}_2\text{O}_2$  on NpGr-72 has been estimated as 15 % which is significantly lower than that of NGr and pGr-72. The nearly 4-electron transfer process as quantified from the K-L plots and the significantly lower percentage of  $\text{H}_2\text{O}_2$  as estimated from the ring current clearly validate the existence of the preferred oxygen reduction kinetics involving the major contribution from the direct reduction of oxygen into water in the system. Even though NpGr-72 exhibits ORR with higher overpotential compared to the commercial E-TEK (20 wt.% Pt/C) as shown in Figure 5. 13b, the overpotential difference between these two catalysts is significantly low (60 mV) compared to the previous reports including the one from our group. [31-33]

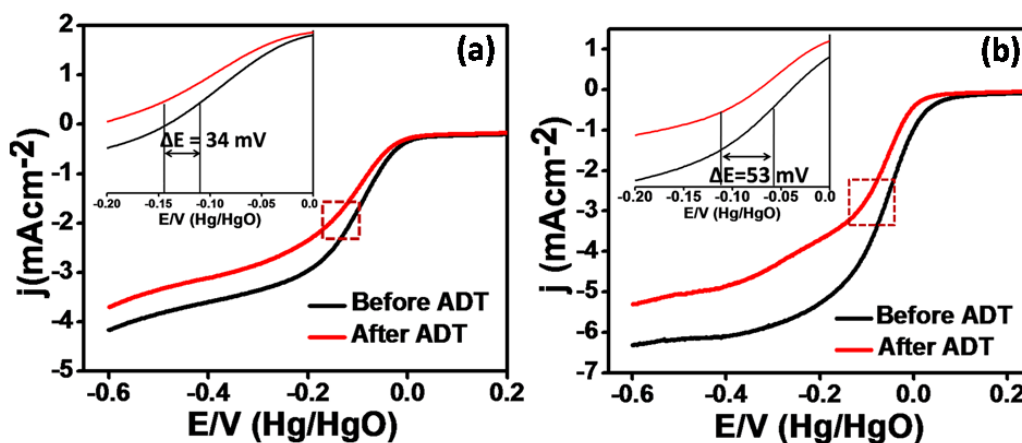


**Figure 5.15.** Accelerated durability test for (a) NpGr-72 and (b) 20 wt % Pt/C (E-TEK).

In addition to the magnificent activity towards ORR, stability of the non-Pt catalysts under electrochemical environments is an important assessment criterion of their suitability in real fuel testing conditions. Hence, in order to compare the stability of

NpGr-72 with respect to the well known E-TEK, we carried out the accelerated durability test (ADT) as shown in Figure 5.15. ADT was implemented by potential cycling of desired material between -0.85 and 0.4 V vs Hg/HgO in oxygen saturated 0.1 M KOH at a scan rate of 100 mV s<sup>-1</sup> for 2500 cycles. Earlier, the LSV was taken at 1600 rpm to envisage its original ORR performance. After 2500 cycles, *i.e.*, after the ADT, LSV was repeated again and the degree of degradation was quantified by comparing the half wave potential of the catalyst before and after ADT. The potential drop for NpGr-72 is 34 mV which is significantly lower than that of Pt/C (53 mV). Thus, the LSV comparison plots before and after ADT evidently shows that NpGr-72 is electrochemically more stable compared to its commercial Pt counterpart in alkaline medium. Obviously, the potential cycling causes the dissolution and sintering of Pt nanoparticles in the case of E-TEK whereas degradation of active sites in NpGr-72 is less prominent due to the stable coordination of nitrogen with the graphene moiety.

### 5.3.6 Single Cell Polarization Test

Finally, demonstration of real fuel cell performance is an important criterion to direct our non-Pt electrocatalyst towards the practical application. The single cell polarization performance of our homemade catalyst was evaluated under anion exchange membrane fuel cell conditions (AEMFCs) (Figure 5.16a). The membrane electrode assembly (MEA) was made by sandwiching NpGr-72 or NGr coated (2.5 mg cm<sup>-2</sup>) gas diffusion layer (GDL) in cathode side and E-TEK coated GDL in anode side with FumaTech FAA membrane. In all the cases, 40 wt % Pt/C with a loading of 0.8 mg cm<sup>-2</sup> was used as the anode catalyst. The MEA derived from NpGr-72 exhibits an open circuit potential (OCP) of 0.82 V which is slightly higher than the OCP value of 0.73 exhibited by NGr. NGr

exhibits a current density of  $26.3 \text{ mA cm}^{-2}$  at  $0.4 \text{ V}$  whereas NpGr-72 gives a value of  $67.3 \text{ mA cm}^{-2}$  which is two times higher than that of NGr. In addition, NpGr-72 displays a maximum power density of  $27 \text{ mW cm}^{-2}$  which is significantly higher than the corresponding value obtained on NGr ( $10 \text{ mW cm}^{-2}$ ).

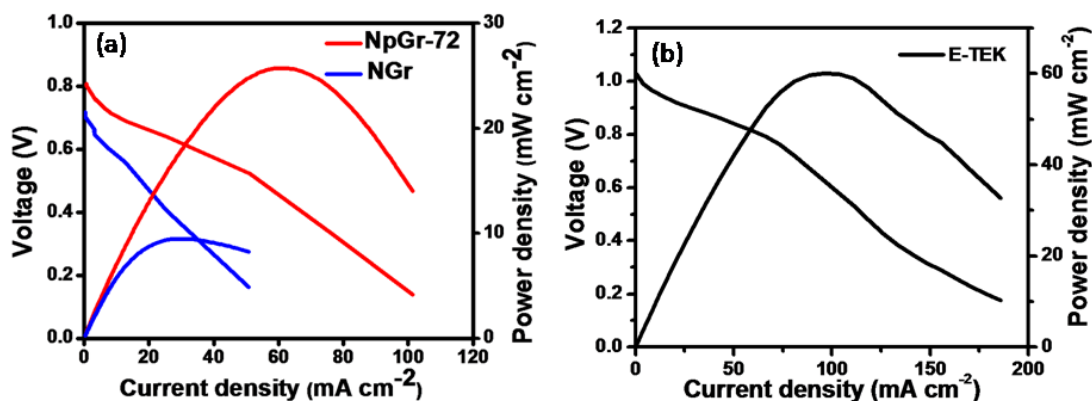


**Figure 5.16.** (a) Single cell polarization data by using NpGr-72 and NGr (b) Pt/C (E-TEK) as the cathode catalysts (loading:  $2.5 \text{ mg cm}^{-2}$ ) and FumaTech FAA as the anion exchange membrane.  $40 \text{ wt.}\%$  Pt/C (E-TEK) (loading:  $0.8 \text{ mg cm}^{-2}$ ) was used as the anode catalyst. The operating temperature is  $50 \text{ }^\circ\text{C}$ .  $\text{H}_2$  and  $\text{O}_2$  flow rates are  $50$  and  $100 \text{ sccm}$ , respectively and  $100 \%$  relative humidity was maintained for the  $\text{H}_2$  and  $\text{O}_2$  streams.

Obviously, with the maximum current density at  $0.4 \text{ V}$  ( $129.3 \text{ mA cm}^{-2}$ ) and power density ( $67 \text{ mW cm}^{-2}$ ),  $40 \text{ wt.}\%$  Pt/C (E-TEK) outperforms NpGr-72 (Figure 5.16b). The single cell data of Pt/C is in well agreement with the literature report.[34] The AEMFC performance of our catalyst is nearly comparable to the one reported on nitrogen doped CNT, even though the electrode catalyst loading in this case was  $5 \text{ mg cm}^{-2}$  compared to  $2.5 \text{ mg cm}^{-2}$  in our case.[35]

### 5.3.7. Structural Analysis

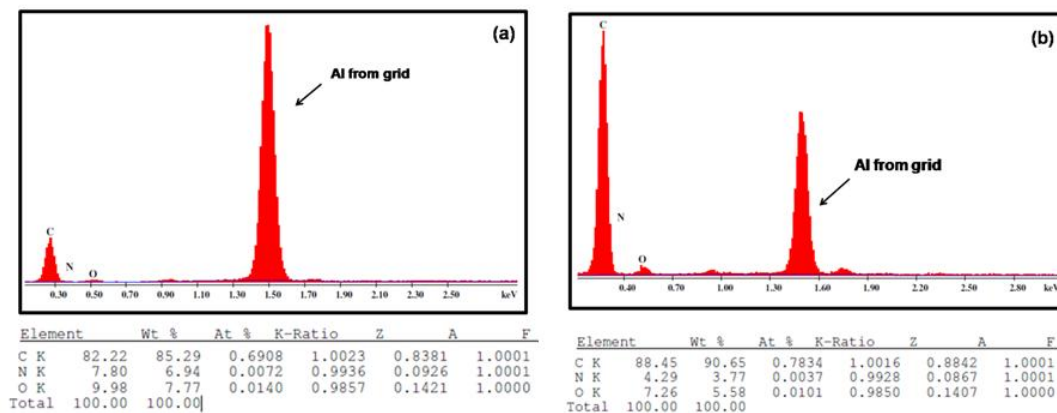


**Figure 5.17.** EDAX spectra with elemental quantification of (a) NpGr-72 and (b) NGr.

Overall, this enhanced performance towards ORR can be attributed not only to the higher nitrogen content but its preferred coordination on the rich edge sites of the pore openings of NpGr-72 is also expected to play a vital role in reducing the overpotential for the process. In this context, it is important to understand the type and content of nitrogen and the role of the unsaturated sites of carbon along the pore openings in generating the desired coordination with nitrogen during the doping process. The electronegativity difference between doped nitrogen and carbon atom facilitates the adsorption of oxygen molecule on the carbon surface. Among the different types of nitrogen coordination with carbon in the graphitic carbon materials, the pyridinic and graphitic nitrogen are generally believed to be more active for ORR.[36-38] However, such claims are still under debate with few reports highlighting the efficiency of pyrrolic nitrogen coordination towards ORR.[33, 39-40]

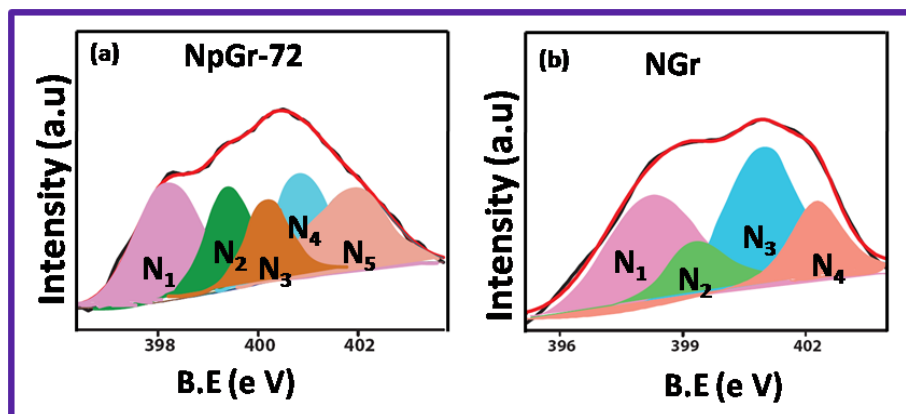


**Figure 5.18.** Deconvoluted N1s spectra of NpGr-72 and NGr. The various nitrogen moieties as designated for the samples are as follows: (a) NpGr-72:  $N_1$  (Pyridinic),  $N_2$  (Pyrrolic),  $N_3$  (Graphitic),  $N_4$  (Quaternary) and  $N_5$  (Pyridinic  $N^+O^-$ ); (b) NGr:  $N_1$  (Pyridinic),  $N_2$  (Pyrrolic),  $N_3$  (Graphitic) and  $N_4$  (Pyridinic  $N^+O^-$ ).

Here, the higher amount of the doped nitrogen and its chemical environment of NpGr-72 have been identified by energy dispersive X-ray analysis (EDAX) (Figure 5.17) and N1s spectra of XPS, respectively (Figure 5.18). For an effective comparison, the amount and chemical nature of nitrogen in NGr is also investigated along with NpGr-72. The estimated nitrogen contents in NGr and NpGr-72 by EDAX are 4.2 and 7.8 wt. %, respectively. This trend is in accordance with the expected greater extent of unsaturated carbon moieties along the pore openings of NpGr-72, which is expected to accommodate more nitrogen atoms compared to the case of using pristine Gr. Figure 5.18 shows the deconvoluted XPS N1s spectra of NpGr-72 and NGr. The N1s spectra of NpGr-72 in Figure 5.18a show the presence of five different peaks at 398.4 ( $N_1$ ), 399.4 ( $N_2$ ), 400.3 ( $N_3$ ), 401.1 ( $N_4$ ) and 402.4 eV ( $N_5$ ) corresponding to pyridinic, pyrrolic, graphitic, quaternary nitrogens and nitrogen bound with oxygen (pyridinic  $N^+O^-$ ), respectively. A

quantification of the percentage of the types of nitrogens as calculated from the peak intensities of the different types of nitrogen is given in Figure 5.19.

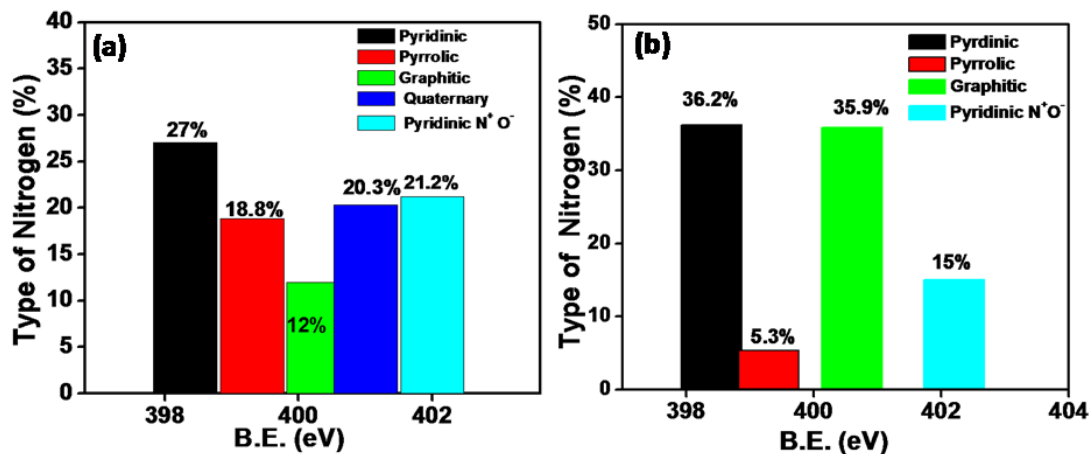


**Figure 5.19.** Quantification of the types of nitrogen in their relative percentages out of the total doped nitrogen in (a) NpGr-72 (b) NGr.

Similarly, the deconvoluted N1s spectra of NGr in Figure 5.18b show the presence of four different peaks at 398.5 (N<sub>1</sub>), 399.3 (N<sub>2</sub>), 400.6 (N<sub>3</sub>), and 402.2 (N<sub>4</sub>) corresponding to pyridinic, pyrrolic, graphitic and nitrogen bound with oxygen (pyridinic N<sup>+</sup>O<sup>-</sup>), respectively. In case of NpGr-72, the 27 % of pyridinic nitrogen contribution in the overall nitrogen content is believed to be the main active site for ORR. Apart from this, another major nitrogen moiety is the pyridinic N<sup>+</sup>O<sup>-</sup>, which gives an overall contribution of 21.2 % in the total nitrogen content. Now, considering NGr, the estimated value of the pyridinic nitrogen from the overall amount of the doped nitrogen present in the system is nearly 36 %. However, since the overall doped nitrogen content in NGr is already significantly lower than that in NpGr-72, the 27 % of the pyridinic nitrogen content in NpGr-72 is indicating a prominent enhancement in its distribution due to the presence of large number of surface pores and hence carbon unsaturation. Along with the

relatively large proportion of the pyridinic nitrogen, NpGr-72 also possesses a high contribution from the pyrrolic form of the nitrogen, which is estimated to be 18.8 % in the overall nitrogen content. However, the estimation of the pyrrolic nitrogen content is not very straight forward as another form of nitrogen moiety named pyridone also has a very resembling chemical environment as that of pyrrole which makes both chemically indistinguishable.[41-42] Pyridone contains one nitrogen atom in a six membered ring as similar to the pyridinic nitrogen (Figure. 5.20). Although, the chemical structure of pyridone is similar to the pyridinic nitrogen (six membered ring), it is not found in the same binding energy as pyridinic nitrogen but it is very similar to the pyrrolic nitrogen. This is attributed to the existence of two tautomers of pyridone with stable carbonyl forms giving a matching chemical environment as that of the pyrrolic nitrogen (Figure 5.20). [43]

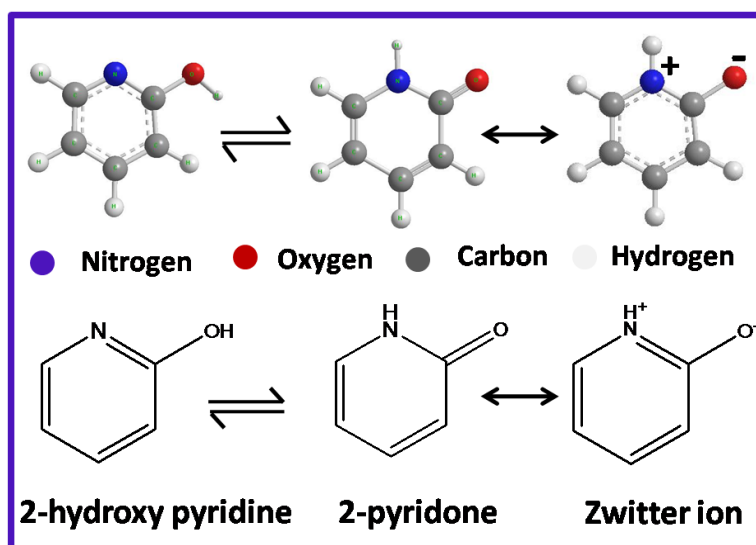


**Figure 5.20.** Tautomerization of 2- pyridone between hydroxyl and Zwitter ion forms.

Interestingly, compared to NpGr-72, the pyrrolic/pyridone contribution is significantly low in the case of NGr. Therefore, the co-existence of pyridinic and pyrrolic/pyridone types of nitrogen in the case of NpGr-72 is expected to contribute together towards the observed enhanced ORR activity of the system. Such a desired enhancement in the type and density of the nitrogen doped active sites could be established due to the success in creating unsaturated carbon centers along the substrate by engraving nanometer sized pores without making any adverse effect on its 2-D architecture.

## 5.4. Conclusions

An unprecedented way for the *in-situ* synthesis of both luminescent graphene quantum dots with higher yield and high quality nanoporous graphene simultaneously through a simple process could be demonstrated. This is achieved by the judicious oxidative etching of graphene (Gr) with hydrogen peroxide ( $H_2O_2$ ), which results in the chipping out of nanometer sized flakes of Gr mediated by the epoxide linkage resulting in the formation of graphene quantum dots (GQDs) and porous graphene (pGr) simultaneously. The size correlation between the etched GQDs and the pore size on the graphene surface confirms the derivation of GQDs from graphene. The created pores on Gr could be effectively utilized for nitrogen doping due the rich defect sites along the pore openings. The nitrogen doped pGr (NpGr-72) exhibits excellent performance towards electrochemical oxygen reduction reaction (ORR) compared to the nitrogen doped non-porous graphene (NGr) and pGr systems. Superiority of NpGr-72 for ORR is attributed to the proportionally higher contents of pyridinic and pyrrolic/pyridone type nitrogens in the system and this enrichment is attained to the doping directly at the defect

sites along the pore openings. As NpGr-72 appears like a potential cost-effective electrocatalyst for ORR, its counterpart GQD-72 also highlights its unique luminescent properties, which can have potential applications in nano electronics. Overall, the method discussed here gives a simple and easily scalable process for developing two potentially value added products having greater prospects in nano electronics and energy applications.

## 5.5. References

- [1] L. Qu, Y. Liu, J-B. Baek, L. Dai, *ACS Nano*, **2010**, *4*, 1321.
- [2] K. S. Novoselov, A. K. Geim, S. V. Morozov, D. Jiang, Y. Zhang, S. V. Dubonos, I. V. Grigorieva, A. A. Firsov, *Science* **2004**, *306*, 666.
- [3] L. A. Ponomarenko, F. Schedin, M. I. Katsnelson, R. Yang, E. W. Hill, K. S. Novoselov, A. K. Geim, *Science* **2008**, *320*, 356.
- [4] S. Zhu, J. Zhang, C. Qiao, S. Tang, Y. Li, W. Yuan, B. Li, L. Tian, F. Liu, R. Hu, H. Gao, H. Wei, H. Zhang, H. Sun, B. Yang, *Chem. Commun.* **2011**, *47*, 6858.
- [5] X. Yan, X. Cui, L.S. Li, *J. Am. Chem. Soc.* **2010**, *132*, 5944.
- [6] D. Pan, J. Zhang, Z. Li, M. Wu, *Adv. Mater.* **2010**, *22*, 734.
- [7] J. Peng, W. Gao, B. K. Gupta, Z. Liu, R. R. Aburto, L. Ge, L. Song, L. B. Alemany, X. Zhan, G. Gao, S. A. Vithayathil, B. A. Kaiparettu, A. A. Marti, T. Hayashi, J. J. Zhu, P. M. Ajayan, *Nano Lett.* **2012**, *12*, 844.
- [8] Y. Li, Y. Hu, Y. Zhao, G. Shi, L. Deng, Y. Hou, L. Qu, *Adv. Mater.*, **2011**, *23*, 776.
- [9] L. Lin, S. Zhang, *Chem. Commun.*, **2012**, *48*, 10177.
- [10] V. Gupta, N. Chaudhary, R. Srivastava, G. D. Sharma, R. Bhardwaj, S. Chand, *J. Am. Chem. Soc.* **2011**, *133*, 9960.

- [11] X. Zhou, Y. Zhang, C. Wang, X. Wu, Y. Yang, B. Zheng, H. Wu, S. Guo, J. Zhang, *ACS Nano* **2012**, *6*, 6592.
- [12] S. H. Jin, D. H. Kim, G. H. Jun, S. H. Hong, S. Jeon, *ACS Nano* **2013**, *7*, 1239.
- [13] I. Gur, N. A. Fromer, M. L. Geier, A. P. Alivisatos, *Science* **2005**, *310*, 462.
- [14] N. Tessler, V. Medvedev, M. Kazes, S. H. Kan, U. Banin, *Science* **2002**, *295*, 1506.
- [15] A. P. Alivisatos, W. Gu, C. Larabell, *Annu. Rev. Biomed. Eng.* **2005**, *7*, 55.
- [16] F. Yang, M. Zhao, B. Zheng, D. Xiao, L. Wu, Y. Guo, *J. Mater. Chem.* **2012**, *22*, 25471.
- [17] (a) Q. Li, S. Zhang, L. Dai, L-S. Li, *J. Am. Chem. Soc.* **2012**, *134*, 18932; (b) Y. Li, Y. Zhao, H. Cheng, Y. Hu, G. Shi, L. Dai, L. Qu, *J. Am. Chem. Soc.* **2012**, *134*, 15.
- [18] A. Du, Z. Zhu, S. C. Smith, *J. Am. Chem. Soc.*, **2010**, *132*, 2876.
- [19] T. Palaniselvam, H. B. Ayiappa, S. Kurungot, *J. Mater. Chem.* **2012**, *22*, 23799.
- [20] (a) D. Jiang, V. R. Cooper, S. Dai, *Nano Lett.* **2009**, *9*, 4019; (b) M. Shan, Q. Xue, N. Jing, C. Ling, T. Zhang, Z. Yan and J. Zheng, *Nanoscale*, **2012**, *4*, 5477.
- [21] D. C. Tanugi, J. C. Grossman, *Nano Lett.* **2012**, *12*, 3602.

- [22] (a) J. Xiao, D. Mei, X. Li, W. Xu, D. Wang, G. L. Graff, W. D. Bennett, Z. Nie, L. V. Saraf, I. A. Aksay, J. Liu, J. G. Zhang, *Nano Lett.* **2011**, *11*, 5071; (b) Z. L. Wang, D. Xu, H. G. Wang, Z. Wu, X. B. Zhang, *ACS Nano*, **2013**, *7*, 2422.
- [23] H. Wang, Q. Wang, Y. Cheng, H. Li, Y. Yao, Q. Zhang, C. Dong, P. Wang, U. Schwingenschlogl, W. Yang, X. X. Zhang, *Nano Lett.* **2012**, *12*, 141.
- [24] S. Yin, Y. Goldovsky, M. Herzberg, L. Liu, H. Sun, Y. Zhang, F. Meng, X. Cao, D. D. Sun, H. Chen, A. Kushmaro and X. Chen, *Adv. Funct. Mater.* **2013**, *23*, 2972.
- [25] D. Bourissou, O. Guerret, F. P. Gabbai, G. Bertrand, *Chem. Rev.* **2000**, *100*, 39.
- [26] Z. Li, W. Zhang, Y. Luo, J. Yang, J. Hou, *J. Am. Chem. Soc.* **2009**, *131*, 6320.
- [27] M. Acik, G. Lee, C. Mattevi, M. Chhowalla, K. Cho and Y. J. Chabal, *Nat. Mater.*, DOI: 10.1038/NMAT2858. (b) J. U. Lee, W. Lee, J. W. Yi, S. S. Yoon, S. B. Lee, B. M. Jung, B. S. Kim and J. H. Byun, *J. Mater. Chem. A*, **2013**, *1*, 12893.
- [28] C. X. Guo, Y. Wang, C. M. Li, *ACS Sustainable Chem. Eng.* **2013**, *1*, 14.
- [29] (a) A. Ghosh, S. Basu, A. Verma, *Fuel cells*, **2013**, *13*, 355. (b) R. Kou, Y. Shao, D. Wang, M. H. Engelhard, J. H. Kwak, J. Wang, V. V. Viswanathan, C. Wang, Y. Lin, Y. Wang, I. A. Aksay, J. Liu, *Electrochem. Commun.*, **2009**, *11*, 954. (c) A. K. Mishra, S. Ramaprabhu, *Desalination.*, **2011**, *282*, 39.
- [30] A. Ghosh, K. S. Subrahmanyam, K. S. Krishna, S. Datta, A. Govindaraj, S. K. Pati, C. N. R. Rao. *J. Phys. Chem. C.* **2008**, *112*, 15704.

- [31] Z. Lin, M. Song, Y. Ding, Y. Liu, M. Liua, C. Wong, *Phys. Chem. Chem. Phys.*, **2012**, *14*, 3381.
- [32] Z. Luo, S. Lim, Z. Tian, J. Shang, L. Lai, B. MacDonald, C. Fu, Z. Shen, T. Yu, J. Lin, *J. Mater. Chem.*, **2011**, *21*, 8038.
- [33] S. M. Unni, S. Devulapally, N. Karjulea, S. Kurungot, *J. Mater. Chem.* **2012**, *22*, 23506.
- [34] J. R. Varcoe, R. C. T. Slade, G. L. Wright, Y. Chen, *J. Phys. Chem. B* **2006**, *110*, 21041.
- [35] C. V. Rao, Y. Ishikawa, *J. Phys. Chem. C* **2012**, *116*, 4340.
- [36] P. H. Matter, L. Zhang, U. S. Ozkan, *J. Catal.* **2006**, *239*, 83.
- [37] Z-H. Sheng, L. Shao, J-J. Chen, W-J. Bao, F-B. Wang, X-H. Xia, *ACS Nano* **2011**, *4*, 4350.
- [38] Z. Luo, S. Lim, Z. Tian, J. Shang, L. Lai, B. MacDonald, C. Fu, Z. Shen, T. Yu, J. Lin, *J. Mater. Chem.* **2011**, *21*, 8038.
- [39] G. Wu, Z. Chen, K. Artyushkova, F. H. Garzon, P. Zelenay, *ECS Trans.* **2008**, *16*, 159.
- [40] Y. Shao, S. Zhang, M. H. Engelhard, G. Li, G. Shao, Y. Wang, J. Liu, I. A. Aksay, Y. Lin, *J. Mater. Chem.* **2010**, *20*, 7491.
- [41] J. R. Pels, F. Kapteijn, J. A. Moulijn, Q. Zhu, K. M. Thomas, *Carbon*, **1995**, *33*, 1641.

[42] G. Wu, P. Zelenay, DOI: 10.1021/ar400011z.

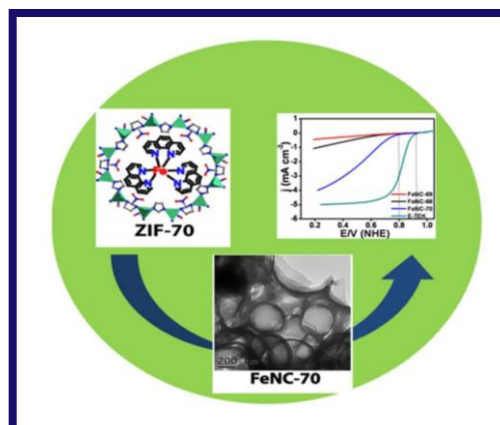
[43] R. Silva, D. Voiry, M. Chhowalla, T. Asefa, *J. Am. Chem. Soc.* **2013**, *135*, 7823.

## Chapter 6

### ZEOLITIC IMIDAZOLATE FRAMEWORKS DERIVED HOLLOW CORE, NITROGEN-DOPED CARBON NANO STRUCTURES FOR OXYGEN REDUCTION REACTION IN FUEL CELLS

---

Facile synthesis of porous carbon doped with iron coordinated nitrogen active sites (FeNC-70) is demonstrated by following an inexpensive synthetic pathway by using a Zeolitic Imidazolate Framework (ZIF-70) as a template. In order to emphasize the possibility to tune the porosity and surface area of the resulting carbon based on the structure of the parent ZIF, two other ZIFs, *viz.* ZIF-68 and ZIF-69, are also taken along with ZIF-70 as the templates. The HRTEM images of FeNC-



70 reveal that the carbon particles have bimodal structure composed of spherical macroscopic pore and mesoporous shell. The XPS discloses the presence of Fe-N-C moiety, which is the primary active site for the ORR. This active porous carbon enriched with the Fe-N-C moiety reduces the O<sub>2</sub> molecule with an onset potential at 0.80 V *vs* NHE through a pathway involving 3.3-3.8 e<sup>-</sup> under acid condition, which is much closer to the favored 4 e<sup>-</sup> pathway towards ORR.

---

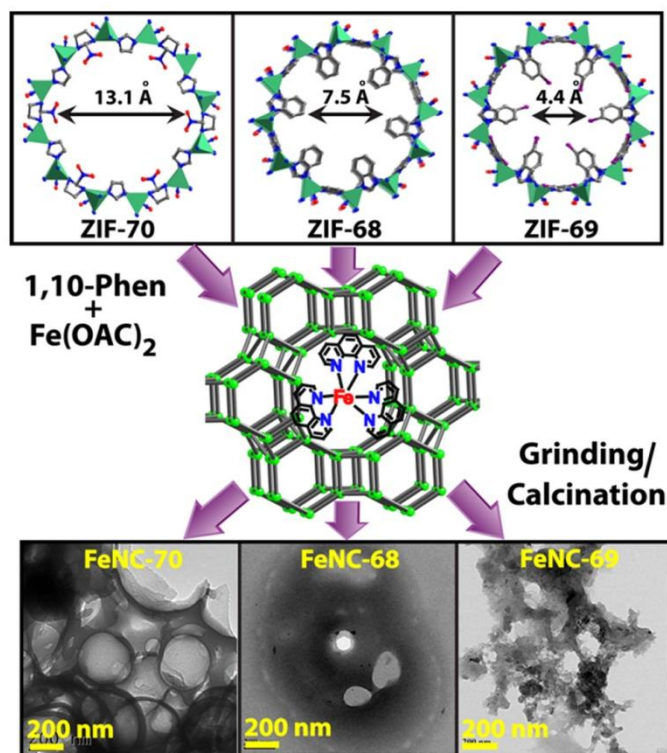
\*The contents of this chapter have been published in *Chem. Eur. J.*, **2013**, *19*, 9335.

## 6.1. Introduction

It is a unanimously accepted fact that platinum group metals (PGM) are benchmark catalysts for oxygen reduction reaction (ORR) in polymer electrolyte fuel cells (PEFCs). However, the scarcity of Pt in the earth's crust ( $3.7 \times 10^{-6}$  %) [1] along with the sluggish ORR kinetics on its surface impede the prospects of Pt as a commercially viable electrocatalyst for PEFC applications. Ever since the pioneering work of Jasinski *et al* [2], several research groups have dedicated themselves towards the development of a new class of non-precious electrocatalysts composed of metal/nitrogen/carbon (M/N/C, M-Fe or Co) for ORR in PEFCs. Even though an in-depth understanding on the nature of the active sites responsible for ORR on these systems is lacking at this moment, it is identified that a majority of such potential compounds possesses either doped nitrogen or metal coordinated nitrogen in the carbon matrix. Several reports [3] including the one by our group [4] have realized that Fe plays a crucial role in creating the active site for ORR. Moreover, recent hypothesis highlights that among the five possible active sites in M/N/C based catalysts, two, *viz.*,  $\text{FeN}_4/\text{C}$  and  $\text{N-FeN}_{2+2}/\text{C}$  are more active for ORR. [5] Apart from these M/N/C based catalysts, several non-platinum catalysts such as nitrogen doped carbon with different carbon nano structures and, most recently, nitrogen doped graphene (N-Gr) have been developed to replace PGM. [6]

Meanwhile, nanostructured porous carbons have attracted several applications namely gas adsorption, supercapacitors *etc.* [7] The preparation of such porous carbonaceous materials often involves inexpensive synthetic pathway which is an added advantage to reduce the cost of fuel cells. Recently, metal-organic frameworks (MOFs), a class of new crystalline materials, have attracted global attention due to their tunable pore

size, high surface area and also as potential candidates for gas storage [8], drug delivery [9] and heterogeneous catalysis. Porous MOFs have nano sized inner cavities and channels which afford easy access to the guest molecules and therefore can be used as templates for the synthesis of porous carbons. [10]



**Scheme 6.1.** Synthetic pathway of Fe-N-doped porous carbons (FeNC-70, FeNC-68 and FeNC-69) from isorecticular ZIFs.

Indeed, MOF itself can also act as a carbon precursor. [11] Recently, inexpensive porous ZIFs with nano sized inner cavities and channels have been used as templates for the synthesis of porous carbons which in turn could be further explored for electrochemical charge storage and gas adsorption applications. [12] Very recently, Dodelet *et al* [13], inspired by other reports [14], synthesized few porous M/N/C catalysts by using ZIF-8 as a template and executed them as efficient ORR catalysts. Earlier, we

reported porous carbons for high H<sub>2</sub> and CO<sub>2</sub> uptake using ZIF-70, 68 and 69 as hard templates. [15]

Taking the advantage of this study, herein, we report three doped carbons containing Fe-N active sites (FeNC-68, -69 and -70) synthesized by embedding iron phenanthroline ([Fe(phen)<sub>3</sub>]<sup>2+</sup>) complex in the inner cavity of ZIF-68, -69 and -70 with varying pore size ([Fe(phen)<sub>3</sub>]<sup>2+</sup>@ZIF-68, -69 and -70) followed by annealing at 900 °C in Ar atmosphere. These porous ZIFs act as templates for the porous carbon synthesis. We, in this study, attempted to emphasize the possibility to tune the resulting carbons' porosity *via* changing the porosity of the parent ZIFs. Scheme 1 represents the synthetic pathway of FeNC-68, -69 and -70. The structural characteristics of the active carbon materials with Fe-N coordination were analysed by X-ray diffraction pattern (XRD), X-ray photo electron spectroscopy (XPS), energy dispersive X-ray analysis (EDAX) and high resolution transmission electron microscopy (HRTEM). The electrochemical activity of the FeNC based catalysts was analyzed by cyclic voltammetric (CV) and rotating disc electrode (RDE) methods. Among the three resulting Fe-N doped carbon materials, the FeNC-70 exhibits tremendous ORR activity with key feature of higher nitrogen content. Moreover, the active Fe-N doped carbon material (FeNC-70) exposes the bimodal structure composed of spherical macroscopic pore (*ca.* 200 nm) and mesoporous shell during high resolution transmission electron microscopic (HRTEM) analysis. This nano confinement is expected to provide the distinctive condition for the facile electrochemical reaction in terms of mass transport and apparent electrokinetics.

## 6.2. Experimental Section

### 6.2.1. General Remarks

2-Nitroimidazole (2-NIm) was purchased from 3B Scientific Corporation,  $\text{Zn}(\text{NO}_3)_2 \cdot 6\text{H}_2\text{O}$ , 5-chlorobenzimidazole, benzimidazole, imidazole, methanol and dichloro methane (DCM) were purchased from Sigma Aldrich Chemicals. N, N-dimethylformamide (DMF) was purchased from Rankem Chemicals. All starting materials were used without further purification. All experimental operations were performed in 5 mL glass vial inside a programmed oven for Zeolitic Imidazolate Frameworks (ZIFs) synthesis.

### 6.2.2. Synthesis of ZIF-70

(ZIF-70)  $\text{Zn}(\text{IM})(\text{nIM})$ ; In a 5ml glass vial 0.12 mL 2-nitroimidazole stock solution (0.20 M,  $2.4 \times 10^{-5}$  mol) and 0.12 mL imidazole stock solution (0.20 M,  $2.4 \times 10^{-5}$  mol) were mixed together. To this solution, 0.060 mL  $\text{Zn}(\text{NO}_3)_2 \cdot 6\text{H}_2\text{O}$  stock solution (0.15 M,  $1.2 \times 10^{-5}$  mol) was added. Subsequently, the mixture was heated in an oven at 120 °C and allowed to react solvothermally for 72 h. The product was in the form of prism-shaped single crystals. The product was washed with DMF several times and was subsequently dried.

### 6.2.3. Synthesis of ZIF-68 and 69

(ZIF-68)  $\text{Zn}(\text{nIM})(\text{bIM})$  and (ZIF-69)  $\text{Zn}(\text{nIM})(5\text{cbIM})$  were synthesized by using similar procedure as described above (for ZIF-70) but in these cases instead of imidazole, benzimidazole and 5-chlorobenzimidazole secondary ligands were used for the synthesis

of ZIF-68 as well as ZIF-69, respectively. All IRZIFs were confirmed by matching the PXRD patterns with the simulated one derived from single crystal X-ray data.

#### 6.2.4. Synthesis of Fe-N-Doped Porous Carbon (FeNC-70)

The light yellow-colour prism shaped crystals of ZIF-70 was immersed in methanol and DCM for 72 h, dried and then pre-treated under reduced pressure condition at 120 °C for 12 h and 150 °C for about 6 h in order to make guest-free framework. The degassed ZIF-70 (1.00 g) was then mixed with 1, 10-phenanthroline (0.25 g, 1.3 mmol) and iron (II) acetate (0.015 g, 0.08 mmol) in ethanol (5ml). Then, the mixture was filtered, washed and dried well. The dry powder of  $[\text{Fe}(\text{phen})_3]^{2+}@\text{ZIF-70}$  was placed in a mortar and grounded for 2 h. The resulting fine powder was pyrolysed at 900 °C for 3 h under Argon flow in a programmed furnace. The carbon resulted was washed thoroughly in 3 N  $\text{H}_2\text{SO}_4$  to remove Zn and other uncoordinated Fe metal. Carbon samples were dried at 90 °C for 6 h. The carbon resulted was used further for electrochemical study. Similarly, FeNC-68 and FeNC-69 were prepared by following similar experimental procedure (as for FeNC-70) by using ZIF-68 and ZIF-69 as the starting materials.

## 6.3. Results and Discussion

### 6.3.1 HRTEM Analysis

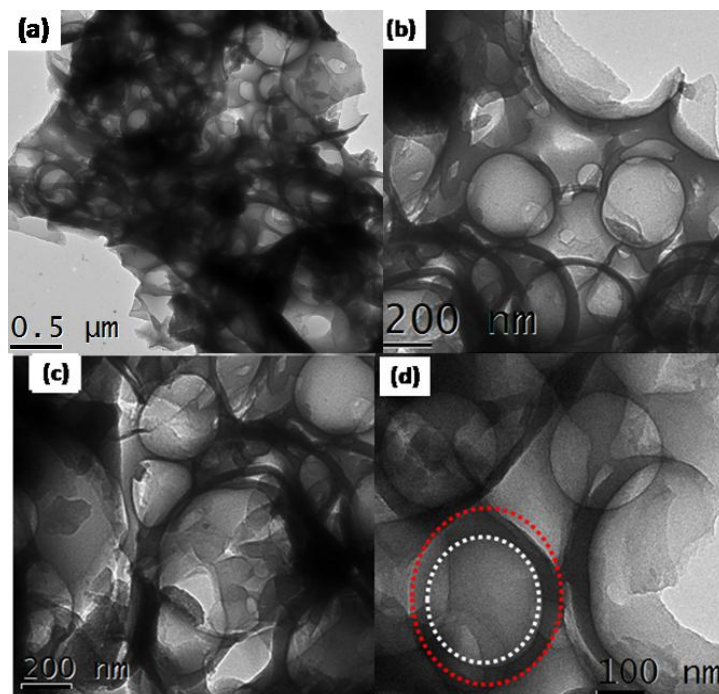


**Figure 6.1.** (a-d) HR-TEM images of macro porous FeNC carbon (FeNC-70) in different magnifications.

The structural characteristics of  $[\text{Fe}(\text{phen})_3]^{2+}@\text{ZIF-70}$  composite derived carbon (FeNC-70) were examined by high resolution transmission electron microscopy (HRTEM). From the HRTEM images, we ensured that the  $[\text{Fe}(\text{phen})_3]^{2+}@\text{ZIF-70}$  composite transformed into the porous carbon (Figure 6.1a-d). The metal impurities (Zn and Fe) retained in the system (Figure 6.2) have been removed by acid [3 M  $\text{H}_2\text{SO}_4$ ] wash. The carbon particles thus formed are spherical in nature with well structured macropores containing  $\text{Fe}^{\text{II}}$  and  $\text{Fe}^{\text{III}}$  ions coordinated to the nitrogen doped in the carbon, which could be ensured by XPS analysis as detailed in a later section.

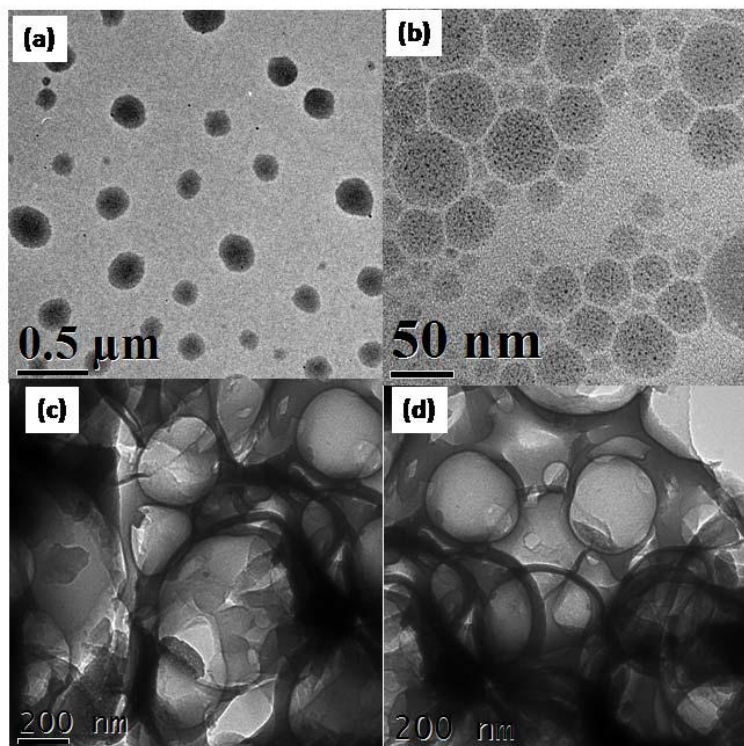


**Figure 6.2.** *a, b) HRTEM images of FeNC-70 (before acid wash) which show the spherical spots due to the unreacted Zn and Fe particles; c-d) the images taken after the acid wash (3 M H<sub>2</sub>SO<sub>4</sub>).*

The HRTEM images (Figure 6.1a-d) clearly reveal that the carbon particles have bimodal structure composed of spherical macroscopic pore (*ca.* 200 nm) and mesoporous shell. It is important to note that the macropore is distributed uniformly on the entire surface of FeNC-70 which is well supported by SEM analysis (Figure 6.3). On the other hand, the pore dimensions of FeNC-68 and FeNC-69 synthesized in similar manner (Figure 6.4) are significantly different from that of FeNC-70 which clearly reveals that the pore dimensions of ZIF determine the formation of micro and macro pore in the final carbon matrix.

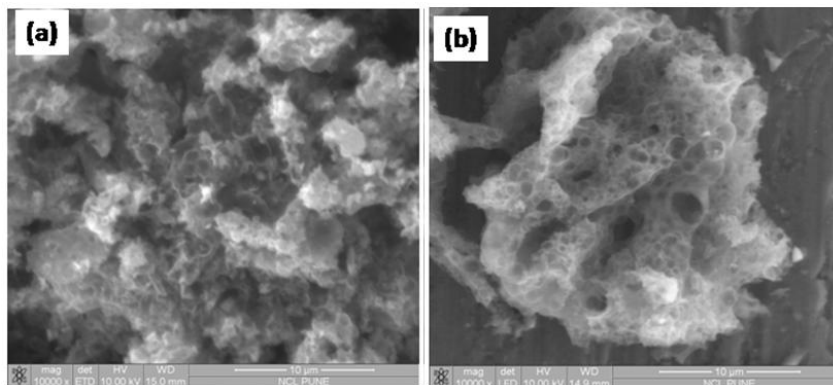


*Figure 6.3. SEM images representing the sponge like structure of FeNC-70.*

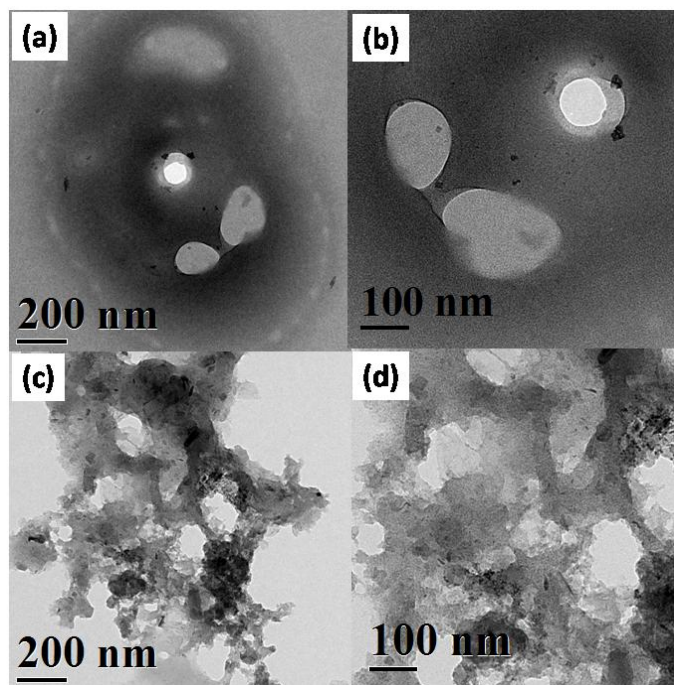


*Figure 6.4. HRTEM images of (a-b) FeNC-68 and (c-d) FeNC-69 (after acid wash).*

### 6.3.2. Surface Area Measurements

Further, nitrogen adsorption-desorption experiments were performed on the as synthesized samples of FeNC-70, FeNC-68 and FeNC-69, to examine the surface areas of these materials. The isotherms collected at 77 K temperature and 1 atm pressure show

typical Type-I behavior with steep increase at low relative pressure, suggesting the dominating micropore characteristic (Figure 6.5). The activated sample of FeNC-70 exhibits the highest BET surface area of  $262 \text{ m}^2 \text{ g}^{-1}$ , whereas FeNC-68 shows a surface area of  $148 \text{ m}^2 \text{ g}^{-1}$ . The activated sample of FeNC-69 also shows similar isotherms with a lower BET surface area of  $60 \text{ m}^2 \text{ g}^{-1}$ . This variation in the surface area for FeNC-70, FeNC-68 and FeNC-69 is well justified due to the variable uptake of  $[\text{Fe}(\text{phen})_3]^{2+}$  complex inside the pores of ZIFs, depending on their porosity and pore aperture for guest entry.

The most porous ZIF-70 ( $1730 \text{ m}^2 \text{ g}^{-1}$ ) which leads to FeNC-70 has higher surface area, while ZIF-68 ( $1060 \text{ m}^2 \text{ g}^{-1}$ ) and ZIF-69 ( $950 \text{ m}^2 \text{ g}^{-1}$ ) have lower porosity and subsequently accommodate lower amount of  $[\text{Fe}(\text{phen})_3]^{2+}$  inside the pores. Therefore, calcinations of ZIF-69 and -68 yield FeNCs possessing less surface area. To confirm the loading of  $[\text{Fe}(\text{phen})_3]^{2+}$ , we analyzed the samples of  $[\text{Fe}(\text{phen})_3]^{2+}@ZIF-70$ ,  $[\text{Fe}(\text{phen})_3]^{2+}@ZIF-68$  and  $[\text{Fe}(\text{phen})_3]^{2+}@ZIF-69$  composites after 2 h grinding by looking into their  $\text{N}_2$  adsorption behaviour, which shows the BET surface areas of 12, 15 and  $23 \text{ m}^2 \text{ g}^{-1}$ , respectively for the above series of samples. This result clearly indicates that, higher the loading of  $[\text{Fe}(\text{phen})_3]^{2+}$  inside the ZIF pore, lesser the surface area of the composite.  $[\text{Fe}(\text{phen})_3]^{2+}@ZIF-70$  composite has larger pore as well as more loading, which blocks the pores to access nitrogen gas. It is expected that the variable nano confined space obtained in FeNC-68, -69, and -70 will provide the distinctive condition for the facile electrochemical reaction in terms of mass transport and apparent electrokinetics.[16] The uniqueness of nanoporous electrodes also depends on the morphology and dimensions along with the surface area of the electrode. We believe that

the molecular motion will be facile due to this nano confinement and this will have a favoring influence on the electro-kinetics.

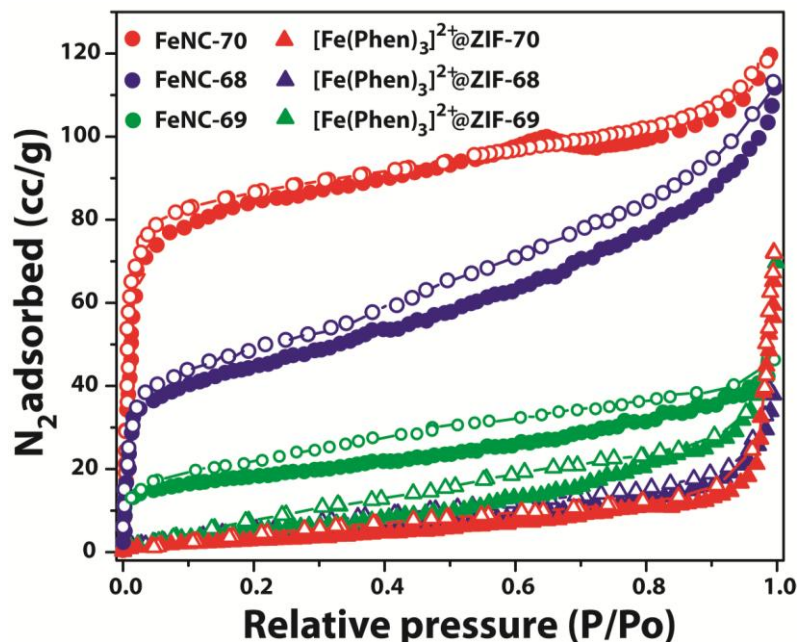


**Figure 6.5.**  $N_2$  adsorption isotherms of the prepared catalysts [(FeNC-70, 68, 69) after calcinations at 900 °C, followed by acid wash] were collected at 77 K and 1 atm pressure (filled and open spheres are adsorption and desorption branches, respectively.); comparison is made with the corresponding  $[Fe(phen)_3]^{2+}@ZIFs$  (ZIF- 70, 68 and 69) composites after neat 2 h grinding (filled and open triangles are for adsorption and desorption branches, respectively).

### 6.3.3. Thermogravimetry Analysis

The thermal stability of the prepared samples with their ancestors has been evaluated by thermogravimetric analysis (TGA) (Figure 6.6). The TGA profiles for ZIF-68, 69 and 70 (after activation at 150 °C) under  $N_2$  atmosphere show only slight weight loss up to 358 °C (ZIF-68), 371 °C (ZIF-69) and 332 °C (ZIF-70). This observation confirms that there

are no guest solvent molecules inside the ZIFs pores and they are stable up to those temperatures. In the cases of ZIF-68 and 69, a gradual weight loss step has been observed between 350-415 °C (~20%) corresponding to partial decomposition of ZIF. On the other hand, in the case of ZIF-70, the partial thermal degradation occurs in between 325 to 415 °C presumably due to the variation of the ligand in the frameworks.

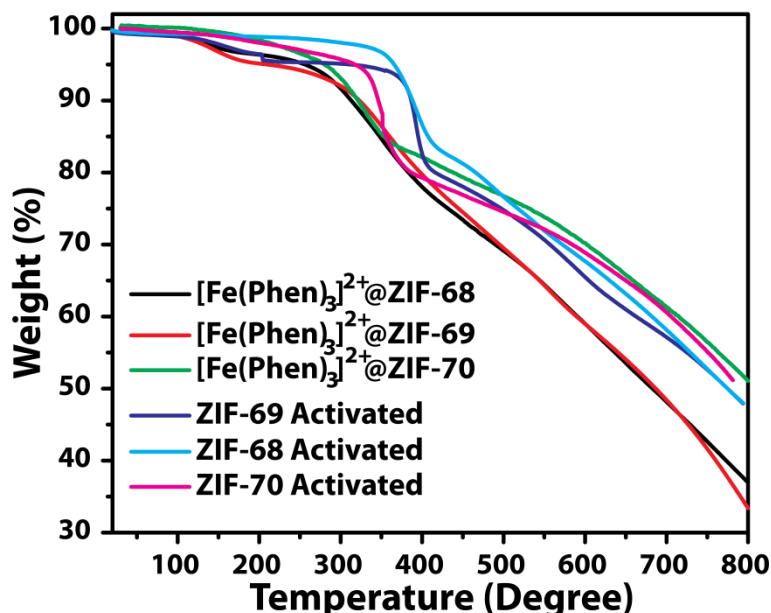


**Figure 6.6.** Thermogravimetric analysis (TGA) of ZIF-70, ZIF-68 and ZIF-69 of guest-free samples as well as with  $[\text{Fe}(\text{phen})_3]^{2+}$  complex as guest inside the frameworks of ZIF-68, 69 and 70.

Further, the thermal degradation is extended up to 800 °C with ~30% weight loss could be due to complete degradation of ZIFs. However, in case of ZIF-68 and 69 with  $[\text{Fe}(\text{phen})_3]^{2+}$ , the weight loss has been observed at early 120 °C than the guest-free ZIFs (ZIF-68 and 69) which is mainly due to the gasification of unreacted phenanthroline molecules (melting point of 1,10 phenanthroline is 117 °C). Whereas, in the case of ZIF-70 with  $[\text{Fe}(\text{phen})_3]^{2+}$  complex, the weight loss started from ~280 °C is apparently due to

the decomposition of the  $[\text{Fe}(\text{phen})_3]^{2+}$  complex and partial degradation of ZIF in the framework which emphasise the confinement of  $[\text{Fe}(\text{phen})_3]^{2+}$  complex within the pores of ZIF-70. Subsequently, in the cases of ZIF-68 and 69 with  $[\text{Fe}(\text{phen})_3]^{2+}$ , the weight loss at 350 °C is due to the partial degradation of ZIF and the 40% weight loss from the 400-800 °C which could be due to the complete degradation of the framework for the composites  $[\text{Fe}(\text{phen})_3]^{2+}$ @ZIF-68 and 69. However, in the case of  $[\text{Fe}(\text{phen})_3]^{2+}$ @ZIF-70, only 30 % weight loss occurs from 400 °C which further confirms the more amount of  $[\text{Fe}(\text{phen})_3]^{2+}$  complex accessed inside the ZIF-70 pore due to its large pore aperture.

#### 6.3.4. XRD Analysis

Powder X-ray diffraction (PXRD) was performed to ensure the crystallinity as well as phase purity of the specimens (Figure 6.7a-c). The pattern of the as-synthesized ZIF-70 (green) confirms the phase purity by comparing with the simulated PXRD pattern from single crystal data. After grinding the  $[\text{Fe}(\text{phen})_3]^{2+}$ @ZIF-70 composite for 2 h, a notable peak broadening is observed which indicates that majority of  $[\text{Fe}(\text{phen})_3]^{2+}$ @ZIF-70 composite material becomes partially amorphous in nature compared to the as-synthesized ZIF-70. As we can see that some of the characteristic peaks of ZIF-70 are still observed in the composite, which further indicates that the mechanical grinding does not significantly destroy the ZIF-70 framework (red curve). The amorphization results due to the prolonged irreversible pressure applied to the  $[\text{Fe}(\text{phen})_3]^{2+}$ @ZIF-70 composite during the grinding process. After annealing, the PXRD pattern of the as-synthesized FeNC-70, shows two characteristic carbon peaks at 2 $\theta$  (25 and 44°) which signify the complete conversion of the carbonaceous material after the heat treatment (900 °C) of the  $[\text{Fe}(\text{phen})_3]^{2+}$ @ZIF-70 composite. A similar result was also observed in

the case of  $[\text{Fe}(\text{phen})_3]^{2+}@\text{ZIF-68}$  and  $[\text{Fe}(\text{phen})_3]^{2+}@\text{ZIF-69}$  as shown in the HRTEM results.

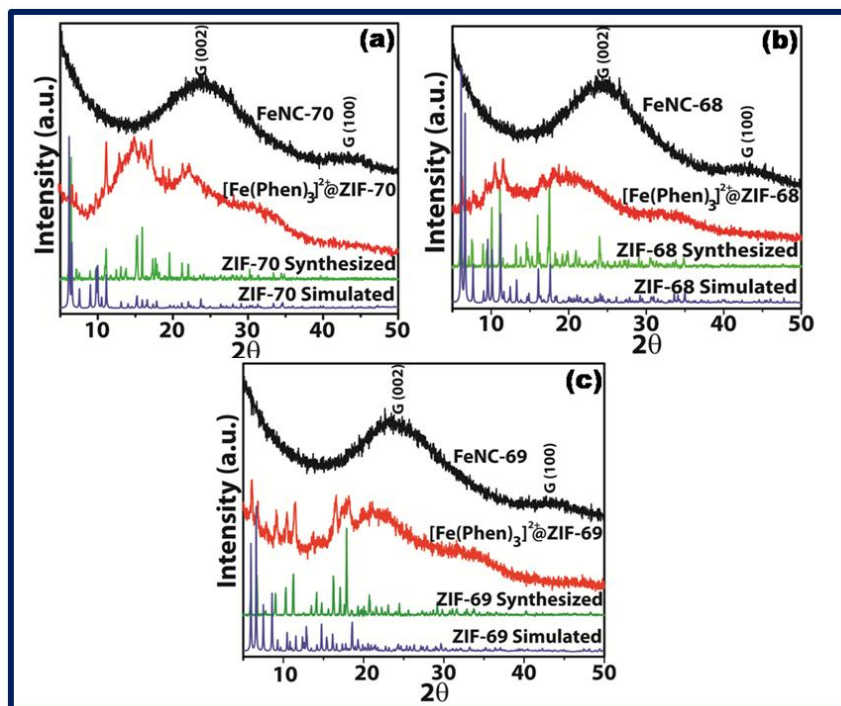


**Figure 6.7.** Comparison of the experimental powder X-ray diffraction (PXRD) patterns of (a) as-synthesized ZIF-70 (green),  $[\text{Fe}(\text{phen})_3]^{2+}@\text{ZIF-70}$  composite (red) and FeNC-70 (black) with simulated one (blue) from single crystal XRD, (b) as-synthesized ZIF-68,  $[\text{Fe}(\text{phen})_3]^{2+}@\text{ZIF-68}$  composite and FeNC-68 with simulated one, (c) as-synthesized ZIF-69,  $[\text{Fe}(\text{phen})_3]^{2+}@\text{ZIF-69}$  composite and FeNC-70 with simulated one.

### 6.3.5. XPS Analysis

The complementary structural evidence of FeNC-70, which is recognized as the most active electrocatalyst among the prepared samples is obtained from X-ray photoelectron spectroscopy (XPS). The full range spectrum of FeNC-70 (Figure 6.8a) shows the

presence of carbon, nitrogen, oxygen and iron in the matrix. The peak at 284.5 eV corresponds to C (Figure 6.8a) which ensures the complete conversion of MOFs and carbon precursors into graphitic carbon. This is well line up with the results of HRTEM, PXRD and Raman analyses.

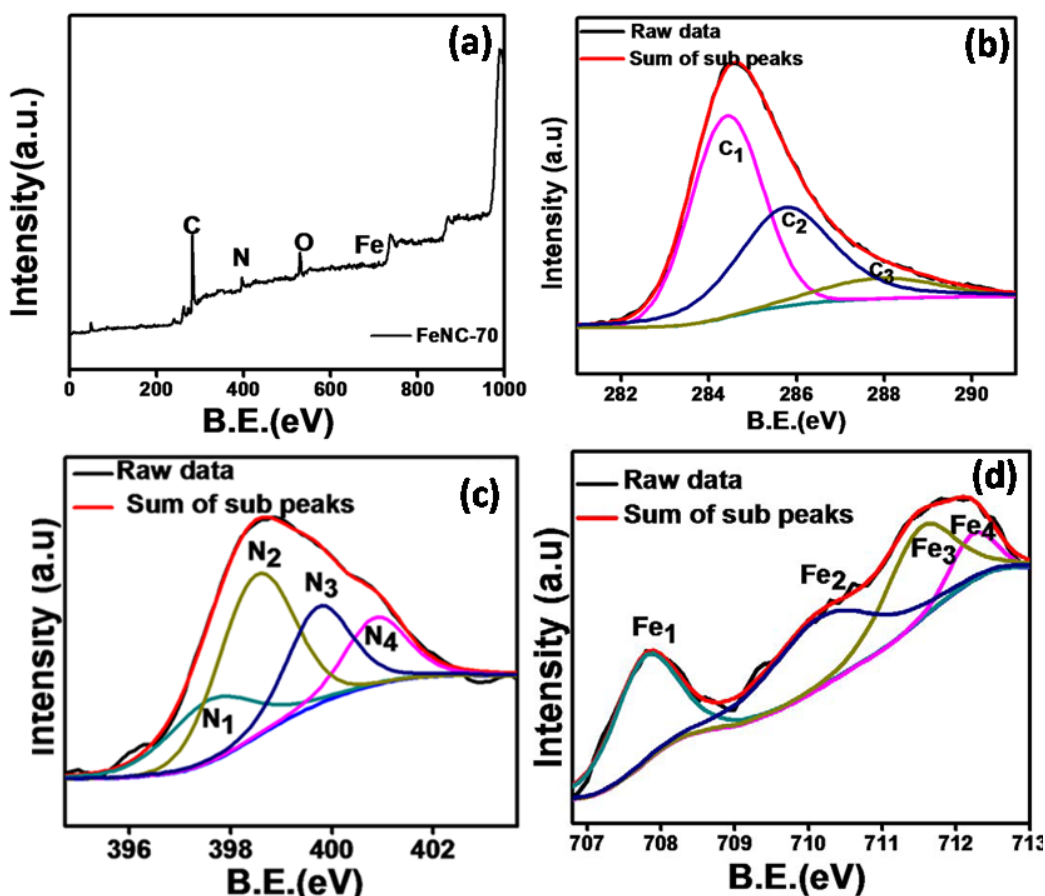


**Figure 6.8.** (a) Long range XPS spectrum of FeNC-70, (b) C1s spectra of FeNC-70, (c) N 1s spectra of FeNC-70 and (d) Fe 2p spectra of FeNC-70.

Further, the C 1s spectrum of FeNC-70 has been deconvoluted into three sub peaks namely C<sub>1</sub>, C<sub>2</sub> and C<sub>3</sub> which are shown in Figure 6.8b. The intense peak at 284.5 eV corresponds to the graphitic carbon (C=C) which gives the clear indication of complete conversion of ZIF based composite into graphitic carbon. The peak at 285.8 eV

corresponds to the  $sp^3$  carbon where carbon may bind with oxygen or nitrogen (C-O or C-N). The peak at higher binding energy 287.9 eV corresponds to the epoxy carbon (C-O-C). Subsequently, the N 1s spectrum shown in Figure 6.8c is deconvoluted into four peaks. The peak  $N_1$  at 397.5 eV is recognized as the nitrogen bound with Fe. [17] The peaks  $N_2$ ,  $N_3$  and  $N_4$  at 398.8, 399.9 and 400.9 eV correspond to pyridinic, [18] pyrrolic [19] and graphitic nitrogen, [20] respectively. Among the four peaks, the intensity of  $N_2$  corresponds to pyridinic nitrogen is more suggesting that the contribution of pyridinic nitrogen (41 at.wt %) is more than the other nitrogen species of the total nitrogen content. Most importantly, the pyridinic nitrogen is believed as the responsible active site for ORR.

Further, the Fe 2p spectrum of FeNC-70 has been deconvoluted into four sub peaks as shown in Figure 6.8d. The peak at 707.8 eV was recognized as  $Fe_1$  due to zero state of Fe or iron carbide ( $Fe_3C$ ). The formation of  $Fe_3C$  may occur during the annealing process of  $Fe(phen)_3@ZIF-70$  composite. The peaks at 710.2 eV and 711.5 eV are named as  $Fe_2$  and  $Fe_3$  corresponding to the Fe in the form of ionic state such as  $Fe^{2+}$  and  $Fe^{3+}$ , respectively. From this, we infer that, Fe may be bound with nitrogen in the form of  $Fe^{2+}N_4/C$  or  $Fe^{3+}N_4/C$ . It is important to note that,  $Fe^{3+}N_4/C$  is inactive for ORR and it could be neglected from the raw of active sites. The presence of  $Fe^{2+}$  peak at 710.1 eV corresponding to the Fe bonded with N, which further helps to claim the coordination of N with Fe as already evident from the  $N_1$  peak. The role of Fe is expected to enhance the stable incorporation of the pyridinic N on the carbon matrix.

### 6.3.6. EDAX Analysis

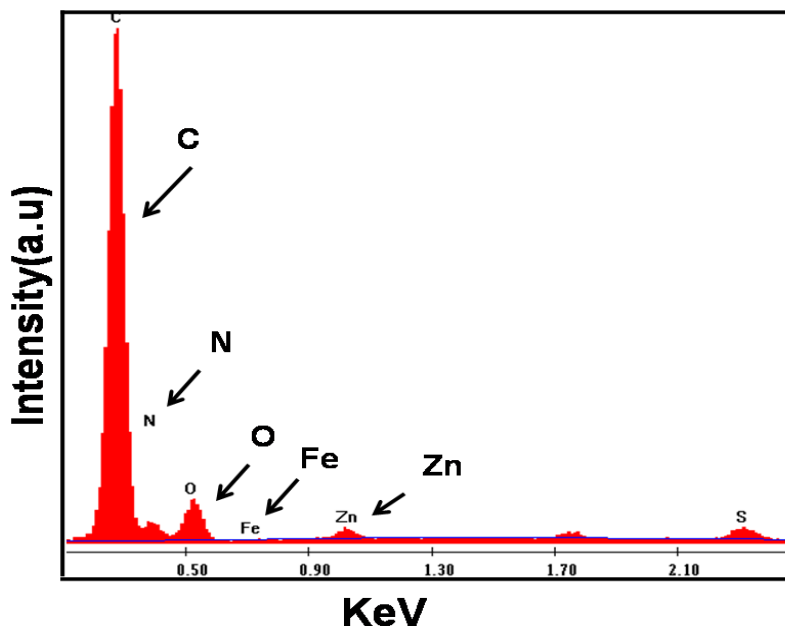


*Figure 6.9. EDAX analysis of FeNC-70.*

The EDAX analysis of the samples derived from ZIF was carried out to evaluate the amount of elemental doping on the resulting carbon materials (Figure 6.9). Accordingly, Table 6.1 summarizes the EDAX quantification of the elements present in the active catalyst FeNC-70. The resulting catalyst shows that carbon is predominant which ensures the complete carbonization of the ZIF molecules into the nitrogen doped carbon. The content of nitrogen is 14 at. wt. %, which is remarkably higher than the other reported values. The higher content of nitrogen is presumably due to the inherent content of nitrogen from ZIF and from the phenanthroline molecule. The EDAX spectrum also discloses the presence of Fe with in trace amount in the active FeNC-70 catalyst as similar to the XPS analysis. Of course, oxygen molecule also present in the resulting nitrogen doped carbon material which is mainly due to adsorbed oxygen from the

atmosphere. The negligible amount of Zn is mainly due to the unremoved Zn metal impurities during the acid wash.

Table 6.1. EDAX quantification of elements in the active FeNC-70 catalyst.

Element	Weight Percentage %	Atomic Percentage %
C K	72.26	77.09
N K	14.88	13.61
O K	11.06	8.86
ZnL	1.27	0.25
S K	0.43	0.17
FeK	0.10	0.02
Total	100.00	100.00

### 6.3.7. Raman Spectral Analysis

In general, the Raman spectral analysis is an important tool to analyze the defects and disorder of the carbon based materials. Accordingly, the defects and disorder nature of the FeNC catalyst was analyzed with the aid of Raman spectra (Figure 6.10). The FeNC catalyst exhibits two discrete peaks at 1320 and 1526  $\text{cm}^{-1}$ , corresponding to the D and G band, respectively. The graphitic peak (G band) due to the  $E_{2g}$  vibrational mode appears at 1515-1530  $\text{cm}^{-1}$  whereas the defective band (D band) due to the  $A_{1g}$  vibrational mode

appears at 1315-1330  $\text{cm}^{-1}$ . The extent of defects of the FeNC catalyst was estimated by measuring the intensity ratio of the D and G band ( $I_D/I_G$ ), which gives the highest ratio (1.36) for FeNC-70. This is attributed mainly to the higher defects imparted in the system with variable pore size distribution as  $[\text{Fe}(\text{phen})_3]^{2+}$ @ZIF-70 transforms to FeNC-70. Further, the higher  $I_D/I_G$  ratio of FeNC based catalysts ensures the complete transformation of ZIF composite into the graphitic porous carbon.

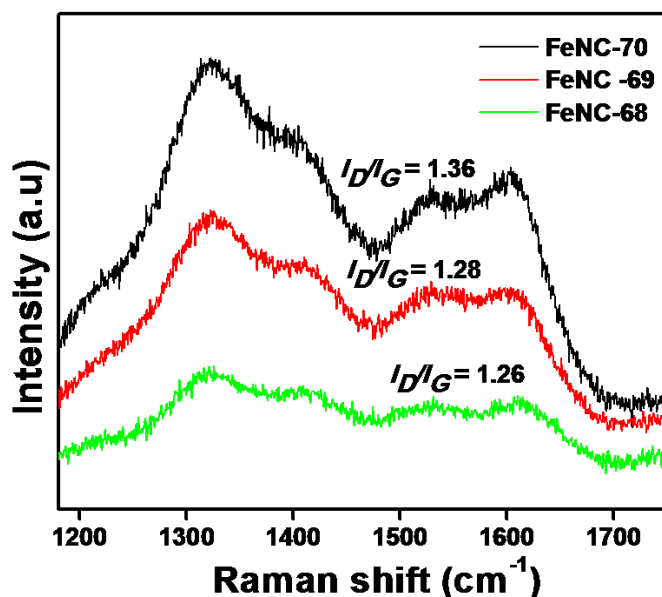


Figure 6.10. Raman spectra of FeNC based catalysts.

### 6.3.8. Electrochemical Studies

#### 6.3.8.1. Cyclic Voltammetry (CV)

The electrocatalytic activity of the synthesized catalysts was examined by using cyclic voltammetry (CV) and rotating disc electrode (RDE) methods. The CV profile of our catalysts in oxygen saturated 0.5 M  $\text{HClO}_4$  solution cycled between 1.2 to 0.0 V vs NHE at a scan rate of 5  $\text{mV s}^{-1}$  is shown in Figure 6.11a. The voltammogram for FeNC-68 has

a well resolved cathodic peak corresponding to ORR with 0.51 V as the peak potential and 0.73 V as the onset potential. In the case of FeNC-69, the peak appears at 0.43 V with the onset potential at around 0.67 V. Obviously, more positive onset potential with larger current density exhibited by FeNC-68 is a good indication of faster ORR kinetics on FeNC-68 compared to FeNC-69. More interestingly, in the case of FeNC-70, the peak corresponding to ORR occurs at 0.64 V with the onset potential at 0.80 V, which is 70 mV positive than FeNC-68. The more positive onset potential and higher oxygen reduction current clearly emphasize that FeNC-70 possesses higher catalytic activity compared to FeNC-68 and -69. This undoubtedly indicates the determining role played by the optimum pore size distribution and nitrogen content for ORR.

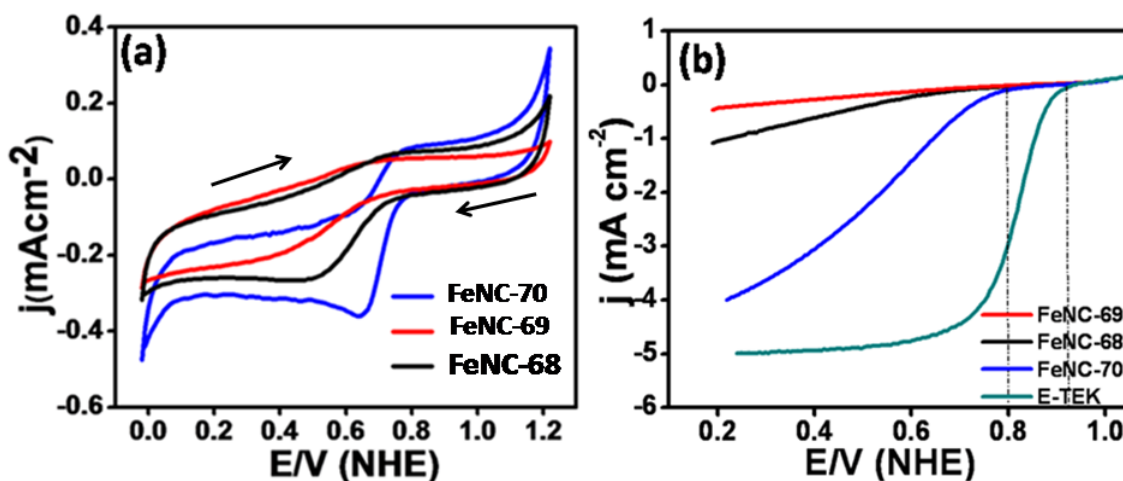


**Figure 6.11.** (a) CVs for FeNC-68, FeNC-69 and FeNC-70 recorded in oxygen saturated solution of 0.5 M  $\text{HClO}_4$  at a scan rate of  $5 \text{ mV s}^{-1}$  (b) ORR polarization plots of FeNC-68, FeNC-69, FeNC-70 and 20 wt. % E-TEK catalysts recorded at a scan rate of  $10 \text{ mV s}^{-1}$  (rotation rate: 1600 rpm).

### 6.3.8.1. Rotating Disc Electrode Method (RDE)

The RDE of the catalysts in 0.5 M HClO<sub>4</sub> gives more concise information on the ORR activity of the systems. The study testifies the significant ORR activity of FeNC-70 as can be seen from the linear sweep voltammograms (LSVs) taken at 1600 rpm (Figure 6.11b). The LSVs of FeNC-69 and FeNC-68 show mixed kinetic diffusion currents from 0.30 to 0.50 V with an onset potential at 0.67 and 0.73 V, respectively. However, FeNC-70 shows the mixed diffusion kinetics from 0.50 to 0.72 V with the onset potential at around 0.80 V. The strong ORR activity of FeNC-70 is again reflected in its highest half-wave potential among the three compositions, which follows the order: FeNC-70 (0.58 V) > FeNC-68 (0.47 V) > FeNC-69 (0.40 V). We have effectively compared the ORR activity of our catalysts with 20 wt % Pt/C (E-TEK). Even though FeNC-70 exhibits an overpotential difference of 110 mV and lower limiting current density with respect to E-TEK, the performance profile of FeNC-70 is comparable or even higher than the few similar systems reported in the literature.

### 6.3.8.3. Koutecky-Levich (K-L) Plots

The number of electrons transferred during ORR was calculated by using Koutecky-Levich (K-L) plot [21] (Figure 6.12a). The K-L equation and the parameters involved in it are explained as follows:

$$1/j = 1/nFkC_{O_2} + 1/0.62nFAD_{O_2}^{2/3}C_{O_2}^*v^{-1/6}\omega^{1/2}$$

where, 'j', 'n', 'A' and 'F' are the measured current density, number of transferred electrons per oxygen molecule, area of the electrode and Faraday constant (96500 C mol<sup>-1</sup>), respectively. 'D<sub>O<sub>2</sub></sub>' is the diffusion coefficient of the electrolyte, 'C<sub>O<sub>2</sub></sub><sup>\*</sup>' is the

concentration of the dissolved oxygen in the electrolyte, ' $\nu$ ' is the kinematic viscosity of the electrolyte, ' $\omega$ ' is the angular velocity of the electrode. In this study, the values used for  $D_{O_2}$ ,  $C_{O_2}^*$  and ' $\nu$ ' are  $1.9 \times 10^{-5} \text{ cm}^2 \text{ s}^{-1}$ ,  $1.22 \times 10^{-6} \text{ mol cm}^{-3}$  and  $0.01 \text{ cm}^2 \text{ s}^{-1}$ , respectively. Finally, the K-L slope ( $1/B$ ) has been attained by plotting  $1/j$  against  $1/\omega^{-1/2}$  as illustrated in Figure 6.12a. Further, from the resulted value of  $1/B$ , the ' $n$ ' at different potential has been calculated from the K-L equation. The values of ' $n$ ' as a function of potential are plotted in Figure 6.12b.

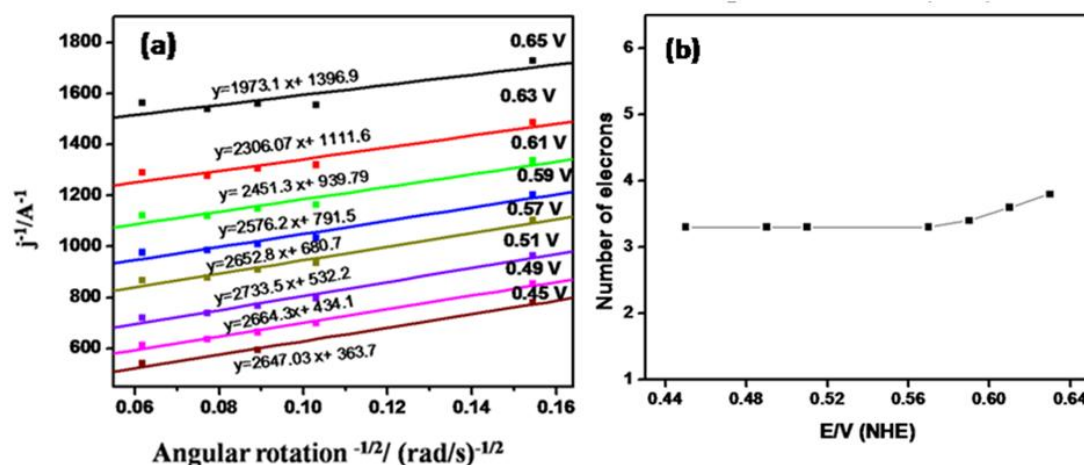


**Figure 6.12.** (a) Koutecky-Levich (K-L) plots of FeNC-70 and (b) the number of electrons transferred for ORR as calculated from the K-L plots.

The resulting values of ' $n$ ' are 3.3 to 3.8 along the considered potential range, which indicate that FeNC-70 reduces the oxygen molecule predominantly into water *via* the four electron pathway with trace amount of  $\text{H}_2\text{O}_2$ . A comparison between the ' $n$ ' values as reported in some of the recent studies and the present work clearly reveals that, except few systems, the performance displayed by our system is either comparable or even superior to many of the reported results.

#### 6.3.8.4. Accelerated Durability Test (ADT)

The stability of non precious ORR catalysts is an important performance criterion to successfully project them as replacements to the Pt based catalysts. To get some insights into the durability aspects of our catalyst, we have carried out an accelerated durability test (ADT) by comparing with a commercial E-TEK catalyst. ADT was performed by subjecting the materials a potential cycling between 1.2 to 0.0 V vs NHE in oxygen saturated 0.5 M HClO<sub>4</sub> at a scan rate of 100 mV s<sup>-1</sup> at room temperature for 1000 cycles. Prior to the experiment, LSV was taken at different rotation rates to evaluate the original performance characteristics of the catalyst. After the 1000 cycles, *i.e.* after ADT, the LSV was again taken and calculated the extent of degradation.

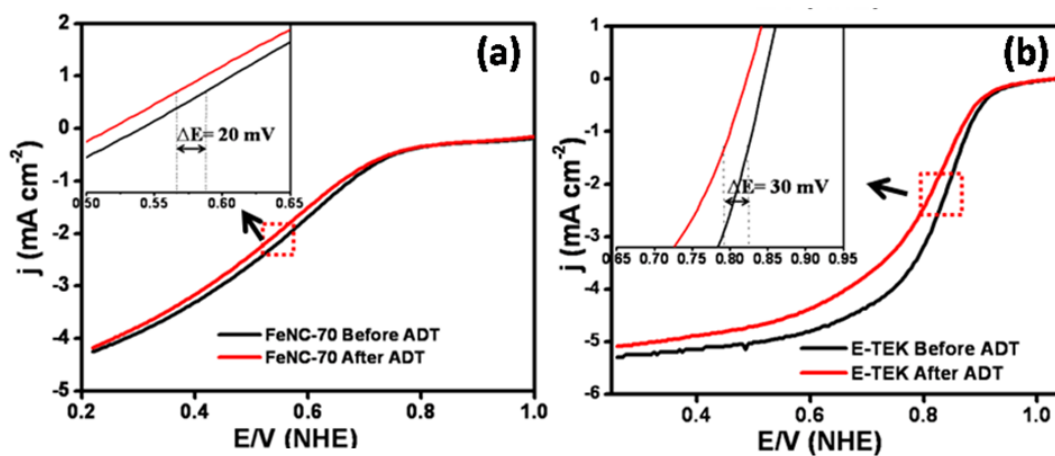


**Figure 6.13.** Accelerated durability test (ADT) for (a) FeNC-70 and (b) 20 wt. % Pt/C (E-TEK).

The comparison of the LSVs before and after ADT clearly depicts that FeNC-70 is electrochemically more stable than the commercial Pt catalyst in the acid medium even after long cycles. From Figure 6.13, it could be observed that, the Pt catalyst suffers from

a 30 mV negative shift in the ORR activity at a half wave potential of 0.82 V vs. NHE after ADT, whereas FeNC-70 displays a drop of only 20 mV at its half wave potential of 0.58 V vs. NHE. The potential cycling in the ADT experiment is expected to trigger Pt dissolution and sintering which results the 30 mV drop after the test. However, in case of FeNC-70 the potential cycling does not affect significantly due to the stable coordination of Fe with nitrogen and carbon (Fe-N-C). This observation further supports that the Fe-N coordination with the carbon framework is reasonably stable and the normal testing conditions and acidic environments in a real fuel cell testing system may not trigger significant leaching of the active species. Since ADT states that FeNC-70 catalyst is more stable in acid medium, formation of an undesirable oxidizing species like Fenton's reagent (*i.e.*  $\text{Fe}^{2+} + \text{H}_2\text{O}_2 \rightarrow \text{Fe}^{3+} + \text{OH}^\cdot + \text{OH}^-$ ) under the acidic environment of cell testing is unlikely in the present case.

### 6.3.8.5. Methanol Tolerance Study

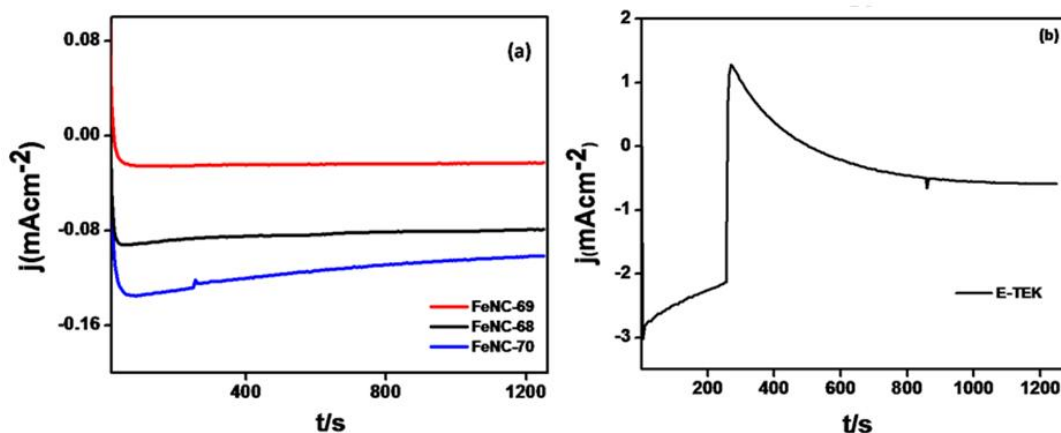


**Figure 6.14.** (a) Chronoamperometric response for the methanol crossover study of FeNC-68, FeNC-69, FeNC-70 and (b) E-TEK in oxygen saturated 0.5 M HClO<sub>4</sub>.

Tolerance towards CO and methanol is an important criterion for a good cathode catalyst especially in direct methanol fuel cells (DMFCs) where the crossover methanol not only reduces the performance but also the durability. Hence, to study the methanol tolerance and poisoning effect, we carried out the ORR studies by adding methanol (3 M MeOH) in to the 0.5 M HClO<sub>4</sub> by chronoamperometry technique. Figure 6.14 shows the comparative methanol tolerance study of the FeNC and E-TEK catalysts by means of chronoamperometric responses. The experiment was performed by changing the initial potential 0.3 to 0.64 V for 1250 s where more oxygen reduction takes place. After the addition of 3 M methanol in 0.5 M HClO<sub>4</sub> at 250 s, the FeNC based catalysts do not show any change in the ORR current whereas in case of E-TEK, the ORR current suffers by sudden fluctuation. The aforementioned results clearly reveal that the FeNC based catalysts are inactive for methanol oxidation which further emphasis that these systems can serve as fuel tolerant cathode electrocatalysts for direct methanol fuel cells (DMFCs).

### 6.3.9. Structure of Active Sites

Addressing the nature of the active site which determines the ORR activity is an important issue in non PGM catalysts. In XPS, the Fe 2p spectra (Figure 6.8d) indicate the presence of Fe<sup>2+</sup> and Fe<sup>3+</sup>, which suggests that the possible active sites can be Fe<sup>2+</sup>N<sub>4</sub> and Fe<sup>3+</sup>N<sub>4</sub>. However, the later gets expelled as the effective ORR active site due to its strong bonding affinity with water. As proposed by Jaouen *et al.*, the Fe/N/C based active site is favoured only at a lower content of Fe (up to 0.1 wt %). [22] Later, it was found that among the three FeN<sub>4</sub>/C like coordinations, FeN<sub>2+2</sub>/C is inactive for ORR due to its inability to form adduct with oxygen. On the other hand, N-FeN<sub>2+2</sub>/C and FeN<sub>4</sub>/C (Fe

coordinated with four pyrrole type nitrogen) are more active towards the reaction. [5] However; the possibility for the formation of later is negligible in graphitic systems. The Fe content in the present case as quantified by EDAX (Figure 6.9) is nearly 0.1 wt. % and is expected to favour the formation of  $\text{FeN}_x\text{C}$  based active sites with more contributions from N- $\text{FeN}_{2+2}/\text{C}$  coordination. Previously, we scrutinized the optimum content of Fe for the preparation of the Fe/N/C catalysts and found that an amount exceeding 0.5 wt. % leads to the formation of  $\text{Fe}_3\text{C}$ . [4] Even though we maintained 0.5 wt. % of Fe for the preparation of FeNC-70 in the present case, the Fe content estimated by EDAX was only 0.1 wt. % presumably due to the intercalation of Fe into the graphite porous carbon matrix.

#### 6.4. Conclusions

In conclusion, preparation of well-structured Fe-N-doped porous carbon was demonstrated by embedding followed by pyrolysis of  $[\text{Fe}(\text{phen})_3]^{2+}$  complex into the ZIF-68, 69 and 70. Among the three resulting composite catalysts, FeNC-70 shows the highest BET surface area compared to FeNC-68 and 69. FeNC-70 is highly efficient to reduce  $\text{O}_2$  molecule through the desired  $4e^-$  pathway. The resultant onset potential and ' $n$ ' values have been compared with that of the reported non-platinum catalysts. This comparison clearly reveals that, except few systems, the performance displayed by our system is either comparable or even superior to many of the reported results. The existences of micro porosity of ZIFs are replicated in terms of the porosity of the carbons derived from them. The nano confined space as demarcated by the porous carbon walls along with the heteroatom doped active sites on the walls provide the exceptional conditions for ORR. Therefore, looking at the present performance status of FeNC-70

and the great prospect of these classes of materials to further reduce the overpotential for oxygen reduction, the strategy adopted here signifies facile routes for making cost effective and mass producible oxygen reduction electrocatalysts for PEM fuel cell applications.

## 6.5. References

- [1] Retrieved from the web <http://www.platinum.matthey.com/pgm-prices/price-charts/>
- [2] R. Jasinski, *Nature*, **1964**, *201*, 1212.
- [3] (a) M. Lefevre, E. Proietti, F. Jaouen and J. P. Dodelet, *Science*, **2009**, *307*, 71; (b) P. H. Matter, E. Wang, J. M. M. Millet, U. S. Ozkan, *J. Phys. Chem. C.*, **2007**, *111*, 1444; (c) H. R. Byon, J. Suntivich, E. J. Crumlin and Y. S. Horn *Phys. Chem. Chem. Phys.*, **2011**, *13*, 21437; (d) K. Kamiya, K. Hashimoto and S. Nakanishi, *Chem. Commun.*, **2012**, *48*, 10213.
- [4] T. Palaniselvam, R. Kannan, S. Kurungot, *Chem. Commun.*, **2011**, *47*, 2910.
- [5] U. I. Kramm, J. Herranz, N. Larouche, T. M. Arruda, M. Lefevre, F. Jaouen, P. Bogdanoff, S. Fiechter, I. Wurmbach, S. Mukerjee and J. P. Dodelet, *Phys. Chem. Chem. Phys.*, **2012**, *14*, 11673.
- [6] (a) L. Qu, Y. Liu, J. B. Baek and L. Dai, *ACS Nano*, **2010**, *4*, 1321; (b) T. Chen, Z. Cai, Z. Yang, L. Li, X. Sun, T. Huang, A. Yu, H. G. Kia and H. Peng, *Adv. Mater.* **2011**, *23*, 4620; (c) Z. Lin, M. Song, Y. Ding, Y. Liu, M. Liua and C. Wong, *Phys. Chem. Chem. Phys.*, **2012**, *14*, 3381; (d) Z. Sheng, L. Shao, J. Chen, W. Bao, F. Wang and X. Xia, *ACS Nano*, **2011**, *5*, 4350.
- [7] (a) W. Zhang, Z. H. Huang, C. Zhou, G. Cao, F. Kang and Y. Yang., *J. Mater. Chem.*, 2012, *22*, 7158; (b) L. Liu, Q. F. Deng, T.Y. Ma, X. Z. Lin, X. X. Hou, Y. P. Liu and Z. Y. Yuan, *J. Mater. Chem.*, **2011**, *21*, 16001.

- [8] R. Banerjee, A. Phan, B. Wang, C. Knobler, H. Furukawa, M. Keefe, O. Yaghi, *Science*, **2008**, *319*, 939.
- [9] P. Horcajada, C. Serre, G. Maurin, N. A. Ramsahye, F. Balas, M. Regi, M. Sebban, F. Taulelle, G. Férey, *J. Am. Chem. Soc.* **2008**, *130*, 6774.
- [10] B. Liu, H. Shioyama, T. Akita and Q. Xu, *J. Am. Chem. Soc.* **2008**, *130*, 5390.
- [11] J. Hu, H. Wang, Q. Gao, H. Guo, *Carbon*, **2010**, *48*, 3599.
- [12] (a) B. Liu, H. Shioyama, H. Jiang, X. Zhang and Q. Xu, *Carbon*, **2010**, *48*, 456; (b) H. L. Jiang and Q. Xu, *Chem. Commun.*, **2011**, *47*, 3351; (c) H. L. Jiang, B. Liu, Y. Q. Lan, K. Kuratani, T. Akita, H. Shioyama, F. Zong and Q. Xu, *J. Am. Chem. Soc.*, **2011**, *133*, 11854.
- [13] E. Proietti, F. Jaouen, M. Lefèvre, N. Larouche, J. Tian, J. Herranz and J. P. Dodelet, DOI: 10.1038/ncomms1427.
- [14] (a) G. Goenaga, S. Ma, S. Yuan and D. J. Liu, *ECS Trans.* **2010**, *33*, 579; (b) S. Ma, G. A. Goenaga, A. V. Call and D. J. Liu, *Chem. Eur. J.*, **2011**, *17*, 2063; (c) D. Zhao, J. L. Shui, C. Chen, X. Chen, B. M. Repogle, D. Wang and D. J. Liu, *Chem. Sci.*, **2012**, *3*, 3200.
- [15] P. Pachfule, B. P. Biswal and R. Banerjee, *Chem. Eur. J.*, **2012**, *18*, 11399.
- [16] J. H. Bae, J. H. Han and T. D. Chung *Phys. Chem. Chem. Phys.*, **2012**, *14*, 448.
- [17] E. Y. Jiang, D. C. Sun, C. Lin, M. B. Tian, H. L. Bai and S. L. Ming, *J. Appl. Phys.*, **1995**, *78*, 2596.

- [18] B. Stohr, H. P. Boehm, R. Schlögl, *Carbon*, **1991**, 29, 707.
- [19] P. H. Matter, L. Zhang, U. S. J. Ozkan, *Catal.* **2006**, 239, 83.
- [20] J. R. Pels, F. Kapteijn, J. A. Moulijn, Q. Zhu and K. M. Thomas, *Carbon*, **1995**, 33, 1641.
- [21] S. M. Unni, V. M. Dhavale, V. K. Pillai and S. Kurungot, *J. Phys. Chem. C*, **2010**, 114, 14654.
- [22] F. Jaouen, J. P. Dodelet, *Electrochim. Acta*, **2007**, 52, 5975.

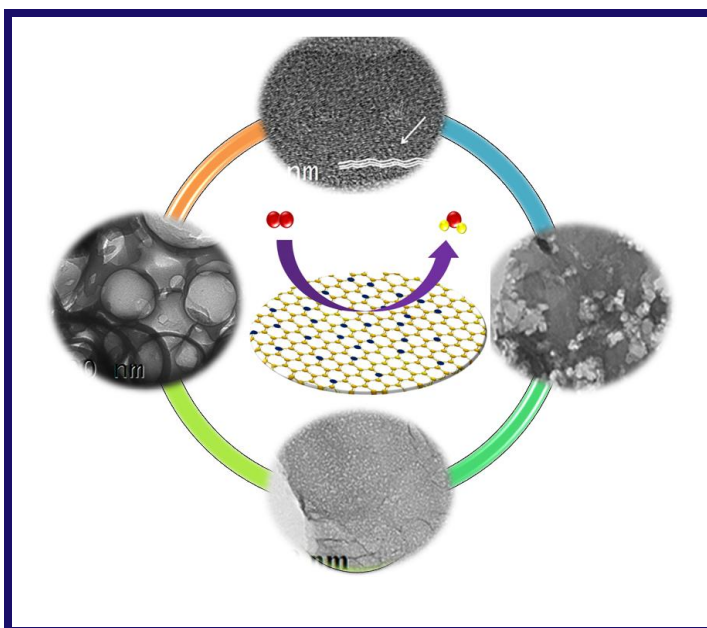
## Chapter 7

### Summary and Conclusions

---

This final chapter of the thesis deals with remarkable conclusions of the present study on the development of various nitrogen doped carbon nano morphologies for ORR. It highlights the novel aspects

of the methodology adopted here for the synthesis of the electrocatalysts. It also signifies the choice of the materials towards the effective nitrogen doping. Further, it précis the advantages of this approach



including the identification of nitrogen doped activesites, inclusion of pores on graphene and creation of edge sites by chipping off the quantum dots *etc.* Finally, related promising developments and challenges faced by the existing catalysts are also outlined to explain the future scope applicable to this work.

---

It is clear that polymer electrolyte fuel cells particularly PEMFCs offer clean and efficient technology from renewable resources to accomplish the future energy needs. However, in present scenario, the technology is hampered towards commercialisation by several factors including expensive fuel cell components and material related challenges. Therefore, usage of cheaper materials, particularly catalyst, possessing intrinsic higher efficiency could help to overcome the cost related challenges of PEMFCs. In this perspective, heteroatom doped carbonaceous materials, mainly nitrogen-doped systems, are regarded as the potential candidates owing to their remarkable electrical and electronic properties as they play the critical role in the cathode catalysis in fuel cells. Very recently, there has been some breakthrough using nitrogen-doped carbonaceous materials based electrocatalysts as possible replacements for Pt in fuel cells. The usage of nitrogen-doped carbonaceous materials reduces the cost of the MEAs significantly which has been discussed in Chapter 1. Therefore, the main prerequisite for the future development of fuel cells is the finding of suitable non-noble electrocatalysts with higher efficiency to compete Pt/C, the most expensive component in an MEA. Accordingly, the entire thesis work deals with the focused effort to develop the suitable non-Pt electrocatalyst by means of nitrogen doping on different carbon nano morphologies. Besides, the influences of the edge effects and nanoconfinement of carbon nanostructures (CNS) also could be studied thoroughly by changing the morphology of CNS from one dimensional to three dimensional.

The major accomplishments of the present thesis work could be summarized as follows:

### **7.1. Facile Construction of Iron Nitride-doped Carbon Nanofiber as a Non-Pt Electrocatalyst**

It is widely believed that the nitrogen doping on carbon especially with coordination of transition metal (Fe or Co) is the possible way for the replacement of Pt/C. Very recently, one dimensional carbon materials, particularly CNF, gains much attention due to their unique morphology, reasonable surface area, anisotropy and their inherent electrical conductivity. By taking the advantage of the unusual morphology of the CNF, iron nitride doping on the inner wall of CNF was attempted to design the non-Pt electrocatalyst. For the effective comparison, the metal free nitrogen doped CNF also was prepared. In both the cases, the nitrogen was identified as the key element for the remarkable ORR of the homemade catalyst. While nitrogen doping is done along with Fe, the ORR performance improved significantly due to the synergistic effect between Fe-N and carbon. Moreover, it was identified that the doped nitrogen causes the buckling of graphene layers (*nanopockets*) on the side wall of CNF due to the introduction of pentagonal defects. It is also worthy to mention that the remarkable ORR of the prepared nitrogen doped CNF catalysts has a specialty with respect to its structure. This structural feature is the key factor which helped to achieve both effective FeN<sub>x</sub> doping and creation of nanopockets. The open tips and slanting graphene planes which have terminal edges along the inner wall of CNF provide channels for the penetration of the decomposition products of the iron phenanthroline complex at high temperature. Ultimately, this leads to creation of higher number of activesites, which eventually resulting into the higher ORR activity of the homemade non-Pt electrocatalyst. Although the FeN<sub>x</sub> based system shows

notable ORR, the performance of the catalyst is limited by few factors. For example, the nitrogen doping could occur predominantly on the inner wall of CNF owing to the inert outer surface of CNF. Moreover, the developed activesites on the inner wall of CNF could not be detected effectively by the CV and RDE methods due to the resistance imposed for solvent entry. This could be a problem only in aqueous systems where surface tension dominates whereas in real fuel cell testing, the gaseous reactants under semi-vapor condition are expected to diffuse easily towards the active sites for ORR. Therefore, the appreciable ORR activity displayed by the homemade  $\text{FeN}_x\text{CNF}$  catalyst opens up great scope for the fabrication of thin non-Pt fuel cell electrodes.

## **7.2. Study on the Influences of Iron Nitride-Doping for the Development of Low-Pt Electrocatalyst**

As mentioned in Chapter 1, development of the low-Pt electrocatalyst with higher efficiency is one of the possible ways to reduce the cost of the MEA. Accordingly, we have demonstrated the influences of surface functionalization by  $\text{FeN}_x$  doping on the carbon nanofiber ( $\text{FeN}_x\text{CNF}$ ) for the development of low-Pt electrocatalyst. The resulting catalyst (10 wt. %  $\text{PtFeN}_x\text{CNF}$ ) outperforms the commercial Pt/C in terms of higher electrochemical surface area and positive ORR onset potential. This is attributed mainly to the higher dispersion of Pt particles (2-3nm) achieved by the excellent morphological alterations of the graphene matrix upon heteroatom doping. The method provides an effective means to create active centres for nanoparticles decoration, devoid of the normally practising acid and oxidative treatments which are strong enough to impart significant damages to the carbon framework. The novelty of this process is that, while creating potential ORR sites by doping  $\text{FeN}_x$  moiety, the surface morphology acquires

favourable nanodimensional changes to trigger tiny particle dispersion of Pt. The particle size is well maintained between 2-3 nm and the quality of dispersion is excellent. These benefits such as synergistic effects, small and narrow particle distribution and high quality dispersion together helped the system in its 10 % Pt loading to outperform a 20 wt. % Pt/C catalyst in terms of the ORR activity. Moreover, from the polarization plots, a clear benefit with the PtFeN<sub>x</sub>CNF catalyst could be observed throughout the polarization region, starting from the activation polarization to the mass-transfer controlled region. Especially, the favourable onset in the low current density region (activation controlled) implies the enhanced ORR activity of the system. Thus, the enhanced ORR activity of Pt on nitrogen doped catalysts is clearly visible, which emphasizes the pivotal role of nitrogen-doping for the development of low-Pt electrocatalysts.

### **7.3. Development of Efficient ORR Electrocatalyst by Generating Pores and Nitrogen Doped Activesites on Graphene**

It is well known that an electrochemical reaction on the edge planes of carbon nanostructures is more facile than that of the basal planes. Hence, it is highly desirable to develop a suitable carbon material with more edge sites, which could significantly facilitate the nitrogen doping and, hence, to higher ORR activity. Accordingly, significant efforts are given towards the preparation of nitrogen-doped graphene as the ORR electrocatalysts. However, making carbon vacancy on graphene matrix is experimentally challenging. It is also known that the created vacancy in Gr is a perfect trapping site for heteroatom doping such as nitrogen (N), and boron (B). Here, we have demonstrated the efficient method for preparing porous graphene with the aid of the *in-situ* generated Fe<sub>2</sub>O<sub>3</sub> nanoparticles and creation of potential N-doped active sites along the pore

openings. This could be achieved entirely through a chemical process which involves *in-situ* generation of Fe<sub>2</sub>O<sub>3</sub> nanoparticles by the decomposition of a precursor which also contains N. Since the Fe<sub>2</sub>O<sub>3</sub> nanoparticles are of few nanometers in size, the pores created by etching of carbon at the Gr-Fe<sub>2</sub>O<sub>3</sub> interfaces are also of few nanometer in size. The process also successfully demonstrated an efficient way of *in-situ* nitrogen doping at the exposed edges of Gr as and when the pores are being generated. This is conceived as the precursor creates not only the Fe<sub>2</sub>O<sub>3</sub> nanoparticles but it also generates nitrogen moieties during its decomposition and some portion of this will be trapped by the nascent surface of the pore openings of Gr. Further enrichment of the doped nitrogen content could be achieved by subjecting the material for a second round of doping process using an iron-free nitrogen precursor. In this way, both porosity and efficient nitrogen doped active sites could be generated very effectively in a sequential process. The catalyst derived from this study has significantly high electrochemical oxygen reduction activity and, in terms of the overpotential difference, the homemade catalyst is superior to many of the nitrogen doped graphenes. An issue associated with the present study is the creation of the pores solely related to the size the metal oxides and thus controlling parameter remains as an experimental challenge. Considering the ongoing quest for developing metal-free electrodes for PEM fuel cells, this development has great importance.

#### **7.4. Facile Preparation of Nanoporous Graphene by Quantum Dots Removal towards the Effective Nitrogen-Doping for ORR**

From the inspiration of the preparation of nanoporous graphene by drilling with the Fe<sub>2</sub>O<sub>3</sub> nanoparticles, our next aim was to prepare the nanoporous graphene

with controlled size of pores by chemical synthesis method. Since the existing methods to make a hole on graphene are experimentally challenging and expensive, we have introduced the novel route to synthesis the nanoporous graphene by a simple chemical method. The process demonstrated here is very simple and highly scalable. Without using any sophisticated techniques like ion beam or inorganic additives, a simple oxidative treatment provided well distributed and highly size controlled nanopores on graphene. Looking at the commercial viability, this process is easily adaptable for various energy applications. Normally, compared to the other methods of creating nanopores on graphene (such as by using ion ablation, induced by metal nanoparticles *etc.*), the eliminated portion of graphene could be recovered in the present process and they are identified as excellent graphene quantum dots. Thus, two value added products could be produced with high yield and by following relatively easy and scalable process. Further, looking at the design strategy of the material for oxygen reduction application, the novelty lies in the fact we have created lots of edge sites on graphene in a very controlled way to increase the nitrogen doping to get enhanced ORR performance. In the case of normal graphene, there exists a severe limitation in increasing the number of nitrogen doped active sites as the nitrogen doping can be mainly done along the edge sites. By creating nanopores, a concomitant increase in the nitrogen doped active sites is achieved (NpGr). This is actually reflected in its electrochemical oxygen reduction activity as well. The ORR activity of NpGr is much higher than that of the nitrogen-doped non-porous graphene (NGr) and many other reported nitrogen-doped carbon materials. The

superior activity of NpGr is also due to the higher content of nitrogen particularly pyridinic nitrogen. As, nitrogen doped porous graphene appears like a potential cost-effective electrocatalyst for ORR, its counterpart GQD also highlights its unique luminescent properties, which can have potential applications in nano electronics. Overall, the method discussed here gives a simple and easily scalable process for developing two potentially value added products having greater prospects in nano electronics and energy applications.

### **7.5. Development of Porous Carbon Enriched with Iron Nitride Doped Activesites for ORR**

From the through literature survey, it is understood that the nano structured porous carbons have attracted several applications namely gas adsorption, supercapacitors, fuel cells *etc.* The preparation processes of such porous carbonaceous materials often involves inexpensive synthetic pathway which is an added advantage to reduce the cost of fuel cells. Accordingly, Isorecticular Zeolitic Imidazolate Frameworks (IRZIFs) with diverse pore structure and fascinating morphological features were employed as the hard templates to prepare the new classes of iron nitride doped porous carbons by impregnating with iron-phenanthroline complex followed by pyrolysis. Porous structure of IRZIFs has been replicated in the carbons derived from them. This microporous network significantly favours creation of the nitrogen doped active sites and subsequently higher ORR activity. Indeed, the process is very simple and is less expensive compared to the several reported processes for developing the M/N/C catalysts, where expensive carbon nano morphologies like CNFs and graphenes are being used. The methodology adopted here provides a well-structured porous carbon with the walls clearly demarcated

with graphitic frameworks where iron nitride doping could be simultaneously established. These doped sites display potential activity for ORR, leading to a highly efficient, cost-effective electrocatalyst for PEFC applications.

Overall, the present thesis discloses the effect of peculiar morphology, nanoconfinement and edge sites of carbon material varied from one dimensional to three dimensional to design novel non-Pt electrocatalysts with higher efficiency by means of nitrogen doping for ORR in PEFCs.

## List of Publications

1. “Artificially designed membranes using phosphonated multiwall carbon nanotube-polybenzimidazole composites for polymer electrolyte fuel cells”, R. Kannan, P. Aher, **T. Palaniselvam**, K. Sreekumar, U. K. Kharul and V.K. Pillai, *J. Phys. Chem. Lett.* 2010, 1, 2109-2113.
2. “Facile construction of non-precious iron nitride-doped carbon nanofibers as cathode electrocatalysts for proton exchange membrane fuel cells”, **T. Palaniselvam**, R. Kannan and S. Kurungot, *Chem. Commun.*, 2011, 47, 2910-2912.
3. “Activity modulated low-platinum content oxygen reduction electrocatalysts prepared by inducing nano-order dislocations on carbon nanofiber through N<sub>2</sub>-doping”, **T. Palaniselvam**, A. Irshad, B. Unni, and S. Kurungot., *J. Phys. Chem. C*, 2012, 116, 14754-14763.
4. “An efficient oxygen reduction electrocatalyst from graphene by simultaneously generating pores and nitrogen doped active sites”, **T. Palaniselvam**, H. B. Aiyappa and S. Kurungot., *J. Mater. Chem.* 2012, 22, 23799-23805.
5. “Zeolitic Imidazolate Framework (ZIF) - derived, hollow-core, nitrogen-doped carbon nanostructures for oxygen reduction reactions in PEFCs”, **T. Palaniselvam**, B. P. Biswal, R. Banerjee and S. Kurungot., *Chem. Eur. J.* 2013, 19, 9335-9342.

6. “Nanoporous graphene by quantum dots removal from graphene and its conversion as potential oxygen reduction electrocatalyst *via* nitrogen doping”, **T. Palaniselvam**, O.V. Manila and S. Kurungot, *Energy Environ. Sci*, 2014, DOI:10.1039/C3EE43648A.
7. “An efficient nitrogen and sulphur co-doped carbon as a potential electrocatalyst for oxygen reduction reaction”, **T. Palaniselvam** and S. Kurungot, *manuscript under preparation*, 2014.
8. “Facile preparation of iron/cobalt oxides supported on nitrogen doped porous graphene for oxygen reduction reaction in low temperature fuel cells”. **T. Palaniselvam** and S. Kurungot, *manuscript under preparation*, 2014.

### **Patents**

1. Nanoporous graphene by chipping of graphene quantum dots and its conversion to oxygen reduction electrocatalyst through nitrogen doping, Indian patent application No: **1564DEL2013**.

# Erratum